MAGNETIC RESONANCE ELASTOGRAPHY FOR APPLICATIONS IN RADIATION THERAPY

A Thesis Submitted to the College of

Graduate and Postdoctoral Studies

In Partial Fulfillment of the Requirements

For the Degree of Master of Science

In the Division of Biomedical Engineering

University of Saskatchewan

Saskatoon

By

Lumeng Cui

PERMISSION TO USE

In presenting this thesis in partial fulfillment of the requirements for a Postgraduate degree from the University of Saskatchewan, I agree that the Libraries of this University may make it freely available for inspection. I further agree that permission for copying of this thesis in any manner, in whole or in part, for scholarly purposes may be granted by the professor or professors who supervised my thesis work or, in their absence, by the Head of the Department or the Dean of the College in which my thesis work was done. It is understood that any copying or publication or use of this thesis or parts thereof for financial gain shall not be allowed without my written permission. It is also understood that due recognition shall be given to me and to the University of Saskatchewan in any scholarly use which may be made of any material in my thesis.

DISCLAIMER

Reference in this thesis to any specific commercial products, process, or service by trade name, trademark, manufacturer, or otherwise (CIRS Inc., Eclipse, GE, ImageJ, MATLAB, Mayo Clinic, MRE/Wave, Resoundant®, Resoundant Inc., Saskatchewan Cancer Agency, Siemens, Varian Medical Systems, and 3D Slicer), does not constitute or imply its endorsement, recommendation, or favoring by the University of Saskatchewan. The views and opinions of the author expressed herein do not state or reflect those of the University of Saskatchewan, and shall not be used for advertising or product endorsement purposes.

Requests for permission to copy or to make other uses of materials in this thesis in whole or part should be addressed to:

Head of the Division of Biomedical Engineering
University of Saskatchewan
Saskatoon, Saskatchewan S7N 5A9
Canada

OR

Dean
College of Graduate and Postdoctoral Studies
University of Saskatchewan
Room 116 Thorvaldson Building
110 Science Place
Saskatoon, Saskatchewan S7N 5C9
Canada

ABSTRACT

Magnetic resonance elastography (MRE) is an imaging technique that combines mechanical waves and magnetic resonance imaging (MRI) to determine the elastic properties of tissue. Because MRE is non-invasive, there is great potential and interest for its use in the detection of cancer. The first part of this thesis concentrates on parameter optimization and imaging quality of an MRE system. To do this, we developed a customized quality assurance phantom, and a series of quality control tests to characterize the MRE system. Our results demonstrated that through optimizing scan parameters, such as frequency and amplitude, MRE could provide a good qualitative elastogram for targets with different elasticity values and dimensions. The second part investigated the feasibility of integrating MRE into radiation therapy (RT) workflow. With the aid of a tissue-equivalent prostate phantom (embedded with three dominant intraprostatic lesions (DILs)), an MRE-integrated RT framework was developed. This framework contains a comprehensive scan protocol including Computed Tomography (CT) scan, combined MRI/MRE scans and a Volumetric Modulated Arc Therapy (VMAT) technique for treatment delivery. The results showed that using the comprehensive information could boost the MRE defined DILs to 84 Gy while keeping the remainder of the prostate to 78 Gy. Using a VMAT based technique allowed us to achieve a highly conformal plan (conformity index for the prostate and combined DILs was 0.98 and 0.91). Based on our feasibility study, we concluded that MRE data can be used for targeted radiation dose escalation. In summary, this thesis demonstrates that MRE is feasible for applications in radiation oncology.

ACKNOWLEDGEMENTS

I first would like to express my gratitude to my supervisors, Dr.'s Niranjan Venugopal, Paul Babyn, and Francis Bui for their extremely generous support and selfless mentoring. Their professionalism always encourages and inspires me in an academic setting. In life, each of them is a man with a good soul. I could have never finished this work without their guidance and help. It is and will always be a great honor for me to be their student. They will always have my respect.

I also want to thank my committee members, Dr.'s Emily McWalter, Andrew Alexander, and Mark Eramian for taking their time to read my thesis and sharing their professional views on my thesis. To me, there was no doubt that their invaluable opinions will help me improve myself in the long term.

I am also grateful to the staff from Royal University Hospital, particularly Shawn Kisch, Alain Lalonde, Elaine Roesler, and Dawn Senko for providing technical assistance on the MRI equipment. In the meantime, I would also like to extend my thanks to Dr. Gavin Cranmer-Sargison, the Director of Medical Physics Department in Saskatchewan Cancer Agency, for offering the research resources in the cancer centre.

I appreciate the technical support from our industrial partners, in particular Dr. Gerald Moran from Siemens Canada and Dr. Ted Lynch from CIRS Inc. I would also like to acknowledge Mr. Conrad Yuen from British Columbia Cancer Agency for his help on my project during his Sabbatical.

I would like to express my appreciation to the sources of my funding source, U of S-BIT Master Scholarship and Prostate Cancer Canada Network – Regina.

Lastly, I want to give my very special thanks to my parents, all my family and friends, and Shuyu Shang. I could have never made it this far without their support, encouragement, and love.

TABLE OF CONTENTS

LIST OF TABLES

Table **Page number**

LIST OF FIGURES

Figure **Page number**

LIST OF ABBREVIATIONS

(by alphabetic order)

AC	Alternating Current
ADC	Analog-to-Digital Converter
aveHD	Average Hausdorff Distance
bSSFP	balanced Steady-State Free Precision
CI	Conformity Index
CT	Computed Tomography
CTV	clinical target volume
DI	Direct Inversion
DICOM	Digital Imaging and Communications in Medicine
DIL	Dominant Intraprostatic Lesion
DRE	Digital Rectal Examination
DS	Dice Similarity
DVH	dose-volume histogram
DWI	Diffusion Weighted Imaging
EBRT	External Beam Radiation Therapy
EI	Elasticity Imaging
EMI	Electromagnetic Interference
EPI	Echo Planar Imaging
FE	frequency encoding
FEM	Finite Element Method
FID	Free-Induction Decay
fMRI	functional Magnetic Resonance Imaging
FOV	Field of View
FT	Fourier Transform
GRE	Gradient-Recalled Echo
GTV	gross target volume
Gy	Gray
HD	Hausdorff Distance
LFE	Local Frequency Estimation
LINAC	linear accelerator
MEG	Motion Encoding Gradient
MRA	Magnetic Resonance Angiography
MRE	Magnetic Resonance Elastography
MRI	Magnetic Resonance Imaging
MRS	Magnetic Resonance Spectroscopy
NEX	number for signal averaging

NMR	Nuclear Magnetic Resonance
OAR	organ at risk
PE	phase encoding
PET	Positron Emission Tomography
PTV	planning target volume
PWI	Perfusion Weighted Imaging
PZ	peripheral zone
QA	Quality Assurance
QC	Quality Control
RF	radiofrequency
ROI	regions of interest
RT	Radiation Therapy
RTOG	Radiation Therapy Oncology Group
SCA	Saskatchewan Cancer Agency
SE	Spin Echo
SNR	Signal-to-Noise Ratio
SPAMM	SPAtial Modulation of Magnetization
SPECT	Single Photon Emission Computed Tomography
SS	slice selection
T1W	T1-weighted
T2W	T2-weighted
TE	Transient Elastography
TE	time to echo
TPS	treatment planning system
TR	time to repetition
TV	target volume
USE	Ultrasound Elastography
USFDA (FDA)	United States Food and Drug Administration
VMAT	volumetric modulated arc therapy
WIP	works-in-progress
95%HD	95% Hausdorff Distance

Thesis Overview

There are two main objectives in this thesis: (1) a parameter optimization investigation of Magnetic Resonance Elastography (MRE) scans with the aid of a specialized, newly-developed MRE Quality Assurance (QA) phantom, and (2) a feasibility investigation of the integration of MRE into radiation therapy (RT) workflow using a tissue-equivalent prostate phantom. This thesis itself is broken up into six main chapters:

- Chapter 1: This chapter contains the general introduction and motivation for this work. It also provides a detailed survey of the technology, development, and application of MRE and lists the specific objectives and plans of this thesis.

- Chapter 2: This chapter presents a comprehensive introduction of MRI on its physics, technical realization, and related techniques that will be used in this work.

- Chapter 3: In this chapter, we explain the applied theory and system framework of MRE.

- Chapter 4: This chapter concentrates on the optimization of parameters, the validation of the system's imaging quality, and the development of quality control (QC) tests. To achieve this, a customized QA phantom was developed and used with the MRE system. The phantom and designed tests reveal important concepts, principles, and features of the MRE system, providing the general guidelines and knowledge necessary for using MRE in daily clinical work and other extended applications. A series of QC tests will be developed in this part.

- Chapter 5: In this chapter, we investigate the feasibility of integrating MRE into conventional RT workflow, and will discuss the potential clinical value of MRE. All experiments will be carried out on an anatomically correct tissue-equivalent prostate phantom with three mimicked intraprostatic lesions embedded within it. The MRE-integrated RT framework developed with this phantom will simulate *in vivo* conditions, and allow its application to routine clinic work, as well as potentially extending it to other clinical sites (such as cervix and breast). An MRE-integrated RT framework with a comprehensive scan protocol will be proposed in this part.

- Chapter 6: Finally, this last chapter summarizes the entire work and discusses the future applications of this study.

Peer Reviewed Abstracts and Manuscripts

This work has resulted in peer review contributions to the scientific community. To date these are (see RELATED WORK in page 154 for details)

1. **Lumeng Cui**, Conrad Yuen, Ted Lynch, Paul Babyn, Francis M. Bui, and Niranjan Venugopal, "Development of a novel phantom for routine quality assurance of an MR elastography system", *International Society for Magnetic Resonance in Medicine 2016, Singapore*. (Accepted and presented with a traditional poster on the exhibition)
2. **Lumeng Cui**, Paul Babyn, Francis M. Bui, and Niranjan Venugopal, "Utilization of MR Elastography for selective boost to dominant intraprostatic lesions", *International Society for Magnetic Resonance in Medicine 2017, Honolulu, Hawaii, USA*. (Accepted, presented with a traditional poster on the exhibition along with a 3-minute oral presentation in the Magnetic Resonance Elastography study group session)

Chapter 1

Introduction

Chapter Synopsis

Physicians often use palpation when initially examining patients for changes in tissue density for a variety of examinations. Palpation is a time-tested physical examination technique in clinical medicine. While medical imaging systems such as X-ray, Computed Tomography (CT), Ultrasound, and Magnetic Resonance Imaging (MRI) can provide us with an objective internal view of anatomical structures from deep inside the human body, these modalities cannot completely replace palpation because none of them have the ability to access tissue's mechanical properties. In this chapter, we introduce Magnetic Resonance Elastography (MRE), its historical development and applications, and the objectives of this thesis.

1.1. What is Magnetic Resonance Elastography?

Abnormalities in soft tissues or organs are often characterized by variations in mechanical properties such as elasticity. Cancerous tumours or fibrotic organs such as breast tumours, thyroid nodules, prostate cancer, and liver cirrhosis are often stiffer than healthy tissues [1, Ch. 93, 176–177, 190], [2]–[5]. To take advantage of the correlation between the abnormality and the resulting change in elasticity, physicians often use palpation[1] when initially examining patients. Palpation is a time-tested physical examination technique in clinical medicine. By using the hand or fingers to directly apply pressure to the surface of the body, a practitioner is able to determine the condition of a specified part or organ: for example, palpation can reveal information about an organ's size or consistency. While medical imaging systems such as X-ray, Computed Tomography (CT), Ultrasound, and Magnetic Resonance Imaging (MRI) can provide us with an objective internal view of anatomical structures from deep inside the human body, these modalities cannot completely replace palpation because none of them have the ability to access tissue's mechanical properties. This explains why palpation is still widely performed today and why palpation techniques have become a routine part of clinical examination. For example, abdominal palpation is used to examine palpable masses on the liver, while Digital Rectal Examination (DRE) is a key tool in detecting prostate cancer. Gynecological examinations (usually divided into breast examinations and pelvic

[1]"The act of feeling with the hand; theapplication of the fingers with light pressure to the surface of the body for the purposeof determining the condition of the parts beneath in physical diagnosis."—*Dorland's Medical Dictionary for Health Consumers.* S.v. "palpation." Retrieved March 14 2017 from http://medical-dictionary.thefreedictionary.com/palpation

examinations) are based on palpation as well [1, Ch. 176–177], [2], [3], [6], [7, p. 1], [8]. As a widely-used examination tool, palpation is inexpensive and can be performed with great ease. However, it still has deficiencies: it is superficial, qualitative, subjective, and limited by the touch sensitivity of the practitioner. For example, there are non-palpable tumours in breast cancer and prostate cancer [9]–[11]. Those limitations suggest that some small and deeply located tumours cannot be easily detected via palpation. Even if these abnormalities are successfully detected, due to the subjectivity of palpation they might not be identified as tumours until a further procedure is conducted. Biopsy is the gold standard for the diagnosis of tumours or fibrosis, but it is an invasive procedure and a painful experience for most patients [4], [11]–[14].

Given the limited efficacy of palpation and the pain of biopsy, a non-invasive imaging technique known as elastography was developed. This technique combines the principles of palpation with the use of medical imaging modalities. There are two main types of elastography modalities: Ultrasound Elastography (USE) and Magnetic Resonance Elastography (MRE). They are both able to non-invasively obtain the mechanical properties of tissue, and with the aid of Ultrasound or MRI, small and deeply hidden cancerous tissues become visible due to the difference in stiffness when compared to surrounding healthy regions [15]–[18]. To tackle the deficiencies of palpation, elastography converts palpation's qualitative diagnostic results into an objective and quantitative representation that straightforwardly reflects the elasticity distribution. Moreover, instead of applying physical pressure to the body surface, elastography uses a low frequency mechanical vibration to reach the small and deeply located suspicious regions: this is done through the propagation of a harmonic wave. In summary, elastography transforms the qualitative palpation examination into a quantitative imaging tool.

Tissue contrast is one of the most important factors when evaluating the performance of medical imaging systems. Contrast in X-ray and CT is based on the differential attenuation of X-rays in tissues, while the contrast in MRI is typically determined by the density and relaxation properties of the hydrogen atoms in the tissue. Contrast in Ultrasound is determined by the reflections and scatterings of the ultrasound wave in the tissue, while Elastography's contrast is primarily based on tissue elasticity. The scale of contrast determines the performance of the systems: for example, it is well known that MRI can demonstrate more soft tissue contrast than CT [19]. However, Elastography's contrast scale spans more orders of magnitude than other conventional modalities', such as X-ray, CT, MRI, and ultrasound [18]. Therefore, the broader scale of contrast suggests that on the basis of elasticity, Elastography has a greater potential to increase the dynamic range of tissues in regard to their pathological and healthy states.

The information gained from Elastography can be expressed as Young's Modulus, Shear Modulus, or Bulk Modulus, depending on the methods of loading and measurement. As mentioned before, USE and MRE are the two-current medical imaging elastography techniques. With the help of MRI, MRE is able to directly capture the shear wave generated by the mechanical driver and then calculate the elastogram from the acquired wave propagation through an inversion algorithm

[18]. The MRE technique was invented at the Mayo Clinic in 1995 by Muthupillai et al. [20]. After nearly one decade of development, the first commercial MRE system approved by the United States Food and Drug Administration (USFDA, and hereinafter to be referred as FDA) became available in 2009. By 2015, around 450 individual systems were available for clinical use worldwide. MRE is carried out in three steps: (1) mechanical excitation, (2) displacement measurement, and (3) elastogram calculation. In the first step, the tissue is excited by a driver system at a fixed frequency. In the second step, the MRI scanner (with the help of a special pulse sequence) will record the states of motion in tissue over a period of time, generating a series of "screenshots" of the wave propagation. In the third and final step, the acquired displacement maps will be converted into an elastogram through an inversion algorithm for display. The whole process is described in Figure 1.1 (A) and (B). These subsystems will be described in further detail in Chapter 3.

MRE was originally designed to assess liver hardening caused by chronic liver disease, although it was assumed to have potential applications for other parts of the body [21]. Because of this, the clinical applications of MRE mainly focus on liver diseases: for example, the detection and staging of liver fibrosis. MRE's successful application to liver diseases has gradually led to the study of other clinical sites, including the prostate, breast, and brain [22]. However, to improve consistency of results and maintain overall system performance, a series of Quality Assurance (QA)[2] procedures would need to be developed. QA focuses on the systems processes and uses data to analyze service delivery. Furthermore, it encourages a team approach to problem solving and quality improvement [23]. The QA process is primarily concerned with the quality of care, the identification of possible issues in care delivery, the approach to the identified issues, and using repeated measures to verify solutions and improvements. Dimensions of quality include technical competence, access to service, effectiveness, interpersonal relations, efficiency, continuity, safety, and amenities [23]. In the setting of using MRE for clinical care, a QA process ensures that MRE applications are reliable and reproducible prior to the *in vivo* scan. Furthermore, the MRE QA program helps to create generalized guidelines for MRE applications: not only does it provide user instruction, but it also expands the potential MRE applications to additional clinical sites (such as prostate, cervix, and breast).

[2]"A system for evaluating performance, as in the delivery of services or the quality of products provided to consumers, customers, or patients."—*The American Heritage® Medical Dictionary*. S.v. "Quality Assurance." Retrieved March 14 2017 from http://medical-dictionary.thefreedictionary.com/quality+assurance

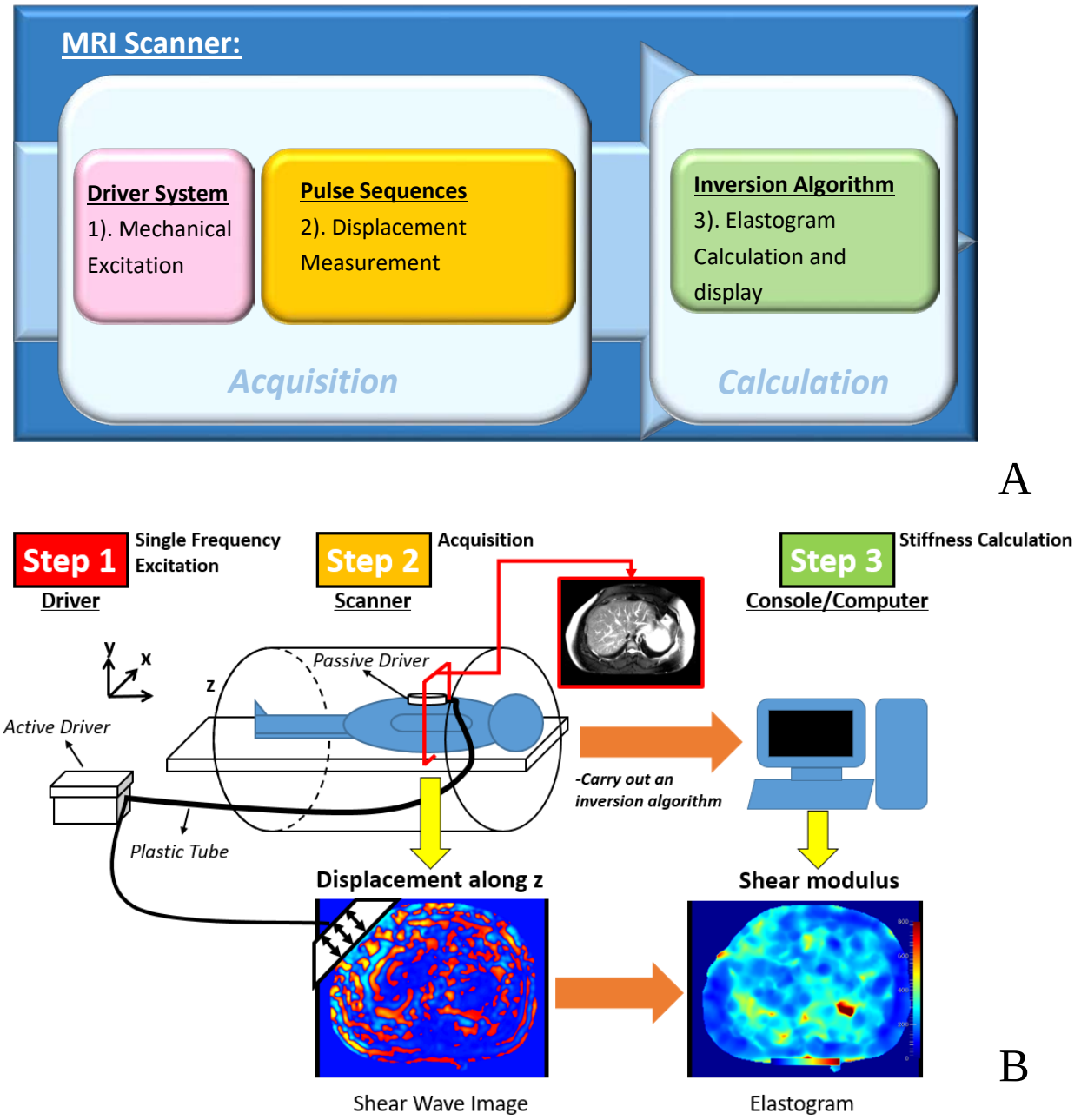

Figure 1. 1 (A) Flowchart and three main components of MRE; and **(B)** An overview of an MRE process describing MRE's three main steps and corresponding outputs.

1.2. Historical Development of Elastography Techniques and MRE's Applications

The investigation of elastic theory can be traced back to the seventeenth century, when a British physicist named Robert Hooke proposed Hooke's Law. By contrast, the study of Elasticity Imaging (EI) began in the 1950s when Oestreicher et al. investigated the behaviors of the body surface when subjected to intense sound fields or excited mechanical vibration [16], [24], [25]. After applying a piston driven by an electrodynamic loudspeaker system to the surface of the body, Oestreicher's group photographed the wave propagation with the help of a synchronized stroboscopic light. They then estimated the shear stiffness from the wave propagation via the wave motion equation [25]. Their studies identified three key components of EI: (1) the driver system (consisting of a piston driven by an electrodynamic loudspeaker in their works), (2) the imaging system (comprised of a strobe light and photography here), and (3) the strategy for estimating shear stiffness using a wave motion equation.

In 1982, Dickinson et al. used ultrasound to measure the motion of soft tissues [26]. They regarded the arterial pressure pulse as a driving force, using the correlation coefficient between two successive A-scans (also known as the cross-correlation technique) as a characteristic parameter to reflect tissue motion. In their conclusions, they claimed that the motion pattern would vary in terms of the difference of elasticity. However, they only measured the motion of soft tissues in healthy volunteers and did not provide estimates of the tissue's elasticity. In 1986, Tristam et al. continued the study of tissue motion using the same A-scan technique (i.e. correlation analysis) [27]. Specifically, they used ultrasound measurement to analyze the correlation coefficients, comparing the differences in soft tissue motion between volunteers with normal livers and patients with abdominal tumours. Moreover, the correlation coefficients between the two successive A-scans were generalized as the parameter in order to reflect the state of the tissue. In 1988, Tristam et al. successfully separated the normal liver tissue in the healthy volunteers, the cancerous tissue in the patients, and the normal liver regions in the same cancer patient by applying Fourier analysis to the acquired correlation patterns [28]. However, in the correlation analysis, the results are reported as the correlation coefficients between two successive A-scans varying with time, instead of an image reflecting elasticity information.

In 1982, Wilson et al. used the Doppler velocity technique to measure soft tissue deformation caused by arterial pulsation while using a M-mode scan [29]. With the help of the Doppler velocity technique, they recorded the motion data along a select ultrasound line (a manually-chosen segment in the inspected tissue) in velocities varying with time. Subsequently, the displacement information along this segment was calculated from the integral of the recorded velocities over the scanned time. Compared to the A-scan technique, the Doppler velocity measurement is able to use velocity to calculate displacement, which more straightforwardly reflects the wave propagation along a selected segment in a mono-dimension: the cardiac-induced motion can be clearly observed in Fig.

1 (a) in [29]. However, Wilson et al. did not extract the elasticity information from wave propagation obtained in their studies. In 1990, Yamakoshi et al. used the Doppler velocity measurement technique and an external, low-frequency, mechanical harmonic excitation to acquire a wave propagation image in the B-mode: this illustrated the Doppler velocity technique's potential value for demonstrating the mechanical properties of soft tissues [30].

Though studies on acquiring tissue motion had progressed since the introduction of ultrasound, using acquired motion patterns to estimate elasticity did not occur until Lerner et al. (1990) and Parker et al. (1990) presented a qualitative stiffness map overlaying a B-scan image [31], [32]. They proposed using the term "Sonoelasticity" to describe this technique. Then, in 1991, Ophir et al. introduced the term "Elastography" because their group obtained an elastic modulus map. In their works, the elastic modulus map is calculated, according to Hooke's Law, from a stress map estimated from a static compressed force as well as a strain map measured using a cross-correlation technique [33]. Another ultrasound-based EI technique is Transient Elastography (TE): the technique was proposed by Sandrin et al. in 2003 and developed by de Lédinghen et al. in 2007 [34], [35]. They used a cross-correlation technique combined with an external vibrator to acquire the velocity information of the introduced transient shear wave, calculating Young's Modulus by using the velocity of the transient shear wave. This ultrasound-based elasticity imaging technique has become one of the two major EI techniques to date. However, further investigation of ultrasound-based elasticity imaging techniques (generally referred to as Ultrasound Elastography) is beyond the scope of this thesis. The general introduction to the principles, techniques, advantages, and limitations of Ultrasound Elastography (USE) can be found in [36], [37].

Another major EI technique is based on Magnetic Resonance Imaging (MRI). In 1995 Muthupillai et al. developed Magnetic Resonance Elastography (MRE) while working at the Mayo Clinic [20]. MRE is able to quantitatively image the shear modulus of tissues via mechanical excitation and a MRI platform. There are generally three steps for MRE: (1) generate shear waves in the tissue via an external driver, (2) use a MRI platform to image the wave propagation through a special acquisition pulse sequence, and (3) convert the wave images obtained in step 2 into a quantitative image displaying the stiffness distribution [18]. Each of these three steps has a corresponding component: the driver system, the MRE pulse sequence, and the inversion algorithm, respectively.

There are many methods for categorizing the driver system. First, the driver system can be categorized by its design of configuration and applied technique. The first type of driver system is an active-passive model with a long transmission. For example, Talwalkar et al. used a soft plastic tube to connect an active loudspeaker driver placed in the mechanical room to a passive driver located in the scanner room [38]. This design has good MR compatibility, a relatively simple configuration, and a low cost, but the long transmission between the active driver and passive driver can cause phase lags in the periodic mechanical motion and energy loss. Sack et al. demonstrated a similar driver design for brain MRE in their paper [39]. Their driver system contained a passive

driver (which is compatible to the structure of brain), an active driver (another loudspeaker), and a rigid carbon fiber rod connecting the drivers. The carbon fiber rod solved the phase lag issue, but due to its rigid conducting medium, the active driver had to be placed inside the scanner room, potentially causing Electromagnetic Interference (EMI). Moreover, the rigid rod also restricted the orientation of the driver and the placement of patients. Lewa et al. replaced the loudspeaker with a magnet-embedded vibrator and used a rigid carbon fiber rod for both the passive driver and the transmission tool [40]. While the magnet-embedded vibrator located in the scanner room was easy to control and calibrate, the permanent magnet inside affected MR compatibility. A different active-passive driver solution that used an ultrasound motor as the transmission tool managed to achieve good MR compatibility, avoid EMI, and offer precise control over synchronization [41], [42]. However, the configurations of this design were relatively complicated. An alternative is a driver system that uses electromagnetic coils and a magnetic field. This driver design uses the Lorentz force (which is generated by introducing Alternating Current (AC) in the main magnetic field) as its driving force [43]. This design was relatively inexpensive and simple, but it was inflexible and EMI could be an issue as well. Driver systems can also be based on piezoelectric materials. Doyley et al. used a piezoelectric actuator in their work [44]. Though the piezoelectric-based actuator offered precise control and had good MR compatibility, piezoelectric materials are expensive and the produced displacement was relatively small. To address this shortcoming, Uffmann et al. built a 247-mm-long piezoelectric stack bar for the actuation device, significantly elongating the produced displacement [45]. However, this long piezoelectric stack bar was very expensive to build. Similarly, Chan et al. developed a bending stack that consisted of two stack bars, a contracting bar and an extending bar [46].

Alternatively, the driver system can be categorized according to whether it is a surface driver or a needle-based driver. Most current driver systems are surface drivers: these drivers are preferred due to their non-invasive characteristics [38]–[45]. However, the surface driver has limited penetration. In order to better reach deep targets, groups such as Rossman et al. developed the needle-based driver [43]. Additionally, the piezoelectric-based driver designed by Chan et al. is also a needle-based driver [46]. Though the needle-based driver has good penetration and can easily reach deep targets, the application of needle turns MRE scan into an invasive process.

The driver can also be categorized as a single driver or a multiple driver. Most driver designs are single drivers, but Mariappan et al. proposed a multiple-driver design, the phase-array driver [47]. Compared to a single driver, a driver with multiple vibrating sources can compensate for attenuation during the wave propagation.

Finally, the driver can be categorized as being either research oriented or clinic oriented. Though there are many published driver systems, the Resoundant® driver system is the only FDA-approved driver system available to clinics. As a result, it has been adopted by many groups to date [48]. However, researchers often develop customized driver systems for their studies. These designs might be suitable for specific problems, but they lack a unified standard or design criteria.

For example, Honarvar et al. developed a customized inversion algorithm using a self-designed driver system [49]. The MRE technique was originally invented for assessing hepatic fibrosis in the liver, so the Resoundant® system's applications are typically limited to liver-related studies [22], [50], [51]. However, in 2015 Sudhakar et al. demonstrated the Resoundant® system's potential use for other clinical sites including kidney and pancreas, depending on the placement of the passive driver [22].

In order to measure the tissue motion excited by the driver system, MRE uses a special technique named phase-contrast MRI [52]. The phase-contrast technique relies on the Motion Encoding Gradient (MEG) realized by two successive bipolar pulses with opposite polarity. In 1985, Wedeen et al. successfully applied the phase-contrast technique to Magnetic Resonance Angiography (MRA) [53]. The MEG pairs used in MRA helped visualize blood vessel flow by encoding the velocity at each point into a phase value [54]. Similarly, in 1995 Muthupillai et al. used MEG pairs to translate shear wave propagation into a phase-contrast image [20]. The MRE sequences are adapted from the conventional MRI sequences by inserting MEG pairs into a specific gradient direction(s). For example, Muthupillai et al. used a MRE sequence based on Gradient-Recalled Echo (GRE) [20]. Other groups have developed MRE pulse sequences based on conventional MRI pulse sequences such as Spin Echo (SE), Echo Planar Imaging (EPI), SPAtial Modulation of Magnetization (SPAMM), and balanced Steady-State Free Precision (bSSFP) [39], [40], [55]–[59]. These combinations absorb the unique characteristics and features of each MRI pulse sequence or technique. For example, the application of EPI can accelerate the acquisition of MRE. Likewise, the MRE pulse sequence, which is approved by the FDA for liver inspection and able to work with the Resoudant system, is based on GRE and largely used in clinical settings [60]. This sequence inserts MEG pairs into the Slice-Selection direction (Z direction), and the frequency of MEG is locked at 60 Hz.

Different stiffness levels are demonstrated by variations in wave propagation. Wave propagation can be converted into information about tissue stiffness using a special calculation called an inversion algorithm. The driver system and MRI scanner (the MRE pulse sequence) acquire wave images, while the inversion algorithm converts the wave images to stiffness information, also known as an elastogram or stiffness map. The conversion from wave images to elastogram is achieved by using assumptions about isotropy, homogeneity, and incompressibility to solve the tissue's motion model [18], [20], [61], [62]. The measurement values for this model are the mechanical wave's displacement fields in all directions, while the estimate values for this model are the first Lamé parameter λ (unrelated to the elastogram) and the second Lamé parameter μ (the quantity reported by elastogram: it is also known as the shear modulus). Moreover, to rapidly compute the shear modulus, the motion model can be transformed into a simpler equation, $\mu = \rho V_s^2$, where ρ represents the density of tissue (usually assumed as 1000 kg/m^3) and V_s is the velocity of the shear wave. The earliest MRE inversion algorithm was the Local Frequency Estimation (LFE) developed by Manduca et al. in 1996 [61]. This algorithm is less complicated and is widely used by the MRE community [50], [51], [63]–[71]. The principle and technical

realization of LFE will be further discussed in Chapter 3, section 3.4.2.1. In 2001, Oliphant et al. proposed another major inversion algorithm known as Direct Inversion (DI) [72]. This algorithm simplifies the tissue's motion model to a Helmholtz equation: more details can be found in Chapter 3, section 3.4.2.2. The tissue's motion model can be also solved by an inversion algorithm based on the Finite Element Method (FEM) without any mathematical simplification: this will be further discussed in detail in Chapter 3, section 3.4.2.3. The FEM-based inversion algorithm is usually divided into direct and iterative methods, and is sometimes combined with other signal processing techniques to improve the quality of the elastogram [49], [73]–[80].

The assessment of hepatic fibrosis and cirrhosis via MRE is the most successful clinical application so far [50], [60], [64], [69], [81]–[86]. The only commercial MRE system is primarily used for liver examination [50], [64], [84], [85]. Research has been largely dedicated to finding and interpreting clinical values from the elastogram, or searching for potential factors affecting the results [51], [66]. For instance, there is still no consensus about the cutoff-elasticity that would reveal the pathologic state of liver tissue [18], [51], [87, pp. 46–49]. Another promising MRE application is the detection of breast tumours that are significantly harder than normal tissues [18]. Many groups have achieved some success using MRE to examine breast tumours [88]. Using MRE to access the mechanical properties of the brain is also a valuable application, because changes to brain tissue stiffness may indicate certain brain diseases [88]. Some researchers have also extended MRE to the examination of prostate tumours, due to the difference in stiffness between the pathological and healthy tissues [63], [67], [89]–[92].

Though most of MRE's clinical applications are for the liver, the MRE community is keen to extend MRE to more clinical sites (such as prostate, cervix, and breast), including the investigation of scan protocol and the development of related subsystems. MRE has demonstrated enormous clinical value by using variations in mechanical properties to identify diseases that other traditional imaging techniques are unable to discover/characterize.

1.3. Research Objectives

The over all goal of this work is to bring MRE into daily clinical use. However, realistically, before achieving this goal, it would be necessary develop a specialized QA (Quality Assurance) phantom to validate the MRE system and study the imaging parameters and its impact on image quality. Furthermore, these investigations would be instructive for others who wish to explore other MRE-related applications and lastly, these MRE-related applications could be translated to clinical scenarios depending on their feasibility, safety, and practicality.

The specific objectives of this thesis are:

1) To develop a novel specialized MRE QA phantom (Chapter 4);
2) To validate the elasticity measurements of a commercial MRE system with the help of the novel QA phantom (Chapter 4);

3) To optimize MRE image acquisition parameters and investigate the impact associated with the selection of these parameters to the image quality with the help of the novel phantom (Chapter 4);
4) To investigate the potential feasibility of integrating MRE process to radiation therapy procedure with the aid of a prostate phantom (Chapter 5).

Chapter 2

Magnetic Resonance Imaging

Chapter Synopsis

Magnetic Resonance Imaging (MRI) is an imaging modality that has been widely used in medical imaging. MRI is based on a physical phenomenon in which the nuclear spins in a magnetic field emit an electromagnetic signal when receiving a radiofrequency (RF) pulse. This phenomenon is described as Nuclear Magnetic Resonance (NMR). With the help of RF pulse (which is used to excite the nuclear spins) and gradient fields (which are used to encode the spatial position information of the excited nuclear spins), these resonance signals can be reconstructed into an image reflecting the anatomical structure of the human body: this is called a NMR image. Purell et al. discovered the phenomenon of NMR in 1946, but it was only in 1973 that Lauterbur et al. acquired the first NMR image [93]. *Unlike conventional imaging systems such as X-ray or Computed Tomography (CT), Magnetic Resonance Imaging is not based on ionizing radiation and thus results in less direct damage to the human body. In addition, when compared to other imaging modalities such as X-Ray, CT, and ultrasound, MRI usually has better soft tissue contrast. Moreover, because of its three-dimensional gradient fields, MRI is able to acquire anatomical planes from any of the three dimensions or a 3D volume.*

This chapter presents the basic physics behind MRI imaging and serves as a pre-cursor to discuss Magnetic Resonance Elastography (MRE) in the next chapter. To better understand the technical realization of MRE, the related MRI technique, i.e. pulse sequence, is necessary; and to further comprehend the pulse sequence, the physics behind MRI must be explicitly explained first. Therefore, this chapter begins with describing the MRI physics including nuclear spin, magnetic fields, and relaxation; then it covers the basis of MRI technique, such as radiofrequency excitation, spatial encoding gradients, K-space, and the Fourier Transform for reconstruction; and lastly, it introduces the pulse sequence to provide a theoretical and technical background for the MRE technique in Chapter 3.

2.1. Spins, Magnetic Fields, and Relaxation

The concept of angular momentum originates from classical mechanics, and describes the intensity of an object's rotation around an axis. There are two types of angular momenta, orbital angular momentum and spin angular momentum. As their names suggest, each type of momentum corresponds to a different type of rotation: orbital angular momentum corresponds to orbital motion, and spin angular momentum corresponds to spin. In 1925, Uhlenbeck and Goudsmit claimed that

the electron possesses a spin angular momentum with an associated magnetic moment, building upon Stern and Gerlach's 1921 experiment results. According to Uhlenbeck and Goudsmit, the spin angular momentum of an electron (as the mass or charge of a particle) is an intrinsic characteristic. In addition, in Stern and Gerlach's results, an electron interacting with the external magnetic field ended up with only two independent states instead of a continuous distribution of states: because of this, the spin angular momentum (spin for short) of the electron is defined as a strict quantum mechanical property. In summary, the orbital motion and spin of charged particles are both able to produce their own magnetic moments. Likewise, a nucleus (comprised of protons with positive charges and neutrons with no charges) also possesses spin: this consists of a vector sum called nuclear spin, and it is also an intrinsic quantum mechanical property. However, because the nucleus is located at the center of the atom, it has no orbital motion.

Nuclear Magnetic Resonance (NMR) is the response of atomic nuclei with spin and its associated magnetic moment to an external magnetic field. The nuclear spin can be visualized in classical mechanics, even though it is a quantum mechanical property. For a charged particle (nucleus or electron) rotating about an axis as shown in Figure 2.1, a constant quantity, gyromagnetic ratio γ, can bridge the relationship between the particle's spin angular momentum $\boldsymbol{L}$ and its magnetic moment $\boldsymbol{\mu}$ associated with the spin [94, p. 65]:

$$\boldsymbol{\mu} = \gamma \boldsymbol{L}, \tag{2.1}$$

where the magnetic moment $\boldsymbol{\mu}$ and angular momentum $\boldsymbol{L}$ have the same direction, and the gyromagnetic ratio γ can be found in Table 2.1.

When an atom is placed in an external magnetic field ($\boldsymbol{B_0}$), the magnetic moment associated with the spin $\boldsymbol{\mu}$ will interact with the external magnetic field, initiating a phenomenon called precession. Specially, precession describes that when an external force (e.g. magnetic field) is applied to an object (e.g. nucleus) rotating about its own axis (i.e. spin), the object's rotational axis will rotate about the direction of the force with an angular velocity $\boldsymbol{\omega_0}$ as shown in Figure 2.1 [95, pp. 58–63].

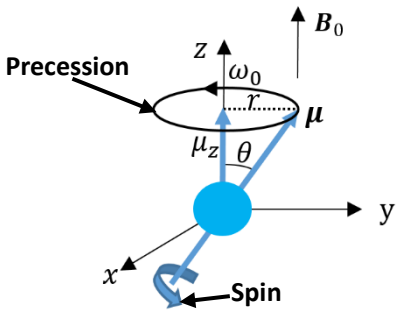

Figure 2. 1 Precession of a nuclear spin with associated magnetic moment ($\boldsymbol{\mu}$) about an external magnetic field $\boldsymbol{B_0}$ with an angular velocity $\boldsymbol{\omega_0}$.

The angular velocity of precession $\boldsymbol{\omega_0}$ can be obtained through the following equation (for derivation see [95, pp. 61–63]):

$$\boldsymbol{\omega_0} = \gamma \boldsymbol{B}_0. \tag{2.2}$$

Moreover, a spin with its associated magnetic moment also possesses a potential energy that is defined as (see [94, p. 66])

$$\boldsymbol{E} = -\boldsymbol{\mu} \cdot \boldsymbol{B}_0 = -\mu B_0 \cos\theta. \tag{2.3}$$

In classical physics, the angular momentum's direction is assumed to be random, so the potential energy carried by the magnetic moment falls within a range of $[-\mu B_0, \mu B_0]$ [94, p. 66]. However, according to Stern and Gerlach's 1921 experiment, there is only a restricted number of directions for the spin of an elementary particle (proton, electron, or any other nuclei) and its associated magnetic moment: this is summarized as the space quantization [94, p. 66]. In summary, it is incorrect to use classical physics to explain the precession of an elementary particle's spin, and the spin and its associated magnetic moment are strict quantum mechanical properties [95, pp. 59–61].

According to the quantum mechanics, the amplitude of the spin is defined as follows [96, pp. 4–6]:

$$L = \frac{h}{2\pi}\sqrt{I(I+1)}, \tag{2.4}$$

where I is the spin quantum number defined as an integral or half-integral, and h is Plank's constant. Table 2.1 lists the spin quantum number of an electron and several other common nuclei [94, p. 65].

Table 2. 1 Spin quantum numbers of an electron and several common nuclei

Particle	Spin (I)	$\frac{\gamma}{2\pi}$ (*)
Electron	1/2	28.03 GHz/T (**)
$^{1}_{1}$H (Hydrogen atom, or Proton)	1/2	42.57 MHz/T
$^{12}_{6}$C (Carbon atom)	0	-
$^{14}_{7}$N (Nitrogen atom)	1	3.08 MHz/T
$^{16}_{8}$O (Oxygen atom)	0	-

* γ is the gyromagnetic ratio; and $\frac{\gamma}{2\pi}$ can replace γ in (2.2) calculating the frequency of precession f_0 since $f_0 = \omega_0/2\pi$;
** T represents Tesla which is the SI unit of magnetic field;

Given that the direction of spin is limited to a restricted number of quantized orientations instead of varying continuously from 0° to 360°, the component of spin along the z direction is written as follows [96, pp. 4–6]:

$$L_z = \frac{h}{2\pi}m, \tag{2.5}$$

where m has $2I+1$ values, given by

$$m = I, I-1, I-2, \ldots, -I. \tag{2.6}$$

and $I = \frac{1}{2}$ especially for protons, electrons and neutrons.

The quantized magnetic moment along the z direction can be denoted as follows [96, p. 5]:

$$\mu_z = \gamma\left(\frac{h}{2\pi}m\right) \tag{2.7}$$

combining (2.1) and (2.5). The magnetic potential energy of the spin is also quantized as follows [96, p. 5]:

$$\boldsymbol{E} = -\boldsymbol{\mu}\cdot\boldsymbol{B}_0 = -\mu B_0\cos\theta = -\mu_z B_0 = -\gamma\left(\frac{hm}{2\pi}\right)B_0 \tag{2.8}$$

according to (2.3) and (2.7). In quantum mechanics, for protons for example, there are two possible energy states for its magnetic moment, namely, a lower and a higher energy state. To excite the spin from the lower energy state to the higher energy state, the required energy (which can be provided by an electromagnetic wave) must equal to

$$\Delta\boldsymbol{E} = h\gamma\left(\frac{1}{2\pi}\right)B_0 = hv_{RF}, \tag{2.9}$$

where v_{RF} is the frequency of the electromagnetic wave, and it is given by

$$v_{RF} = \gamma\left(\frac{1}{2\pi}\right)B_0, \tag{2.10}$$

and therefore,

$$\boldsymbol{\omega_{RF}} = \gamma\boldsymbol{B_0}, \tag{2.11}$$

where $\boldsymbol{\omega_{RF}}$ is called Larmor (angular) Frequency [94, pp. 66–67]. According to (2.2), the precession angular frequency $\boldsymbol{\omega_0}$ is also equal to $\gamma\boldsymbol{B_0}$; therefore, $\boldsymbol{\omega_{RF}} = \boldsymbol{\omega_0}$ is the resonance condition [95, pp. 69–70]. From the angle of energy, the spin with the lowest energy state can switch to the highest energy state during resonance.

According to Table 2.1, each atomic nuclear spin can only be excited by its corresponding Larmor frequency: this is the only situation in which the resonance condition is met, even for the electron spin in the same atom. For example, when a hydrogen atom with one proton and one electron is placed in a 3.0 Tesla external magnetic field, the Larmor frequency for the proton spin and electron spin are 127.71 MHz and 84.09 GHz, respectively. Therefore, theoretically speaking, the electron spin of this hydrogen atom will not reach its resonance condition when its proton spin does. Because of the abundant distribution of hydrogen in the human body (in water, fat, etc.), NMR is mainly about the magnetic resonance of the hydrogen nucleus' spin (proton spin) [94, p. 67]. A radiofrequency (RF) pulse (an electromagnetic wave) is used to excite the magnetic resonance of the proton spin by using the proton spin's Larmor frequency.

Several spins with magnetic moments in each small region can maintain a dynamic equilibrium where the sum magnetic moment of the spins can be equivalent to a net macroscopic magnetization along the z direction with zero magnetization in the transverse plane as Figure 2.2 (A) shows [94,

pp. 67–68]. As previously stated, there are two possible energy states for the spin aligning with the external magnetic field. As demonstrated in Figure 2.2 (A), the spin marked by α is the lowest energy state that is preferentially occupied [96, pp. 6–8]. The spin labelled β is the highest energy state with fewer spins than α in each small region. Therefore, the net macroscopic magnetization in each small region always has the same direction as the external magnetic field, and the sum of it, $\boldsymbol{M_0}$, can be expressed as follows [94, p. 67]:

$$\boldsymbol{M_0} = \sum_{i=1}^{s} \boldsymbol{\mu_i}, \tag{2.12}$$

where s is the number of the spins with their associated magnetic moments in each small region, and $\boldsymbol{\mu_i}$ is each individual magnetic moment.

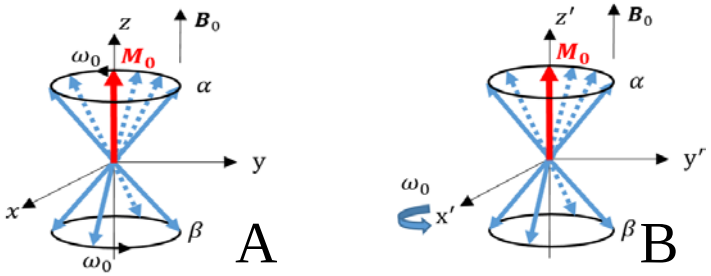

Figure 2. 2 (A) shows magnetic moments in a static frame of reference; and **(B)** illustrates magnetic moments in a dynamic frame of reference. Blue vectors are magnetic moments produced by spins within a region, and the red vector is the net macroscopic magnetization of these magnetic moments.

As Figure 2.2 (A) shows, in a magnetic field $\boldsymbol{B_0}$, the angular velocity of the precession for each spin is $\boldsymbol{\omega_0}$. Therefore, the net magnetization $\boldsymbol{M_0}$ comprised by these spins can also be assumed continuously rotating about the z-axis at $\boldsymbol{\omega_0}$ under a dynamic equilibrium. This macroscopic net magnetization under the dynamic equilibrium can be viewed as a static magnetization when it is in another frame of reference ($x'y'z'$) rotating likewise at $\boldsymbol{\omega_0}$ as shown in Figure 2.2 (B). However, when compared to the strong main external magnetic field, the net magnetization $\boldsymbol{M_0}$ is too small to be detected directly. Therefore, in MRI, $\boldsymbol{B_1}$ (an external magnetic field perpendicular to $\boldsymbol{B_0}$) is applied to flip $\boldsymbol{M_0}$ to the transverse plane where the detection of the net magnetization becomes viable. The $\boldsymbol{B_1}$ magnetic field oscillates at Larmor frequency and is realized by the RF wave with the same frequency. Therefore, the physical explanation of the resonance is that the net magnetization in dynamic equilibrium produces a longitudinal and a transverse component due to an RF wave excitation. In other words, the net magnetization in dynamic equilibrium will swing to $\boldsymbol{B_1}$ with a prescribed angle α° after the RF wave is delivered, as is shown in Figure 2.3 (A) [94, pp. 68–69]. The angle of the magnetization flipping from $\boldsymbol{B_0}$ is jointly controlled by the amplitude and duration of $\boldsymbol{B_1}$. The two angles most commonly used in practices are 90° and 180° [94, pp. 68–69]. A 90° pulse tips the magnetization down to the y' axis, with no magnetization left in the longitudinal direction: this is demonstrated in Figure 2.3 (B). A 180° pulse brings the magnetization to the $-z'$ axis, as is shown in Figure 2.3 (C). This pulse is also known as an inversion pulse. The dynamic equilibrium will be disturbed by the RF wave. When the RF field is turned off, the transverse component will

return to zero and the longitudinal component will revert to the original $\boldsymbol{M_0}$: the system returns to dynamic equilibrium. This process is described as relaxation.

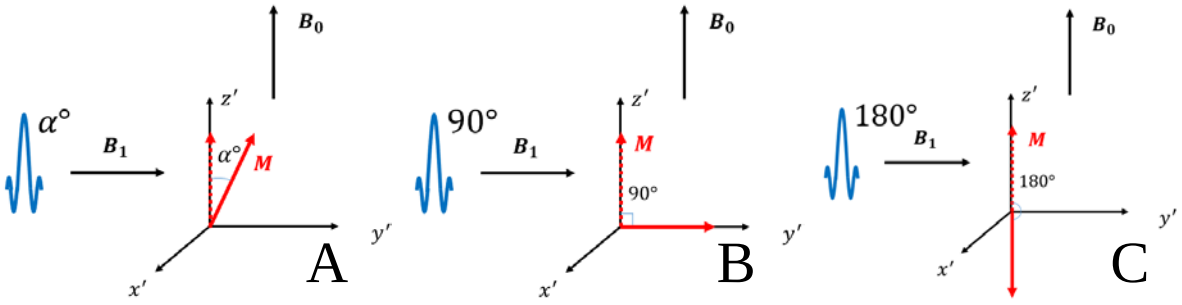

Figure 2. 3 RF Pulses. **(A)** Excitation with a α° RF pulse; **(B)** 90° pulse; and **(C)** 180° pulse.

The relaxation process can be separated into two independent events: spin-spin relaxation and spin-lattice relaxation [94, pp. 69–71]. Spin-spin relaxation primarily contributes to the loss of transverse magnetization. At the beginning of relaxation, all the individual spins still rotate in phase in the transverse plane. The local magnetic field occupied by each spin is affected by the magnetic moment from the surrounding spins. This interaction between spins disrupts the local phase coherence. Each local individual spin rotates at a slightly different angular frequency: this is known as dephasing. As a result, the transverse magnetization is reduced. Moreover, due to the different chemical environments of each type of tissue, the dephasing of the spins in each type of tissue is different: this is the basis of MRI contrast. When the spin-spin relaxation ends, all the individual spins have completely lost their phase coherence, and transverse magnetization goes back to zero. This decrease in transverse magnetization, considered in a rotating frame of reference, can be expressed in the exponential decay model [94, p. 69]:

$$M_{tr_{rotating}}(t) = M_0 \sin\alpha \, \mathrm{e}^{-t/T_2} \tag{2.13}$$

where $M_0 \sin\alpha$ is the transverse magnetization after the RF pulse is applied. If a 90° pulse is applied, the transverse magnetization becomes M_0. T_2 is a tissue-depended constant, describing the time moment when the transverse magnetization of a certain type of tissue decreases to 37% of its initial magnetization [95, pp. 91–93]. Moreover, because of the inhomogeneity of the main magnetic field, the decrease in transverse magnetization will accelerate and the time constant of the decay will further reduce to T_2^* [95, pp. 110–111].

Spin-lattice relaxation, the other relaxation event, is an important contributor to the restoration of longitudinal magnetization. After the RF wave is transmitted, the energy of the RF wave is absorbed by the spins, initiating resonance. When the resonance is finished and relaxation is just beginning, some of spins will gradually switch back to the lowest energy state, returning to dynamic equilibrium. During this process, the energy transferred to the surrounding macromolecules (or "lattice") will increase the vibration of lattice molecules, eventually converting to heat. This spin-lattice interaction brings the longitudinal magnetization back to the state of dynamic equilibrium. The restoration of longitudinal magnetization, considered in a rotating frame of reference, can be

expressed in the exponential decay model [94, p. 70]:

$$M_{l\_rotating}(t) = M_0 \cos\alpha \, \mathrm{e}^{-t/T_1} + M_0\left(1 - \mathrm{e}^{-t/T_1}\right) \tag{2.14}$$

where $M_0 \cos\alpha$ is the longitudinal magnetization after the RF pulse is applied. If a 90° pulse is applied, the longitudinal magnetization is 0. T_1 is a tissue-depended constant as well, describing the time moment when the longitudinal magnetization of a certain type of tissue recovers to 63% of its initial magnetization [95, pp. 91–93]. Furthermore, T_1 also depends on the external magnetic field. To be specific, T_1 extends longer with the increase of the external magnetic field. Finally, it is worth mentioning that T_1 is always longer than T_2 for each type of tissues [94, p. 70].

In practice, the RF pulse is applied many times in a pulse sequence. Under this circumstance, (2.13) and (2.14) can be integrated into the following equation [94, p. 71]:

$$M_{tr_{rotating}}(t) = M_0\left(1 - \mathrm{e}^{-TR/T_1}\right)\mathrm{e}^{-t/T_2}, \tag{2.15}$$

where TR denotes the time to repetition (TR), and the physical meaning of $M_0(1 - \mathrm{e}^{-TR/T_1})$ represents the remaining longitudinal magnetization after the repeated RF pulse is delivered. Only the transverse components of net magnetizations during the relaxation process are measurable. The relaxation process of the transverse components described in (2.24) is considered in a rotating frame of reference, but the measurement of transverse magnetization is carried out in a static frame of reference. In practice, the measurement of the transverse magnetization is conducted by placing two static coils in the x and y axes: this is illustrated in Figure 2.4 (A). The circularly moving transverse components of the net magnetizations pass through the coils: the coils then acquire electrical signals from the induced circular motion as explained by Faraday's Law of Induction. In a static frame of reference, the excited spins retain precession at their corresponding Larmor frequencies during the relaxation process. This process is demonstrated in Figure 2.4 (A). As Figure 2.4 (B) and (C) show, $M_x(t)$ and $M_y(t)$ demonstrate Free-Induction Decay (FID) [95, pp. 109–113]. The envelop of FID is subject to T_2 relaxation, and the actual decay signal oscillates at the Larmor frequency of excited spins [95, pp. 110–111]. Since $M_x(t)$ and $M_y(t)$ are recorded at the x and y axes respectively, they can be summarized as follows [94, p. 71]:

$$\begin{aligned} M_{tr\_static}(t) = M_x(t) + iM_y(t) = M_0\left(1 - e^{-TR/T_1}\right)e^{-t/T_2}\cos\omega_0 t - \\ iM_0\left(1 - e^{-TR/T_1}\right)e^{-t/T_2}\sin\omega_0 t = M_0\left(1 - \mathrm{e}^{-TR/T_1}\right)\mathrm{e}^{-t/T_2}e^{-i\omega_0 t}, \end{aligned} \tag{2.16}$$

where $e^{-i\omega_0 t}$ describes the rotation of the excited spins in a static frame of reference and can be omitted when discussed in a rotating frame of reference.

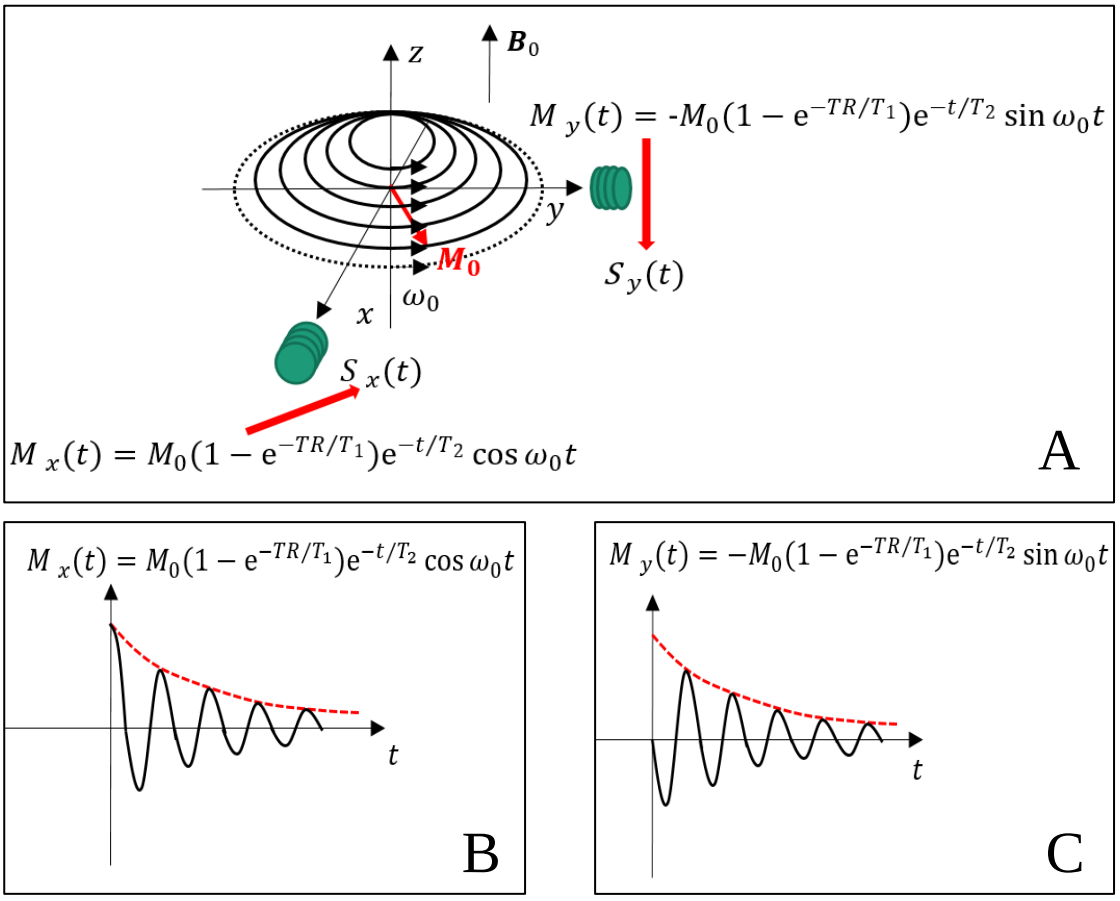

Figure 2. 4 (A) Relaxation and signal acqusition; **(B)** signal acquired by the coil in the x axis; and **(C)** signal acquired by the coil in the y axis.

2.2. Gradient Fields and Encoding Techniques

The NMR phenomenon of spins in an external magnetic field can be easily observed by using a RF wave for excitation. However, in order to obtain a MR image, the NMR phenomenon of each spin has to be spatially encoded. This can be accomplished by using an encoding technique based on linear magnetic gradient fields.

2.2.1. Slice Selection

The first step of spatial encoding is to superimpose the gradient field on the z axis in order to select the designated slice [94, pp. 72–73]. After switching on the magnetic gradient field's coil along the z direction, the magnetic gradient field varying linearly in the z direction adds to the main magnetic field. Due to the gradient fields, the new magnetic field become position-dependent, which is useful for spatial encoding.

According to the Larmor equation, the Larmor frequency for the new magnetic field containing the gradient field can be generalized as follows [94, p. 72]:

$$\omega(z) = \gamma(B_0 + G_z z), \tag{2.17}$$

where $\boldsymbol{G_z}$ is the amplitude of the slice selection (z direction) gradient. Thus, every spatial position along the z direction can be linearly encoded with a frequency value with the aid of the RF excitation. According to the Larmor equation of (2.17), after a RF pulse is delivered, all the net magnetizations ($\boldsymbol{M_0}$) corresponding to the central frequency ω_{z_0} (of the RF pulse) will initiate a resonance together, constituting a slice. In addition, the thickness of this slice is jointly governed by the bandwidth of the RF pulse and the amplitude of the gradient along the z direction [94, p. 73]:

$$\Delta z = \frac{\Delta\omega}{\gamma G_z}. \tag{2.18}$$

The principle of slice selection is demonstrated in Figure 2.5. The following graphs in this chapter use the following anatomy directional terms indicating orientations of the human body: A represents anterior; P represents posterior; L represents left lateral; R represents right lateral; S represents superior; and I represents inferior.

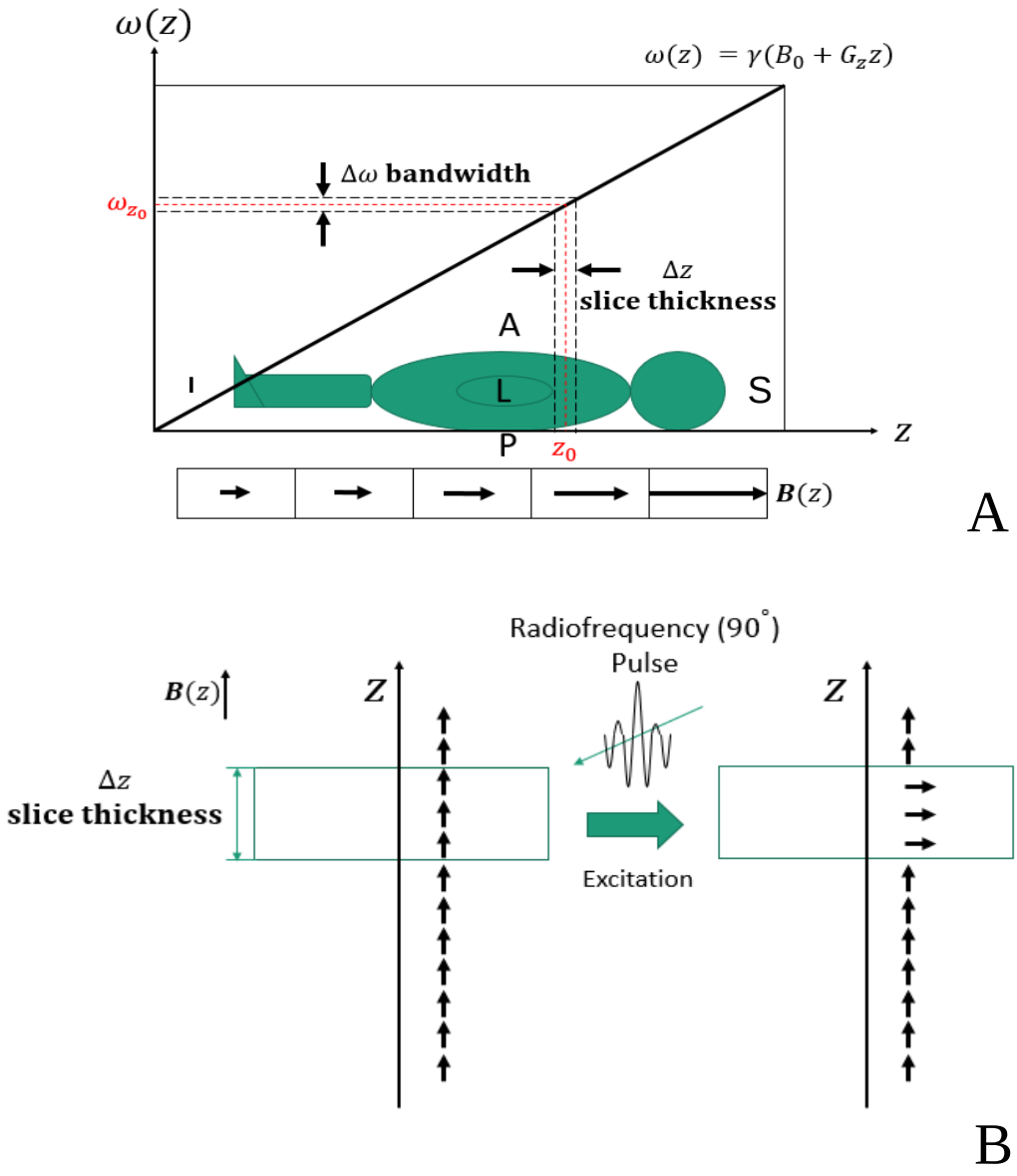

Figure 2. 5 (A) Gradient and slice selection; and **(B)** RF excitation in the slice selection direction.

2.2.2. Frequency Encoding

As previously discussed, after a slice selection gradient is turned on, a RF pulse (90°, for example) will excite all net magnetizations ($\boldsymbol{M_0}$) in a specific slice, and each net magnetization will completely flip to the transverse plane; once the RF coil is turned off, the relaxation of the excited net magnetizations will occur. During the relaxation process, if a frequency encoding gradient field is applied (along with the L-R anatomical direction for example), each excited magnetization then starts rotating at a different frequency prescribed by its spatial location along the gradient direction. However, the rotations mixed with these different frequencies are usually collected as one signal by the coils. Besides, the frequency encoding gradient must remain on until

the signal is completely acquired, as illustrated in Figure 2.6 (A): otherwise, the frequency encoding process will fail, as shown in Figure 2.6 (B). This process is described as the frequency encoding: it records the net magnetizations' location information along one of the directions in the transverse plane [95, pp. 153–155]. In other words, the net magnetizations tipped down to the transverse plane rotate at different frequencies during the frequency encoding, which can produce a signal containing the location information in the coils and transmit it to MRI scanner. The frequency encoding gradient is also referred to as the readout gradient because the signal must be collected when the frequency encoding gradient is on: this will be further explained in section 2.4.

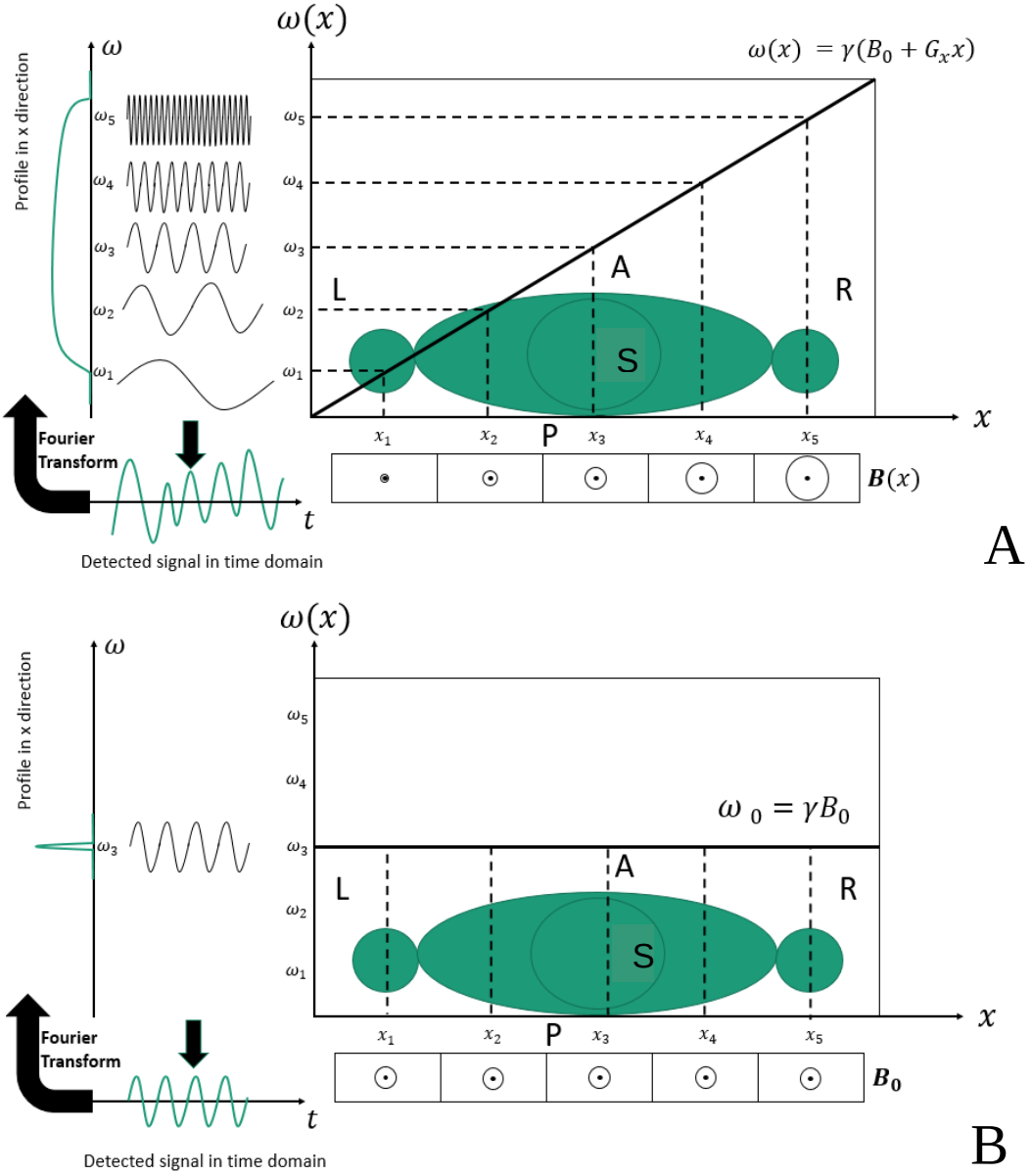

Figure 2. 6 (A) Acquired signal with a frequency encoding gradient; and **(B)** acquired signal without a frequency encoding gradient.

2.2.3. Phase Encoding

The encoding along the other transverse direction (A-P anatomical direction, or y axis) is achieved using a phase encoding gradient (in practice, a frequency or a phase encoding gradient field can be applied in either transverse direction) [95, pp. 155–157]. The phase encoding gradient is usually applied after the slice selection and before the frequency encoding is applied. Similar to the frequency encoding gradient, when the phase encoding gradient is switched on, the net magnetizations ($\boldsymbol{M_0}$) along the y axis also start rotating at different frequencies: this is shown in Figure 2.7 (A). When the phase encoding gradient is switched off, the spins along the y axis will return to the same rotating frequencies, however, with a different phase as shown in Figure 2.7 (B). Eventually, a signal resulting from the net magnetizations (all over the transverse plane) with multiple frequencies along the x axis and different phases along the y axis will be detected: this is demonstrated in Figure 2.7 (C). Though this resultant signal is encoded from the 2D transverse plane, it is detected in a 1D time series: this time series can only reflect the difference of the spatial position along the frequency encoding direction. If to encode the spatial position information containing the other direction, the phase encoding gradient must be repeated multiple times with a different gradient amplitude each time, depending on the final image resolution along this direction. Figure 2.8 illustrates the principle of the phase encoding gradient, which shows that a group of phases resulting from all the varied phase encoding gradients are used to encode each spatial position along the A-P direction (the y axis). Each group of phases is unique, encoding each spatial position along the y axis. During each repetition cycle, a repeated slice selection and frequency encoding gradients must be applied along with each varied phase encoding gradient. Figure 2.9 (A) shows that at the end of each repetition cycle, a 1D signal is generated, containing same frequency components but different phase components. After all the phase encoding processes are finished, each acquired 1D signal will constitute a 2D space (a signal storage space instead of the actual spatial plane) where each row is specified by a different phase encoding gradient. Each repetition cycle contains all the frequency components prescribed by the frequency encoding gradient, as illustrated in Figure 2.9 (B). This composed space, called K-space, varies with the amplitude of the phase encoding gradient (along the y axis) and time (along the x axis). The next section will discuss K-space in further detail.

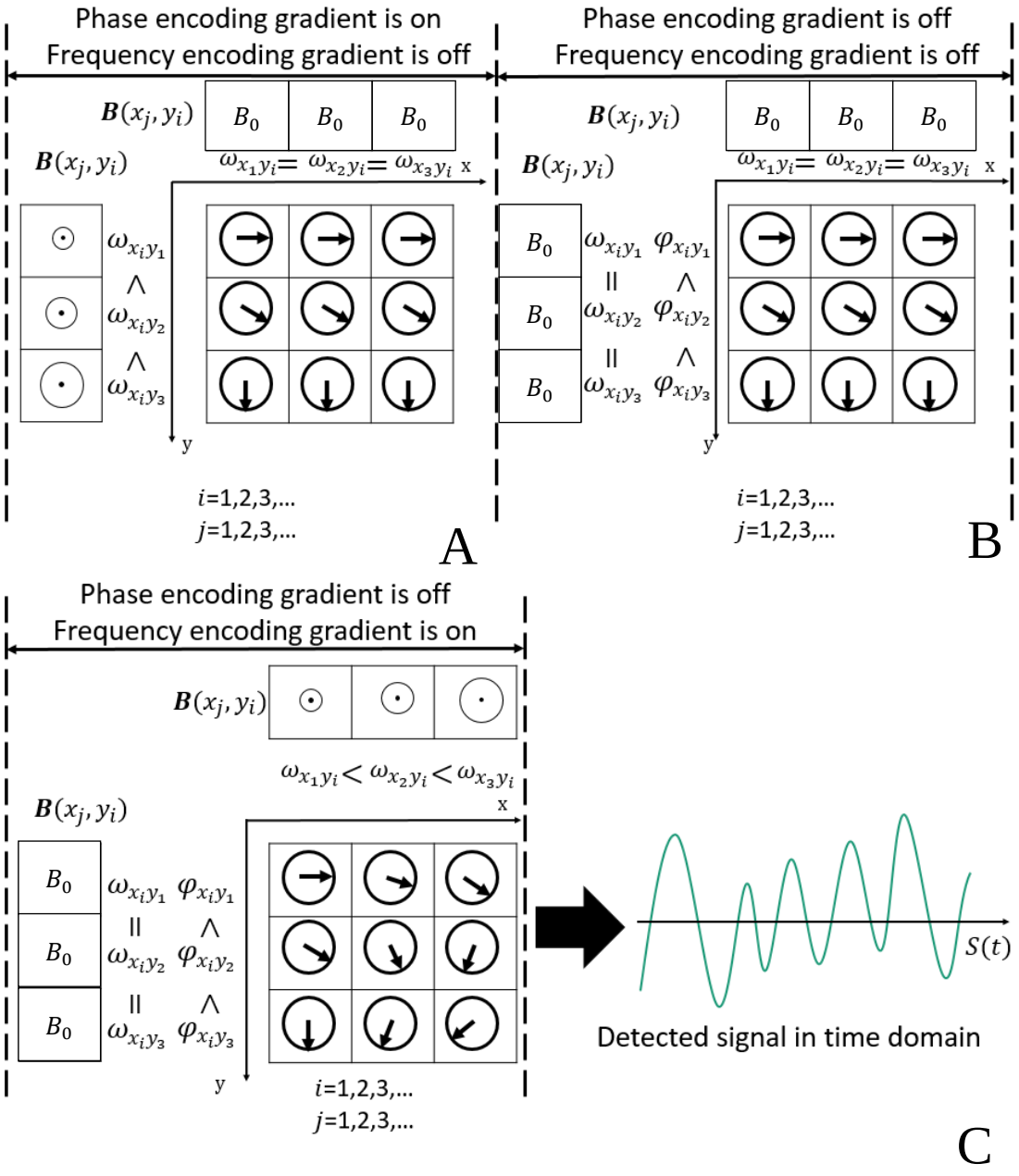

Figure 2. 7 (A) Phase shift varies along phase encoding gradient; **(B)** phase shift remains once phase encoding gradient is switched off; and **(C)** integrated signal created by phase encoding gradient.

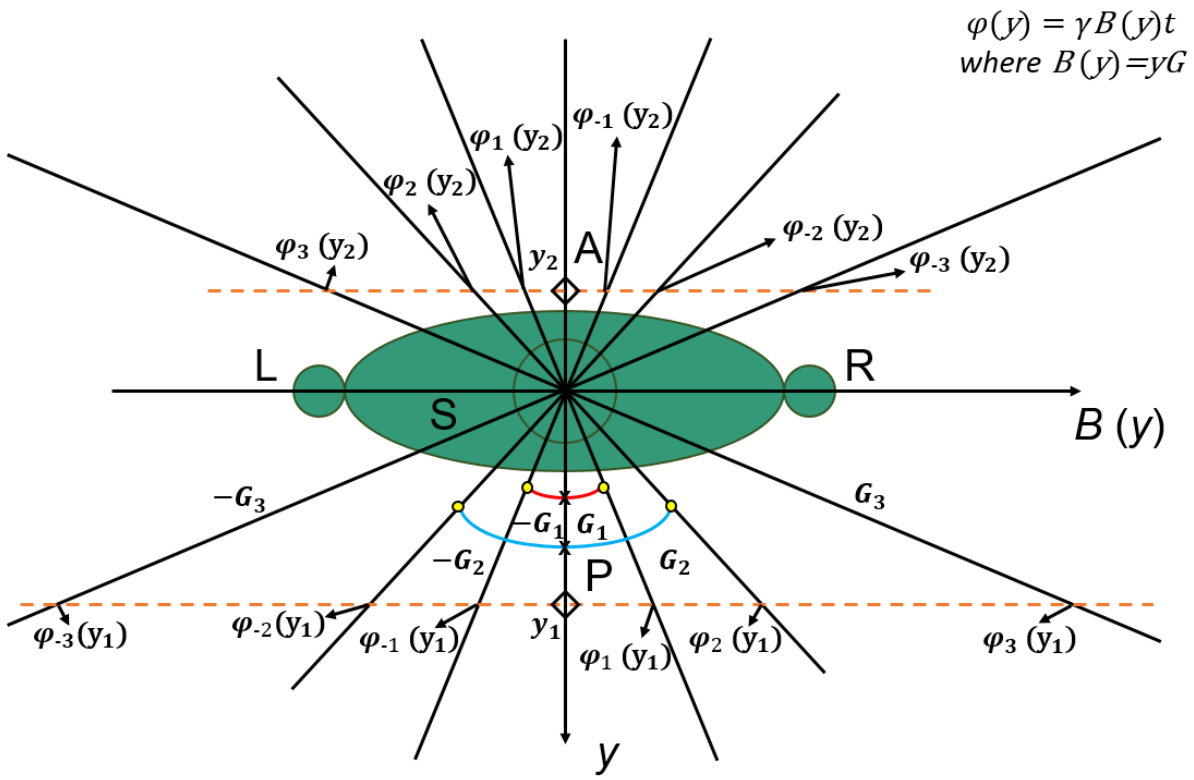

Figure 2. 8 Physical interpretation of the phase encoding gradient. In this figure, G_i (where *i*=1, 2, 3) represents each different phase encoding gradients' magnitude G.

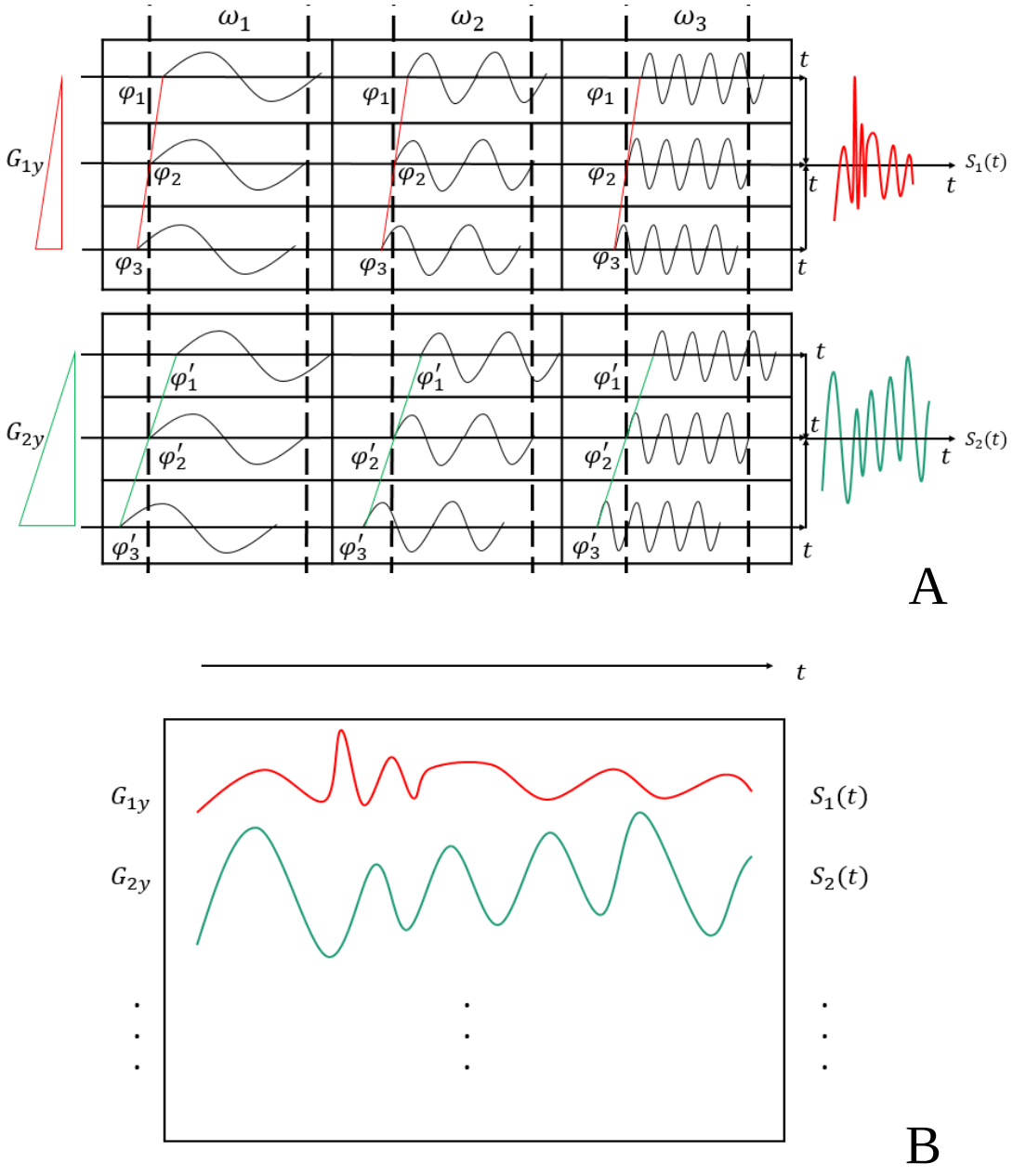

Figure 2. 9 (A) Signal components from each individual phase encoding gradient step; and **(B)** composition of each signal component in a 2D space.

2.2.4. K space

In practice, frequency encoding is scheduled after phase encoding has been applied, and both processes are repeated multiple times with a variable phase encoding gradient. A complete cycle starts with an excitation pulse and ends with a signal acquisition. As mentioned before, the frequency encoding gradient and signal acquisition occur simultaneously. Though a signal is generated immediately after the excitation pulse is applied (i.e., the FID signal is produced at this

moment), the signal will not be fully encoded and subsequently acquired until the frequency encoding gradient (or readout gradient) is applied. The signal acquired during the readout gradient is switched on is called "Echo" which is fully encoded by gradient fields. The echo has a symmetric structure, and the moment at the middle of echo is defined as "the time to echo" (TE). The echo from each cycle is filled into K-space sequentially, as shown in Figure 2.9 (B). Supposing that a 90° RF excitation pulse is applied, the echo can be described mathematically as follows [94, pp. 73–75]:

$$S(t, G_{ly}) = \iint_{-\infty}^{+\infty} \rho(x,y)(1 - \mathrm{e}^{-\mathrm{TR}/T_1})\mathrm{e}^{-t/T_2}\, \mathrm{e}^{-2\pi i x \frac{\gamma}{2\pi}\int G_x(t)dt - 2\pi i y \frac{\gamma}{2\pi}\int_{T_a}^{T_b} G_{ly}(\tau_y)d\tau_y} dxdy, \tag{2.19}$$

where t is the time moment during the signal acquisition, x and y are coordinates of an image, ranging from $[-x_{max}, x_{max}]$ and $[-y_{max}, y_{max}]$ respectively; $\rho(x,y)$ represents the density distribution of the x-y plane; G_x is the amplitude of the frequency encoding gradient; G_{ly} is the amplitude of the phase encoding gradient; and $l = 1,2,3,\dots,\mathrm{N}$ where N is the time of applying variable G_{ly}; T_a and T_b are the start and end time of the phase encoding gradient; and τ_y is the duration time of the phase encoding gradient.

Particularly, if $k_x(t)$ and $k_y(G_{ly})$ are defined as

$$k_x(t) = \frac{\gamma}{2\pi}\int G_x(t)dt \tag{2.20}$$

and

$$k_y(G_{ly}) = \frac{\gamma}{2\pi}\int_{T_a}^{T_b} G_{ly}(\tau_y)d\tau_y, \tag{2.21}$$

then (2.19) can be rewritten as

$$S\left(k_x(t), k_y(G_{ly})\right) = \iint_{-\infty}^{+\infty} \rho(x,y)(1 - \mathrm{e}^{-TR/T_1})\mathrm{e}^{-t/T_2}\, \mathrm{e}^{-2\pi i(xk_x(t) + yk_y(G_{ly}))} dxdy, \tag{2.22}$$

where (2.22) should be able to appropriately describe the measurement of the signal from the receiver coils after each repeated cycle [94, pp. 74–75]. After all the repeated cycles are done, the signals will combine to signal storage space, namely, "K-space" [94, pp. 73–75]. Therefore, (2.22) can also be described as the mathematical expression of K-space which is determined by the time and the amplitude of phase encoding gradient. However, K-space is not equivalent to the physical space, the final image. Thus, the signals in K-space need to be further transformed to reconstruct a final MR image.

2.3. Reconstruction and the Fourier Transform

The collected signals in K-space, described in (2.22), can be assumed in a 2D Fourier domain, considering that the 2D Fourier Transform (FT) and inverse Fourier Transform fulfill the following

descriptions [94, p. 74]:

$$F(k_x, k_y) = \iint_{-\infty}^{+\infty} f(x,y)\, \mathrm{e}^{-2\pi i(xk_x+yk_y)} dxdy, \tag{2.23}$$

and

$$f(x,y) = \iint_{-\infty}^{+\infty} F(k_x, k_y) \mathrm{e}^{+2\pi i(xk_x+yk_y)} dk_x dk_y. \tag{2.24}$$

That is, the latter part in (2.22), $\mathrm{e}^{-2\pi i(xk_x(t)+yk_y(G_{ly}))}$, is regarded satisfying the transform basis of the FT—i.e. $\mathrm{e}^{-2\pi i(xk_x+yk_y)}$—while the spatial domain $f(x,y)$ is defined as follows [94, p. 75]:

$$f(x,y) = \rho(x,y)(1-\mathrm{e}^{-TR/T_1})\mathrm{e}^{-TE/T_2}. \tag{2.25}$$

The part of $\rho(x,y)(1-\mathrm{e}^{-TR/T_1})\mathrm{e}^{-t/T_2}$ in (2.22) describes the T_2 relaxation process of transverse magnetizations per location unit during the signal measurement each repetitive cycle. However, to strictly fulfill the FT form and retrieve a spatial map, $f(x,y)$ must be irrelevant to time; therefore, given that the time of each signal measurement is relatively short, the variable t is replaced with the constant TE [94, p. 75]. Under this assumption, all the acquired signals, $S\left(k_x(t), k_y(G_{ly})\right)$, stored in K-space can be reconstructed by an inverse FT to an MR anatomical image, $f(x,y)$:

$$f(x,y) = \iint_{-\infty}^{+\infty} S\left(k_x(t), k_y(G_{ly})\right)\, \mathrm{e}^{+2\pi i\left(xk_x(t)+yk_y(G_{ly})\right)} dk_x(t) dk_y(G_{ly}), \tag{2.26}$$

where $S\left(k_x(t), k_y(G_{ly})\right)$ is mathematically equivalent to $F(k_x, k_y)$.

Based on the assumption of (2.25), an MR image's contrast is defined by T1, T2, and proton density $\rho(x,y)$, which are all related to the intrinsic characteristics of tissues [94, pp. 69–70]. The weight contributed by each factor (T1, T2, and $\rho(x,y)$) is controlled by TE and TR [95, pp. 223–224]. Therefore, TE and TR are the two most important parameters manipulating the MR image's contrast. For example, a long TR and long TE produce a T2-weighted MR image, a short TR and short TE result in a T1-weighted MR image, and a long TR and short TE provide a proton density-weighted MR image. However, this case is only true if the image is obtained by a Spin Echo sequence. When a Gradient-Recalled Echo sequence is applied, there will be a new $T2^*$ contrast replacing T2. These concepts will be further discussed in subsequent sections. These contrasts are able to reveal important anatomical and clinical information depending on which part, tissue, or pathology is inspected.

2.4. Pulse Sequence

A pulse sequence defines and executes the excitation, encoding, and acquisition processes of MRI. As Figure 2.10 shows, the pulse sequence primarily controls the value, duration, and

activation of the radiofrequency wave and the gradient fields in a time series. The pulse sequence also aids in the acquisition and digitalization of raw data.

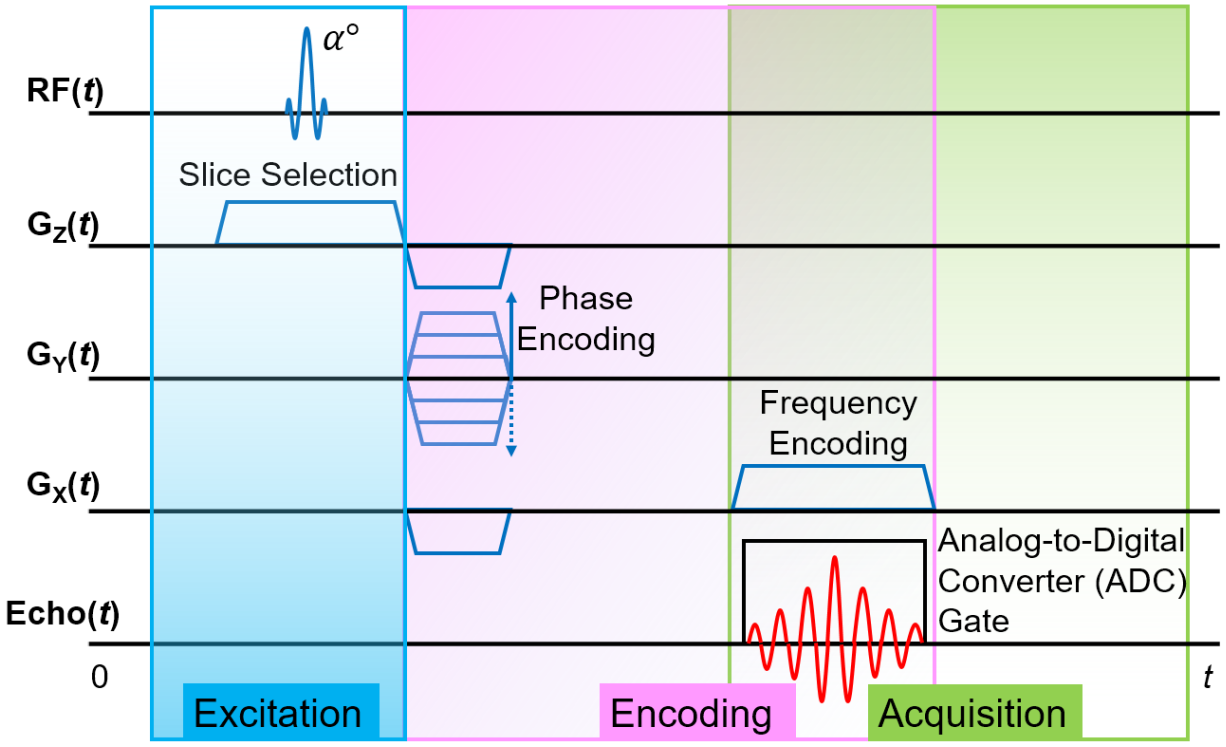

Figure 2. 10 Basic diagram of a MRI pulse sequence.

The pulse sequence determines the methods, quality, categories, and duration of the signal acquisition, sophisticatedly manipulating the magnetizations to achieve various purposes. Pulse sequences are typically classified into two main types: the Spin Echo (SE)-based sequence and the Gradient-Recalled Echo (GRE)-based sequence [94, pp. 77–79]. Most of the pulse sequences in MR are based on or adapted from these two fundamental sequences.

2.4.1. Spin Echo Pulse Sequence

The most significant feature of the SE sequence is the insertion of one or more refocusing pulses after each excitation pulse [94, pp. 77–79]. In most cases, the flip angles of the excitation and refocusing pulses are set at 90º and 180º, respectively [97, p. 630]. The refocusing pulses are used to compensate for the signal loss caused by off-resonance effects [97, p. 631]. The inhomogeneity of the main magnetic field and magnetic susceptibility variations will accelerate the dephasing of the transverse magnetization, reducing the relaxation time constant T2 to $T2^*$ and leading to significant signal loss, as Figure 2.11 “1” shows [94, pp. 75–77]. At first, the refocusing pulse will flip the transverse magnetization (and longitudinal magnetization) by 180º. Then, at TE/2 (when the refocusing pulse is effective), the dephased transverse magnetizations will rephase, as Figure 2.11 “2” shows. With the aid of the refocusing pulse and slice selection gradient, the

dephasing caused by the inhomogeneity of the main magnetic field and magnetic susceptibility variations will eventually be restored, extending the relaxation time back to T2 from $T2^*$ and producing an echo signal, or Spin Echo, at the TE. One of the many advantages of the SE sequence is its ability to compensate for dephasing, caused by the inhomogeneity of the main magnetic field and the magnetic susceptibility variations, by using a 180º refocusing pulse to produce a stable spin echo at the TE [97, p. 631].

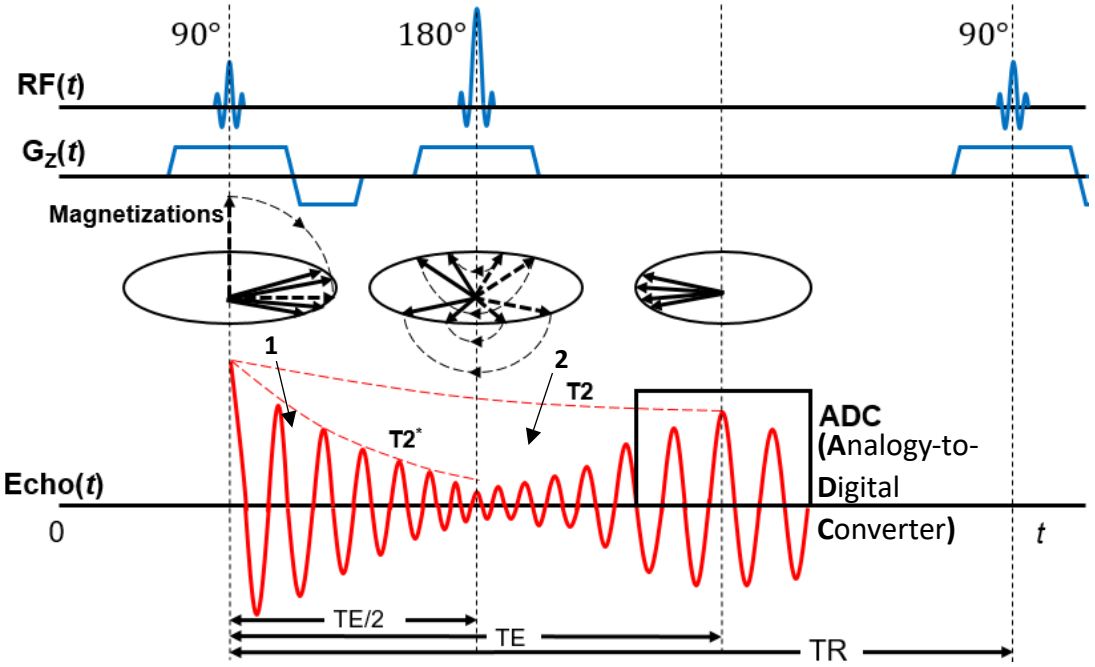

Figure 2. 11 The magnetization changes and the corresponding signal types in the spin echo sequence. The FID signal is generated after the 90º RF pulse and labeled with number 1, and spin echo signal is generated at TE and labeled with number 2.

As Figure 2.12 shows, the slice selection gradient is followed by a reversal polarity gradient which has half the area of the former. This gradient lobe, known as a rephasing gradient, is used to eliminate the phase dispersion caused by the slice selection gradient [97, p. 635]. Due to the slice selection gradient, the spins along the z direction rotate at different Larmor frequencies after a 90º RF excitation pulse is employed, accumulating different phases: this will reduce the net magnetization and induce further signal loss in the intravoxel. The rephasing gradient has half the area of the slice selection due to the assumption that the central of the slice selection gradient is where the RF excitation exactly happens. Therefore, the spins along the slice selection direction are supposed to be back in phase at the end of the rephasing gradient. Unlike the 90º pulse, the refocusing pulse (a 180º pulse) does not require a rephasing gradient because the phase dispersion caused by the first half of the slice-selection gradient is cancelled out by the second half of the slice-selection gradient [97, pp. 347–348].

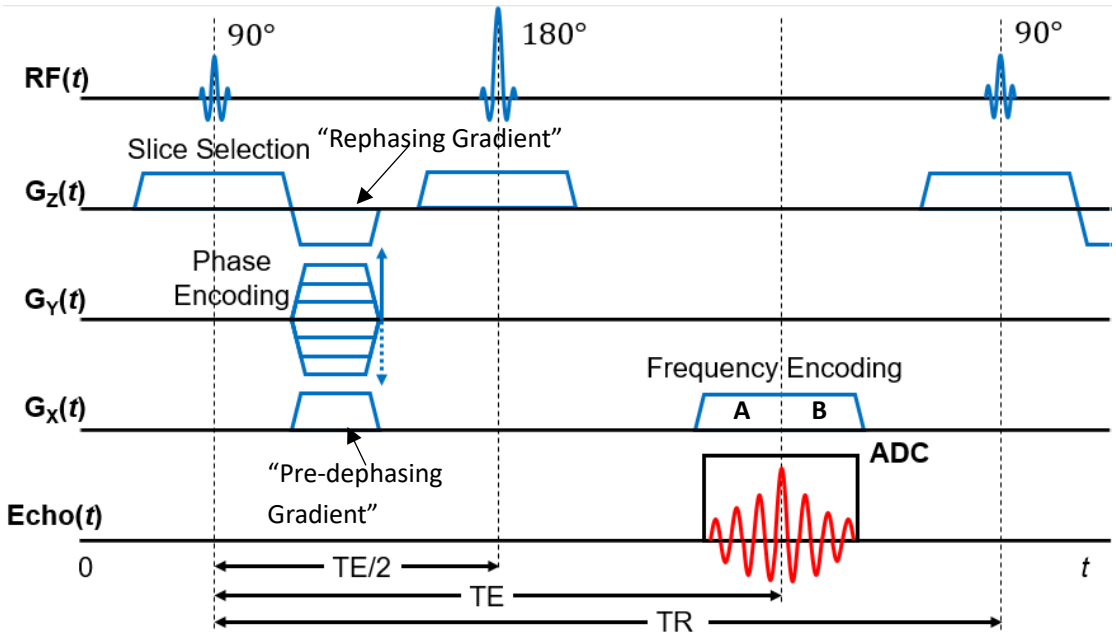

Figure 2. 12 Diagram of a spin echo (SE) pulse sequence.

A similar rephasing gradient is applied to the frequency encoding gradient because signal decay is caused by not only spin-spin interactions and main magnetic field inhomogeneities, but also other magnetic gradient fields [94, p. 78]. While the frequency encoding (or readout) gradient is used to realize frequency encoding, the linear frequency encoding gradient field creates a local inhomogeneity-scenario where the spins within each single voxel will rapidly dephase and heavily damp the echo signal during the readout process [94, pp. 75–76]. As Figure 2.12 shows, a pre-dephasing gradient (with the same polarity as the frequency encoding gradient) is prepared in the frequency encoding gradient direction before using the refocusing pulse to compensate for the additional dephasings and subsequent signal damping. This extra gradient will pre-dephase the transverse magnetizations before the readout gradient is employed. If the area of this preset gradient field lobe is set as half of the readout gradient (A=B), the dephasing occurring in this gradient lobe will be rephased during the first half of readout gradient due to the 180° refocusing pulse. Moreover, the extra signal damping will be fully recovered at the central of the readout gradient the moment that the TE arrives. That is, the first lobe of the readout gradient is set as a rephasing gradient lobe, and will cancel the dephasing process intentionally applied before. The pre-dephasing lobe and first readout lobe, which have same areas, allow the signal damped by the frequency encoding gradient to be maximally restored at the TE moment, producing a readout signal with the best Signal-to-Noise Ratio (SNR) [94, p. 77].

Since the phase shifts resulting from the phase encoding gradient are used for encoding, rephasing gradients are not required in the phase encoding gradient direction. The amplitude of the phase encoding gradient is set at even steps (intervals) every TR cycle. The number of steps also determines the resolution along the y-axis (that is, the phase encoding gradient direction) and the

acquisition time. A typical 2D SE sequence is shown in Figure 2.12. In this sequence, the data-filling to K-space is one line per phase encoding step, as demonstrated in Figure 2.13. In this case, the acquisition time is determined by

$$T_{\text{scan}} = TR \times N_{\text{phase}} \times \text{NEX}, \tag{2.27}$$

where N_{phase} is the number of phase encoding steps, and NEX is the number for signal averaging [97, p. 632]. For a scan with TR=1500 ms, 256 phase encoding steps, and no signal averaging, the total scan time will be up to 6.4 minutes. Because NEX and N_{phase} partly determine the acquisition time, a high-quality MRI image (with a high SNR and a fine resolution) usually comes at the cost of a long acquisition time if using an SE pulse sequence. However, many pulse sequences derived from the SE, such as the Fast SE, SE-Echo Planar Imaging (EPI), and Hybrid Echo technique, have improved their scan speed while keeping the primary characteristics of the SE pulse sequence. These derived sequences modify many factors, such as the excitation method, encoding strategy, and K-space filling trajectory.

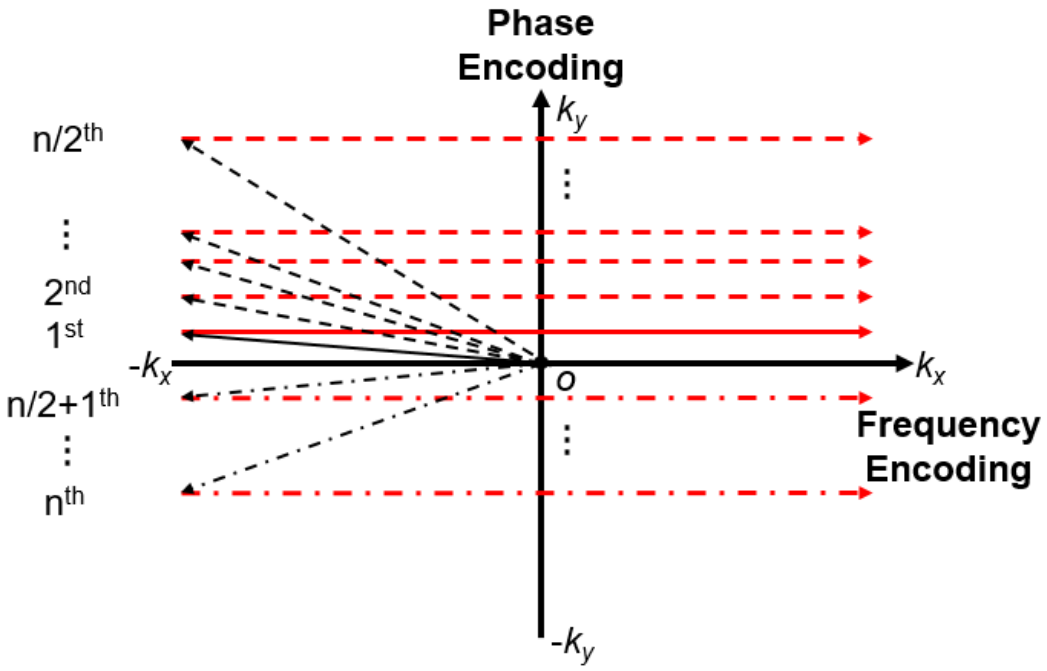

Figure 2. 13 Conventional K-space filling trajectory of signals.

By manipulating TR and TE, an SE pulse sequence can acquire either a T1-, T2-, or a proton density-weighted image, as listed in Table 2.2 [97, pp. 630–631].

Table 2. 2 Image contrast regularized by TE and TR

	Short TE	**Long TE**
Short TR	T1 weighted	None
Long TR	Proton density weighted	T2 weighted

In summary, SE-based pulse sequences have been widely used in both routine clinical scans and cutting-edge applications because of their better SNR and remarkable ability to correct the effects brought by the magnetic field inhomogeneities and materials susceptibility variations. The SE-based pulse sequence has become one of the options to realize Magnetic Resonance Elastography (MRE) scans (see Chapter 3, section 3.3.3).

2.4.2. Gradient-Recalled Echo Pulse Sequence

The Gradient-Recalled Echo (GRE) pulse sequence is characterized by its nonexistence of refocusing pulses, and by its RF pulse with a flip angle less than 90º: see Figure 2.14 [94, p. 79]. The absence of refocusing pulses potentially reduces the GRE pulse sequence's TR and scan time. Additionally, the low flip angle not only allows a faster restoration in longitudinal magnetizations, reducing the TR, but also serves as a selectable scan parameter able to maximize or minimize signals from specific tissues in terms of their different T1s [95, pp. 227–229]. The optimal flip angle for a given TR and T1 is known as the Ernst Angle [97, p. 587]. These two features give the GRE pulse sequence a short scan time which is necessary for a 3D acquisition [94, p. 79].

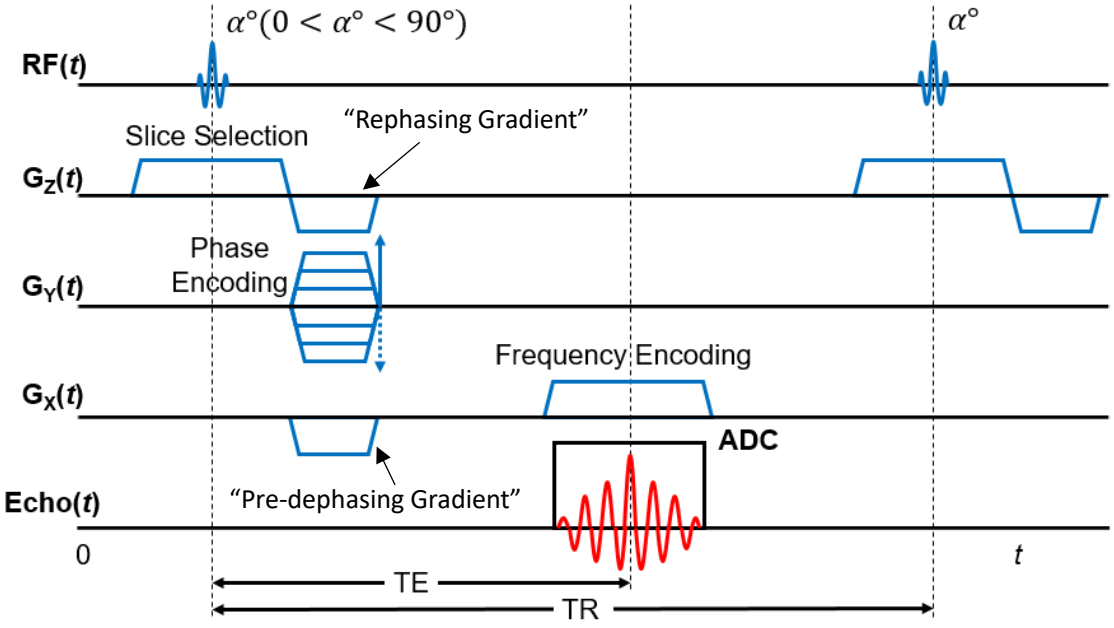

Figure 2. 14 Diagram of a gradient-recalled echo (GRE) pulse sequence.

Similar to the SE pulse sequence, the GRE pulse sequence also employs a reversal rephasing gradient lobe after the slice selection gradient to compensate for the dephasing caused by gradient fields [94, pp. 79–80]. To undo the dephasing caused by the magnetic field gradients, a pre-dephasing gradient is played before the frequency encoding gradient. By keeping the pre-dephasing gradient's area equal to the readout gradient's first lobe, the decayed signal caused by the magnetic gradient field (the pre-dephasing lobe) will be completely recovered at the TE. After the TE, the rest of readout gradient will cause the newly rephased transverse magnetizations to lose phase again,

producing a new decayed signal. This complete signal (combined with the restored and decayed signal) acquired during the readout gradient is switched on is called the gradient-recalled echo. Due to the absence of the 180º refocusing pulse, the signal loss from the inhomogeneity of the main magnetic field and magnetic susceptibility variations cannot be recovered: no spin echo will be produced. In other words, the echo in the GRE pulse sequence is solely recalled by the gradient, which is why it is named after the gradient-recalled echo. The major difference between the spin echo and the gradient-recalled echo is that the former produces T2 relaxation while the latter produces T2* relaxation which decays more quickly than the former. That is, the GRE sequence eventually generates a T2*-weighted image instead of a T2-weighted image. However, if a T2*-weighted image is collected from the GRE pulse sequence, its signal is possibly very low and significantly vulnerable to the magnetic field inhomogeneities and magnetic susceptibility variations: this results in an unrecoverable signal loss in the T2*-weighted image [94, pp. 79–80].

For a typical GRE pulse sequence (Figure 2.14), the phase encoding gradients before the signal acquisition are identical to its counterparts in a SE pulse sequence, which means that the acquisition time of the GRE pulse sequence is also jointly decided by the NEX, N_{phase}, and TR: see (2.27). However, in practice, comparing to the SE pulse sequence, the GRE pulse sequence's TR and acquisition time are largely reduced due to its absence of 180º refocusing pulses and its primary use for T1-weighted scans. Besides, GRE pulse sequences' K-space filling trajectory is usually same as SE pulse sequences' (illustrated in Figure 2.13). The GRE-based pulse sequence is another approach to realize MRE scans [22].

2.4.3. Echo Planar Imaging Pulse Sequence

Echo Planar Imaging (EPI) is recognized as the fastest acquisition technique in MRI [94, pp. 82–83]. A EPI technique usually adds on either an SE or a GRE pulse sequence. As the following paragraph explains, a EPI-based pulse sequence is noted for its design on the encoding and acquisition techniques. The design's strongest advantage is that the image can be acquired (for the simplest EPI-based pulse sequence) within one TR cycle, instead of needing many TR cycles which are required by other regular pulse sequences. As depicted in Figure 2.15, all the phase encoding steps and frequency encoding gradients are accomplished within one TR duration, and the Analog-to-Digital Converter (ADC, this acronym only stands for "Analog-to-Digital Converter" in this thesis) gates are switched on and off multiple times within one TR duration as well [94, pp. 82–83]. All the echoes obtained during this one TR duration are filled into K-space with a unique filling method: this is depicted by the solid red line shown in Figure 2.16 [96, pp. 208–209]. The filling pathway follows a "Z" shape where each horizontal line corresponds to the echo collected from each readout gradient lobe. The direction of this continuously zigzaging filling is directly controlled by the oscillating gradient polarity of the sequential gradient lobes, while the vertical K-space filling line is controlled by the phase encoding gradients. Each step of the zigzag-filling along the y-axis (phase encoding direction) illustrated in Figure 2.16 corresponds to each "blip" gradient (each phase encoding gradient lobe) shown in Figure 2.15. The acquisition accomplished in one

TR cycle is called a Single-Shot EPI [96, p. 208], [97, pp. 721–722]. However, the acquisition can also be achieved through multiple TR cycles, which is described as a Multi-Shot EPI [96, p. 208], [97, pp. 722–725]. The implementation of a Multi-Shot EPI improves the spatial resolution along the direction of the phase encoding gradient. The dashed black line shown in Figure 2.16 demonstrates a common type of Multi-Shot EPI known as the interleave multi-shot [96, p. 208]. The EPI sequence substantially reduces acquisition time, but results in reduced image quality. For example, artifacts commonly found in EPI include distortion and Nyquist N/2 Ghosts. The distortion in EPI is usually caused by magnetic susceptibility, and emerges along the phase encoding direction [97, pp. 733–734]. Since multiple phase and frequency encoding gradients are continually being turned on and off to collect echoes, the persistent magnetic susceptibility keeps disturbing the spatial encoding and signal acquisition, resulting in distortion. The solution to distortion artifacts is to either improve receiver bandwidth, which decreases the phase encoding gradients steps to reduce echo train, or to apply shimming fields to compensate for magnetic susceptibility. To retain the speed of imaging when implementing these distortion-reducing measures, parallel imaging and multi-shot imaging (interleaved) are usually adopted in routine clinical practice. Another artifact, the Nyquist N/2 Ghost, is normally caused by sequence imperfections or Eddy currents [97, pp. 726–732]. Because EPI generates its image from a series of echo train under one excitation (or a limited number of excitations), it is unsurprising that a minor echo delay could cause a chain reaction such as shifting all subsequent echoes. This would result in a situation where each peak of both odd and even echoes possesses an equal time difference from the center, as shown in Figure 2.17. The Nyquist N/2 Ghost artifact is common to and unique for EPI images. The alternate mal-posed odd- and even- echoes are equally likely to be under-sampled in half of the original K-space, and together create two aliased images which are specifically shifted with N/2 pixels along the phase encoding direction (assuming that N steps phase encoding gradients are applied): this is depicted in Figure 2.17. There are many measures used to deal with the Nyquist N/2 Ghost artifact, including perfecting the pulse sequence design, reducing echo train, and implementing multi-shot and compensating Eddy currents.

Though the artifacts produced by the EPI sequence can be challenging to deal with, the EPI sequence's efficiency is quite impressive. For instance, for an image with a size of 128×128, one single slice acquisition can be finished in 100 ms. Additionally, the short acquisition time makes the single-shot EPI sequence much less susceptible to motion effects. For these reasons, the EPI sequence is widely used in Diffusion Weighted Imaging (DWI), Perfusion Weighted Imaging (PWI), and functional Magnetic Resonance Imaging (fMRI), as well as for fast anatomical imaging [94, pp. 82–83]. The EPI technique is already applied in MRE scans: see Chapter 3, section 3.3.3.

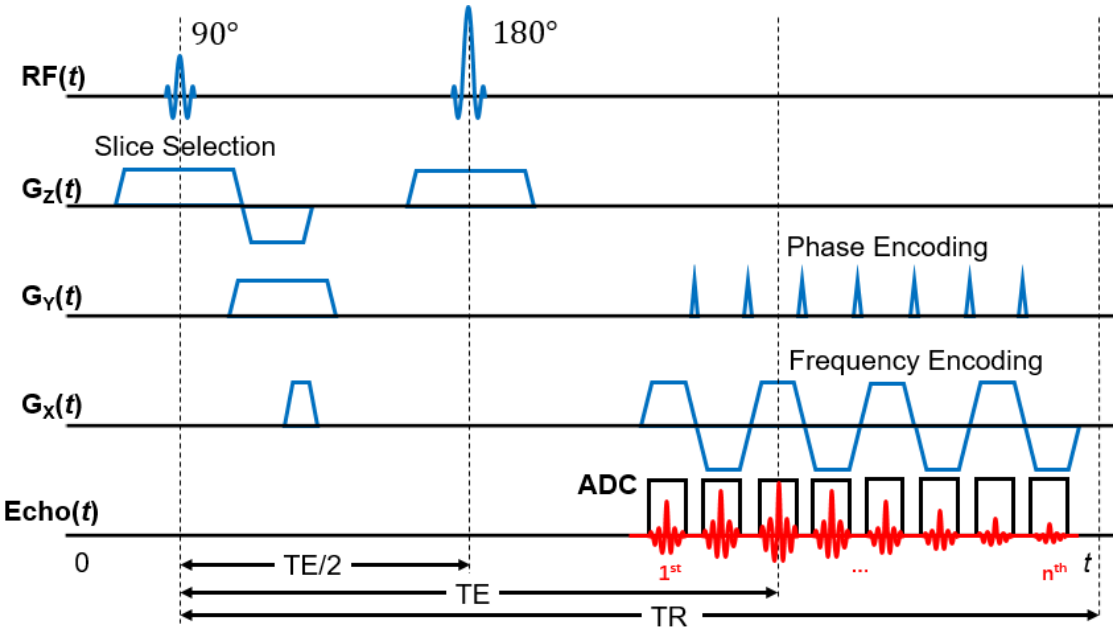

Figure 2. 15 Diagram of a spin echo-echo planar imaging (SE-EPI) pulse sequence.

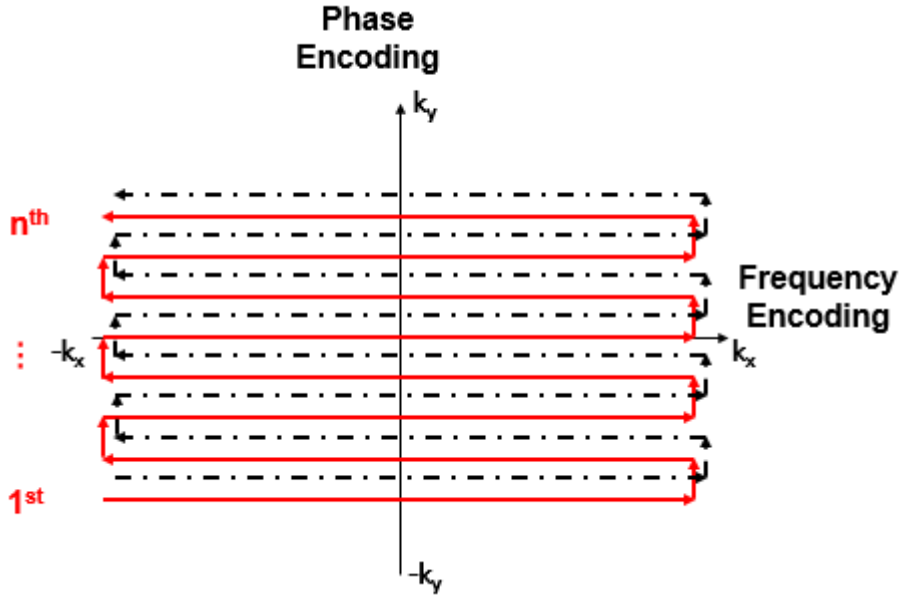

Figure 2. 16 SE-EPI K-space filling trajectory of signals.

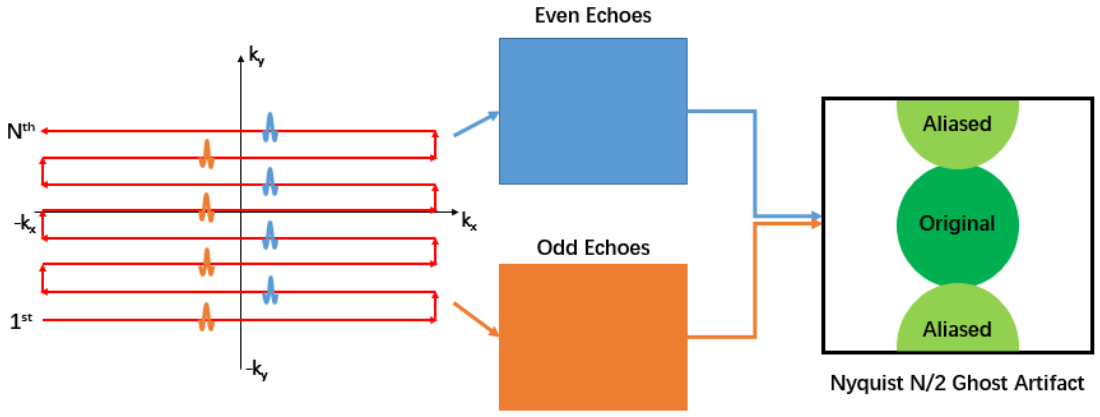

Figure 2. 17 Nyquist N/2 ghost artifact in SE-EPI.

2.5. Summary

This chapter introduces the fundamental physics and technical realization behind MRI, which helps readers better understand the applied principles and techniques in Magnetic Resonance Elastography (MRE). For example, the basic concepts, such as gradient fields, are explained in detail in this chapter since the MRE technique is completely based on MRI. Moreover, pulse sequences are also explicitly covered in this chapter: they are the core carrying out MRE scans. Chapter 2 is regarded as a precursor discussing Magnetic Resonance Elastography (MRE) in the next chapter.

Chapter 3

Magnetic Resonance Elastography

Chapter Synopsis

Magnetic Resonance Elastography (MRE) is a system that applies a dynamic force to an object while scanning with Magnetic Resonance Imaging (MRI) and directly records the responses that are for the subsequent elastic information calculation. MRE is a recent imaging development system that can be used to obtain mechanical information—specifically elasticity that other current Magnetic Resonance (MR) techniques are not able to provide.

This chapter briefly provides a basic theoretical explanation for MRE including its physics and technical realization.

3.1. Elasticity

Before introducing MRE, it is important to introduce some basic concepts regarding elasticity. Elasticity describes the ability of an object (body) to respond to an external force and how this object restores back to its original physical state (size and shape). Robert Hooke first initiated an elasticity study on a spring and proposed Hooke's Law [98, pp. 125–126]:

$$F = -k\Delta x, \tag{3.1}$$

where F denotes an external force that drives the spring to change (to either extend or compress); Δx is the length change along the force's direction; and k reflects the elastic ability of the spring and is determined by the spring's intrinsic characteristic. Although the Hooke's Law describes a one-dimensional scenario, it can be generalized to higher dimensions and more complex situations.

3.1.1. Stress

Stress is defined as an internal resistance against an applied external force per unit area of the enforced object [98, p. 99]. Stress is usually recorded as σ with Pascal or N/m^2 as S.I. unit and defined as follows [98, pp. 99–100]:

$$\sigma = \frac{F}{A}, \tag{3.2}$$

where A is the area subjected to the force F. Since stress is an internal resistance it is important to clarify the difference between the external and the internal force undergone by the forced object.

Figure 3.1 shows a beam subjected to a uniaxial tensile load; F is the external force, applying at the right end of this beam. To find the internal force of this beam, an imaginary cut (labelled with

red dash outline) is applied, creating two cross planes shown in green in Figure 3.1. In Figure 3.1, assuming this enforced beam is in an equilibrium state, an internal force can be found at each internal (created) plane. However, as no real cut is performed, all the internal forces are assumed to be provided by inherent particles of this beam, and to resist the external forces to retain stability and integrity of the beam's inside microstructure and microenvironment. Specifically, an internal force at an internal plane is assumed to be from the interactive force provided by the plane next to this plane. Stress is a direct result of internal force, so in (3.2) A and F respectively correspond to the internal plane and the internal force. For an object that is under an unforced state, there are still internal forces inside for self-supporting the object's inner structure; however, within each unit area, these internal forces are assumed to cancel each other out creating a zero net-sum: this suggests that no stress is produced here either. Therefore, external force is an origin of internal force and stress. In order to avoid ambiguity, the subsequent figures of this chapter satisfy the following rules: all the objects and the labelled forces, unless specifically mentioned, are respectively recognized as the inner parts and the internal forces; the external forces, unless specifically mentioned, are intentionally not displayed.

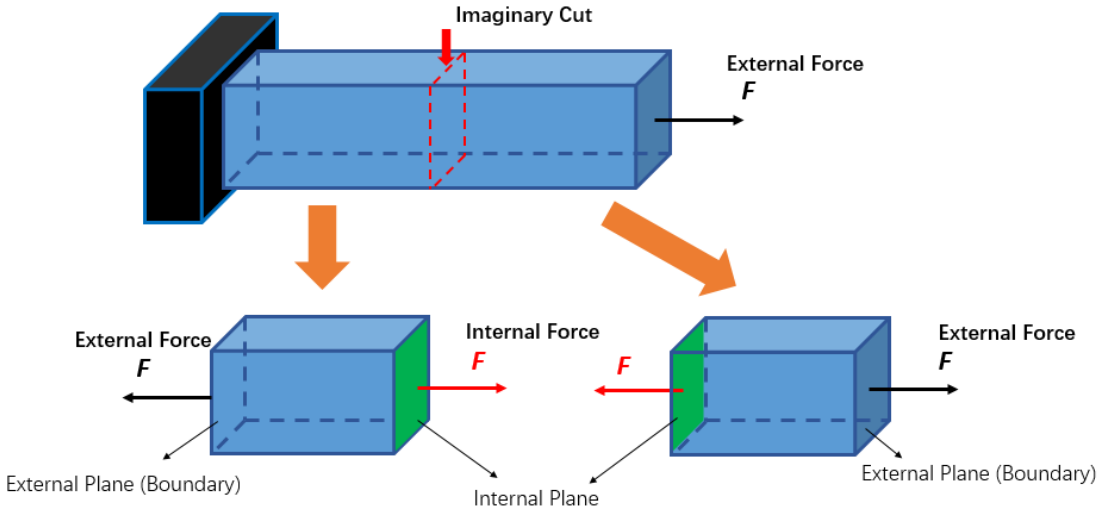

Figure 3. 1 An elastic beam that is fixed at one end and undergoes an external force at the other end. To analyze internal forces disturbed inside the beam, an imaginary cut is performed generating two internal planes where two internal forces are hypothetically produced with two opposite directions.

As introduced previously, stress is defined as an inherent resistance responding to an external load. However, this internal resistance may vary significantly inside an object due to a possibly complicated distribution of internal forces as shown in Figure 3.2. In Figure 3.2, if an area A is defined on plane S (labelled with the yellow box), as the size of A varies, the sum force within A will change as well (as the orange and red arrows respectively labelled with F_1 and F_2 shown in the figure). Therefore, based on (3.2), the definition of stress is revised and presented within an infinitesimal area [99, Sec. 3.3]:

$$\sigma = \lim_{A \to 0} \frac{F_A}{A}. \tag{3.3}$$

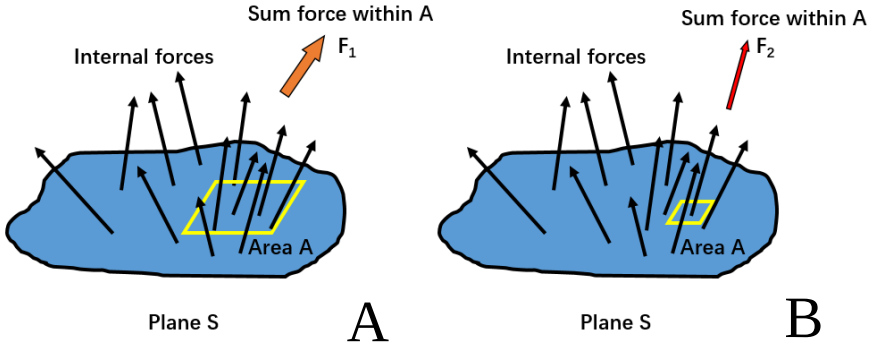

Figure 3. 2 Under the same distribution of internal forces, a relatively larger area A is drawn in **(A)**, while a relatively smaller area A' is drawn in **(B)**; each scenario has a different sum force within its drawn area.

The concept of stress can be generalized to an infinitesimal 3D case as shown in Figure 3.3. In Figure 3.3, the internal force is resolved to the x, y, and z axes as F_x, F_y and, F_z, respectively. Each resolved force produces a different stress at each plane. For a better demonstration, symbol σ_{ij} is used to differentiate each different stress—i.e. the first subscript i represents each plane's normal vector direction, and the second subscript j denotes each resolved force's direction. Specifically, in a normalized coordinate system, three stresses—one along longitudinal and two along orthogonally transverse directions—are found at each normalized plane (perpendicular to the x, y, or z axis): as Figure 3.3 shows, the longitudinal stresses are labelled by the red arrows and represented by σ_{ij} where $i = j$, and the transverse stresses are labelled by green arrows and symbolized by σ_{ij} where $i \neq j$. Furthermore, the longitudinal stress is defined as normal stress, and the transverse stress is defined as shear stress. As Figure 3.3 show, each internal force simultaneously produces the normal and the shear stresses at different planes: for example, F_x not only acts on plane $CDEF$ as an extending force, contributing normal stress σ_{xx}, but also acts on plane $EFGH$ and $BCFH$ as a shear force, producing shear stress σ_{zx} and σ_{yx}.

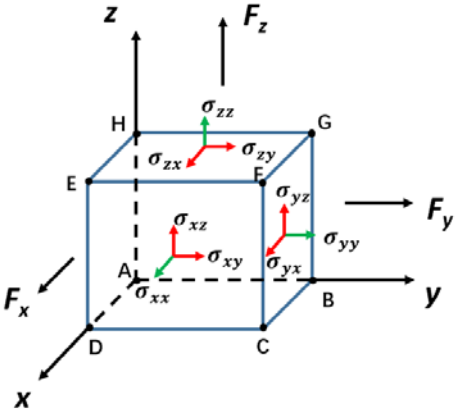

Figure 3. 3 An infinitesimal cube's stress distribution.

In most cases in practice, the body force[3], such as gravity or electromagnetic force, is assumed to be absent inside an infinitesimal element. Therefore, in Figure 3.4, all the forces acting on this infinitesimal plane can be expressed by stresses. Another important assumption that needs to be made is that this infinitesimal plane is in an equilibrium state of force. That is, in the equilibrium state, the net-sum of force equals to zero at each point over the plane (the point A for instance) [99, Sec. 3.4]: this also derives a zero net-sum of moment[4],

$$\sum M_A = 0 : 2 \cdot \left[\sigma_{xy}\Delta yt \cdot \frac{\Delta x}{2} \cdot \sin 90^\circ\right] - 2 \cdot \left[\sigma_{yx}\Delta xt \cdot \frac{\Delta y}{2} \cdot \sin 90^\circ\right] + 2 \cdot \left[\sigma_{xx}\Delta yt \cdot \frac{\Delta x}{2} \cdot \sin 0^\circ\right] + 2 \cdot \left[\sigma_{yy}\Delta xt \cdot \frac{\Delta y}{2} \cdot \sin 0^\circ\right] = 0 \text{ leading to } \sigma_{xy} = \sigma_{yx}. \tag{3.4}$$

The similar relations—i.e. $\sigma_{yz} = \sigma_{zy}$ and $\sigma_{xz} = \sigma_{zx}$—are found in the 3D case shown in Figure 3.3, which reduces the independent stresses from nine to six. All the stress components can be represented in a tensor matrix [98, p. 102]:

$$\sigma_{ij} = \begin{bmatrix} \sigma_{xx} & \sigma_{xy} & \sigma_{xz} \\ \sigma_{yx} & \sigma_{yy} & \sigma_{yz} \\ \sigma_{zx} & \sigma_{zy} & \sigma_{zz} \end{bmatrix} \rightarrow \begin{bmatrix} \sigma_{xx} & \sigma_{xy} & \sigma_{xz} \\ & \sigma_{yy} & \sigma_{yz} \\ & & \sigma_{zz} \end{bmatrix}. \tag{3.5}$$

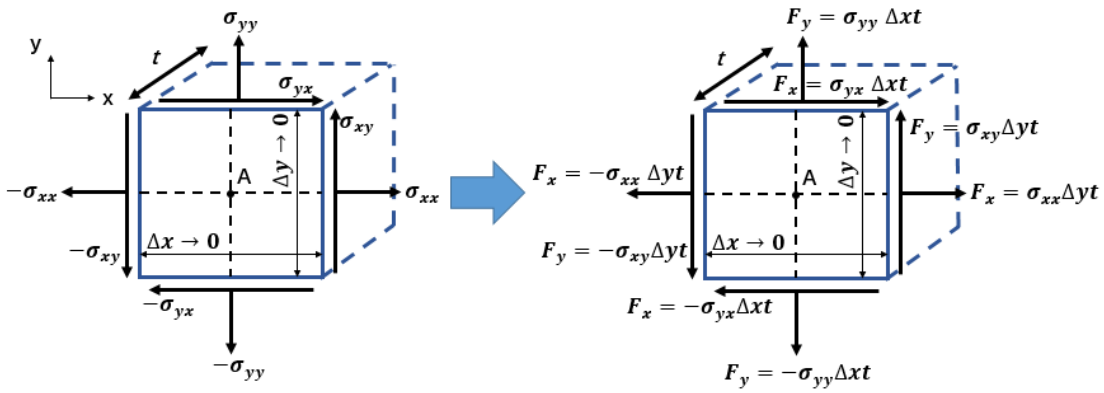

Figure 3. 4 When an infinitesimal transverse-plane (x-y) with a thickness t is under a force equilibrium state, the normal and the shear stresses provide a zero net-sum along each direction ($\pm\sigma_{ij}$, where $i, j = x, y$); these normal and shear stresses can be also retrieved back to the internal forces.

[3]"An external force, such as gravity, which acts on all parts of a body."—*McGraw-Hill Dictionary of Scientific & Technical Terms, 6E*. S.v. "Body force." Retrieved January 24 2017 from http://encyclopedia2.thefreedictionary.com/body+force

[4]"In physics, moment is defined as the perpendicular distance from a point to a line or a surface, and is derived from the mathematical concept of moments." —*McGraw-Hill Dictionary of Scientific & Technical Terms, 6E*. S.v. "Moment (physics)." Retrieved January 24 2017 from http://encyclopedia2.thefreedictionary.com/Moment+(physics)

3.1.2. Strain

Strain describes dimensional changes of an object (such as a shape or size change) in comparison to the object's original dimensions when an external force is applied; it is defined as follows [99, Sec. 4.1]:

$$\varepsilon = \frac{\Delta l}{l}, \tag{3.6}$$

where ε is the strain, l represents the original dimension of the object, and Δl denotes the dimensional change. Strain is defined as a ratio without a unit.

To further explain strain in detail, Figure 3.5 shows a beam (blue with dashed outline) undergoing an external force F. As explained previously, under this external force F, the internal plane of this beam is subject to an internal force with the same magnitude as the external force. Under this internal force, a stress σ is produced at this internal plane as well. However, in Figure 3.5, as a result of the internal force, this internal plane, if it is with a thickness of t (labelled with red dash outline), might not only travel a distance (demonstrated by the orange beam frame), but also initiate a deformation within itself—i.e., under the latter scenario, the internal plane might extend to t' (labelled as the orange dot outline). These travel and deformation altogether are generalized as strain [99, Sec. 4.1]. The strain can be also described by two inside points' displacements driven by the internal force (stress), and it is rewritten as

$$\varepsilon = \frac{A'B' - AB}{AB} = \frac{A'A - B'B}{AB}. \tag{3.7}$$

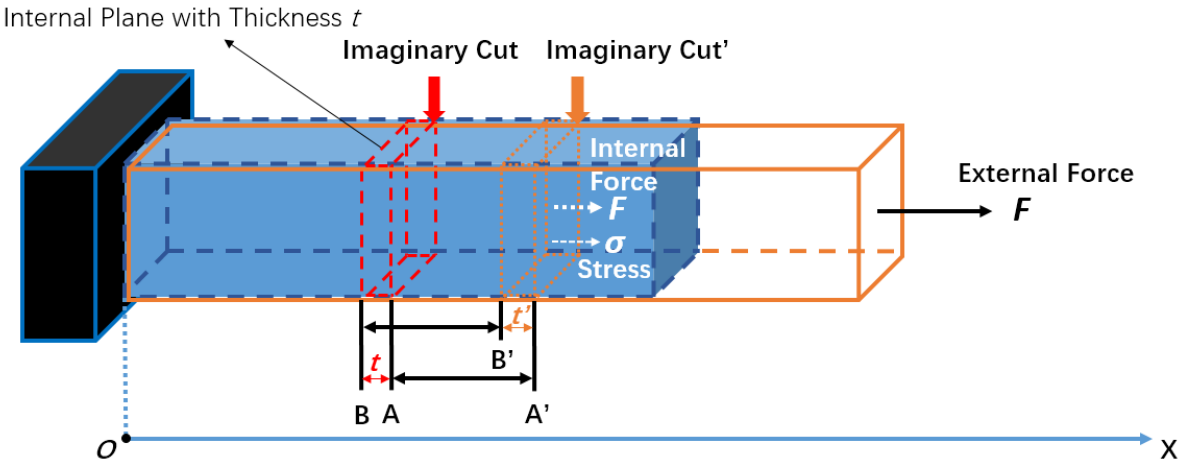

Figure 3. 5 Deformational analysis of a beam. Under an external force F, comparing to the beam's original shape indicated by the blue dashed line, it travels a distance demonstrated by the orange solid block, and for any two points inside this beam—for instance A and B, their positions in the x-axis respectively changes to A' and B'. In addition, during the deformation, the relative position between A and B (i.e., the observed internal plane's thickness t) may change as well (for example, changing to t').

Similar to stress, strain should be redefined in an infinitesimal dimension as well. Figure 3.6 shows a beam before (indicated by the blue frame) and after (indicated by the orange dash outline) an external force is applied to its end. Specifically, in Figure 3.6, after the deformation, segments AB and AC with yellow solid outlines indicated are extended and shift to $A'B'$ and $A'C'$ with yellow dot outlines indicated, respectively. As Figure 3.6 shows, the change from AB to $A'B'$ might be significantly different from the change from AC to $A'C'$ due to a different intrinsic characteristic from point to point inside this beam. Therefore, it is necessary to narrow this distance from point to point (illustrated by Δx in Figure 3.6) to an infinitesimal length that can reflect a unique strain characteristic for each unit segment. Consequently, in an infinitesimal dimension, the strain is redefined with the aid of the displacement of each inside point referring to $u(x)$ in Figure 3.6 as follows [99, Sec. 4.1]:

$$\varepsilon = \lim_{\Delta x \to 0} \frac{u(x+\Delta x)-u(x)}{\Delta x} = \frac{\partial u}{\partial x}, \tag{3.8}$$

where ε represents the strain, x indicates the location along the *x*-axis, Δx is the interval between each labelled point, and u denotes the displacement along the *x*-axis in Figure 3.6.

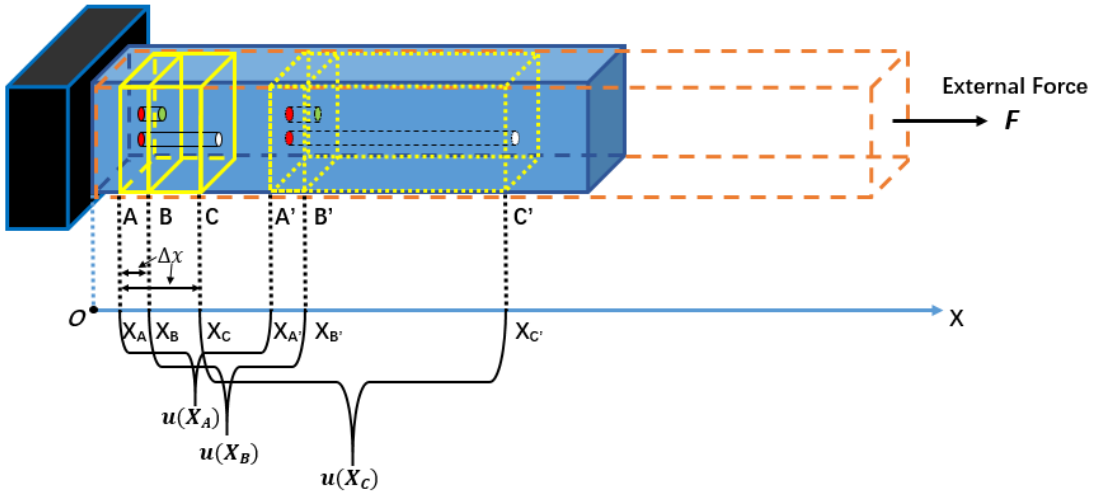

Figure 3. 6 In a beam, three points are defined as A, B, and C, and are indicated by the red, green, and white circles; each has an initial location in the x axis—X_A, X_B, and X_C. After an external force F is applied, each of these points might experience a different displacement—i.e., $u(X_A)$, $u(X_B)$, and $u(X_C)$—arriving at its new location, X_A', X_B', and X_C': this suggests the strain may vary at different locations in an object.

First, when describing the deformed object in one dimension, the dimensional change is simply either an extension or a contraction. However, when described in higher dimensions (2D or 3D), the dimensional changes become more complex. Specifically, Figure 3.7 (A), (B), and (C) show that a uniaxial force acts respectively along the x-axis, y-axis, and z-axis to an infinitesimal 3D cube (indicated by the dark blue outline), and along each direction, a deformation occurs (indicated by the orange dash outline) responding to each constraint force. Additionally, as Figure 3.7 shows, each force—F_x, F_y, and F_z—respectively causes strains at all three direction: ε'_{xx}, ε'_{yy}, and ε'_{zz}

are the result of F_x; ε''_{xx}, ε''_{yy}, and ε''_{zz} are the result of F_y; and ε'''_{xx}, ε'''_{yy}, and ε'''_{zz} are the result of F_z [100, Sec. 5.5.1]. Especially, when all the three forces simultaneously apply to this cube, the strain driven by each of these forces should be summed together to describe the actual deformation occurring along this direction—i.e., $\varepsilon_{ii} = \varepsilon'_{ii} + \varepsilon''_{ii} + \varepsilon'''_{ii}$ where $i = x, y$ and z [100, Sec. 5.5.1]. This type of deformation is defined as normal strain. As Figure 3.7 illustrates, this cube's normal strains under different cases are described as follow:

$$\begin{cases} \varepsilon'_{xx}(\varepsilon''_{xx}\ or\ \varepsilon'''_{xx}) = \frac{E'H'-EH}{EH} = \frac{F'G'-FG}{FG} = \frac{B'C'-BC}{BC} = \frac{A'D'-AD}{AD} \\ \varepsilon'_{yy}(\varepsilon''_{yy}\ or\ \varepsilon'''_{yy}) = \frac{E'F'-EF}{EF} = \frac{G'H'-GH}{GH} = \frac{A'B'-AB}{AB} = \frac{C'D'-CD}{CD} \\ \varepsilon'_{zz}(\varepsilon''_{zz}\ or\ \varepsilon'''_{zz}) = \frac{D'E'-DE}{DE} = \frac{C'F'-CF}{CF} = \frac{B'G'-BG}{BG} = \frac{A'H'-AH}{AH} \end{cases} \quad (3.9)$$

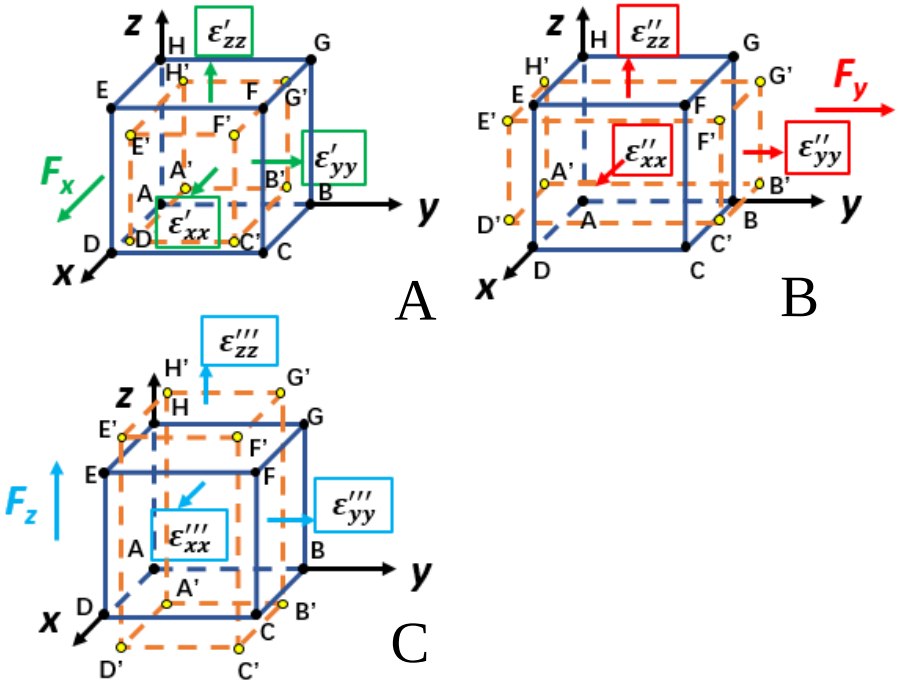

Figure 3. 7 An infinitesimal cube's normal strain distribution **(A)** when a normal force F_x acts along the x axis; **(B)** when a normal force F_y acts along the y axis; and **(C)** when a normal force F_z acts along the z axis. The deformations are indicated by the orange dashed outline.

Second, an object can also go through other deformations as shown in Figure 3.8 where two perpendicular forces simultaneously apply to an infinitesimal cube. Specifically, Figure 3.8 (A), (B), and (C) respectively show this infinitesimal cube and its corresponding 2D projection under a different combination of directions of the perpendicular force pair; in the 2D projections, the blue outlines represent the original states, while the orange outlines indicate the deformed states. In Figure 3.8, under this pair of perpendicular forces, two adjacent, orthogonal planes are squeezed simultaneously, producing two small angles by each of forces—i.e., λ' (λ'' or λ''') and θ' (θ''

or θ''')). This type of deformation is termed as "Pure Shear", and the shear strain (in engineering) is defined by these angles [100, Sec. 4.4]:

$$\begin{cases} \gamma_{xy} = \gamma_{xy} = \lambda' + \theta' \\ \gamma_{yz} = \gamma_{zy} = \lambda'' + \theta'' \\ \gamma_{xz} = \gamma_{zx} = \lambda''' + \theta''' \end{cases}, \tag{3.10}$$

where γ_{ij} and γ_{ji} ($i,j=x,y,z$ *and* $i \neq j$) are the shear strains.

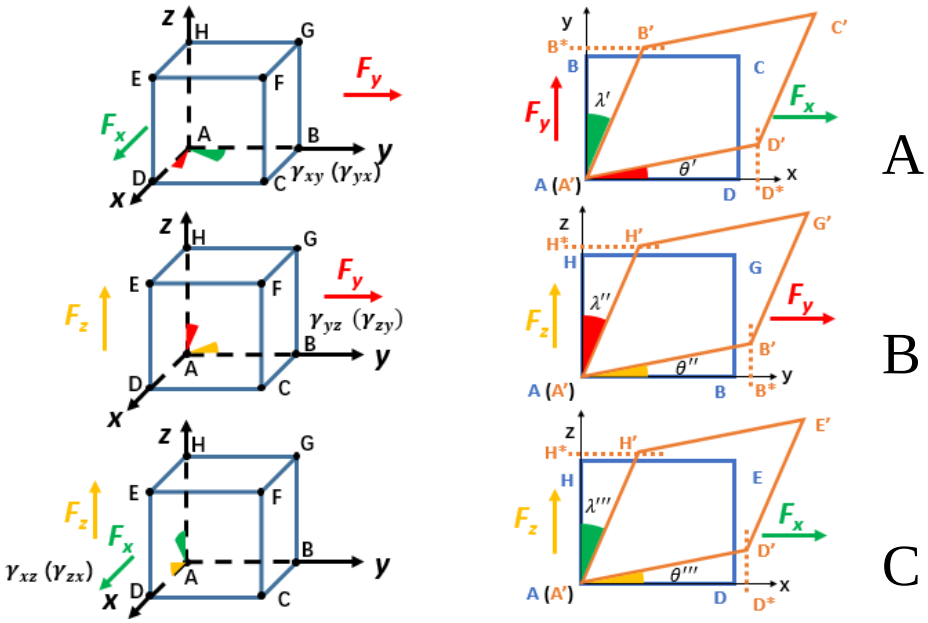

Figure 3. 8 An infinitesimal cube's shear strain distribution **(A)** when two shear forces F_x and F_y respectively act along the x axis and the y axis; **(B)** when two shear forces F_y and F_z respectively act along the y axis and the z axis; and **(C)** when two shear forces F_x and F_z respectively act along the x axis and the z axis. The deformations are presented into 2D projections and indicated by the orange solid outline.

Referring to Figure 3.9, the angles, which define the shear strain, geometrically fulfill the following relations [99, Sec. 4.1]:

$$\lambda \approx \tan\lambda \approx \frac{B'B^*}{AB} \text{ and } \theta \approx \tan\theta \approx \frac{D'D^*}{AD}, \tag{3.11}$$

where the superscript $*$ symbolizes the projection point to the axis. Since the deformation is subtle within such an infinitesimal cube in practice, AB^* and AD^* are replaced by AB and AD. Based on the same reason, the small angles, λ and θ, are assumed as nearly equaling to their corresponding tangents. In addition, besides the shear strains, a normal strain is also produced along each force's direction referring to Figure 3.9 as follows [99, Sec. 4.1]:

$$\varepsilon_{xx} = \frac{A'D' - AD}{AD} \approx \frac{A'D^* - AD}{AD} \text{ and } \varepsilon_{yy} = \frac{A'B' - AB}{AB} \approx \frac{A'B^* - AB}{AB}, \tag{3.12}$$

where $A'D^*$ and $A'B^*$ are respectively the projections of $A'D'$ and $A'B'$ to the axes for simplifying calculation in engineering. Generalized in in an infinitesimal case referring to Figure

3.9, the normal and the shear strains can be rewritten as follows [100, Sec. 4.5]:

$$\begin{cases} \varepsilon_{xx} = \lim\limits_{\Delta x \to 0} \frac{u(x+\Delta x,y)-u(x,y)}{\Delta x} = \frac{\partial u}{\partial x} \\ \varepsilon_{yy} = \lim\limits_{\Delta y \to 0} \frac{v(x,y+\Delta y)-v(x,y)}{\Delta y} = \frac{\partial v}{\partial y} \\ \gamma_{xy} = \gamma_{yx} = \lim\limits_{\Delta x \to 0} \frac{v(x+\Delta x,y)-v(x,y)}{\Delta x} + \lim\limits_{\Delta y \to 0} \frac{u(x,y+\Delta y)-u(x,y)}{\Delta y} = \frac{\partial v}{\partial x} + \frac{\partial u}{\partial y} \end{cases}. \quad (3.13)$$

Similarly, strains can be generalized into a 3D case and can be written into a matrix form as well [100, Sec. 4.4.3]:

$$\begin{bmatrix} \varepsilon_{xx} & \gamma_{xy} & \gamma_{xz} \\ \gamma_{yx} & \varepsilon_{yy} & \gamma_{yz} \\ \gamma_{zx} & \gamma_{zy} & \varepsilon_{zz} \end{bmatrix} \rightarrow \begin{bmatrix} \varepsilon_{xx} & \gamma_{xy} & \gamma_{xz} \\ & \varepsilon_{yy} & \gamma_{yz} \\ & & \varepsilon_{zz} \end{bmatrix}. \quad (3.14)$$

However, (3.14) is not a tensor matrix because the shear strain described here is a scalar quantity (without a direction component), and this non-tensor shear strain is termed as engineering strain. A tensor shear strain, referring to Figure 3.9, is defined as follows [99, Sec. 4.1.2]:

$$\varepsilon_{xy} = \frac{1}{2}\left(\frac{\partial v}{\partial x} + \frac{\partial u}{\partial y}\right), \quad (3.15)$$

where the tensor shear strain is defined as a half of the engineering shear strain. Therefore, a tensor strain matrix is expressed as follow:

$$\varepsilon_{ij} = \begin{bmatrix} \varepsilon_{xx} & \varepsilon_{xy} & \varepsilon_{xz} \\ \varepsilon_{yx} & \varepsilon_{yy} & \varepsilon_{yz} \\ \varepsilon_{zx} & \varepsilon_{zy} & \varepsilon_{zz} \end{bmatrix} = \begin{bmatrix} \varepsilon_{xx} & \frac{1}{2}\gamma_{xy} & \frac{1}{2}\gamma_{xz} \\ \frac{1}{2}\gamma_{yx} & \varepsilon_{yy} & \frac{1}{2}\gamma_{yz} \\ \frac{1}{2}\gamma_{zx} & \frac{1}{2}\gamma_{zy} & \varepsilon_{zz} \end{bmatrix}. \quad (3.16)$$

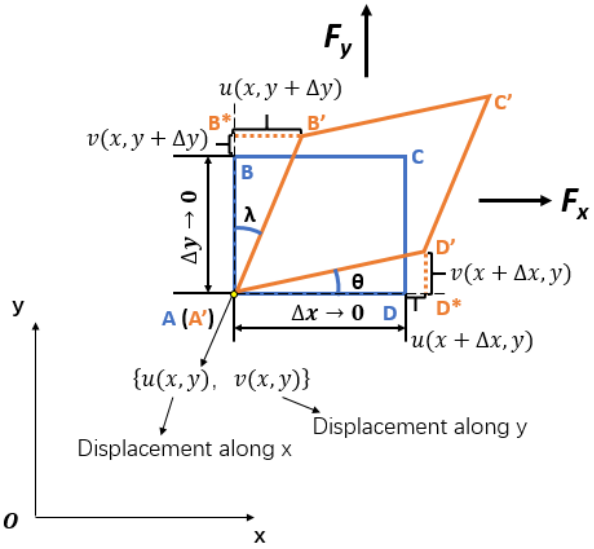

Figure 3. 9 Geometrical analysis of shear strain. An elastic infinitesimal plane ($ABCD$) undergoes two forces F_x and F_y occurring a shear deformation (to $A'B'C'D'$), and two angles λ and θ are produced and can be used to describe the shear strain. (The blue outline indicates the original state, and the orange outline indicates the deformed state.)

3.1.3. Elasticity

The following theory of elasticity is assumed and discussed in an (at least locally) isotropic[5] and homogenous[6] case [98, p. 139]. Hooke's Law can be used to describe an object's elasticity as introduced previously. According to the Hooke's Law, the enforced object is usually assumed possessing a uniform elastic characteristic: this is reasonable for some specific cases such as a uniform spring. However, most materials in nature—especially soft tissues in the human body—usually have an inhomogeneous elasticity distribution, even though this inhomogeneity may not be quite significant sometimes. In mechanics, such an object is defined as a continuum [99, Sec. 5.4], [101, pp. 18–20]. To precisely target and have access to the local elasticity, a continuum is mathematically divided into a set of infinitesimal elements; under a uniaxial tensile stress, an infinitesimal element's elasticity is defined as follows [98, pp. 126–127]:

$$E = \sigma/\varepsilon, \tag{3.17}$$

where E is generally known as Young's Modulus with Pascal as its S.I. unit, and is expressed by the ratio of stress σ and strain ε. Specifically, in a generalized case shown in Figure 3.10, when a uniaxial force is applied, besides a longitudinal deformation occurring along the uniaxial direction y, two other deformations simultaneously appear along the two perpendicular transverse directions x and z. According to the isotropic assumption stated previously, referring to Figure 3.10, the normal strains along the two transverse directions—ε_{xx} and ε_{zz}—equal to each other.

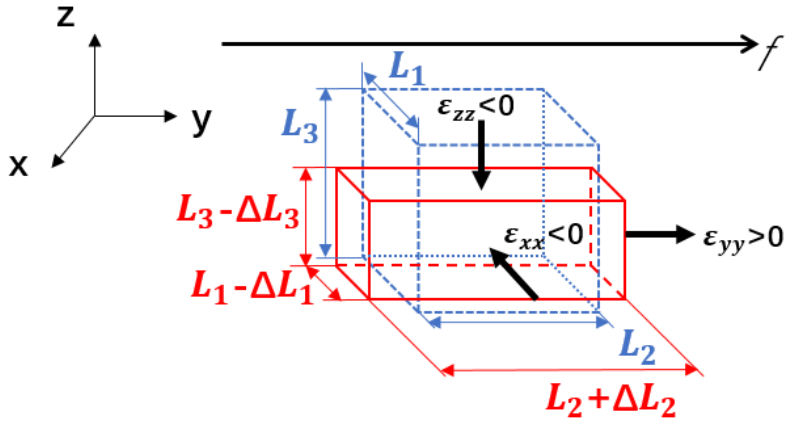

Figure 3. 10 Normal strain analysis. When a uniaxial force f applies to an elastic cube (with the edges of L_1, L_2, and L_3), one deformation ($L_2 + \Delta L_2$) occurs along a longitudinal direction, and two deformations ($L_1 - \Delta L_1$ and $L_3 - \Delta L_3$) occur along two perpendicular, transverse directions.

[5]"Identical in all directions"—Dictionary.com "isotropic," in *The American Heritage® Science Dictionary*. Source location: Houghton Mifflin Company. http://www.dictionary.com/browse/isotropic. Available: http://www.dictionary.com/. Accessed: May 4, 2017.

[6]"Of the same or similar nature or kind." / "
Uniform in structure or composition throughout, as of a chemicalmixture." —Dictionary.com "homogeneous," in The American Heritage® Science Dictionary. Source location: Houghton Mifflin Company. http://www.dictionary.com/browse/homogeneous. Available: http://www.dictionary.com/. Accessed: May 4, 2017.

As for the relationship between the longitudinal and the transverse normal strain, it is linked by another mechanical quantity, Poisson's ratio, which is defined as a ratio of a transverse normal strain to a longitudinal normal strain [98, p. 127]:

$$\nu = -\varepsilon_{xx}/\varepsilon_{yy} = -\varepsilon_{zz}/\varepsilon_{yy}, \tag{3.18}$$

where ν is determined by martials' intrinsic characteristics—i.e., under a uniaxial force, each type of material generally has a unique Poisson's ratio. This Poisson's ratio can be measured by the enforced object's longitudinal and transverse normal strains as demonstrated in (3.18). Normally, most common materials' Poisson's ratio ranges from -1 to 0.5 [102, p. 75]. The Poisson's ratio can also describe volume changes: first, the infinitesimal cube' all normal strains, as shown in Figure 3.10, can be described in a differential scenario as follows [99, Sec. 4.3.2]:

$$d\varepsilon_x = \frac{dx}{x}, d\varepsilon_y = \frac{dy}{y}, \text{and } d\varepsilon_z = \frac{dz}{z}; \tag{3.19}$$

second, as Figure 3.10 shows, these differential strains can be integrated as follows (see equation (3.18)):

$$-\nu \int_{L_2}^{L_2+\Delta L_2} \frac{dy}{y} = \int_{L_1}^{L_1-\Delta L_1} \frac{dx}{x} = \int_{L_3}^{L_3-\Delta L_3} \frac{dz}{z}, \tag{3.20}$$

which yields,

$$\left(\frac{L_2+\Delta L_2}{L_2}\right)^{-\nu} = \left(\frac{L_1-\Delta L_1}{L_1}\right) = \left(\frac{L_3-\Delta L_3}{L_3}\right); \tag{3.21}$$

third, the infinitesimal cube's volumes before and after the deformation are as follows:

$$V_{Before} = L_1 \cdot L_2 \cdot L_3 \tag{3.22}$$

and

$$V_{After} = (L_1 - \Delta L_1) \cdot (L_2 + \Delta L_2) \cdot (L_3 - \Delta L_3); \tag{3.23}$$

and last, the comparison between these two volume states gives

$$\frac{V_{After}}{V_{Before}} = \left(\frac{L_1-\Delta L_1}{L_1}\right) \cdot \left(\frac{L_2+\Delta L_2}{L_2}\right) \cdot \left(\frac{L_3-\Delta L_3}{L_3}\right), \tag{3.24}$$

and in terms of (3.21), (3.24) goes by

$$\frac{V_{After}}{V_{Before}} = \left(\frac{L_2 + \Delta L_2}{L_2}\right)^{1-2\nu}, \tag{3.25}$$

where the Poisson's ratio, ν, exponentially regularizes the volume change that is also determined by the original dimension L_2 and the varied length ΔL_2. Specially, if assigning 0.5 to the Poisson's ratio ν, (3.25) equals to 1: this means that this cube does not go through a volume change before and after the deformation. This case can be described by a special mechanical characteristic, "Incompressibility (Incompressible material)", for materials with a Poisson's ratio of 0.5 [99, Sec. 5.2.1], [103, p. 36]. To sum up, the incompressibility depicts that while undergoing a force, an object's volume retains unchanged (described as incompressible), even though its shape may vary distinctly [99, Sec. 5.2.4]. To the best of our knowledge, Poisson's ratio in most of the soft tissues is close to 0.5: this means that most soft tissues can be assumed as incompressible [103, p. 36].

Figure 3.11 illustrates all the normal and shear stresses (where the green arrows are as the normal stresses, while the red arrows are as the shear stresses) and all the strains (where the blue bold arrows are as the normal strains, while the colored angles are as the shear strains) together. Especially, each normal strain (the blue bold arrow), indicated in Figure 3.11, is contributed by the normal sub-strain (components) produced by the deformations occurring along all three directions (shown by three white arrows that are included in each blue bold arrow). These normal sub-strains with the corresponding normal stresses fulfill the following relations [100, Sec. 5.5.1]:

$$\begin{cases} \varepsilon_{xx}' = \frac{\sigma_{xx}}{E}, \varepsilon_{yy}' = \varepsilon_{zz}' = \frac{-\nu\sigma_{xx}}{E} \\ \varepsilon_{yy}'' = \frac{\sigma_{yy}}{E}, \varepsilon_{xx}'' = \varepsilon_{zz}'' = \frac{-\nu\sigma_{yy}}{E} \\ \varepsilon_{zz}''' = \frac{\sigma_{zz}}{E}, \varepsilon_{xx}''' = \varepsilon_{yy}''' = \frac{-\nu\sigma_{zz}}{E} \end{cases}. \tag{3.26}$$

where $'$ indicates that the produced normal stresses are the results of F'; $''$ indicates that the produced normal stresses are the results of F''; and $'''$ indicates that the produced normal stresses are the results of F'''. As mentioned previously, the normal strain, at same direction but from different deformations, can be summed together as follows [100, Sec. 5.5.1]:

$$\begin{cases} \varepsilon_{xx} = \varepsilon_{xx}' + \varepsilon_{xx}'' + \varepsilon_{xx}''' = \frac{1}{E}\sigma_{xx} - \frac{\nu}{E}(\sigma_{yy} + \sigma_{zz}) \\ \varepsilon_{yy} = \varepsilon_{yy}' + \varepsilon_{yy}'' + \varepsilon_{yy}''' = \frac{1}{E}\sigma_{yy} - \frac{\nu}{E}(\sigma_{xx} + \sigma_{zz}) \\ \varepsilon_{zz} = \varepsilon_{zz}' + \varepsilon_{zz}'' + \varepsilon_{zz}''' = \frac{1}{E}\sigma_{zz} - \frac{\nu}{E}(\sigma_{xx} + \sigma_{yy}) \end{cases}. \tag{3.27}$$

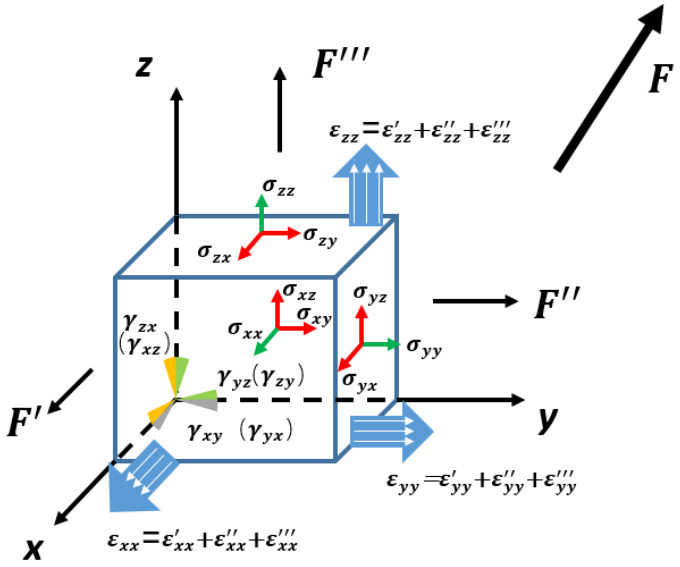

Figure 3. 11 An infinitesimal cube's stress and strain distribution when an internal force F is resolved to three orthogonal directions (the x, y, and z axes) as F', F'', and F'''. Particularly, for the normal strains, the strains produced by the each resolved force can be added together as $\varepsilon_{ii} = \varepsilon_{ii}' + \varepsilon_{ii}'' + \varepsilon_{ii}'''$ where $i = x,\ y,$ and z.

As for the relation between shear stress and shear strain, it is defined by another elastic characteristic, shear modulus, introduced by the shear test shown in Figure 3.12. Unlike the pure shear discussed previously, in Figure 3.12, two opposite shear stresses (σ_{xy}) act at a pair of parallel edges (or planes for a 3D case) generating a shear strain γ_{xy}, and the accompanying deformation is defined as a simple shear. As Figure 3.12 shows, shear modulus is defined by a shear stress and its corresponded shear strain [99, Sec. 5.2.3]:

$$G = \frac{\sigma_{xy}}{\gamma_{xy}}, \tag{3.28}$$

where the shear stress and the shear strain are represented by σ_{xy} and γ_{xy}, respectively; the shear modulus is symbolized by G or μ with a S.I. unit, Pascal. Young's modulus and shear modulus are commonly used to describe materials' elasticity, but they are differentiated by loading measures that objects undergo.

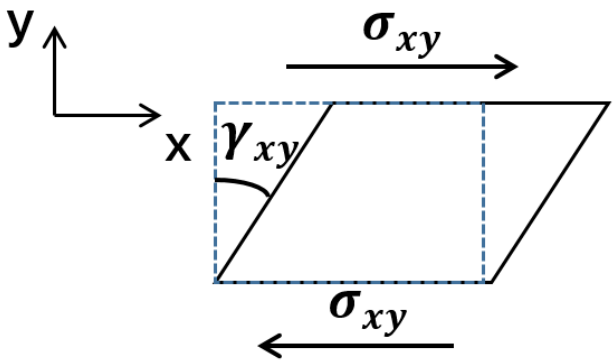

Figure 3. 12 Shear test: two opposite shear stresses (σ_{xy}) act at a pair of parallel edges (or planes for a 3D case) generating a shear strain γ_{xy}.

3.1.4. The Linear Elastic Model

Generally, the linear elastic model is able to model most of materials in nature, if the materials fulfill the following assumptions [99, Sec. 6.1]: (1) the relation between strains and stresses are assumed as linear in a small scale where the strains are quite small that means that the material will not exceed its elastic limit; (2) the material is able to recover to its initial state after removing all the loads, and the stresses and strains respectively remain a same linear mapping after loading and unloading; and (3) the rate or speed of loading or straining is irrelevant to the elastic model.

As stated previously, an object subjected to an external load can be mathematically divided into a set of infinitesimal elements (the black cube extracted in Figure 3.13) for studying materials' elastic characteristic. As Figure 3.13 shows, besides undergoing a body force b with its resolved components—b_x, b_y and b_z, each inherent infinitesimal element also undergoes forces from its adjacent elements, creating stresses—σ_{ij} (i,j=x,y,z)—at its each plane.

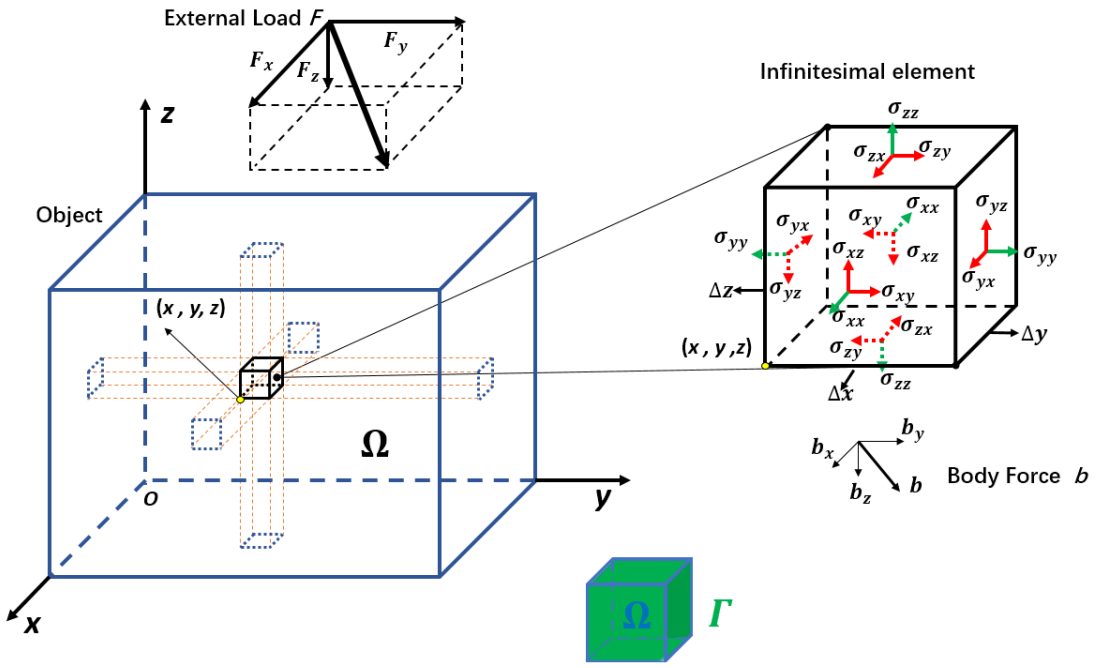

Figure 3. 13 Definition of an infinitesimal element. An enforced object (under an external load F) can be mathematically divided into a set of infinitesimal elements (i.e., $\Delta x, \Delta y$ and $\Delta z \to 0$), and within each infinitesimal element, the normal and shear stresses (σ_{ij} $i,j = x,\ y,$ and z) can be found at each plane. In addition, this object's all outer planes constitute a closed boundary Γ, and the inner space containing all the infinitesimal elements is marked as Ω.

According to the Newton's Second Law, each infinitesimal element's force analysis, as illustrated in Figure 3.13, satisfies the following relations [98, p. 104]:

$$\begin{cases} \left(\sigma_{xx}(x+\Delta x)-\sigma_{xx}(x)\right)\Delta y\Delta z+\left(\sigma_{yx}(y+\Delta y)-\sigma_{yx}(y)\right)\Delta x\Delta z+\left(\sigma_{zx}(z+\Delta z)-\sigma_{zx}(z)\right)\Delta x\Delta y+b_x\Delta x\Delta y\Delta z \\ \qquad\qquad =\rho a_x\Delta x\Delta y\Delta z \\ \left(\sigma_{yy}(y+\Delta y)-\sigma_{yy}(y)\right)\Delta x\Delta z+\left(\sigma_{xy}(x+\Delta x)-\sigma_{xy}(x)\right)\Delta y\Delta z+\left(\sigma_{zy}(z+\Delta z)-\sigma_{zy}(z)\right)\Delta x\Delta y+b_y\Delta x\Delta y\Delta z \\ \qquad\qquad =\rho a_y\Delta x\Delta y\Delta z \\ \left(\sigma_{zz}(z+\Delta z)-\sigma_{zz}(z)\right)\Delta x\Delta y+\left(\sigma_{xz}(x+\Delta x)-\sigma_{xz}(x)\right)\Delta y\Delta z+\left(\sigma_{yz}(y+\Delta y)-\sigma_{yz}(y)\right)\Delta x\Delta z+b_z\Delta x\Delta y\Delta z \\ \qquad\qquad =\rho a_z\Delta x\Delta y\Delta z \end{cases} \tag{3.29}$$

where ρ is the density of materials, and a_x, a_y, and a_z are the accelerated velocity's resolved components.

If discussed in a differential case, (3.29) goes by

$$\begin{cases} \dfrac{\partial\sigma_{xx}}{\partial x}+\dfrac{\partial\sigma_{yx}}{\partial y}+\dfrac{\partial\sigma_{zx}}{\partial z}+b_x=\rho a_x \\ \dfrac{\partial\sigma_{xy}}{\partial x}+\dfrac{\partial\sigma_{yy}}{\partial y}+\dfrac{\partial\sigma_{zy}}{\partial z}+b_y=\rho a_y, \\ \dfrac{\partial\sigma_{xz}}{\partial x}+\dfrac{\partial\sigma_{yz}}{\partial y}+\dfrac{\partial\sigma_{zz}}{\partial z}+b_z=\rho a_z \end{cases} \tag{3.30}$$

and (3.27) and (3.28) yield to the following six relations [100, Sec. 5.5.2]:

$$\begin{cases} \sigma_{xx} = \frac{E}{1+\nu}\varepsilon_{xx} + \frac{E\nu}{(1+\nu)(1-2\nu)}(\varepsilon_{xx} + \varepsilon_{yy} + \varepsilon_{zz}) \\ \sigma_{yy} = \frac{E}{1+\nu}\varepsilon_{yy} + \frac{E\nu}{(1+\nu)(1-2\nu)}(\varepsilon_{xx} + \varepsilon_{yy} + \varepsilon_{zz}) \\ \sigma_{zz} = \frac{E}{1+\nu}\varepsilon_{zz} + \frac{E\nu}{(1+\nu)(1-2\nu)}(\varepsilon_{xx} + \varepsilon_{yy} + \varepsilon_{zz}), \\ \sigma_{xy} = \sigma_{yx} = 2G\varepsilon_{xy} = 2G\varepsilon_{yx} \\ \sigma_{yz} = \sigma_{zy} = 2G\varepsilon_{yz} = 2G\varepsilon_{zy} \\ \sigma_{zx} = \sigma_{xz} = 2G\varepsilon_{zx} = 2G\varepsilon_{xz} \end{cases} \quad (3.31)$$

where $\frac{E\nu}{(1+\nu)(1-2\nu)}$ and $\frac{E}{2(1+\nu)}$ are respectively defined as the first and the second Lamé parameters with symbols—λ and μ, and μ is equivalent to the shear modulus (G).

(3.30) and (3.31) conjointly give the linear elastic model [87, p. 6], [98, p. 140]:

$$(\lambda + \mu)\boldsymbol{\nabla}(\boldsymbol{\nabla} \cdot \boldsymbol{u}) + \mu\boldsymbol{\nabla}^2\boldsymbol{u} + \boldsymbol{b} = \rho\boldsymbol{a} \text{ in } \boldsymbol{\Omega}, \quad (3.32)$$

$$\boldsymbol{u} = \hat{\boldsymbol{u}} \text{ on } \boldsymbol{\Gamma_1}, \quad (3.33)$$

$$[(\lambda + \mu)\boldsymbol{\nabla}(\boldsymbol{\nabla} \cdot \boldsymbol{u}) + \mu\boldsymbol{\nabla}^2\boldsymbol{u} + \boldsymbol{b}] \cdot \boldsymbol{n} = \hat{\boldsymbol{T}} \text{ on } \boldsymbol{\Gamma_2}, \quad (3.34)$$

where λ and μ are respectively the first and the second Lamé parameters; $\boldsymbol{u}$ is the object's displacement field under a motion; $\boldsymbol{b}$ is the body force vector; ρ is the density of materials; $\boldsymbol{a}$ is the accelerated velocity vector; $\boldsymbol{\Omega}$ stands for the internal space of the object; $\boldsymbol{\Gamma_1}$ represents the boundary specified by displacement [101, pp. 9–10]; $\hat{\boldsymbol{u}}$ is the value of the displacement on the boundary $\boldsymbol{\Gamma_1}$; $\boldsymbol{\Gamma_2}$ denotes the boundary specified by force [101, pp. 9–10]; $\boldsymbol{n}$ is the normal unit vector on the boundary; and $\hat{\boldsymbol{T}}$ is the traction of stress on the boundary $\boldsymbol{\Gamma_2}$. The boundary is either defined as a displacement or a force boundary: this means $\boldsymbol{\Gamma_1} \cap \boldsymbol{\Gamma_2} \equiv \emptyset$ [49], [75]; the displacement and force boundary also jointly constitute a complete, closed boundary $\boldsymbol{\Gamma}$—i.e., $\boldsymbol{\Gamma} \equiv \boldsymbol{\Gamma_1} \cup \boldsymbol{\Gamma_2}$ [49], [75]. The boundary's identification depends on each specific case and its force and motion analyses.

(3.32) to (3.34) constitute a model that describes an object under motion, and (3.33) and (3.34), specifically, are known as Boundary Condition [49], [75]. With the help of the boundary conditions, (3.32) becomes solvable. This linear elastic model takes the displacement fields (commonly in 3D) $\boldsymbol{u}$, body force (per infinitesimal element) $\boldsymbol{b}$, density (per infinitesimal element) ρ, and accelerated velocity (per infinitesimal element) $\boldsymbol{a}$ as inputs to solve the unknowns—the first Lamé parameter λ and the shear modulus (or the second Lamé parameter) μ (see (3.31)). However, in some cases, some of the parameters can be intentionally omitted to simplify the solving process: this will be discussed in further details in section 3.4.2.

The above has thoroughly explained the fundamental knowledge of stress, strain, the quantities describing elasticity, and the establishment of the model for materials with a linear elasticity, because MRE is established on the above linear elasticity theory [18].

3.2. Shear Wave and Driver System

As the linear elasticity theory stated above, in order to have ultimately access to an object's elasticity, the external load(s) must be correctly applied prior to the subsequent deformations' measurements. For MRE, the external loads are usually carried out by an acoustic driver system that can provide a continuous, stable mechanical wave at a single frequency. This driver system can normally generate a mechanical wave along either a single or multiple directions, depending on the system's design and configuration. However, in MRE, most the mechanical wave's acquisition strategies and subsequent inversion methods (converting wave images to a stiffness map) only require the wave propagation over a transverse plane—i.e., a shear wave [18].

3.2.1. Shear Wave

A wave propagation occurring in an elastic medium is categorized as either a compressional or a shear wave. When an external excitation is initiated at an elastic object's boundary, this boundary leads to its adjacent particles to repeat its previous motion with a scheduled time delay through internal forces; this motion pattern normally further propagates to another boundary (of the object). If motion's direction is perpendicular to wave propagation's direction, this wave is defined as a shear wave [104, pp. 57–59].

As Figure 3.14 illustrates, an elastic medium is mathematically divided into a set of infinitesimal elements, and a shear external excitation is applied on the elements of this elastic medium's one boundary [104, pp. 57–59]. At first, an internal force (or shear stress, labelled by the red outline), provided by the boundary's elements, drives the adjacent inherent elements to repeat the initial external excited motion with a time delay. Next, this motion sequentially propagates to another group of adjacent elements via another internal force (or shear stress, indicated with the green outline) with a further time delay. Consequently, this propagation reaches another boundary. This whole propagation process does not stop until the external excitation is removed.

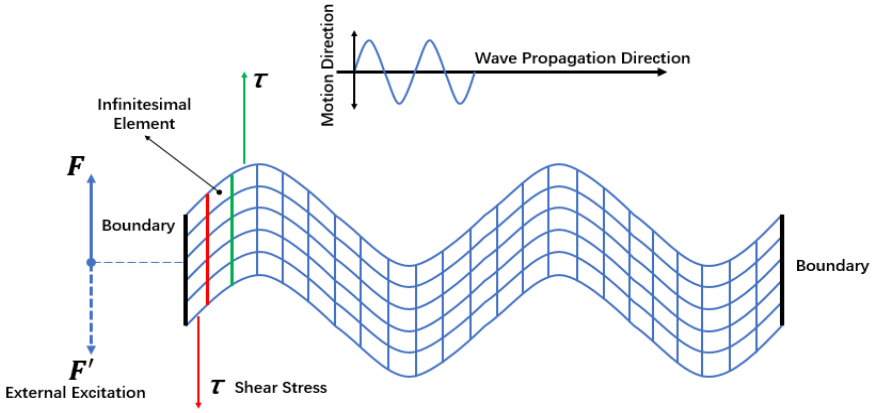

Figure 3. 14 A shear wave propagation and its associated force and stress analyses in an infinitesimal scale.

3.2.2. Driver System

MRE uses a driver system to generate and transmit the shear wave [18]. For safety considerations, the driver system must be designed as at least partly MR-compatible to work within the scanner room. Specifically, the driver system's MR-compatible part provides a direct physical vibration to phantoms or patients in the scanner's magnet bore, while the rest non-MR-compatible part is used to drive the MR-compatible part and to provide a communication, such as parameter settings, to the MRI console. In terms of driver systems' functionalities and configurations, the MR-compatible and the non-MR-compatible parts, which are bridged by a conduction medium, are respectively placed in the scanner room and the electronic room.

Many strategies are used to continuously generate a series of periodic vibrations at the non-MR-compatible terminal, and to provide a continuous, stable, and ample mechanical wave at the MR-compatible terminal (see Chapter 1, section 1.2). The MR-compatible terminal's output pattern and placement combine to decide the shear wave's introduction to the targets in the scanner's magnet bore, since MRE requires the shear wave for the subsequent imaging step. Specifically, Figure 3.15 (A) shows one solution to introduce the shear wave to an object: the shear wave can be introduced by a direct shear motion excitation on the boundary (plane). In this case, the introduced motion is solely along one transverse direction and generates a pure shear wave [18]. Figure 3.15 (B) shows another feasible solution that is the excitation is applied along the longitudinal direction: this approach introduces motions along the longitudinal and the transverse directions and generates a mix of a compressional wave and shear waves [22]. In this scenario, the mixed wave can be resolved to one compressional and two shear wave-components as shown in Figure 3.15 (B), and can be separately extracted by a MRE pulse sequence according to each orthogonal direction [60].

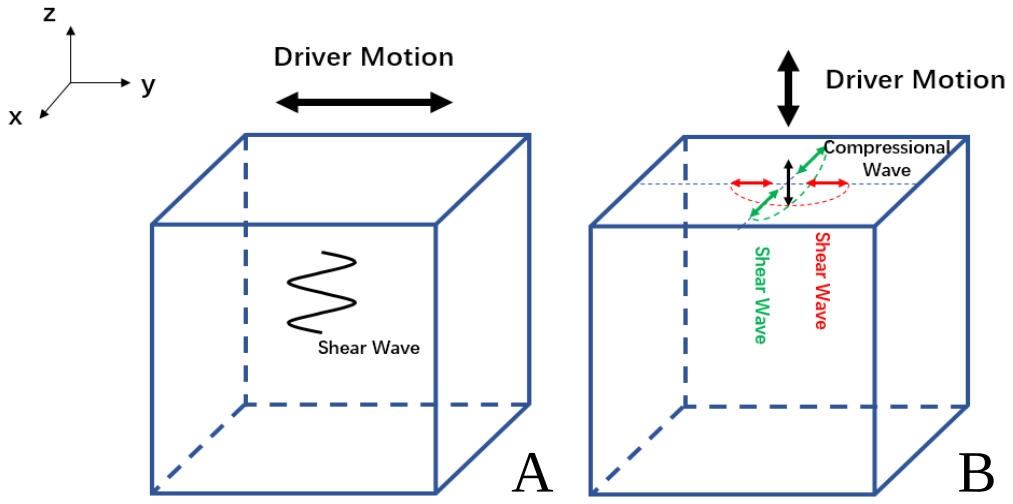

Figure 3. 15 Shear wave excitation methods: **(A)** a pure shear excitation; **(B)** a longitudinal excitation. The first approach produces a pure shear wave, while the second approach produces a mix of a compressional wave and shear waves.

These solutions are usually selected by practical needs, such as the fitting problem between the driver system's designs and patients' shape. However, no matter which scheme is utilized and what the shear wave's orientation is ultimately generated, the expected shear wave must be correctly encoded and be consistent to the MRI system: this is realized by the utilizing of MRE pulse sequences and will be further discussed in the next section.

3.3. MRE Pulse Sequence

A MRE pulse sequence is primarily to image the wave propagation for the subsequent elasticity calculation. The wave propagation's capture process must be synchronized to the introduced mechanical wave. In other words, the driver system and a MRE pulse sequence conjointly accomplish MRE's acquisition step.

3.3.1. Motion Encoding Gradient

As introduced in Chapter 2, MRI's gradient fields can precisely locate and encode an object's position. However, the gradient fields can be also used to encode spins' motion states. To capture the spins' motion along one specific direction, a special gradient, known as Motion Encoding Gradient (MEG), is inserted to a conventional pulse sequence that usually includes a slice selection (SS), a phase encoding (PE), and a frequency encoding (FE) gradients [88]. The MEG can be set for all the three directions (i.e., the SS, PE, and FE directions) depending on the motion's direction that needs to be recorded [60]. Due to the MEG's high sensitivity to motion, it is widely applied in Magnetic Resonance Angiography (MRA) for recording blood flow's velocity in the human veins [94, pp. 85–86].

Because of the MEG's functionality, it is also the most key component for capturing the wave propagation in a MRE pulse sequence. The MEG is realized by a bipolar gradient [18], [94, pp. 85–86]. This bipolar gradient consists of two gradient lobes, and each lobe has an opposite gradient polarity and an equal gradient magnitude and duration to the other one [94, pp. 85–86]. Specifically, the MEG provides an extra phase encoding to spins, and this extra phase accumulation for each spin is unique if the spins are in different motion status.

The spins with a harmonic motion can be described as follows:

$$\boldsymbol{S}(\boldsymbol{r}, t) = S_0 \sin(\boldsymbol{k} \cdot \boldsymbol{r} + \omega t + \theta), \tag{3.35}$$

where $\boldsymbol{S}$ is the spin's displacement, S_0 is the displacement's peak amplitude, $\boldsymbol{k}$ is the wave number, $\boldsymbol{r}$ is the position vector, ω is the wave's angular frequency, t represents time, and θ is the initial phase state also known as the delay for the MEG to the mechanical wave.
The MEG is usually defined as follows [105, p. 49]:

$$\boldsymbol{G_m}(t) = \begin{cases} G; nT \le t < (2n+1)T/2 \\ -G; (2n+1)T/2 \le t < (n+1)T \end{cases}, \tag{3.36}$$

where G is the MEG's magnitude and is generally assumed as a constant; and $n = 0,1,2 \ldots, N -$

1.
Based on the MEG's function in (3.36), the phase shift accumulated by the MEG is expressed as follows [18], [87, p. 9]:

$$\boldsymbol{\varphi}(\boldsymbol{r}, t = NT < \mathrm{TE}) = \gamma \int_0^{t=NT} \boldsymbol{G_m}(t) \cdot S_0 \sin(\boldsymbol{k} \cdot \boldsymbol{r} + \omega t + \theta) dt = \frac{2\gamma NTGS_0}{\pi} \cos(\boldsymbol{k} \cdot \boldsymbol{r} + \theta), \quad (3.37)$$

where $\boldsymbol{\varphi}$ is the phase shift that the MEG accumulates; TE is time to echo (TE); γ is protons' gyromagnetic ratio; τ is the MEG's duration of the; N is the MEG's cycles; and T is the MEG's period. The selection of N may depend on either the practical length of time to echo (TE), time to repetition (TR), and the acquisition time or, more importantly, the wave displacement's order of magnitude. For example, on one hand, N cannot be too large since it might potentially prolong the length of TE, TR, and the acquisition time; however, on the other hand, a larger value of N can help accumulate more extra phase shifts for the vibrated spins possessing a significantly small displacement—i.e., with a relatively large N, the small displacement might become more sensitive to the MEG, reflecting a stronger signal intensity on the acquired image.

In summary, (3.37) indicates a linear relation between the accumulated phase shift acquired by the MEG and the mechanical wave's displacement. This relation allows the mechanical wave to be recorded into a phase image produced by the MRE pulse sequence.

3.3.2. Phase Contrast

In MRE, phase contrast technique, sequentially carried out by a pair of MEGs with two opposite polarities, help accomplish the capture of the mechanical wave [87, pp. 9–10][87, p. 10]. Specifically, Figure 3.16 (A) shows that a MEG encodes the spins oscillating along the MEG's direction and consequently assigns each of the spins a phase accumulation according to its motion during the MEG encoding process. In order to correctly record each individual spin's motion, the MEG's oscillating frequency must be identical to the mechanical wave's oscillating frequency [87, p. 10]. However, these phase accumulations, no matter for the mobile or the stationary spins, are not only contributed by the MEG but also by the main magnetic field and the magnetic fields' inhomogeneity as background phase accumulations (the phase accumulations provided by the frequency and the phase encoding gradients are intentionally not mentioned because they are transformed to coordinate information). Because these background phase accumulations *per se* are not able to reflect the motion pattern, they can be excluded from the acquired image. Therefore, to extract the net phase accumulations that are solely contributed by the MEG, a second MEG with a same magnitude and a reverse polar is applied as shown in Figure 3.16 (B) [87, p. 10]. As Figure 3.16 (B) shows, in comparison to the previous resultant phase accumulations, these ones consist of a same component and a different component: the same component is the background phase accumulations contributed by the main magnetic field and the magnetic fields' inhomogeneity, and the different component is provided by the second MEG. As a result of the subtraction between two phase images respectively generated from the first and the second motion encoding processes

shown as Figure 3.16 (A) and (B), the background phase accumulations are offset, and a phase difference image, containing net phase accumulations, is generated. This phase difference image purely reflects the motion pattern and is given by

$$\Delta\boldsymbol{\varphi}(\boldsymbol{r}) = \frac{4\gamma NTGS_0}{\pi}\cos(\boldsymbol{k}\cdot\boldsymbol{r}+\theta), \tag{3.38}$$

where $\Delta\boldsymbol{\varphi}(\boldsymbol{r})$ is the phase difference at a given position $\boldsymbol{r}$ and an assigned motion phase θ; $\Delta\boldsymbol{\varphi}(\boldsymbol{r})$ is irrelevant with time when a phase difference image is generated. A map of the phase differences is defined as a phase contrast image [87, p. 10]. Particularly, the stationary spins' net phase accumulations are zero, while the mobile spins' net phase accumulations are non-zero and are differentiated by their motion states: in the resultant phase contrast image, this gives zero values for the stationary spins and a contrast among the mobile spins with different motion states [87, p. 10]. Because the phase difference $\Delta\boldsymbol{\varphi}(\boldsymbol{r})$ has a linear relation with the mechanical wave displacement $\boldsymbol{S}(\boldsymbol{r})$ (i.e. $S_0\sin(\boldsymbol{k}\cdot\boldsymbol{r}+\theta)$; see (3.38)), in practice the phase contrast images collected from the MRI scanner are generally assumed as equilvant to the wave (propagation) images.

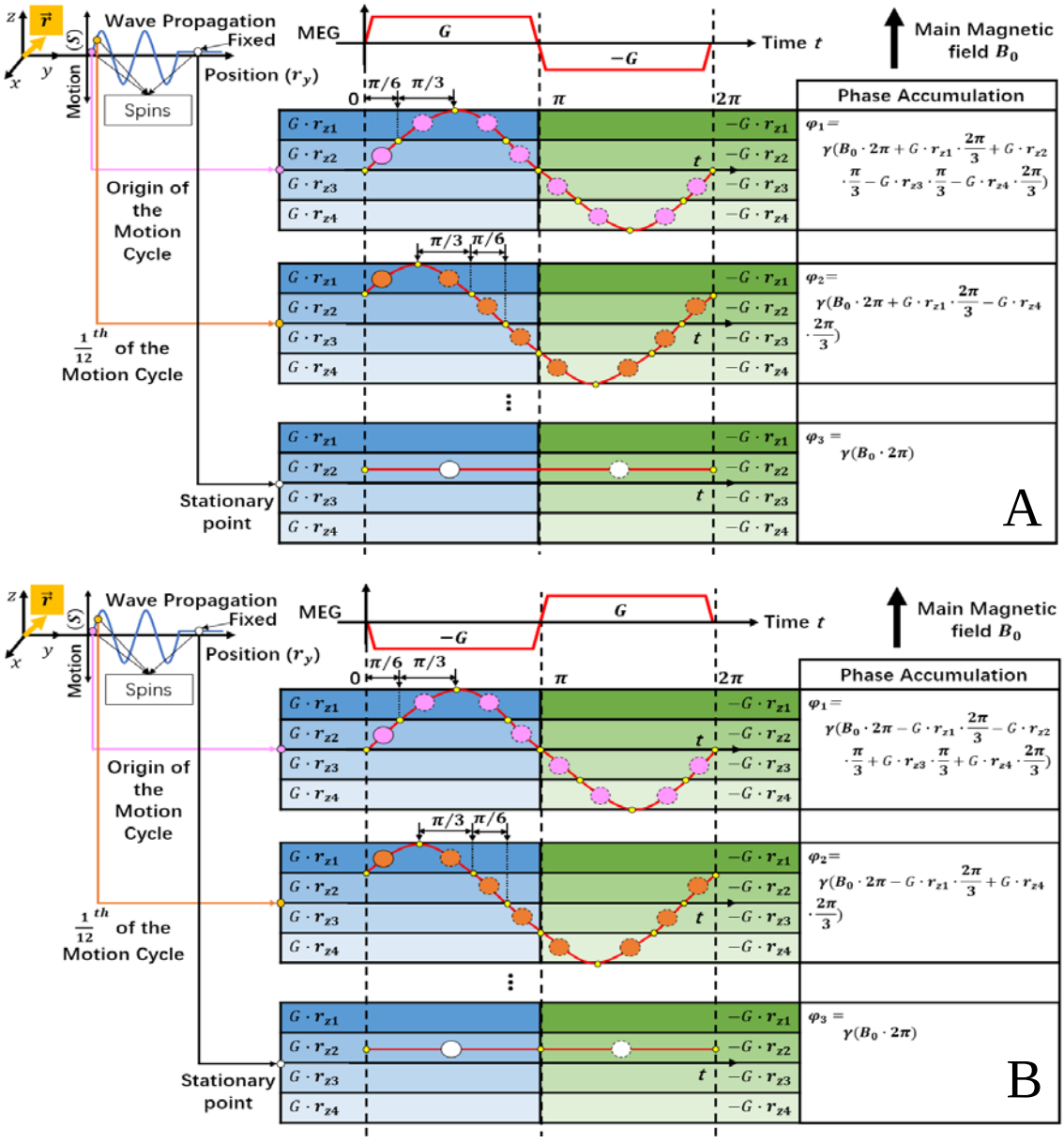

Figure 3. 16 For the spins at different positions along a shear wave's propagation pathway (for example, the origin, the $1/12^{th}$ of the motion cycle, and a fixed point), they are always in different motion states and are differently encoded by the MEGs; after the motion encoding, each of these spins is assigned to a unique phase accumulation (φ_1, φ_2, and φ_3). A pair of MEGs with two opposite polarities are used to generate a phase contrast image: **(A)** is the first phase accumulations generated by the first MEG; **(B)** is the second phase accumulations generated by the second MEG with an opposite polarity to the former one. The difference between the first and the second phase accumulations within a plane constitutes a phase contrast image.

3.3.3. Basic MRE Pulse Sequences

MRE pulse sequences help simultaneously realize the control of the driver system and the acquisition of the wave images with the aid of the phase contrast technique. The MEG pairs can be

combined with many conventional pulse sequences, such as the Gradient Recalled-Echo (GRE) or Spin Echo (SE)-Echo Planar Imaging (EPI), as respectively shown in Figure 3.17 (A) and (B) [88]. This combination integrates and adopts the conventional pulse sequences' unique features and advantages for MRE. For instance, the SE-EPI- based MRE pulse sequence has the acquisition speed of the EPI technique. In Figure 3.17 (A) and (B), the spatial encoding gradients (indicated by the blue sold lines) and the MEG (indicated by the red solid and dotted lines) are independent in the MRE pulse sequences, because the spatial encoding gradients are used to assign positions, while the MEG is primarily used for encoding motion information. That is, with the aid of the MEG insertion, the MRE sequence can simultaneously obtain the anatomical (structural) information and the motion pattern and can respectively encode them into a magnitude and a phase image in the end. In addition, the MEG pairs' placement depends on the motion direction(s) that need(s) to be sensitized: this means, theoretically speaking, the MEG pair can be placed in the slice-selection gradient's, phase-encoding gradient's, or/and frequency-encoding gradient's direction(s) [60].

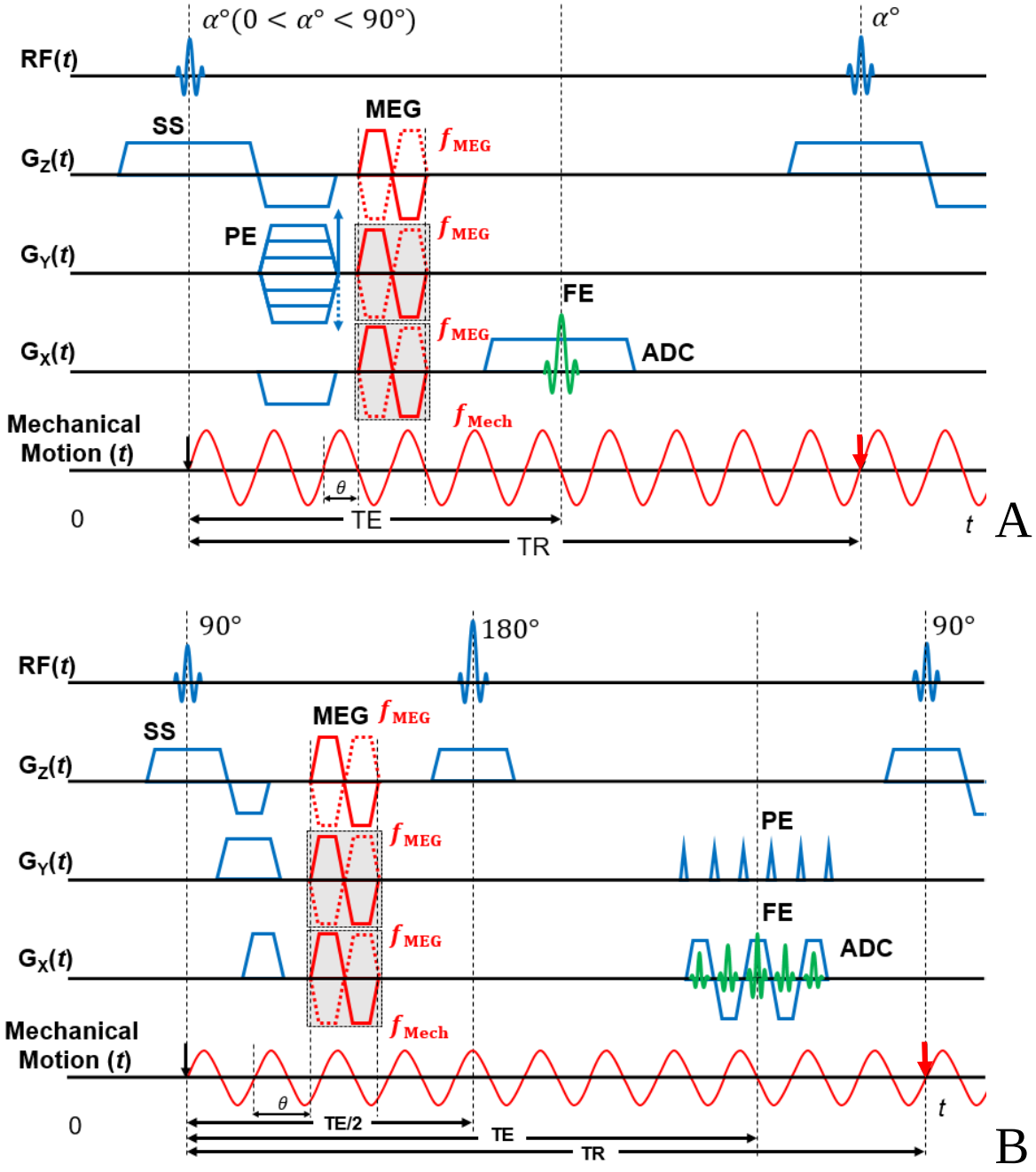

Figure 3. 17 Common MRE pulse sequences: **(A)** a GRE-based MRE pulse sequence; **(B)** an SE-EPI-based MRE pulse sequence.

In MRE pulse sequence, the MEG pairs are inserted ahead of the readout of signals. In a MRE pulse sequence, as briefly mentioned previously, the mechanical wave's oscillating frequency must synchronize with the MEG's oscillating frequency (i.e., $f_{MEG} = f_{Mech}$) [18]. If these two frequency parameters are not matched, the wave propagation cannot be correctly recorded. Additionally, as demonstrated by the red downside arrows in Figure 3.17 (A) and (B), this

synchronization also refers to the mechanical wave's continuous propagation at the boundary between each two successive TR cycles. In other words, to acquire a correct and complete wave image, the motion encoding (recording) process needs to start at a same mechanical wave's temporal state (temporal phase) each TR cycle. In a conclusion, in a MRE pulse sequence, TR's setting not only manages the magnitude image's contrast, but also, more importantly, determines the wave acquisition's correctness. The setting of TR must satisfy a formula as follows [106]:

$$\mathrm{TR} = \frac{n * N_{slice} * N_{cycle}}{f_{mech}}, \tag{3.39}$$

where N_{slice} is the number of slices; f_{mech} is the mechanical wave's frequency(which needs to be identical to the MEG's frequency); n is an integer factor that helps to extend TR; and as for N_{cycle}, in practice, the MRE pulse sequence is scheduled to communicate with the driver by sending a trigger within each TR cycle to initiate N_{cycle} wave cycles. Under such a combination of parameters, each triggered wave-cycle per TR-cycle is well accommodated at each TR moment as indicated by the red downside arrows in Figure 3.17 (A) and (B).

The phase delay θ—shown in Figure 3.17 (A) and (B)—is usually set at multiple, different values (which is normally four); these values are equally placed within each mechanical wave cycle to capture the wave propagation at different temporal states: this generates a dataset containing a continuous wave propagation [87, p. 23].

As introduced previously, most MRE pulse sequences are modified from the conventional MRI pulse sequences. Although this modification allows the pulse MRE sequences to adopt the good features and the advantages of the based MRI pulse sequences, the MRE pulse sequences also share some deficiencies of the based MRI pulse sequences, for example, the distortion or the N/2 Nyquist ghost artifacts caused by the SE-EPI sequence (see Chapter 2, section 2.4.3). Therefore, a MRE pulse sequence's protocol optimization relies on both the based MRI pulse sequence's basic settings and the special settings of the MEG and the driver system for the synchronization.

3.4. Inversion Algorithm

With the help of an inversion algorithm, elasticity information is calculated from the phase contrast images as the last step of MRE. The linear elasticity theory can apply to MRE for obtaining soft tissues' elasticity information[7] [88]. Recalling the linear elastic model expressed from (3.32) to (3.34) in section 3.1.4., if this model is adapted to MRE's scenario, it is redefined as follows [49]:

$$(\lambda + \mu)\boldsymbol{\nabla}(\boldsymbol{\nabla} \cdot \boldsymbol{u}) + \mu\boldsymbol{\nabla}^2\boldsymbol{u} = -\rho\omega^2\boldsymbol{u} \text{ in } \boldsymbol{\Omega}, \tag{3.40}$$

$$\boldsymbol{u} = \hat{\boldsymbol{u}} \text{ on } \boldsymbol{\Gamma_1}, \tag{3.41}$$

[7] 'Many of the approaches to inverting dynamic MRE data assume that the tissue can be modeled, at least in local regions, as a linear, isotropic, homogeneous viscoelastic solid undergoing infinitesimal motion absent any body forces.'—From K. J. Glaser, A. Manduca, and R. L. Ehman, "Review of MR elastography applications and recent developments," J. Magn. Reson. Imaging, vol. 36, no. 4, pp. 757–774, 2012 (Reference [88]).

$$[(\lambda+\mu)\boldsymbol{\nabla}(\boldsymbol{\nabla}\cdot\boldsymbol{u})+\mu\boldsymbol{\nabla}^2\boldsymbol{u}]\cdot\boldsymbol{n}=\widehat{\boldsymbol{T}} \text{ on } \boldsymbol{\Gamma_2}, \quad (3.42)$$

where λ is the first Lamé parameter and is usually irrelevant to the results of MRE; μ is the second Lamé parameter and is equivalent to the shear modulus as MRE's result reflecting the elasticity information; $\boldsymbol{u}$ is the displacement vector of the inspected tissue; ρ is the tissue's density usually assumed as 1000 $\mathrm{kg/m^3}$ in most cases; ω represents the introduced harmonic motion's angular frequency and is determined by the mechanical frequency f through the relation $\omega=2\pi f$; $-\rho\omega^2\boldsymbol{u}$ constitutes the vector of the simple harmonic forces; $\boldsymbol{\Omega}$ is the internal regions of the tissue; $\boldsymbol{\Gamma_1}$ is the defined displacement boundary of the tissue with a boundary value $\widehat{\boldsymbol{u}}$; and $\boldsymbol{\Gamma_2}$ is the defined force boundary with a unit normal vector $\boldsymbol{n}$ and a traction vector $\widehat{\boldsymbol{T}}$ on this boundary.

In summary, the converting from the wave propagation $\boldsymbol{u}$ to the final elasticity information μ is realized by solving the linear elastic model for MRE listed from (3.40) to (3.42), and this solving process is carried out by an inversion algorithm.

3.4.1. MRE Outputs

A series of MRE output images are sequentially generated during and after a MRE scan process. After the driver system and the MRE pulse sequence conducts the mechanical wave's acquisition, a magnitude and a phase contrast images are first generated: the magnitude image, which is related to MRE's based pulse sequence (e.g. GRE or SE-EPI), reflects the scanned subject's (e.g. a phantom's or a human's) anatomical structure; the phase contrast image, realized by the phase contrast technique, displays the wave propagation occurring within the scanned subject. These temporally continuous phase contrast images (collected at multiple even temporal phases in a wave period as introduced in section 3.3.3.) are equivalent to the measurements $\boldsymbol{u}$ to the linear elastic model for MRE. Although these phase contrast images (which are equivalent to wave images) can indirectly reflect the scanned subject's mechanical properties through the local wavelength variation, they are far less straightforward for interpretation. However, with the aid of the inversion algorithm, the wave images can be converted to a more readable map represented by shear modulus μ. This shear modulus map is known as the elastogram or the stiffness map in MRE. Figure 3.18 demonstrates a general MRE's workflow and MRE's major outputs (images) during this workflow.

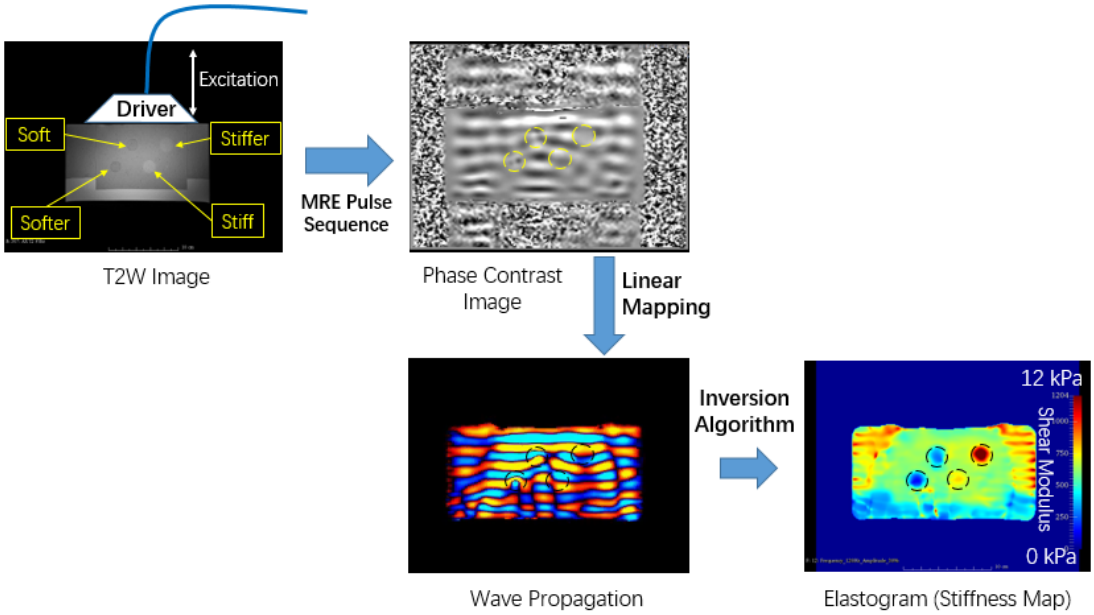

Figure 3. 18 MRE's workflow and its major outputs (images).

3.4.2. Inversion Algorithm

The inversion algorithm's objective is to convert the wave images to the stiffness map as introduced previously. The inversion algorithm's key principle can be summarized as a calculation process that obtains the shear modulus from the linear elastic model for MRE. Nowadays, many inversion algorithms are proposed and developed for addressing this problem, and three of the most common methods are covered below.

3.4.2.1. Local Frequency Estimation

Under the assumptions that most soft tissues are isotropic, homogeneous, and incompressible, the shear modulus reported by the stiffness map can be calculated from shear waves' velocity, since the velocity of shear waves is defined as follows [88], [104, p. 37]:

$$v_s = \sqrt{\frac{\mu}{\rho}}, \tag{3.43}$$

where v_s is the velocity of shear waves; μ is the shear modulus; and ρ represents density that is usually assumed as 1000 $\mathrm{kg/m^3}$ for most soft tissues. Furthermore, this relation can be transformed as follows [87, p. 11]:

$$\mu = \rho v_s^2 = \rho C^2 f^2, \tag{3.44}$$

where C denotes the wavelength of shear waves; and f represents the oscillating frequency of shear waves. Therefore, the shear modulus in MRE can be solved through this relation by acquiring the shear wave's local wavelength at a specific frequency [18]. Additionally, it is important to mention that (3.44) is a simplified relation derived from the linear elastic model for MRE, and this relation only needs 2D data or data with merely one MEG sensitization direction to obtain the shear modulus in elastograms [88]. It is also important to note that this relation is only perfectly

established when assuming the materials are purely elastic (no viscosity, and this condition is only valid to (3.44); however, (3.40) — (3.42) still assume the solid is locally homogeneous viscoelastic), but, in practice, most soft tissues are (or nearly are) qualified for this assumption [88].

To solve the shear modulus in elastograms, the local wavelengths can be directly measured from a 2D wave image in MRE. After several initial attempts that researchers manually measure the local wavelengths from the wave images, Manduca et al, in 1996, applied an algorithm that is able to automatically estimate the local wavelengths [61]. This algorithm was initially proposed by Knutsson et al in 1994 for calculating the local instantaneous frequency of signals [107]. Specially, this algorithm, known as the Local Frequency Estimation (LFE), uses a bandpass filter bank with different center frequencies and bandwidths to achieve an estimation of the local instantaneous spatial-frequency in MRE wave images. The applied filter is a quadrature filter with a radial component (which is usually a Gaussian function on a logarithmic scale) and a directional component. To estimate the local instantaneous spatial frequency, first, this filter bank, which usually consists of six different center frequencies (scales), is applied to the MRE wave images; second the ratio of each two adjacent (at center frequency) filters' outputs multiplies to the geometric mean of these two adjacent center frequencies; and in the final step, combining a weight factor that is related to energy, sums all the results obtained from the last step to produce the estimated results [61]. Although the LFE is limited by its relatively low-resolution results, in practical applications, it is robust in producing a high quality elastogram and efficient on processing time.

3.4.2.2. Direct Inversion

Alternatively, shear modulus can be also calculated by directly solving the linear elastic model for MRE. The linear elastic model for MRE, referring to (3.40), can be expressed in a matrix form as follows [72]:

$$\begin{bmatrix} \frac{\partial}{\partial x}\left(\frac{\partial u_x}{\partial x}+\frac{\partial u_y}{\partial y}+\frac{\partial u_z}{\partial z}\right), & \frac{\partial^2 u_x}{\partial x^2}+\frac{\partial^2 u_x}{\partial y^2}+\frac{\partial^2 u_x}{\partial z^2} \\ \frac{\partial}{\partial y}\left(\frac{\partial u_x}{\partial x}+\frac{\partial u_y}{\partial y}+\frac{\partial u_z}{\partial z}\right), & \frac{\partial^2 u_y}{\partial x^2}+\frac{\partial^2 u_y}{\partial y^2}+\frac{\partial^2 u_y}{\partial z^2} \\ \frac{\partial}{\partial z}\left(\frac{\partial u_x}{\partial x}+\frac{\partial u_y}{\partial y}+\frac{\partial u_z}{\partial z}\right), & \frac{\partial^2 u_z}{\partial x^2}+\frac{\partial^2 u_z}{\partial y^2}+\frac{\partial^2 u_z}{\partial z^2} \end{bmatrix} \begin{bmatrix} \lambda+\mu \\ \mu \end{bmatrix} = -\rho\omega^2 \begin{bmatrix} u_x \\ u_y \\ u_z \end{bmatrix}. \tag{3.45}$$

Consequently, the first and the second Lamé parameters, λ and μ (shear modulus), can be simultaneously solved as follows [72]:

$$\begin{bmatrix} \lambda+\mu \\ \mu \end{bmatrix} = -\rho\omega^2 (A^T A)^{-1} \boldsymbol{A} \begin{bmatrix} u_x \\ u_y \\ u_z \end{bmatrix}, \tag{3.46}$$

where $\boldsymbol{A} = \begin{bmatrix} \frac{\partial}{\partial x}\left(\frac{\partial u_x}{\partial x} + \frac{\partial u_y}{\partial y} + \frac{\partial u_z}{\partial z}\right), & \frac{\partial^2 u_x}{\partial x^2} + \frac{\partial^2 u_x}{\partial y^2} + \frac{\partial^2 u_x}{\partial z^2} \\ \frac{\partial}{\partial y}\left(\frac{\partial u_x}{\partial x} + \frac{\partial u_y}{\partial y} + \frac{\partial u_z}{\partial z}\right), & \frac{\partial^2 u_y}{\partial x^2} + \frac{\partial^2 u_y}{\partial y^2} + \frac{\partial^2 u_y}{\partial z^2} \\ \frac{\partial}{\partial z}\left(\frac{\partial u_x}{\partial x} + \frac{\partial u_y}{\partial y} + \frac{\partial u_z}{\partial z}\right), & \frac{\partial^2 u_z}{\partial x^2} + \frac{\partial^2 u_z}{\partial y^2} + \frac{\partial^2 u_z}{\partial z^2} \end{bmatrix}$.

(3.46) is based on the Least Square Method. In most soft tissues, the first Lamé parameter λ is much larger than the shear modulus μ: this makes the estimation for the both parameters become less accurate [62]. However, if assuming the soft tissues are incompressible, the estimation process is largely simplified and presents a more accurate result—i.e., the shear modulus μ. The incompressibility mathematically means that the Poisson's ratio (ν) of the material equals to 0.5; if assuming the material is also locally isotropic and homogeneous, the following relation is given [72]:

$$\begin{aligned} \nabla \cdot \boldsymbol{u} &= \frac{\partial u_x}{\partial x} + \frac{\partial u_y}{\partial y} + \frac{\partial u_z}{\partial z} = \varepsilon_{xx} + \varepsilon_{yy} + \varepsilon_{zz} = (\varepsilon'_{xx} + \varepsilon'_{yy} + \varepsilon'_{zz}) + (\varepsilon''_{xx} + \varepsilon''_{yy} + \\ &\varepsilon''_{zz}) + (\varepsilon'''_{xx} + \varepsilon'''_{yy} + \varepsilon'''_{zz}) = (\varepsilon'_{xx} - \nu\varepsilon'_{xx} - \nu\varepsilon'_{xx}) + (-\nu\varepsilon''_{yy} + \varepsilon''_{yy} - \nu\varepsilon''_{yy}) + \\ &(-\nu\varepsilon'''_{zz} - \nu\varepsilon'''_{zz} + \varepsilon'''_{zz}), \end{aligned} \tag{3.47}$$

where the strain ε_{ii}'s superscript shares the same meaning with (3.27). Because the Poisson's ratio ν is assumed to be 0.5, the relation $\nabla \cdot \boldsymbol{u} = \boldsymbol{0}$ is yielded: this simplifies the linear elastic model for MRE, referring to (3.40), to a Helmholtz equation [103, p. 72]:

$$\mu \boldsymbol{\nabla}^2 \boldsymbol{u} = -\rho\omega^2 \boldsymbol{u}. \tag{3.48}$$

Under this case, to obtain the shear modulus, (3.48) can be further transformed as follows [103, p. 72]:

$$\mu = \frac{-\rho\omega^2 u_i}{\boldsymbol{\nabla}^2 u_i}, \tag{3.49}$$

where i is the MEG's direction. In MRE, this estimation method for obtaining the shear modulus is known as the Direct Inversion (DI) that requires data with one or more than one MEG sensitization direction(s). That is, although a single 2D shear wave image is enough to generate a stiffness map through use of the DI algorithm, this algorithm can accept more wave images with other directions for a better estimation accuracy. In addition, the DI algorithm does not need to measure the local wavelengths like LFE; however, it requires each point's neighborhood points to obtain a second derivative for the shear modulus estimation. Therefore, the elastogram estimated by this method theoretically has a finer resolution and a more accurate shear modulus estimation than LFE. However, in practice, the second derivative might significantly magnify the noise in the wave images: this possibly degrades the quality of the elastogram on the other hand. Some researchers have integrated several de-noising or smooth filters into this inversion algorithm to address the noise and the signal with a sharp transition to avoid artifacts and an inaccurate shear modulus estimation in the final elastogram [62], [108]. Additionally, some fitting techniques (such as a polynomial fit), as an alternative, were also used to estimate the second derivatives to potentially reduce the noise in the wave images and the artifacts in the elastograms [62], [108].

3.4.2.3. Finite Element Method

Several Finite Element Method (FEM)-based methods can be also used as inversion algorithms for MRE. A FEM-based method is generally divided into two parts: a FEM analysis and a solving process. In general, the FEM analysis, which is widely applied in engineering fields, segments a plane by a grid into a finite number of elements as shown in Figure 3.19 (A), and each element's value is expressed a dot product of its peripheral nodes' values and the shape functions shown in Figure 3.19 (B), as a FEM form [101, pp. 127–139]. In a FEM-based inversion algorithm, all the quantities from the linear elastic model for MRE (e.g., the displacement and the shear modulus) are re-expressed in the FEM forms first, and a weak form (for example, a Galerkin's Method [49]) is adopted to accomplish the solving process. Specifically, to solve the linear elastic model for MRE through the weak form, a test function is multiplied to both hand sides of this model, and an integral over each element region is subsequently applied [49], [101, pp. 42–45]:

$$\int_{\Omega_e} \mu[\nabla \cdot (\boldsymbol{\nabla u} + (\boldsymbol{\nabla u})^{\boldsymbol{T}})] \cdot \boldsymbol{w} d\Omega_e + \int_{\Omega_e} \lambda \boldsymbol{\nabla}(\boldsymbol{\nabla} \cdot \boldsymbol{u}) \cdot \boldsymbol{w} d\Omega_e = -\rho\omega^2 \int_{\Omega_e} \boldsymbol{u} \cdot \boldsymbol{w} d\Omega_e, \tag{3.50}$$

where Ω_e is each element's region. $\boldsymbol{w}$ is a test function and is also known as a weight function. Each quantity in (3.50) is replaced by the FEM form [49]:

$$\begin{cases} \boldsymbol{u} = \sum_{n=1}^{N_u} \bar{\boldsymbol{u}}_{\boldsymbol{n}} \boldsymbol{\psi_n} \\ \mu = \sum_{n=1}^{N_\mu} \bar{\mu}_n \boldsymbol{\psi_n} \\ \boldsymbol{\nabla u} = \sum_{n=1}^{N_u} \overline{\boldsymbol{\nabla u}_{\boldsymbol{n}}} \boldsymbol{\psi_n}, \\ \boldsymbol{w} = \sum_{n=1}^{N_w} \bar{\boldsymbol{w}}_{\boldsymbol{n}} \boldsymbol{\psi_n} \\ \lambda = \sum_{n=1}^{N_\lambda} \bar{\lambda}_n \boldsymbol{\psi_n} \end{cases} \tag{3.51}$$

where $\bar{\boldsymbol{u}}_{\boldsymbol{n}}$, $\bar{\mu}_n$, $\overline{\boldsymbol{\nabla u}_{\boldsymbol{n}}}$, $\bar{\boldsymbol{w}}_{\boldsymbol{n}}$, and $\bar{\lambda}_n$ are the node values of each element; N_u, N_μ, N_w, and N_λ are each quantity's node numbers; and $\boldsymbol{\psi_n}$ represents the shape functions as shown in Figure 3.19 (B). These shape functions may be defined differently among each quantity, as either a constant, linear, or other forms. The unknowns—λ and μ—can be eventually solved out from (3.50). Comparing to the previous two methods, the FEM-based inversion algorithm barely makes any simplifications to the linear elastic model for MRE.

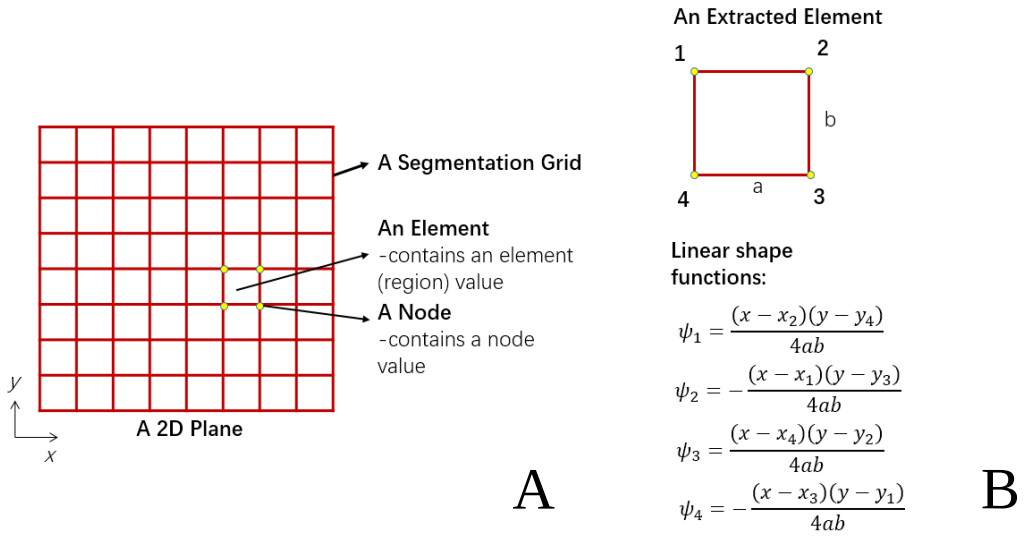

Figure 3. 19 (A) A FEM analysis for a 2D plane; and **(B)** an element with its associated nodes and shape functions.

The challenges found in the FEM-based inversion algorithm are the handling to the boundary problem—referring to (3.41) and (3.42), since an integral operation needs to be applied to this differential equation (3.40). The boundary condition, especially for the force boundary with tractions, is difficult to be defined in practice. To address this issue, some researchers removed all the boundaries' effect to the unknown parameters, even though the handling to the boundaries likely causes an underdetermined problem in solving (3.50) [49], [75]. The underdetermined problem is another challenge that needs to be addressed in the FEM-based inversion algorithm, so the MEG may need to be applied along two or three directions (including the slice-selection, frequency-encoding, and phase-encoding directions) [49], [75].

The final solving process of the FEM-based inversion algorithm can be achieved by either an iterative or a direct method [75], [78]–[80]. Even though the results estimated by the FEM-based inversion algorithm, theoretically, might be more accurate than the previous two inversion algorithms, the FEM-based inversion algorithm's calculation efficiency is lower than those two: this is probably a disappointment in clinical applications.

3.5. Summary

First, this chapter thoroughly explains the theoretical basis of MRE—the linear elastic theory, which help readers to comprehend the meaning of quantities used by MRE, such as the shear modulus and displacement of the mechanical wave. Second, this chapter explicitly introduces the principles and technical realizations of a MRE system as an advanced application of MRI—such as the shear wave and driver system, the phase contrast technique and motion encoding gradient, and the elastogram and inversion algorithm—which serves as an important technical reference and

for the experiments designed and conducted in Chapter 4 and Chapter 5.

Chapter 4

Development of a Novel Phantom for Routine Quality Assurance of an MR Elastograghy System

Chapter Synopsis

Prior to clinical studies, it is necessary to conduct a series of Quality Control (QC) tests to commission the Magnetic Resonance Elastography (MRE) system for clinical use. QC tests are needed to investigate the feasibility of MRE in specific situations, to test the optimal imaging settings, the resolution of the elastogram (also known as the stiffness map), the accuracy of elasticity values, and the limitations of the MRE system. These tests may provide guidelines for future clinical applications. In this chapter, a specialized Quality Assurance (QA) phantom is developed to work alongside the commercial MRE system. The phantom QA program consists of a set of QC tests to investigate the optimal settings and feasibility of the MRE system and to provide a general guideline for future MRE-related applications.

4.1. Introduction

In medical imaging, a phantom is an object that can simulate the structure or characteristics of the human bodies or specific organs. The phantom can help study, analyze, and adjust features, performance, and quality of imaging modalities such as Computed Tomography (CT), MRI, and ultrasound. By using an appropriate phantom, the imaging modality can produce relatively stable and consistent images under the same scan settings. Additionally, scans of a phantom– as a pre-clinical test–can help expose the potential risks of imaging methods or procedures, assuring the safety in subsequent scans on human subjects.

For the same reasons stated above, a phantom for MRE can help investigate the features of MRE system and further aid the investigation into the mechanical properties various human tissue, *in vivo*. The MRE phantom can be used to evaluate the imaging methods or strategies before the MRE clinical applications. At present, there are a limited number of commercial options for MRE phantoms. For example, the 049 Family of phantoms from CIRS (049 and 049A, CIRS, Inc., Norfolk, VA) is a generic QA (Quality Assurance) elastography phantom (however, not specialized for MRE) that can be purchased. For this particular phantom, the manufacturer provides referenced elasticity values for the background and all inclusions through the “Standard Test Methods for Rubber Properties in Compression” (ASTM D575-91) by applying a quasi-static compression load frame using the constant displacement method [109]. Some groups have obtained some high quality

elastograms with this phantom [49], [92]. Another representative phantom is the 053 Phantom family (CIRS, Inc., Norfolk, VA) which is a tissue-equivalent prostate phantom. Since this phantom realistically mimics the anatomies and elastic characteristics of prostate and other periphery structures, some groups used it to conduct the phantom study prior the *in vivo* study and received satisfied results [63], [67], [89]. These commercial phantoms are credibly tested by the manufacturer. Investigators may also design, and build their own MRE phantoms. For example, Oudry et al. developed a series of phantoms with different elasticities linearly varying with the concentration of copolymer to cross-validate MRE and ultrasound-based transient elastography [110]. Another case is that Leclerc et al. built two homogeneous cylindrical phantoms with different dimensions in their study to investigate the pattern and mode of the driver's vibration [111]. Though these individualized MRE phantoms are comparably less expensive, the physical compatibility between the driver's configuration and the corresponding anatomy must be taken into consideration. For instance, Sinkus et al. developed a breast phantom mimicking the breast's realistic shape and size, but this breast phantom needs a specialized driver to be compatible with [112]. Additionally, the self-constructed MRE phantom can provide more flexibility to the researchers to achieve their studies: for example, Madsen et al. developed an anthropomorphic breast phantom encapsulating different targets which mimicked fat, tumours, fibroadenomas, and glandular; however, the complexity of the phantom production is also correspondingly increased [113]. While, these phantoms serve very specific purposes, there isn't a single phantom that works alongside commercially available MRE systems. In addition, no group has used a specialized MRE QA phantom to validate the elasticity imaging of the commercial MRE system (which includes the Resoundant® driver system) and has systematically discussed the imaging parameter optimization of MRE and the association between the parameter selection and image quality. However, for a clinical institute, such information is important to be understood and taken advantage of.

Hence, the novelty of this work is to develop a novel specialized MRE QA phantom and use this phantom to validate the elasticity imaging of the commercial MRE system, optimize MRE's imaging parameter, and investigate the impact associated with the selection of the parameters to the image quality.

4.2. The Role of Phantoms in MRE Experiments

Phantoms can greatly help to evaluate the characteristics of the MRE system being commissioned. Testing with a MRE phantom, investigators can help determine the optimal scan parameters to obtain high-quality elastograms. Additionally, the composition of MRE phantom can also directly reflect the relationship between the produced results and corresponding parameters, which is important for the researchers to study before carrying out MRE in the clinical scenario. Prior to any further specific and advanced MRE applications, it is necessary to validate the efficacy of the MRE system in the imaging of elasticity and investigate the pattern of elastogram quality variation with parameter selection. To tackle these tasks, investigators can set up a series of quality

control tests with the aid of a quality assurance phantom. These QC tests along with a proper QA phantom can provide a solution to the following questions: (1) whether the MRE can precisely detect the difference between different elasticity grades and accurately report the elasticity values; (2) which imaging (scanning) parameters decide the quality of elastograms and how they impact the results; and (3) if there is a correlation between or among these parameters and what the correlation specifically is.

4.3. Preliminary Testing Using an Ultrasound Phantom

The QA phantom plays an important role in conducting quality control tests. In this work, a commercial QA phantom, model 049A (CIRS, Inc., Norfolk, VA), was initially selected and tested. However, this phantom is not specialized or optimized for MRE experiments. The in-house tests have demonstrated some deficiencies when this phantom was used to perform combined MRI/MRE scans. The MRI scan was carried out by a routine T2-weighted (T2W) scan with the following imaging parameters; Field of View (FOV) = 284*350 mm^2, the time to echo = (TE) 102 ms, the time to repetition (TR) = 8830 ms, resolution = 416*512, slice thickness = 2 mm, and voxel size = 0.68*0.68*2 mm^3. The following imaging parameters for MRE scans were used: FOV = 284*350 mm^2, TE = 35 ms, TR = 750 ms, resolution = 208*256, slice thickness = 6 mm, and voxel size = 1.37*1.37*6 mm^3, the Motion Encoding Gradient (MEG) frequency 120 Hz, and the mechanical wave frequency 120 Hz and the mechanical wave amplitude 30% both of which are prescribed by driver system.

Figure 4.1 shows the T2W axial image of the 049A Phantom and its four phase (corresponding to four even moments of one cycle) images which are used to capture the shear wave propagating inside the tissue (or phantom). We observe some reflections on the boundaries (shown with black arrows). To avoid potential problems in acquiring robust MRE data, this interfering factor must be excluded since the quality of wave propagation has the highest weight in the elastogram calculation. Our preliminary analysis of this 049 QA phantom demonstrates the need for a more specialized MRE QA phantom.

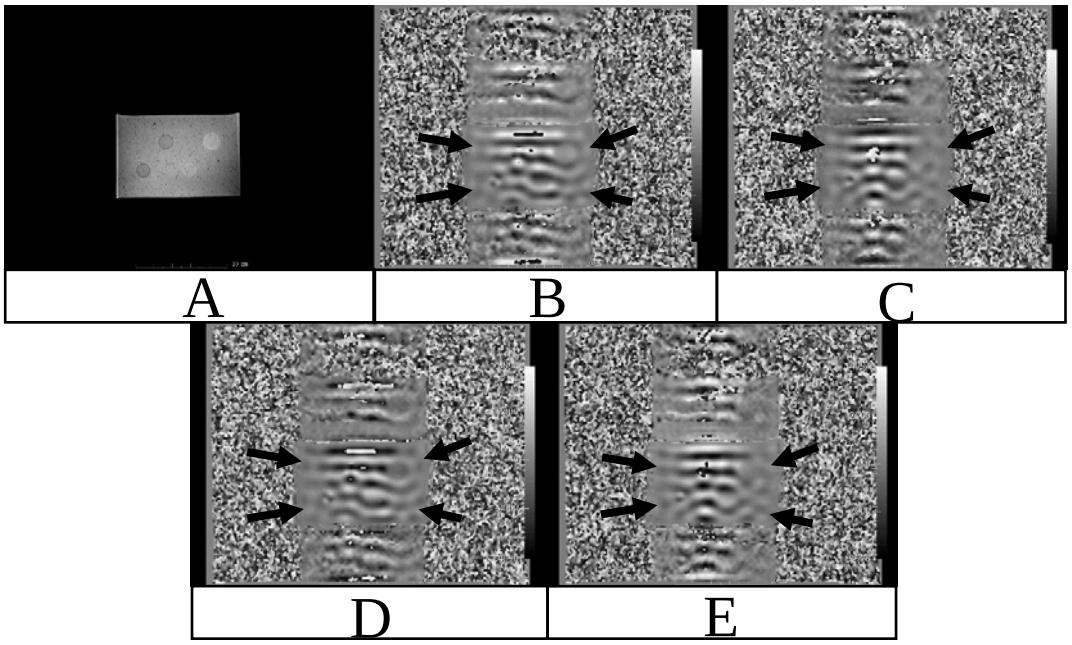

Figure 4. 1 (A) T2W axial image of 049A phantom; **(B)** phase contrast image at phase 1; **(C)** phase contrast image at phase 2; **(D)** phase contrast image at phase 3; and **(E)** phase contrast image at phase 4.

4.4. The Need for a Specialized MRE QA Phantom

In collaboration with the CIRS Inc., a specialized MRE phantom was developed to retain the good features of the 049A phantom and resolve the issues observed in the in-house scans. The original gel block of the 049A phantom was put in a larger housing which allowed a larger scan opening to be compatible with the Resoundant® passive driver (18.5 cm in diameter). Figure 4.2 shows that the background and rods inside this phantom are all made of Zerdine®, a tissue-mimicking gel, with referenced elasticity values. The four rods are shaped into six steps in different diameters. The grey area indicates a dispersive filler gel (Zerdine®) that minimizes shear wave reflections from the housing walls.

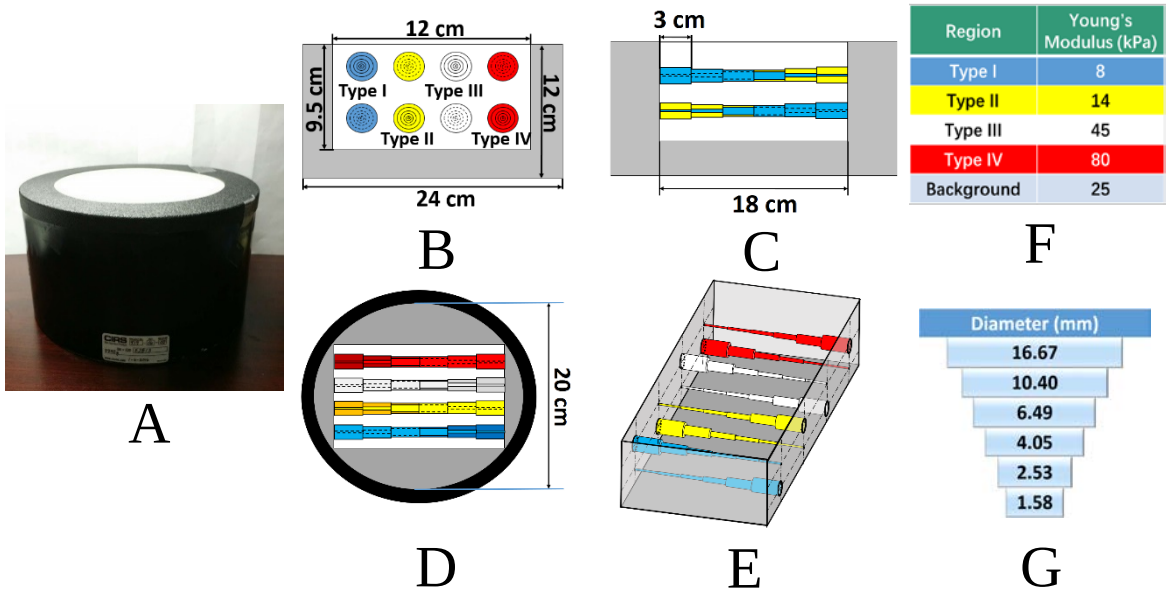

Figure 4. 2 Modified phantom's views and specifications. **(A)** Photo of the modified phantom; **(B)** front view; **(C)** left view; **(D)** top view; **(E)** 3D view; **(F)** elasticity values; and **(G)** diameter values.

The same MRE scans were repeated with the modified phantom. Figure 4.3 shows a blue box (dashed and solid lines) indicating the original gel block (termed as "imaging region" below), and the remaining area in the phantom is the dispersive filler gel. Figure 4.3 (A) shows the T2W axial image of the specialized phantom, and Figure 4.3 (B)–(E) show that the reflections from the boundaries, the interface between the original gel block and filler gel, are well minimized. The dispersive filler works as a buffer without indicating any elasticity values, preserving the wave propagation in the imaging region by dispersing the shear waves. Therefore, potential interfering factor-reflections, which may affect the measurement of results, are excluded. This phantom was modified into a specialized MRE QA phantom to conduct the MRE QC tests.

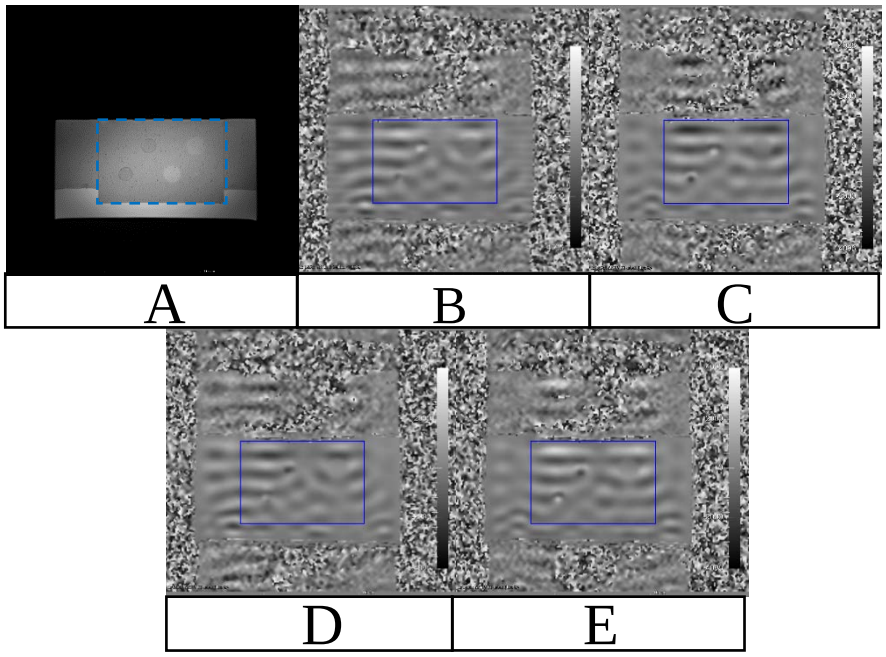

Figure 4. 3 (A) T2W axial image of modified 049A phantom; **(B)** phase contrast image at phase 1; **(C)** phase contrast image at phase 2; **(D)** phase contrast image at phase 3; and **(E)** phase contrast image at phase 4. T2W: FOV = 284*350 mm^2; TE = 90 ms; TR = 15210 ms; resolution = 416*512; slice thickness = 2 mm; and voxel size = 0.68*0.68*2 mm^3. MRE: FOV = 284*350 mm^2; TE = 35 ms; TR = 750 ms; resolution = 208*256; slice thickness = 6 mm; voxel size = 1.37*1.37*6 mm^3; and MEG frequency = 120 Hz. The driver system: frequency =120 Hz; and amplitude = 30%.

4.5. Experimental Validation and Parameter Optimization with the New MRE QA Phantom

This newly modified MRE QA phantom can aid investigators to validate the MRE technique, optimize scan parameters selection, and further explore MRE's potential applications in other clinical fields: this can be accomplished by designing a series of quality control tests as mentioned in section 4.2. The specific tests include the verification of MRE's accuracy in elasticity, the investigation of multi-frequency MRE, the exploration of MRE's resolution, and the correlation between the frequency and amplitude settings in MRE. Sections 4.5.1. and 4.5.2. respectively elaborate the methodology and results of the tests.

4.5.1. Materials and Methods

4.5.1.1. Imaging Setups

All the scans were carried out on a 3 Tesla Siemens Skyra platform (Erlangen, Germany), and the imaging setups are shown in Figure 4.4. In this work, the employed Resoundant® MRE driver

system (Rochester, MN) consists of an active driver located in a mechanical room and a passive driver that makes contact directly with phantoms or patients (in a scanner room). The shear wave propagation from the active driver to the passive driver is realized by a plastic tube (approximately 7.62 m) that passes through the wall and connects the passive driver (scanner) with the active driver in the mechanical room. The Resoundant® system can provide a stable and ample shear wave within a low frequency range. The settings of the Resoundant® system are adjusted through an interface, where the user has access to the frequency, amplitude, duration (one vibration period), phase shift, and the inverted waveform or waveform type in the console, as shown in Figure 4.5.

Once the driver system is set up, it will be excited and synchronically controlled by the MRE pulse sequence. The executed MRE pulse sequence is a work-in-progress (WIP) Spin Echo (SE)-Echo Planar Imaging (EPI) sequence (WIP 923B VE11A, obtained from Siemens) [106]. This sequence allows the user to manipulate multiple parameters in an advanced mode for research purposes, such as the MEG amplitude, the MEG frequency (fixed at 60 Hz in default mode), and the MEG direction. These parameters help to pinpoint the optimal settings in variant MRE applications. The settings of this sequence must be consistent with the driver system's settings. That is, the frequency of the driver system must be synchronized with the MEG frequency to guarantee the wave propagation to be correctly captured by the MRE sequence. Once the MEG and driver frequencies are altered, the TR must be adjusted as well. A simplified diagram of this SE-EPI MRE sequence is shown in Figure 4.6 where the TR must satisfy a mathematical relationship so the wave will be continuously and correctly captured. In Figure 4.6, theoretically, TR = two slices* three cycles/60 Hz = 100 ms. Once the magnitude and phase contrast images are obtained, they need to be further processed by the inversion algorithm calculating the elastogram.

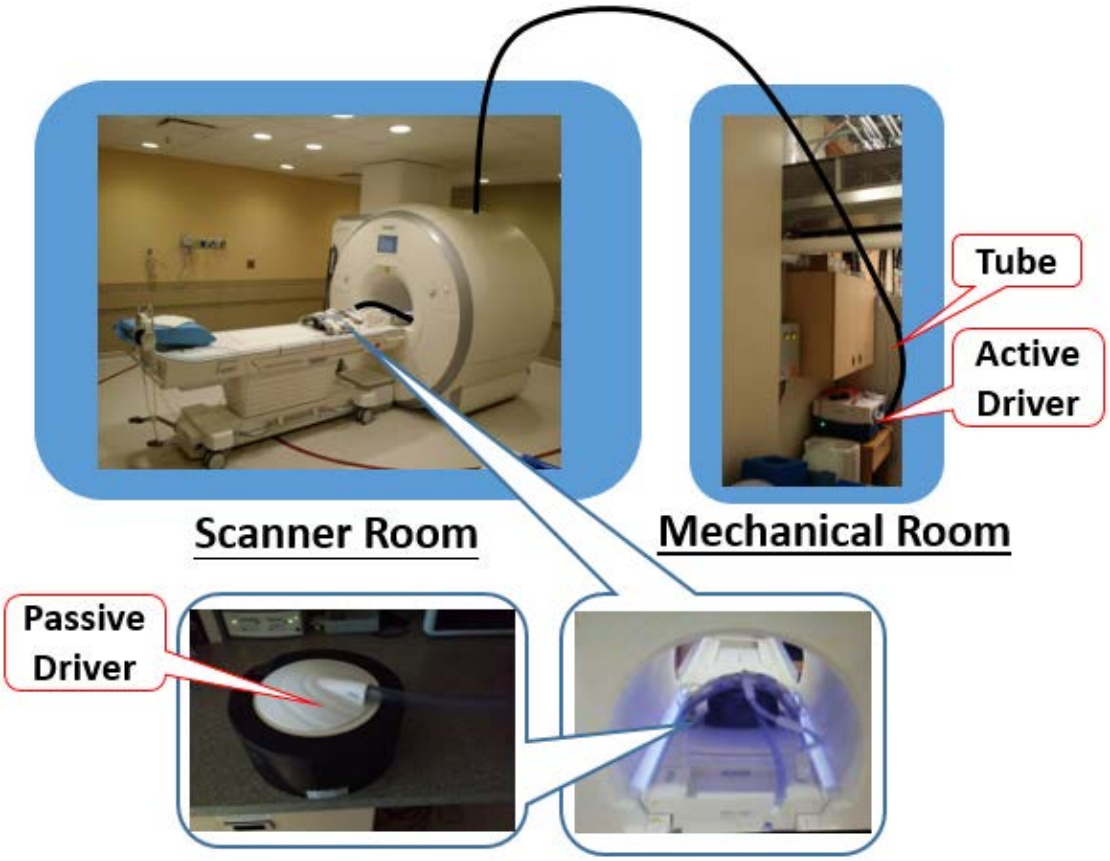

Figure 4. 4 Imaging setups.

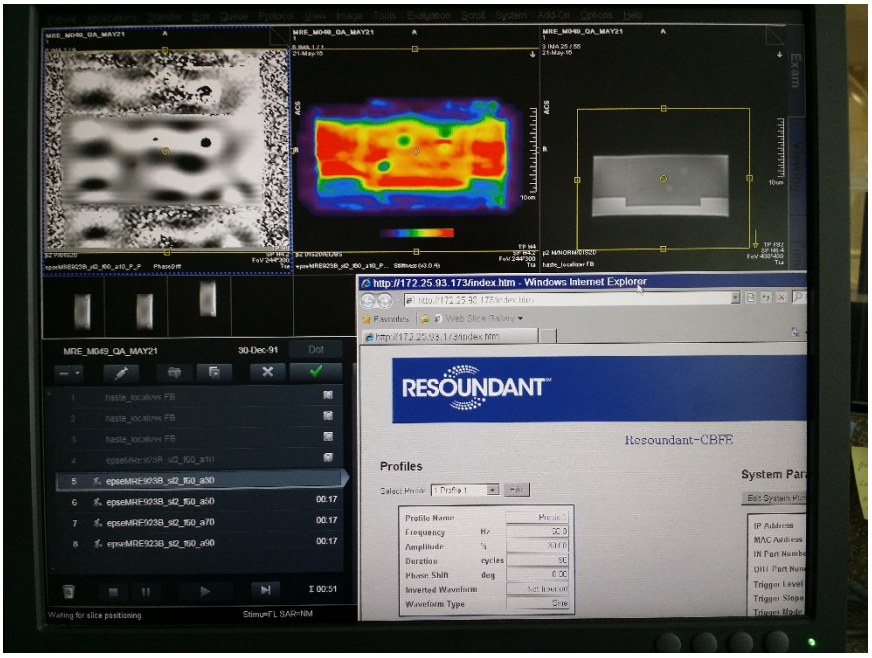

Figure 4. 5 User interface of the MRE system.

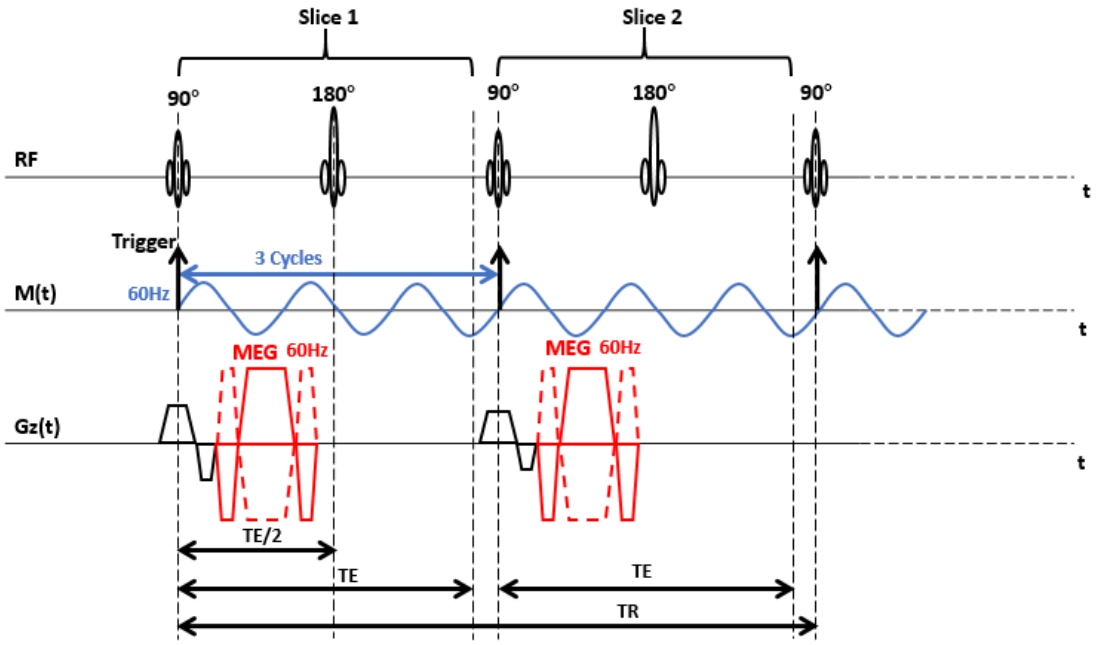

Figure 4. 6 Simplified diagram of the WIP SE-EPI MRE pulse sequence.

4.5.1.2. Imaging Acquisition

Prior to the MRE scans, a T2-weighted axial scan through the entire phantom (FOV = 300*243.75 mm^2, slice thickness = 3 mm, resolution = 512*416, voxel size = 0.59*0.59*3 mm^3, TE/TR = 101/13040 ms, number of slices = 85) was collected for viewing the internal structure of this phantom to display the precise location of the inclusions to provide a reference for the following MRE scans.

The MRE scans were performed on three different slices that included all the rods (including the different rod types, and diameters) as shown in Figure 4.7. The frequencies of the wave and MEG were set at 60 Hz, 90 Hz, 120 Hz, 150 Hz, and 180 Hz (the system frequency range is 30–300 Hz), respectively, on each slice. Frequencies were set at 10%, 30%, 50%, 70%, 90% amplitude (0–100%), respectively. The scan settings are listed in Table 4.1.

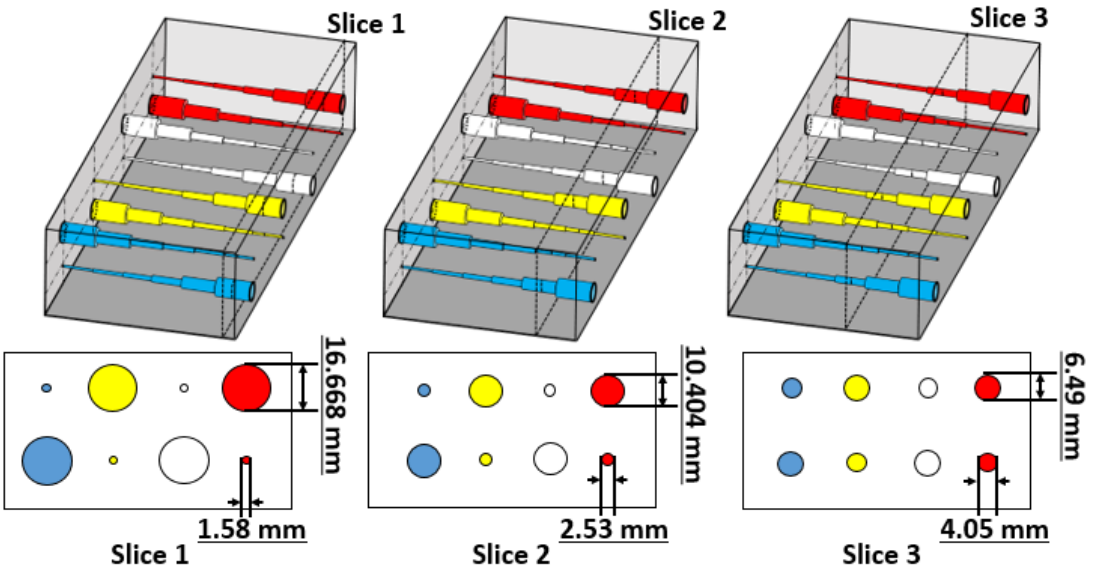

Figure 4. 7 Acquisition strategies for the specialized MRE phantom.

Table 4. 1 MRE scan settings for the three slices of the specialized QA phantom

No.	Frequency (Hz)	Amplitude	FOV (mm^2)	Slice Thickness (mm)	Resolution	Voxel (mm^3)	TE (ms)	TR (ms)
1	60	10%,30%, 50%,70%, 90%	300 * 243.75	6	256 * 208	1.17*1.17*6	48	1500
2	90	10%,30%, 50%,70%, 90%	300 * 243.75	6	256 * 208	1.17*1.17*6	37	1000
3	120	10%,30%, 50%,70%, 90%	300 * 243.75	6	256 * 208	1.17*1.17*6	35	750
4	150	10%,30%, 50%,70%, 90%	300 * 243.75	6	256 * 208	1.17*1.17*6	35	600
5	180	10%,30%, 50%,70%, 90%	300 * 243.75	6	256 * 208	1.17*1.17*6	35	500

The TE was set at the minimum to collect the strongest signal. Though the maximal frequency that the system allows is 300 Hz, the signal loss became severe when the frequency exceeded 200 Hz in the conducted tests.

4.5.1.3. Inversion and Post-processing

Calculation of the elastogram from the collected phase contrast images and the magnitude images was carried out using an offline inversion software MRE/Wave, developed by the Mayo Clinic [114]. This software includes the following processing techniques: masking, filtering, unwrapping, and elasticity calculation [114].

The viewing and analyses of the images were performed using a combination of tools, including 3D Slicer 4.6.2 and ImageJ 1.51. Using 3D Slicer 4.6.2, segmentations were manually performed on the T2 images and elastograms for comparison of match in shape, size, and location. The elasticity values of the inclusions and background can be calculated according to the segmentation to the T2 images. The manual segmentations to the T2 images and elastograms were performed by a module, "Editor", within the 3D Slicer. The "Editor" provides some manual segmentation tools such as a circle-shaped segmentation tool with a radius setting and a direct drawing tool operated by users. In this work, the circle-shaped segmentation tool was used to perform the manual segmentation to the T2 images by directly encapsulating the rods, since the manufacturer provides the diameters of each rod (which is circular in axial view) as a prior knowledge of the segmentation. However, the manual segmentation to the elastograms was done by contouring the rods with the direct drawing tool, because it is assumed that the elastograms sometimes might not well reflect the actual shape of the targets.

4.5.1.4. Imaging Evaluation Method

In this work, three evaluation indices are presented: (1) A comparison between the calculated and referenced stiffness values (mean and standard deviation), (2) Hausdorff Distance (HD) and its two other variants, average Hausdorff Distance (aveHD) and 95% Hausdorff Distance (95%HD), between two segmentations separately performed to the T2 image and elastogram, and (3) Dice Similarity (DS) between two segmentations separately performed to the T2 image and elastogram. The comparison of segmentation was realized by a 3D Slicer toolkit "SlicerRT[8]" with its "Segment Comparison" tool [115]. This comparison tool is able to report the above three HD measures and DS.

Two datasets are shown in Figure 4.8 (A) and help to define three HD measures (HD, aveHD, and 95% HD, and they are mentioned as "three HD measures" in this thesis for simplification) and DS from (4.1) and (4.4). A HD measure (HD, aveHD, or 95%HD) of 0 and a DS of 1 are assumed to be a perfect match, and vice versa, as shown in Figure 4.8 (B).

[8] Home page, http://slicerrt.github.io/index.html

Figure 4. 8 (A) Two datasets, A and B, that help to define HD, average HD, 95% HD, and DS from Equations (4.1) to (4.4); and **(B)** the evaluation of HD, average HD, 95% HD, and DS in match performance.

HD, average HD, 95% HD, and DS are defined as follows [116], [117],

$$HD = \max\{\max_{a\in A}\min_{b\in B}|a-b|,\ \max_{b\in B}\min_{a\in A}|a-b|\}. \tag{4.1}$$

$$average\ HD = \frac{1}{2}\left(\frac{1}{|A|}\sum_{a\in A}\min_{b\in B}|a-b| + \frac{1}{|B|}\sum_{b\in B}\min_{a\in A}|a-b|\right). \tag{4.2}$$

$$95\%\ HD = \frac{1}{2}\left[K_{95\%}\left(\min_{b\in B}|a-b|\right)\forall a\in A + K_{95\%}\left(\min_{a\in A}|a-b|\right)\forall b\in B\right]. \tag{4.3}$$

where $K_{95\%}\left(\min_{b\in B}|a-b|\right)\forall a\in A$ represents that in dataset A, the exact point with the relation of $\min_{b\in B}|a-b|$ which is greater or equal to exactly 95% of the other points, as well as $K_{95\%}\left(\min_{a\in A}|a-b|\right)\forall b\in B$.

$$DS = \frac{2|A\cap B|}{|A|+|B|}. \tag{4.4}$$

4.5.2. Results and Discussion

4.5.2.1. Accuracy of elasticity of an MRE system

The T2 image on slice 1 (with the largest and smallest rods, 16.67 mm and 1.58 mm in diameter, respectively) is shown in Figure 4.9 (A). Figure 4.9 (B) shows the reconstructed elastogram (via the inversion algorithm) from the MRE scan with a frequency of 120 Hz and 30% amplitude. This elastogram qualitatively shows a clear distinction between the peripheral dispersive gel area and the central background region containing all the inclusions. The difference in elasticity among the four types of large diameter (16.67 mm) rods is quite noticeable, but the visibility of the four types of small diameter (1.58 mm) rods is barely noticeable because the voxel size of the MRE images (including the phase contrast images and elastogram) is 1.17*1.17 mm^2, while the size of the smallest rod in a 2D plane is 1.58 mm in diameter. That is, one single voxel in a 2D plane almost

occupies the entire smallest rod, as shown in Figure 4.10. Therefore, within such a voxel, it is a challenge to represent the actual wave propagation correctly, which can lead to this extremely incomplete wave propagation information being passed to the inversion algorithm incurring an incorrect elasticity calculation.

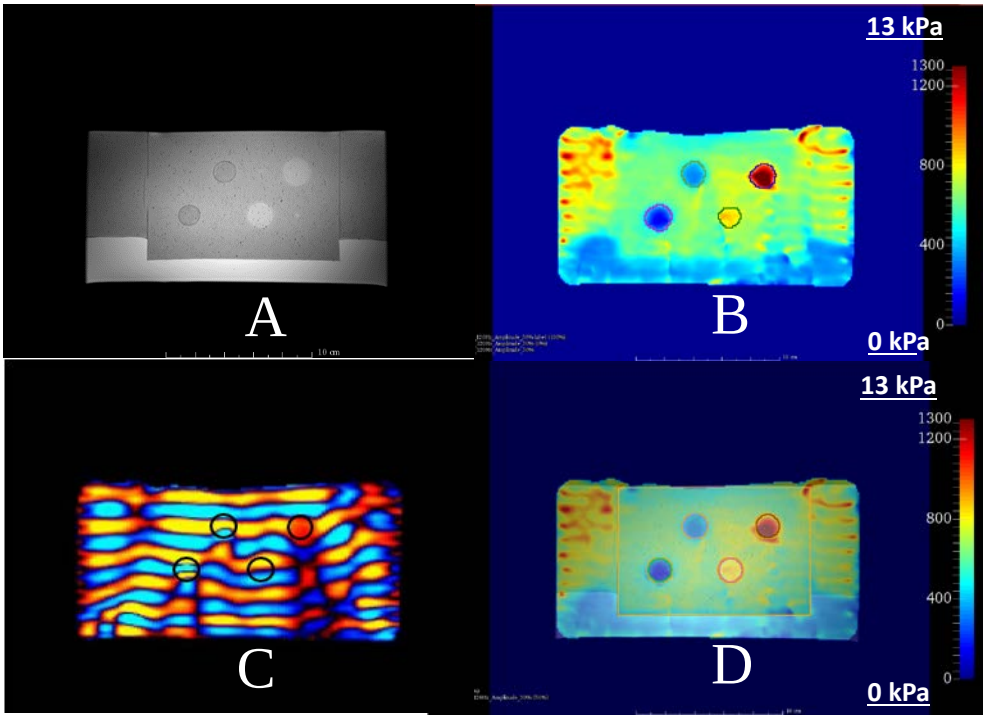

Figure 4. 9 (A) T2-weighted axial image on slice 1 (FOV = 300*243.75 mm^2, slice thickness = 3 mm, resolution = 512*416, voxel size = 0.59*0.59*3 mm^3, TE/TR = 101/13040 ms); **(B)** elastogram from the MRE scan with frequency 120 Hz and amplitude 30%, and the segmentation was performed based on the elastogram; **(C)** wave images from the MRE scan; the black circles indicate the largest rods; and **(D)** elastogram overlays on the T2 image; the segmentation was performed based on the T2 image.

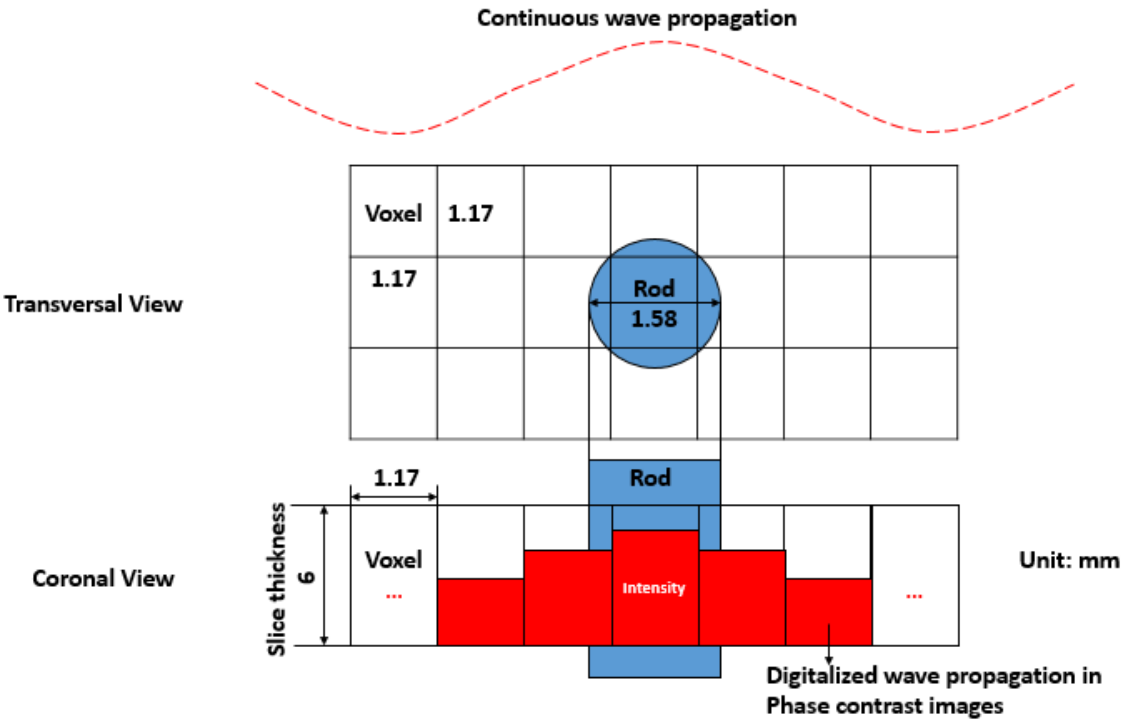

Figure 4. 10 Wave propagation for the smallest rods (1.58 mm in diameter) in a MRE image.

The smallest rods cannot be identified by MRE, whereas the largest rods on the same slice qualify for an investigation of the accuracy of the elasticity. Quantitatively, the elastogram calculated from the inversion algorithm reports the elasticity values in shear modulus (G) which is approximately one third of Young's modulus (E) for soft tissues ($E \approx 3G$) [62], [88]. In using this relation, Young's modulus was calculated for comparison. Figure 4.11 shows a comparison between the Young's modulus reported by the manufacturer (reference) and the Young's modulus reported by the elastogram (calculated as mean with standard deviation). For the relatively soft, visible rods (Type I and Type II, 16.67 mm in diameter) and the background, the elasticity values from the elastogram are close to their reference values; while for the relatively hard visible rods (Type III and Type IV, 16.67 mm in diameter), the values from the elastogram are not as close to their reference values.

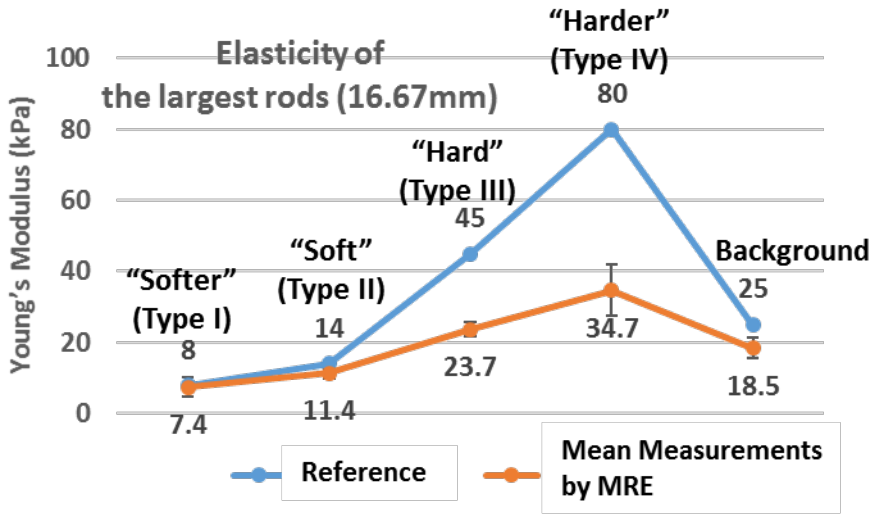

Figure 4. 11 Within each region of the largest rods and the background, their mean elasticity values along with standard deviations reported by the elastogram compares to their reference elasticity values reported by the manufacturer. (The rods are16.67 mm in diameter.)

The relatively soft rods and background region (in the elastogram) are precisely found at the locations indicated by the T2 image and their elasticity values are close to the elasticity values provided by the manufacturer; the relatively hard rods (in the elastogram) are precisely found at the locations indicated by the T2 image but their elasticity values are not quite close to the elasticity values provided by the manufacturer. However, by investigating the wave propagation patterns from the phase contrast image in Figure 4.12 (A), it can be observed that, qualitatively, the wavelength within the rods becomes shorter when passing through the relatively softer regions and longer when passing through the relatively harder regions as shown in Figure 4.12 (B–E). In Figure 4.12, there is one and a half whole wavelengths within the rod (16.67 mm in diameter) in (B) and one whole wavelength within the rod (16.67 mm in diameter) in (C). However, for the harder inclusions in Figure 4.12 (D) and (E), less than a full wavelength is observed within the rod (16.67 mm in diameter). Since the correct calculation of the elasticity relies on the variation of a complete wavelength, in Figure 4.12 (D) and (E) the inversion algorithm cannot correctly calculate the accurate elasticity values. When the passing wavelength is larger than the diameter of the rod, the rod does not qualify for the homogenous condition that is one of the assumptions made for MRE [24], [88]. Another factor that can affect the calculation of elasticity is filtering. Although there are limitations, MRE still can provide a precise qualitative result, as shown in Figure 4.9 (B) where the contrast of the different inclusions and background is well established. Also, Table 4.2 shows the quantitative comparison between the segmentation to the T2 image and the segmentation to the elastogram where the indices reflect a comparable accuracy of the shape, location, and size of the rods in contrast to their diameter of 16.67 mm.

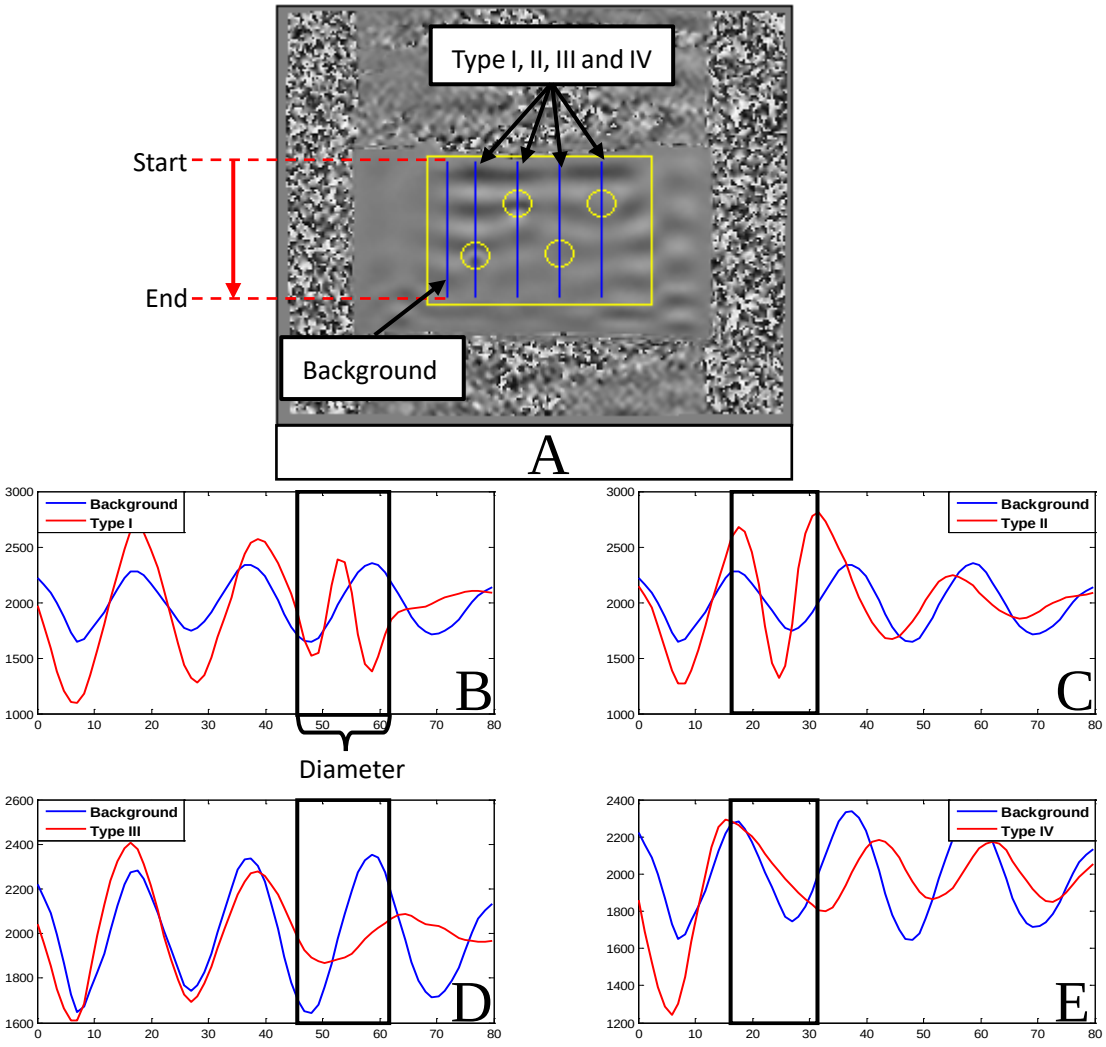

Figure 4. 12 (A) phase contrast image where the yellow box and circles indicate the location of the imaging region and the inclusions with the largest rods, and the blue lines represent profiles of the waves passing through the rods and background; **(B)** profiles of the wave passing through Type I rods (8 kPa) and the background (25 kPa); the black box shows the position of the rods and the size of the diameter; **(C)** profiles of the wave passing through Type II rods (14 kPa) and the background; **(D)** profiles of the wave passing through Type III rods (45 kPa) and the background; and **(E)** profiles of the wave passing through Type IV rods (80 kPa) and the background.

Table 4. 2 Segmentation comparisons between the T2W image and the elastogram

Rods with 16.67 mm in diameter	HD (mm)	Average HD (mm)	95% HD (mm)	DS
Type I (8 kPa)	2.340	0.170	0.830	0.868
Type II (14 kPa)	1.660	0.060	0.590	0.950
Type III (45 kPa)	2.340	0.160	0.830	0.877
Type IV (80 kPa)	3.520	0.300	1.760	0.813

4.5.2.2. Frequency dependence of an MRE system

Since the wave propagation determines the quality of an elastogram, the frequency of the mechanical wave is one of the most important imaging settings. It is necessary to investigate the influence of the frequency adjustment to pinpoint an optimal frequency with the aid of this phantom.

Figure 4.13 (A–F) are the stiffness maps from different frequency settings. In each frequency setting, the window/level is adapted a state where the background presents its most homogenous distribution while all the targets are still clearly visible since the background region contains the most wavelengths comparing to the rod regions as discussed in last section. The adjustment of windows/levels in all the following stiffness maps are also based on this criterion. Figure 4.13 (A–F) show that the image quality within the imaging region is significantly improved as the frequency increases until it reaches 180 Hz where artifacts begin to appear. An increase in frequency can improve the image quality of the elastogram (stiffness map), as a shorter wavelength can help to distinguish smaller targets, however, at higher frequency the image will experience more damping. Though the upper limit of the employed sequence is 300 Hz, in practice the signal loss becomes very severe when the frequency is over 200 Hz.

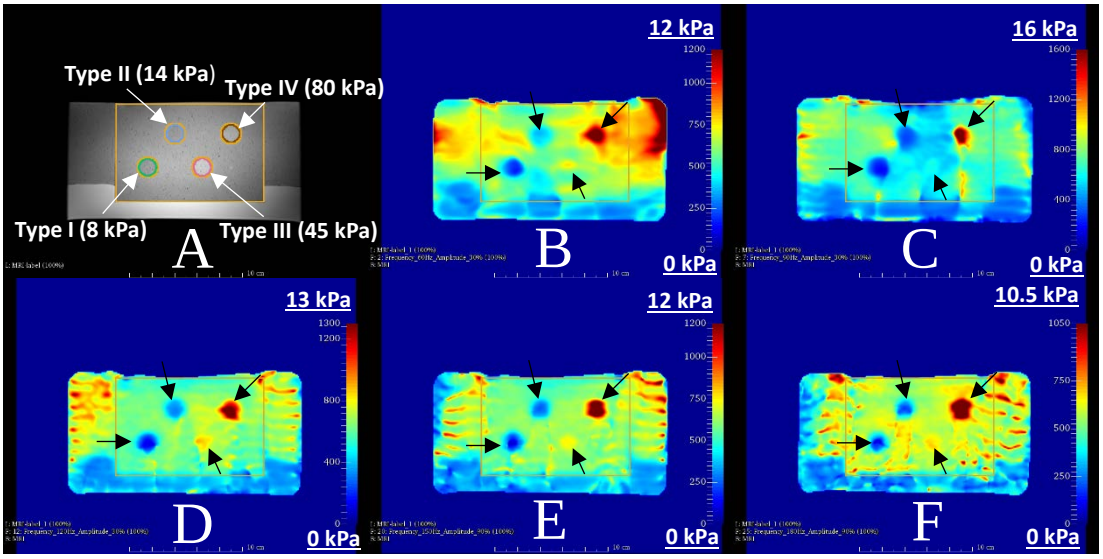

Figure 4. 13 (A) T2-weighted image on slice 1; stiffness map at **(B)** 60 Hz; **(C)** 90 Hz; **(D)** 120 Hz; **(E)** 150 Hz; and **(F)** 180 Hz. (The box in the stiffness map indicates the imaging region, and black arrows indicate the inclusions.)

By quantitatively comparing the image quality with the frequency changes from Figure 4.14 (A–E), it can be seen that though the elasticity values have only minor variations, the mean Hausdorff Distance, average Hausdorff Distance, 95% Hausdorff Distance, and Dice Similarity demonstrate notable descending and ascending tendencies, respectively. This is because that there will be more wavelengths or a more complete wavelength found within a specific dimension of a target as the frequency of the mechanical wave is increased: this will help MRE more accurately reflect the elasticity distribution of the target. That is, the quality of the image improves when the frequency is tuned higher.

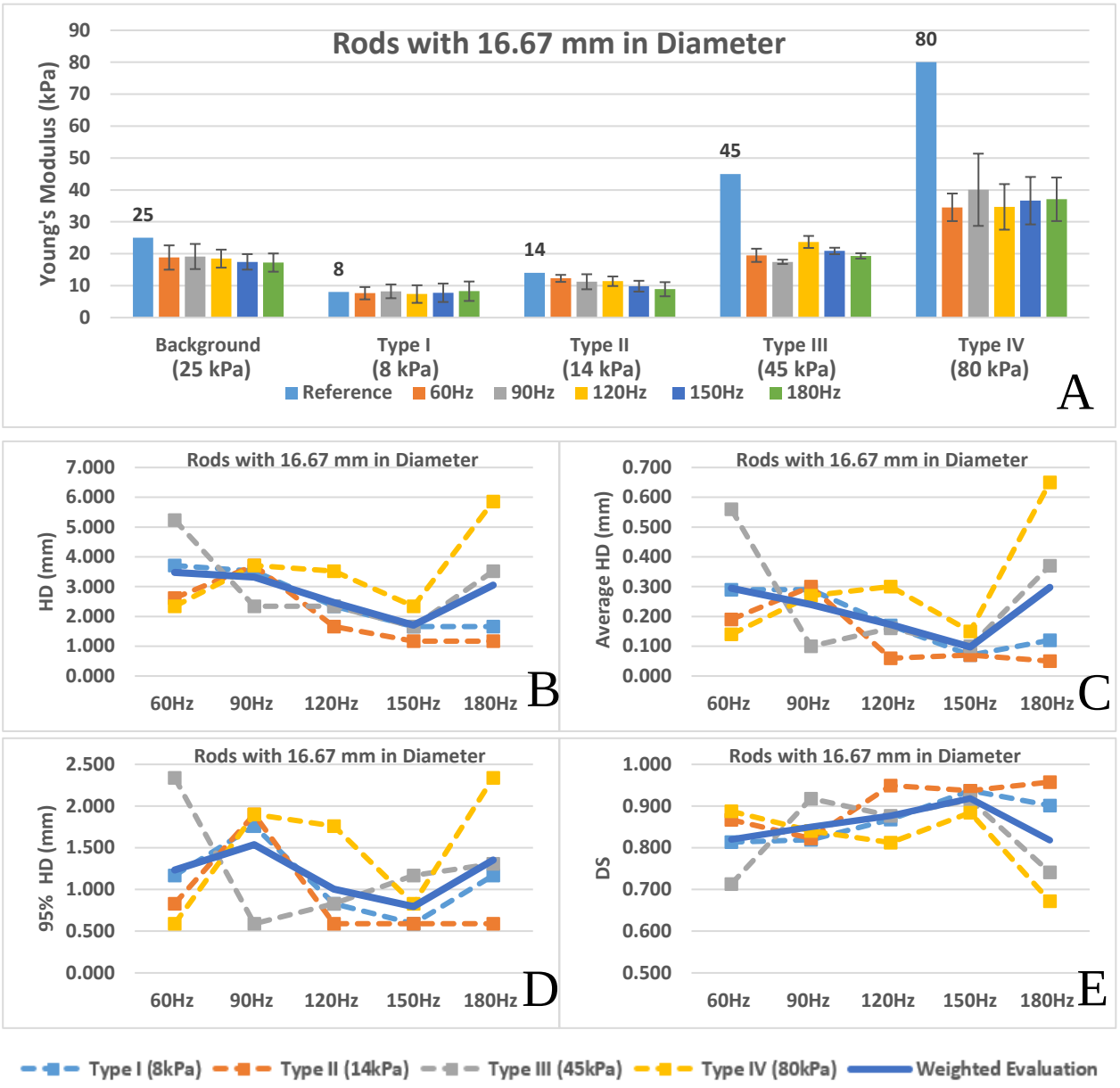

Figure 4. 14 (A) Elasticity; **(B)** Hausdorff Distance; **(C)** average Hausdorff Distance; **(D)** 95% Hausdorff Distance; and **(E)** Dice Similarity. The weighted evaluation is the mean evaluation of these four independent rods, reflecting a comprehensive performance. (See Figure 4.2 for the types of the rods)

As shown in Figure 4.15 (A–F), when the scan is shifted to another slice (slice 2) which contains the second largest and the second smallest rods, the second smallest rod (2.53 mm in diameter) cannot be spotted since it is equivalent to only 2 voxels (2.34*2.34 mm^2) where it is difficult to preserve the actual wave propagation correctly and result in an error as the inversion algorithm calculates the elasticity information from this extremely incomplete wave propagation. Similar to slice 1, the imaging region gradually demonstrates a finer quality when the frequency increases for the same reason that more wavelengths or a more complete wavelength will be found within a specific dimension of a target as the frequency increases, and will help MRE better display the elasticity distribution of the target. However, when the frequency is 180 Hz, the signal dampening deteriorates the image quality again.

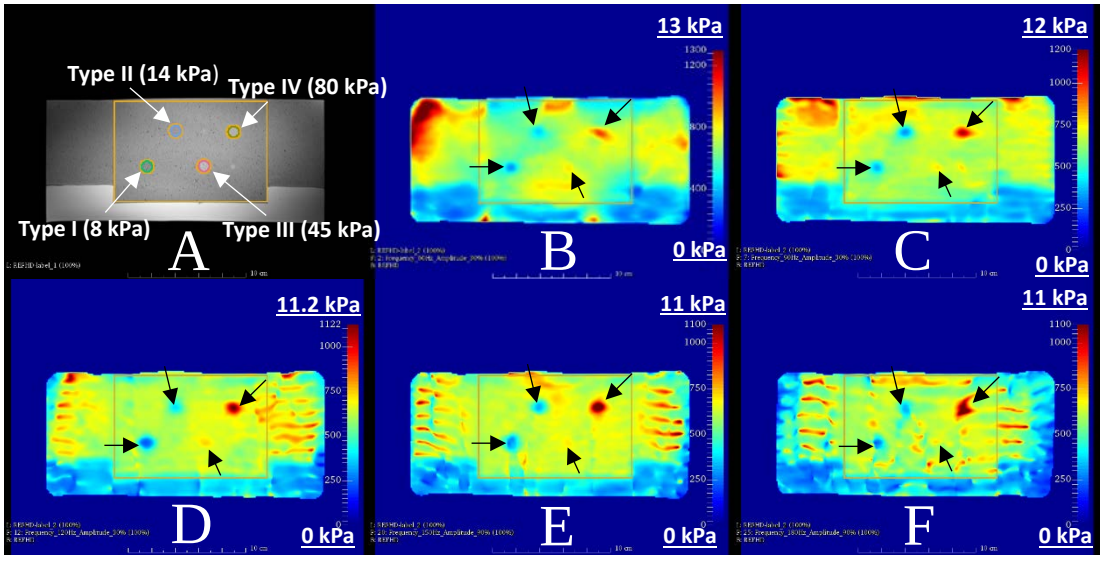

Figure 4. 15 (A) T2-weighted image on slice 2; **(B)** stiffness map at 60 Hz; **(C)** stiffness map at 90 Hz; **(D)** stiffness map at 120 Hz; **(E)** stiffness map at 150 Hz; and **(F)** stiffness map at 180 Hz.

Elasticity values for rods 10.404 mm in diameter on slice 2 are presented in Figure 4.16 (A). Figure 4.16 (B–E) show that although a higher frequency can enhance the clarity of the elastogram (from 60–150Hz in this case), the damping caused by an over-high frequency (180 Hz in this case) may counteract this clarity, producing some artifacts in the elastogram (see Figure 4.15 (F)).

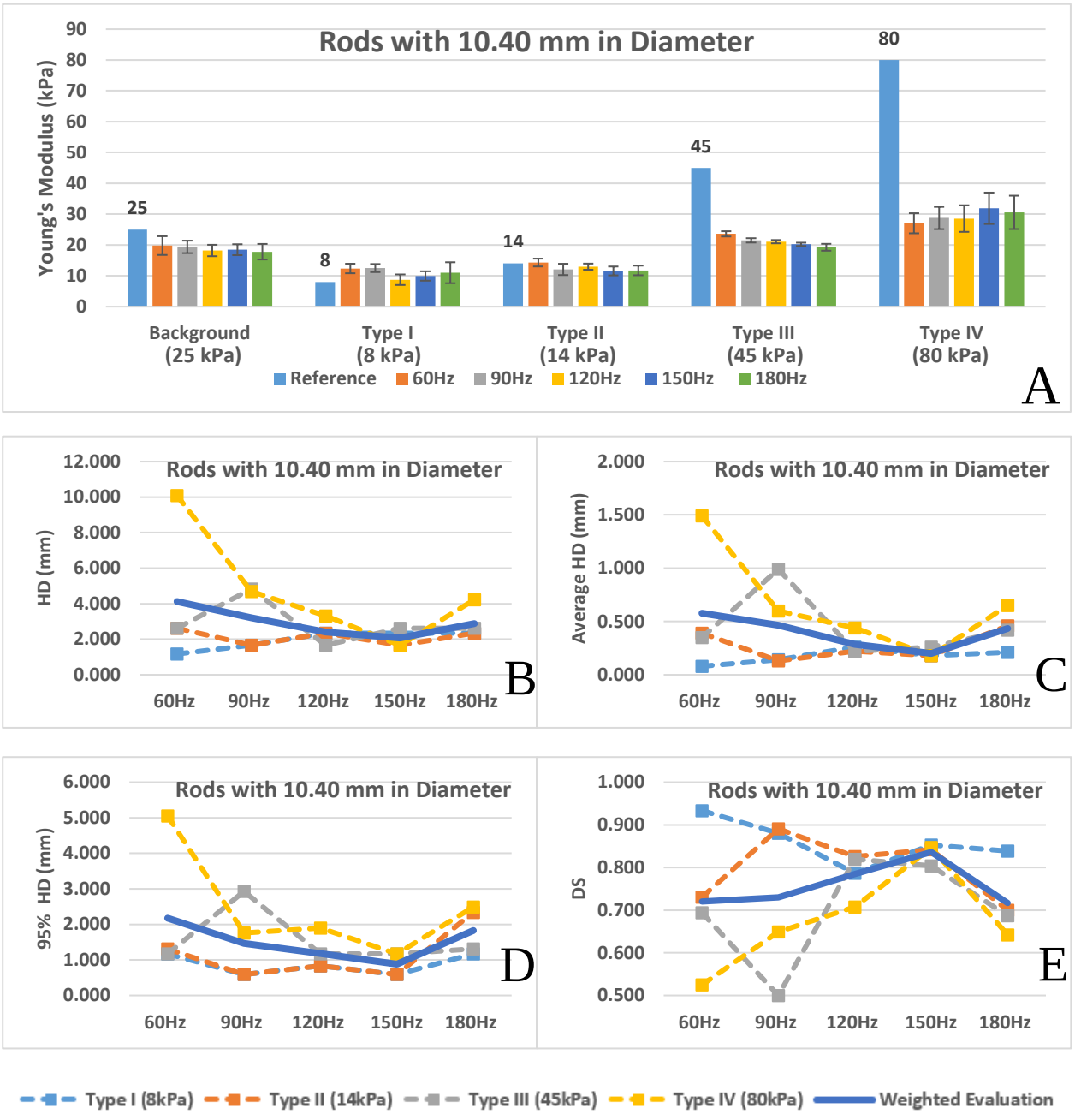

Figure 4. 16 (A) Elasticity; **(B)** Hausdorff Distance; **(C)** average Hausdorff Distance; **(D)** 95% Hausdorff Distance; and **(E)** Dice Similarity. The weighted evaluation is the mean evaluation of these four independent rods, reflecting a comprehensive performance. (See Figure 4.2 for the types of the rods)

Figure 4.17 and Figure 4.18 show that not all the types of rods can be found when the scan shifts to slice 3. In Figure 4.17, Type I, II, and IV rods with 6.49 mm in diameter are identifiable; whereas except for Type III which is 6.49 mm in diameter at 120 Hz in Figure 4.17 (D), Type III rod with 6.49 mm in diameter is barely identifiable at frequency settings of 60 Hz, 90 Hz, 150 Hz, and 180 Hz with respect to Figure 4.17 (B), (C), (E) and (F). Figure 4.18 shows that Type I, II, and IV rods with 4.05 mm in diameter are more identifiable when the windows/levels are adjusted, but Type III rod with 4.05 mm in diameter is nearly unidentifiable at all frequency settings from 60-180 Hz with an interval of 30 Hz. Possibly, the small diameter (4.05 and 6.49 mm) of Type III rod only experiences a slight change in wavelength under certain frequencies, which results in a hardly-identifiable contrast to the background.

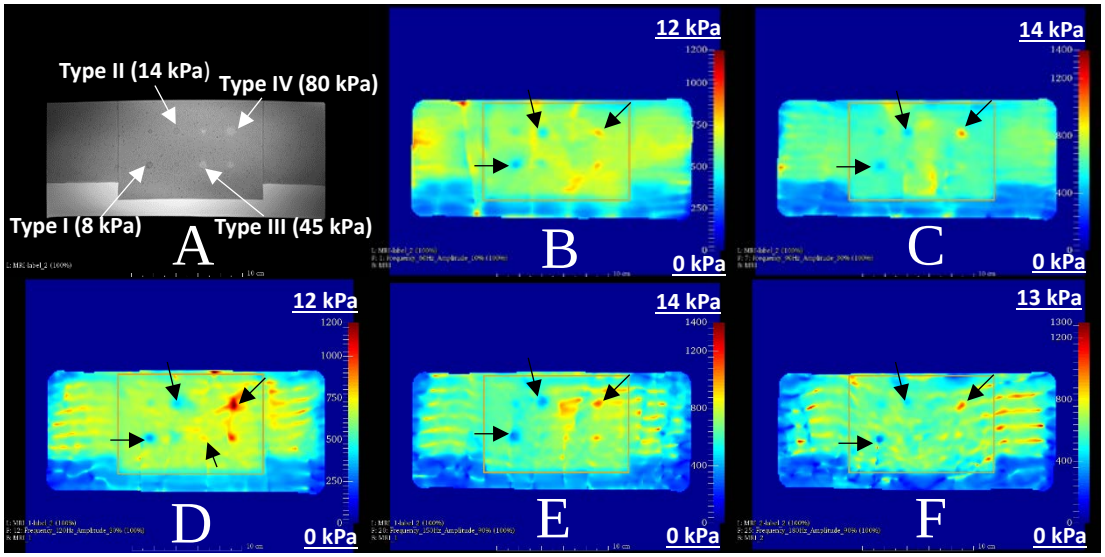

Figure 4. 17 (A) T2-weighted image on slice 3; **(B)** stiffness map at 60 Hz; **(C)** stiffness map at 90 Hz; **(D)** stiffness map at 120 Hz; **(E)** stiffness map at 150 Hz; and **(F)** stiffness map at 180 Hz.

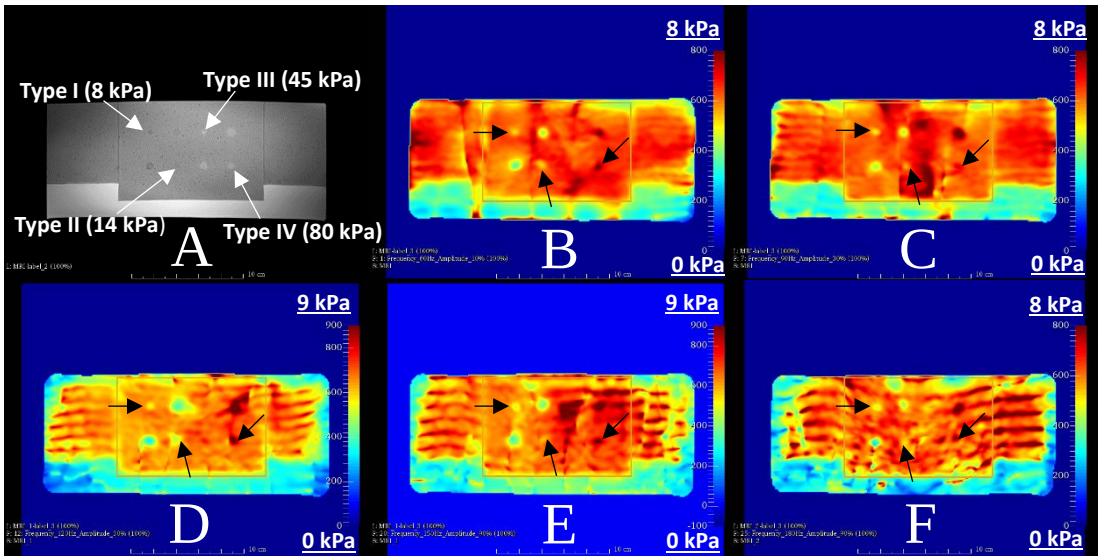

Figure 4. 18 (A) T2-weighted image of slice 3; **(B)** stiffness map at 60 Hz; **(C)** stiffness map at 90 Hz; **(D)** stiffness map at 120 Hz; **(E)** stiffness map at 150 Hz; and **(F)** stiffness map at 180 Hz. (Compared to Figure 4.17, the windows/levels were adjusted for a better visibility for the rods with 4.05 mm in diameter.)

Figure 4.19 shows the elasticity values for the diameters of 6.49 and 4.05 mm under different MEG frequencies from 60-180 Hz with an interval of 30 Hz. However, due to the relatively close sizes between the voxel (1.17*1.17 mm^2) and the diameters of the rods (4.05 mm and 6.49 mm): these rods only cover very limited pixels, segmentation cannot be performed accurately. Therefore, the other four quantitative evaluation indices, the three HD measures and DS, are not available for the rods with the diameters of 4.05 and 6.49 mm in this case.

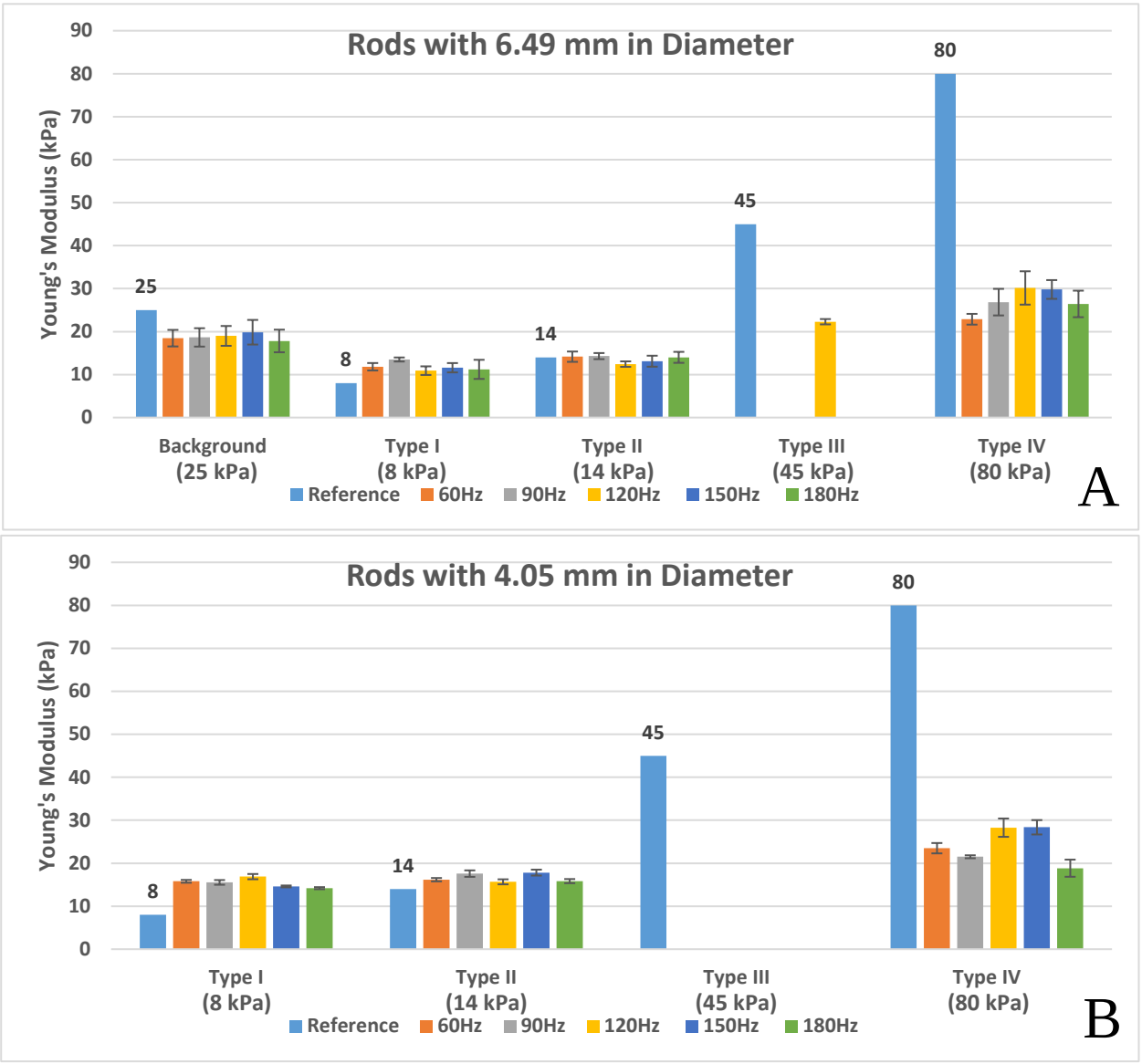

Figure 4. 19 (A) Elasticity values for a rod 6.49 mm in diameter, but Type III rod at frequency settings of 60 Hz, 90 Hz, 150 Hz, and 180 Hz are absent except for 120 Hz; and **(B)** elasticity values for a rod 4.05 mm in diameter, but Type III rod at frequency settings of 60 Hz, 90 Hz, 120 Hz, 150 Hz, 180 Hz are absent. (See Figure 4.2 for the types of the rods)

It should be noted that the calculation of elasticity values is not only affected by the dimension of the targets compared to the frequency, it is also influenced by the other post-processing techniques, such as filtering and unwrapping. Though these post-processing techniques can significantly remove artifacts and noise from the background, they might also alter the waveform passing through the targets. Therefore, there is always a tradeoff between artifact removal and elasticity calculation. From the above results, the optimal frequency for this phantom is probably 120 ~ 150 Hz.

It can be concluded that adjustment of the frequency minorly affects elasticity values but will improve the image quality in accuracy, including the match of locations, sizes, and shapes. However, tuning the frequency to an over-high setting will cause some damping issues which induce many artifacts, so it is necessary to pinpoint an optimal frequency by setting up a series of tests prior to performing other MRE applications.

4.5.2.3. Resolution dependence of an MRE system

From Figure 4.13–4.19, we can conclude that the smallest rod that can be identified is 4.05 mm (for most of the types). Figure 4.20 (A) and (B) show that the elasticity values of the soft rods (Type I and II) tend to decline and deviate from the references with a decrease in diameter. As Figure 4.20 (C) and (D) show, although Type III rods cannot be completely detected with all diameters and at all settings, from information provided by Type IV rods, it can be predicted that the elasticity value of the hard rod will be elevated and approach to the references as the diameter increases. Figure 4.20 (E) illustrates that the elasticity values of the background demonstrate a flat tendency when the scan position shifts from slice 1 to slice 3. This suggests that although the elasticity values of the rods with different diameters were collected from different scans/slices, the Figure 4.20 (E) verifies that the change of the elasticity values are nearly unaffected by the variation of scan situation. It can be also predicted from Figure 4.20 that in MRE scan the larger size of targets will reflect closer measured elasticity values to true elasticity values. Such information can provide a useful reference for other MRE applications.

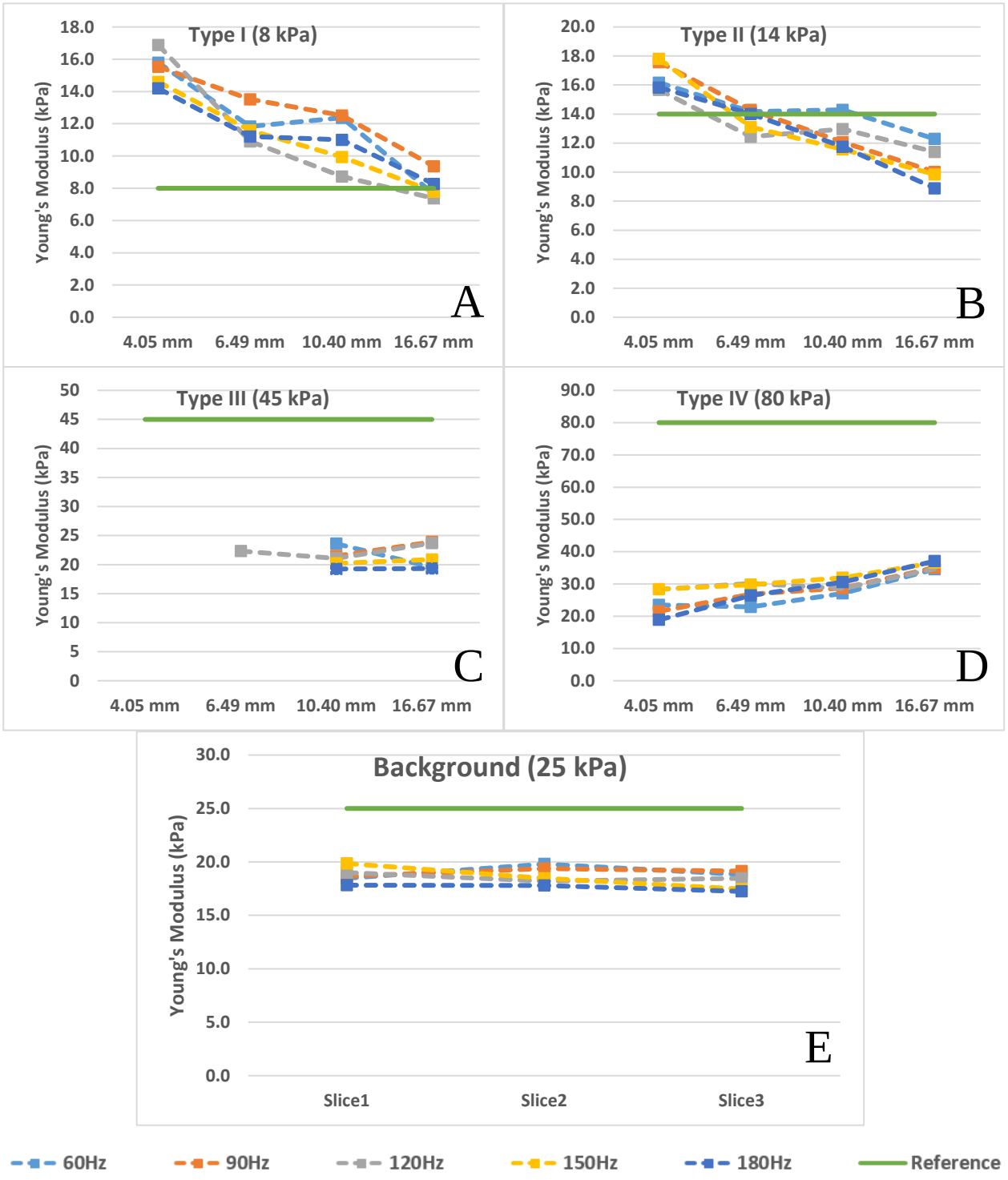

Figure 4. 20 Change of the elasticity value as the targets' size varies for the rods of **(A)** Type I, **(B)** Type II, **(C)** Type III, and **(D)** Type IV at the frequency settings of 60-180 Hz with an interval of 30 Hz; and change of the elasticity value for background **(E)** when the scan situation varies.

4.5.2.4. Correlation between Frequency and Amplitude in an MRE system

Figure 4.21 shows that at 60 Hz, as the amplitude is rising, artifacts begin to appear on the stiffness map and the rods (on the stiffness map) begin to show distortions. However, in Figure 4.22, at 150 Hz, when the amplitude is increased, the quality of the stiffness map becomes finer. Figure 4.23 shows that the wave propagation under different frequencies is largely affected by amplitude. At low frequencies, "phase wrapping artifacts" begin to appear as indicated by the red arrows in Figure 4.23 (A). Figure 4.24 (A) shows a profile across Figure 4.23 (A) artifacts (in a red line), showing that the phases are wrapped. In other words, since the wave capture is based on the phase contrast technique that records the wave amplitude in a range (phase $-\pi \sim \pi$ for instance), the amplitude of the wave could be wrapped if the actual amplitude value is beyond the recording range, as shown in Figure 4.24 (B). At a low frequency, the wrapping will become more significant (multiple wrappings) if the amplitude keeps rising as shown in Figure 4.23 (B). Second, at high frequency, a high amplitude (90%) wave shown in Figure 4.23 (D) shows a better and clearer wave propagation in general than a low amplitude (10%) wave shown in Figure 4.23 (C). Specifically, a profile line (blue line) is drawn on the homogenous background of this phantom as presented in Figure 4.23 (A–D), and the results are shown in Figure 4.24 (C–F). Figure 4.24 (C–D) show that with a low frequency (60 Hz) and low amplitude (10%), the profile shows a clear and ample waveform; while at the same frequency (60 Hz) but a high amplitude (90%), the wrapping artifacts largely disturb the wave propagation—i.e., multiple wrapping as the blue dashed circles indicate in Figure 4.24 (D). However, Figure 4.24 (E–F) show that at high frequency (150 Hz) and low amplitude (10%), the waveform bears much more damping and some unexpected background noise that potentially alter the frequency of the wave as the red trend line and red dashed ellipse, respectively, show in Figure 4.24 (E). At 150 Hz with 90% amplitude, the profile shows a clear waveform, though it also has an obvious damped trend line (the blue line), as shown in Figure 4.24 (F). Therefore, we can conclude that at low frequency there will be less damping but possibly a wrapping issue if the amplitude is set too high, whereas at high frequency the wave experiences more damping which can sometimes be compensated with a higher amplitude.

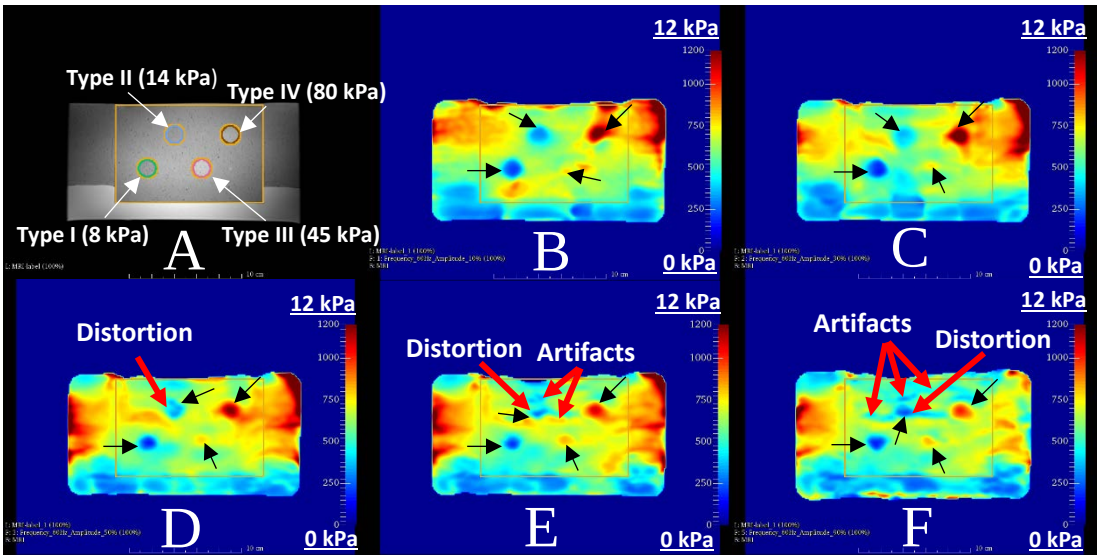

Figure 4. 21 (A) T2-weighted image on slice 1; **(B)** stiffness map at 60 Hz with 10% amplitude; **(C)** stiffness map at 60 Hz with 30% amplitude; **(D)** stiffness map at 60 Hz with 50% amplitude; **(E)** Stiffness map at 60 Hz with 70% amplitude; and **(F)** stiffness map at 60 Hz with 90% amplitude.

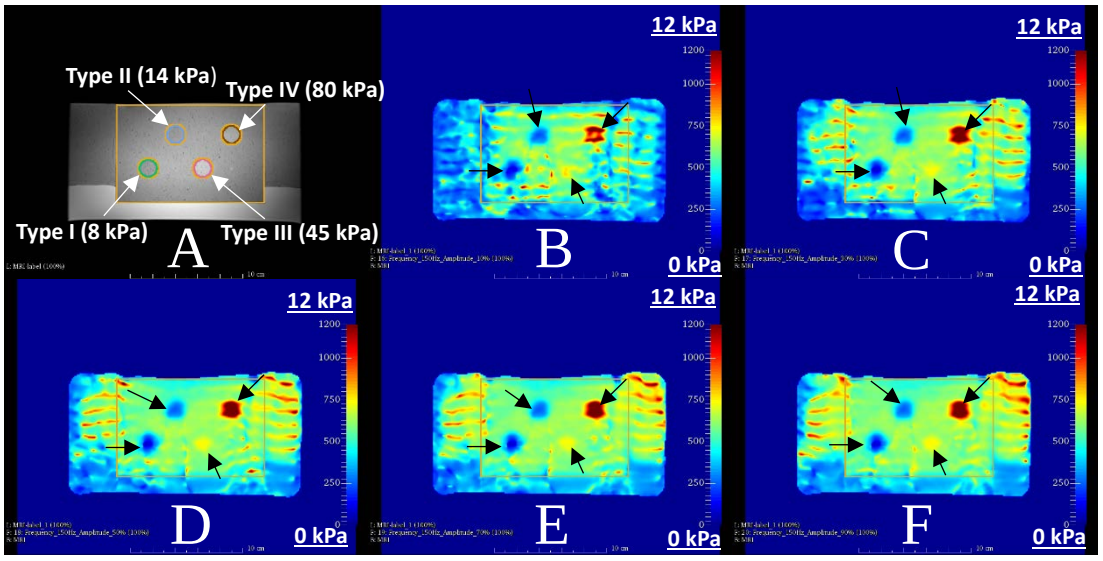

Figure 4. 22 (A) T2-weighted image on slice 1; **(B)** stiffness map at 150 Hz with 10% amplitude; **(C)** stiffness map at 150 Hz with 30% amplitude; **(D)** stiffness map at 150 Hz with 50% amplitude; **(E)** stiffness map at 150 Hz with 70% amplitude; and **(F)** stiffness map at 150 Hz with 90% amplitude.

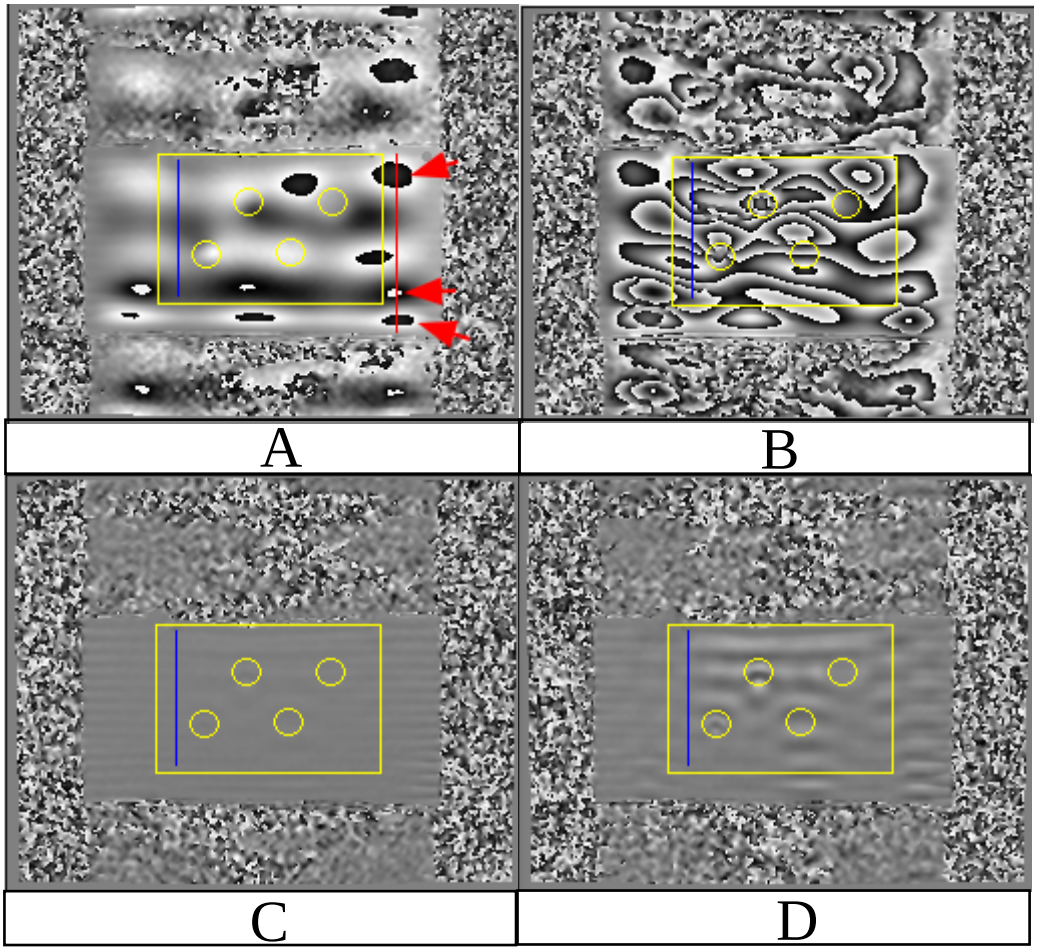

Figure 4. 23 (A) Phase contrast images on slice 1 at 60 Hz with 10% amplitude; **(B)** phase contrast images on slice 1 at 60 Hz with 90% amplitude; **(C)** phase contrast images on slice 1 at 150 Hz with 10% amplitude; and **(D)** phase contrast images on slice 1 at 150 Hz with 90% amplitude. (The yellow box shows the imaging region, yellow circles show the location of the inclusions, and blue and red lines indicate the profiles.)

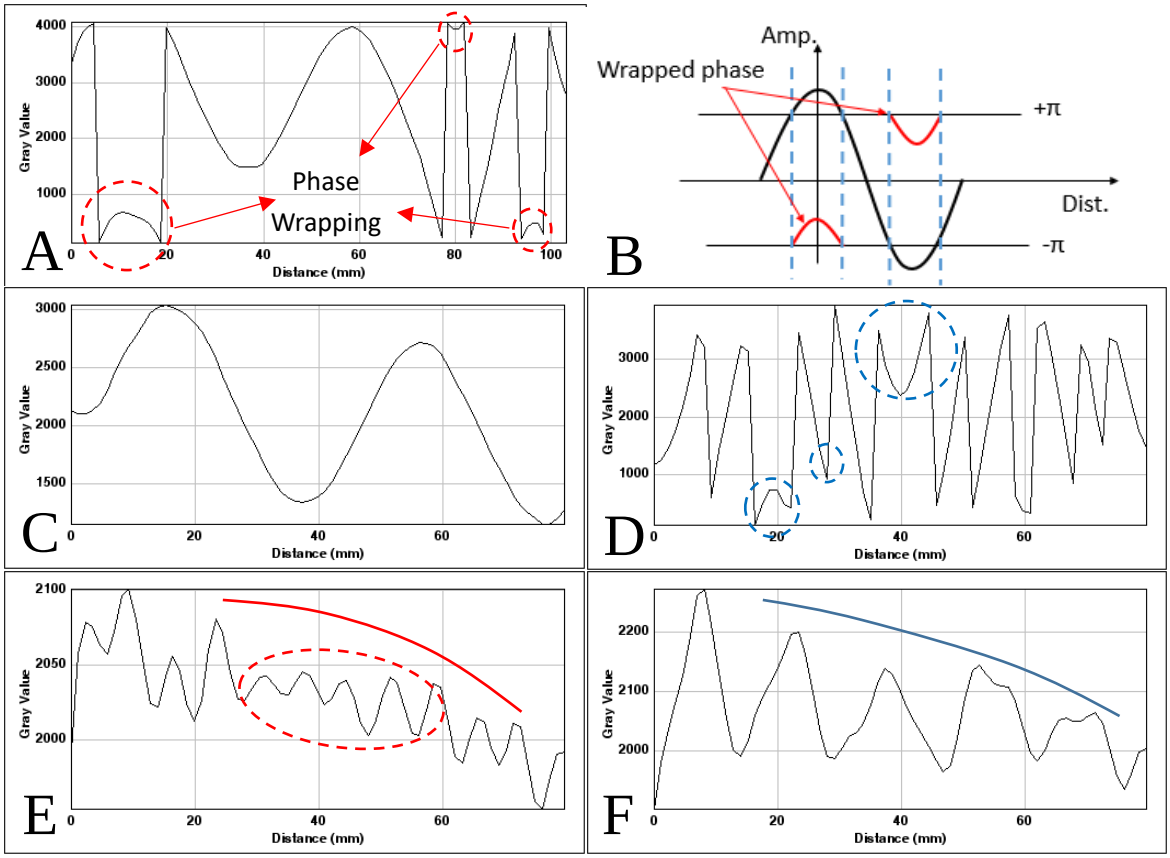

Figure 4. 24 (A) The profile of the red line across the phase wrapping artifact in Figure 4.23 (A), and the red dashed circles indicate phase wrapping; **(B)** demonstration of phase wrapping; **(C)** the profile of the blue line across the phantom's homogenous background in Figure 4.23 (A); **(D)** the profile of the blue line across the phase wrapping artifact in Figure 4.23 (B), and the blue dashed circles indicate multiple phase wrapping; **(E)** the profile of the blue line across the phantom's homogenous background in Figure 4.23 (C), and the red trend line and red dashed ellipse indicate damping and background noise, respectively; and **(F)** the profile of the blue line across the phantom's homogenous background in Figure 4.23 (D), and the blue trend line indicates damping.

Wrapping artifacts can be removed by a post-processing step—i.e. the unwrapping technique, but the quality of unwrapped results depends on how severe the wrapping appears, as shown in Figure 4.25 [114]. Specifically, in Figure 4.25, the unwrapped (processed) phase contrast images on slice 1 at 60 Hz with 90% amplitude, which possesses a more severe phase wrapping artifact previously, has worse quality than the unwrapped (processed) phase contrast images on slice 1 at 60 Hz with 10% amplitude. A comparison of unwrapped phase contrast images on slice 1 at 60 Hz in Figure 4.25 (C) and (D) shows that though the general wave propagation is coarsely restored in both images, the unwrapped phase contrast images on slice 1 at 60 Hz with the high amplitude in Figure 4.25 (D) (90%) produces some new artifacts (indicated by the red arrows) from the unwrapping technique, which is believed to be the main cause of the artifacts and distortion spotted in the elastogram shown in Figure 4.21 (F). To address all these issues, the better strategy is to

compromise by using an optimal frequency with an appropriate amplitude. The QC tests in this phantom indicate that for 60 Hz and 90 Hz the best amplitude is 10–30%, for 120 Hz the best amplitude is 30–50%, and for 150 Hz and 180 Hz the best amplitude is 70–100%. However, the unwrapping technique is necessary if the wrapping exists at these optimal settings, as shown in Figure 4.23 (A).

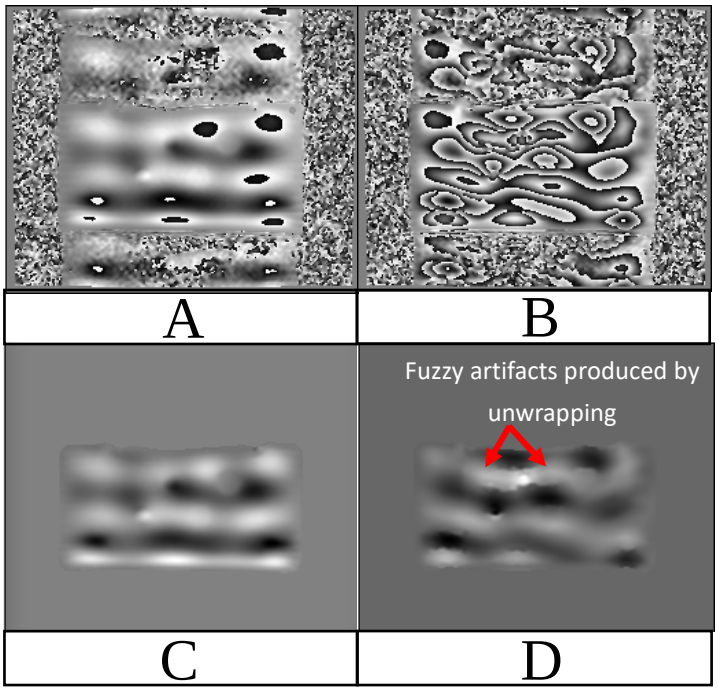

Figure 4. 25 (A) Un-unwrapped (unprocessed) phase contrast images on slice 1 at 60 Hz with 10% amplitude; **(B)** un-unwrapped phase contrast images on slice 1 at 60 Hz with 90% amplitude; **(C)** unwrapped (processed) phase contrast images on slice 1 at 60 Hz with 10% amplitude; and **(D)** unwrapped phase contrast images on slice 1 at 60 Hz with 90% amplitude.

4.6. Conclusion

The above set of tests indicate that MRE can provide a good qualitative image for targets with different elasticity values and dimensions. The quantitative results are related to multiple factors, such as the size of the target and the selection of frequency. The frequency and amplitude of the wave are the two main parameters that decide the image quality. Optimal frequency and amplitude may differ in other applications, but parameter selection should follow similar principles. That is, the QC tests on this QA phantom can provide a good guideline for directing other MRE applications. In conclusion, we have identified a set of optimal parameter settings (in this case, the shear wave is at 120Hz–150Hz with an amplitude of 30%–90%), investigated the feasibility of the MRE, and developed a general imaging protocol to provide a practical guideline for future MRE applications.

Chapter 5

Integration of Magnetic Resonance Elastography to Radiation Therapy

Chapter Synopsis

Magnetic Resonance Elastography (MRE) has the ability to distinguish between elastic properties of the tissue. Furthermore, it is maturing as a technique to differentiate normal and cancerous tissue. In this chapter, we present a strategy to establish high quality MRE data, and present a method to incorporate this information into a radiation treatment planning framework. This new information is used to evaluate the efficacy of dose escalation to dominant intraprostatic lesions using a volumetric modulated arc therapy technique.

5.1. Introduction to Radiation Therapy

One of the most common radiation therapy (RT) procedures used in clinical practice is external beam radiation therapy (EBRT). EBRT is a treatment procedure which utilizes a linear accelerator (LINAC) to deliver high energy x-rays to kill cancer cells. In order to maximize the radiation dose to the gross tumour volume, RT requires a high-level precision to minimize the dose to normal tissues. As the first step of EBRT, a simulation process is usually required to acquire the patient's anatomy, patient's positioning, and dose calculation. This allows the dosimetrist to plan the ensuing treatment and maintain the effectiveness and safety of the therapy process. The simulation process is generally accomplished with the aid of a Computed Tomography (CT) simulator and treatment planning software. In a conventional simulation process, the CT simulator will first proceed with a volumetric scan of the patient. Then the scanned images will be imported to the treatment planning software for dose optimization, which includes the contouring of targets, organs at risk (OAR) and the placement of the treatment beams. Next, all the scanned images, patient's information, and treatment planning settings from the virtual simulation software will be transferred to the LINAC. Finally, the LINAC will perform the radiation therapy according to the treatment planning determined in the virtual simulation software. The workflow of the conventional RT process is shown in Figure 5.1.

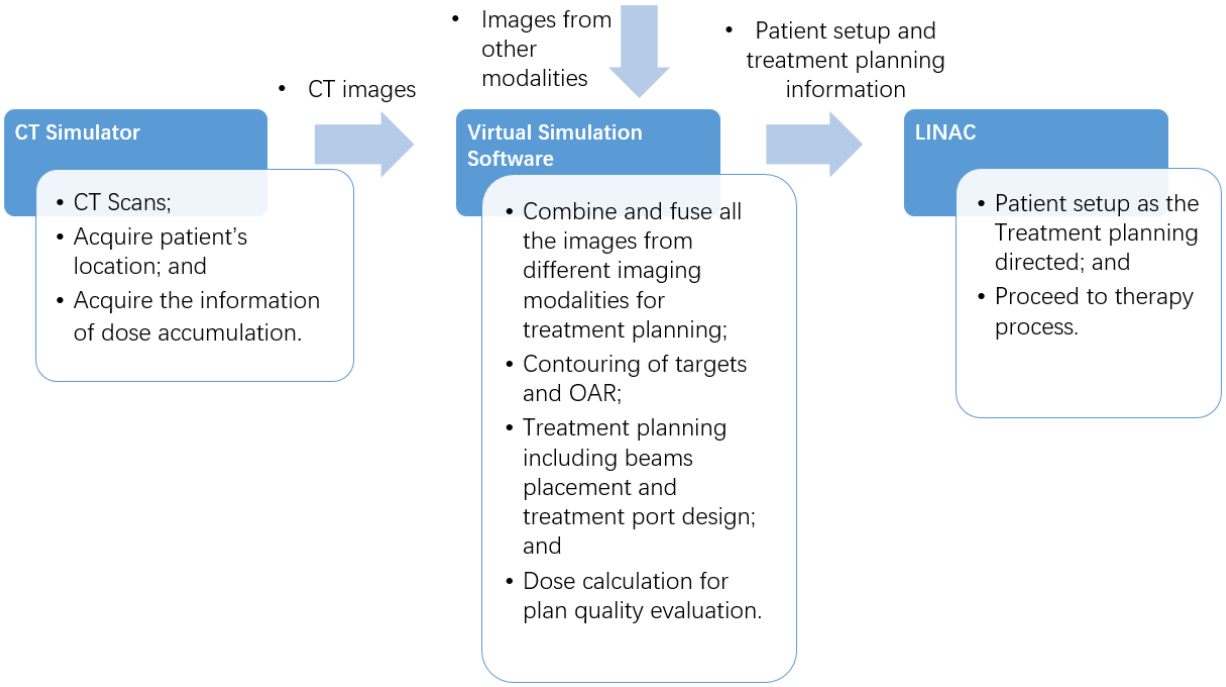

Figure 5. 1 Conventional radiation therapy workflow.

Nowadays, in radiation oncology more advanced imaging techniques are incorporated to better delineate and detect the tumours based on different types of cancer, and the radiation delivery techniques on LINAC are also gradually improved as a result of ongoing medical physics research [118].

There are many imaging modalities becoming a part of the radiation oncology and providing inputs to the RT process in routine clinic nowadays, such as Magnetic Resonance Imaging (MRI), Positron Emission Tomography (PET), Single Photon Emission Computed Tomography (SPECT), and ultrasound. They are all widely used in diagnosing different kinds of pathological changes (cancer) according to their different principles of imaging, sensitivity, and suitability for specific tumours. Integrating these imaging modalities with conventional RT treatment planning with CT scan improves the comprehensive confidence of cancer detection because CT scan does not always have the ability to acquire the cancer's anatomical or morphological information that other imaging modalities are able to provide, such as MRI [119]. For example, MRI has been widely applied in identifying prostate cancer; prostate cancer in the peripheral zone (PZ) usually shows a low-intensity in T2-weighted (T2W) images, which helps define suspected prostate tumours, and the sample extracted within the defined area can proceed to biopsy for further diagnosis [120]. Magnetic Resonance Spectroscopy (MRS) is a more sophisticated and advanced imaging technique which, when combined with MRI, is able to provide the biochemical and metabolic information that can give more details on tumour detection, characterization, staging, growth and development

[121, pp. 27–28], [122], [123]. In this case, the T2W images provide anatomical information, as another kind of contrast reference, while MRS data provides the parametric reference, reflecting the metabolic information. Incorporating this anatomical/parametric information into RT can improve the quality of radiation delivery–enhancing the reliability for dose (treatment) delivery onto the treated area in treatment planning–and potentially increase the effectiveness and safety of the therapy process [123].

As a relatively novel imaging technique, there are a few number of studies on the applications of MRE in cancer in comparison to other conventional imaging modalities. Arani et al. used a custom actuator coupled with an endorectal radiofrequency coil to carry out endorectal MRE scans to a prostate phantom, and their study demonstrated the feasibility of the application of endorectal MRE in localizing prostate cancer [63]. Similarly, Thörmer et al. used another custom actuator, performing endorectal MRE scans to a prostate phantom and transrectal MRE scans to a cadaver porcine; their study also showed a promise of MRE in prostate cancer detection [67]. Sahebjavaher et al. reported ex vivo elastograms of prostate cancer and in vivo prostate elastograms of healthy volunteers and prostate cancer patients, and they also conducted some studies comparing the elastograms of prostate cancer to histopathology [89]–[92]. Though the diagnosis of prostate cancer with MRE is still an ongoing research, their results still show a great promise in detecting prostate cancer [91], [92]. Other MRE applications for cancer detection also include, for example, breast cancer and pancreatic cancer [22], [112], [124]–[128]. However, these studies mainly focused on the cancer detection with MRE. As for the subsequent cancer elimination, no one has conducted any studies on the feasibility of using elastograms to plan a radiation treatment if a RT procedure is required. Therefore, this thesis would take a step further, investigating the potential feasibility of using elastograms to define cancerous regions and incorporating the data to a radiation therapy environment with the help of a prostate phantom that contains three mimicked lesions. The role of this phantom is to make an assumption that these three lesions are already diagnosed as tumours which the radiation treatment will be planned on.

5.2. The Potential of Integrating MRE to Radiation Therapy

Magnetic Resonance Elastography (MRE) has demonstrated the ability to quantitatively and noninvasively obtain the mechanical properties of both healthy and tumorous tissues [18]. This shows a great potential of integrating MRE, as a new advanced parametric imaging technique, to the conventional radiation therapy procedure. Therefore, this chapter focuses on investigating the potential feasibility of integrating MRE into the RT process with the aid of a tissue-equivalent prostate phantom containing three Dominant Intraprostatic Lesions (DILs). However, before this integration can be feasible, high quality MRE images need to be acquired. Since the quality of MRE images are significantly dependent on the selection of the parameters to obtain the high quality MRE image (frequency and amplitude, specifically), a sophisticated optimal-parameters-searching scan protocol needs to be set up. Once the optimal parameters for high quality MRE

images are obtained, a multi-slice scan across the whole volume of the target (referring to the prostate at this phantom) can proceed. Combined with CT and MRI, the MRE scans can be developed into a comprehensive and optimized scan procedure designed for radiation treatment planning. These three groups of datasets can be co-registered and fused together before flowing into the virtual simulation software for treatment planning. The CT scan is used for dose calculation and the assurance of geometrical accuracy during image registration; the MRI scan provides a better contrast in soft tissue and an anatomical reference for MRE data; and the MRE scan acquires the stiffness information and improves the confidence of DILs' detection. This new comprehensive information can be used to validate the efficacy of applying a Volumetric Modulated Arc Therapy (VMAT) technique to treat DILs. To be specific, VMAT is able to achieve a dose escalation to DILs but a dose reduction to OARs: this will be further described in detail in section 5.3.1.3.1.

5.3. Integration of MRE to Radiation Therapy Procedure

The purpose of this chapter is to investigate whether the MRE data could be used to detect and segment a cancerous region within a prostate phantom; and whether this information can be used to selectively boost the amount of radiation to the cancerous region [129].

5.3.1. Materials and Methods

5.3.1.1. Phantom, Scan Tools, and Software Packages

Figure 5.2 shows the training phantom used in this study, a tissue-equivalent prostate phantom (Model 053L CIRS Inc., Norfolk, VA).

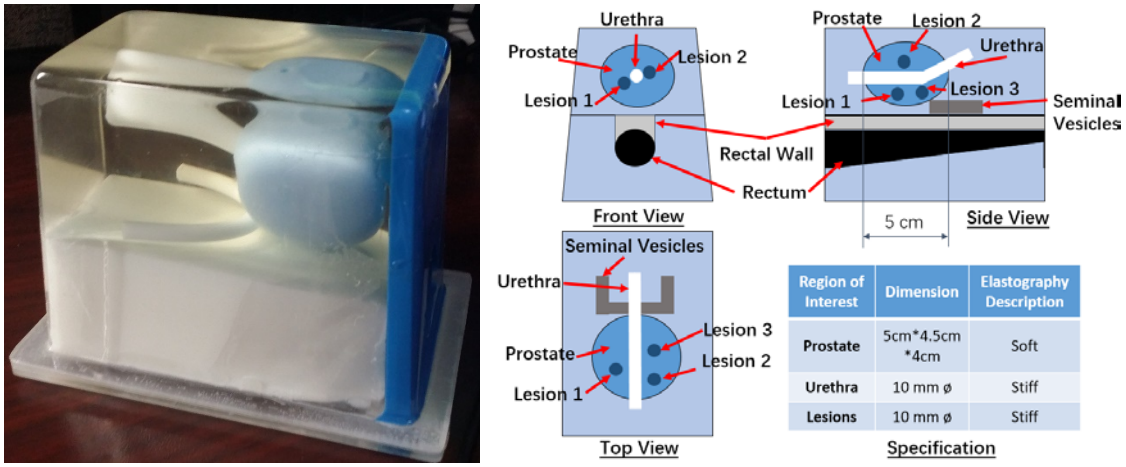

Figure 5. 2 Structure and specifications of the prostate phantom.

The prostate phantom mimics the structure of prostate anatomy. There are three embedded lesions that can be used as elasticity-markers to provide a contrast to the normal "prostate tissue" in the background—i.e., the MRE will contrast the stiff markers versus the soft prostate tissue. This

phantom can help us decide whether in a simulated situation—three stiff lesions each 10 mm in diameter within a soft prostate—the lesions would be detectable to MRE, and further to verify that the detected results can be integrated to RT.

The tools for the acquisition of the prostate phantom's MRI and MRE data were: (1) a 3T Skyra platform (Siemens Healthcare, Erlangen, Germany), (2) a Resoundant® driver system (Resoundant Inc., Rochester, MN), and (3) the MRE Works-In-Progress (WIP) Spin Echo (SE)-Echo Planar Imaging (EPI) pulse sequence (WIP 923B VE11A, Siemens) [106]. The MRE/Wave inversion software based on the Local Frequency Estimation (LFE) algorithm was used to calculate the elastogram (also known as the stiffness map) [114]. Additional software packages, e.g., MATLAB R2014a and 3D Slicer 4.6.2, were used to perform a series of postprocessing operations on the elastogram: the use of MATLAB was to generate DICOM (Digital Imaging and Communications in Medicine) format images for radiation therapy; 3D Slicer was used for image segmentation and registration. All the CT images were acquired from the GE Lightspeed CT simulator (GE Healthcare, Chicago, USA). After all the data were collected and ready for use, they were imported to the Eclipse treatment planning software (Varian Medical Systems, Pal Alto, USA).

5.3.1.2. Part 1 Approaches to Establish Qualified Elastograms for Radiation Therapy

5.3.1.2.1. Imaging Acquisition and Inversion

The flowchart in Figure 5.3 shows the general MRE workflow developed for clinical use. A series of processing steps were used to generate an elastogram for treatment planning. Once the magnitude and phase contrast images are obtained from the MRI scanner, these raw data should flow into the next step, inversion to the elastogram. The inversion step is a comprehensive processing that includes masking, unwrapping, filtering, and the final stiffness calculations. Some of steps can be accomplished automatically, such as the unwrapping and stiffness calculations, while others need to be set and monitored by users, such as the masking and filtering. Specifically, without appropriated settings and supervisions for these user intervention steps, the image quality of the MRE elastogram will be poor. For the masking, a mask is normally extracted from the magnitude image by thresholding to window out the effective wave propagation region from the phase contrast images; this step needs an appropriate setting for the threshold value, because, in some cases, the effective regions could be mistakenly windowed out by an inappropriate threshold of the mask. The phase wrapping artifacts, as described extensively in Chapter 4, can be removed without user intervention through the unwrapping technique provided by the MRE/Wave software. The filtering is the most important step during the inversion procedure, affecting the correctness of the calculation of the stiffness maps (a detailed discussion can be found in Appendix A). This step is usually applied to the wave image before it is converted to the stiffness map to avoid miscalculating the stiffness map. Lastly, after the wave images are perfected, the inversion algorithm is carried out to convert the wave images to a stiffness map; this step is a straightforward, automatic calculation process that does not requires user's intervention (this step is accomplished

by hitting the “continue” button at “lfe” step of “wave inversion” function flow within the MRE/Wave software package without any extra mandatory settings).

Additionally, the results of previous validation and feasibility investigations of MRE scan imply that the setting of mechanical wave’s frequency and amplitude carry significant weight in the quality of the MRE elastogram. Different mediums and structures under a specific frequency of excitation promote unpredictable local wave propagation variations; therefore, as shown in Figure 5.4., a parameter panel test for MRE scan is set up to probe the optimal settings on the slices with the regions of interest (ROI) in this work, and sometimes even a finer parameter panel test is needed to narrow down the setting ranges. According to the feasibility study in Chapter 4, the selections of driven frequency and relative driver amplitude are critical for the quality of the elastogram.

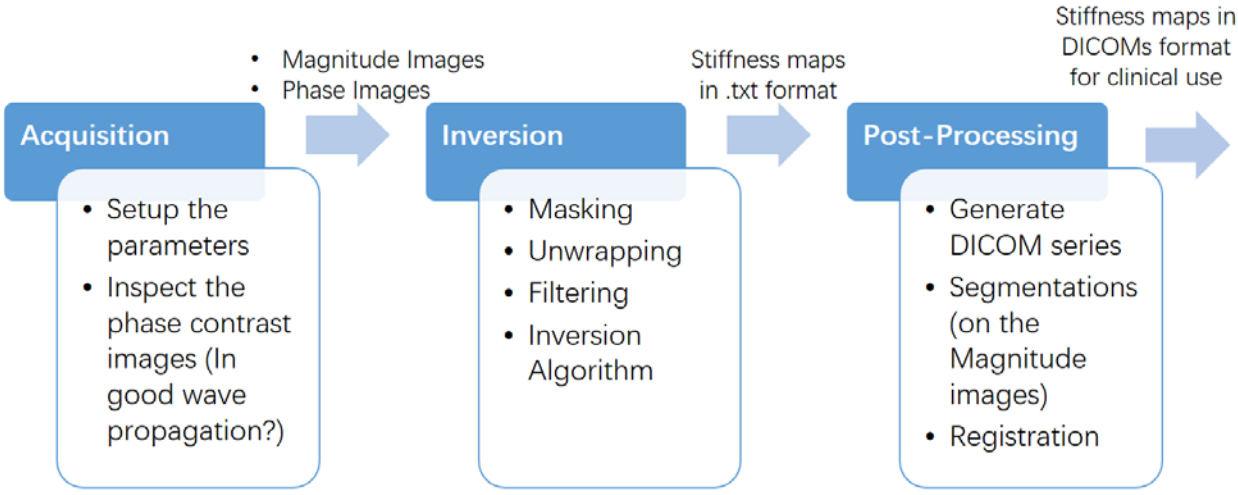

Figure 5. 3 MRE scan workflow. (DICOM is defined as Digital Imaging and Communications in Medicine)

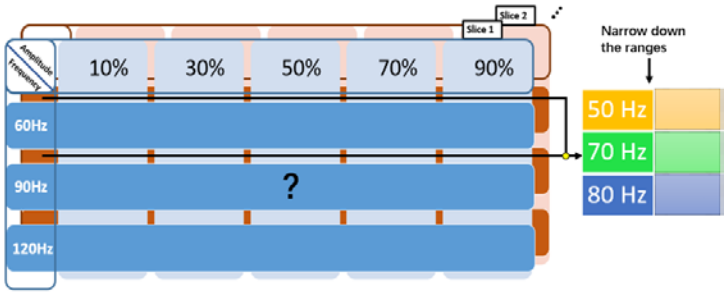

Figure 5. 4 Panel-test schema for optimizing MRE scan parameters.

5.3.1.2.2. Image Registration

Though a magnitude image (shown in Figure 5.5 (A)) is also acquired during the MRE image acquisition process, due to the limited resolution which is restricted by the MRE pulse sequence, an extra T2W axial image with high resolution (shown in Figure 5.5 (B)) is usually required to provide an anatomical reference. The driver vibration or other factors can shift the position of the scanned subject as well. In addition, the distortion (in Figure 5.5 (A)) caused by the EPI technique (see Chapter 2, section 2.4.3.), may also result in a mismatch in ROIs. In (C) and (D) of Figure 5.5 (these two scans came from one acquisition protocol), this mismatch can be demonstrated by the following steps: (1) apply a segmentation to the MRE magnitude image using the circle-shaped segmentation tool of "Editor" module within the 3D Slicer with a prior knowledge of ROIs' diameters provided by the manufacturer; (same as section 4.5.1.3) (2) overlay the segmented label on the axial T2W image; and (3) observe the mismatch.

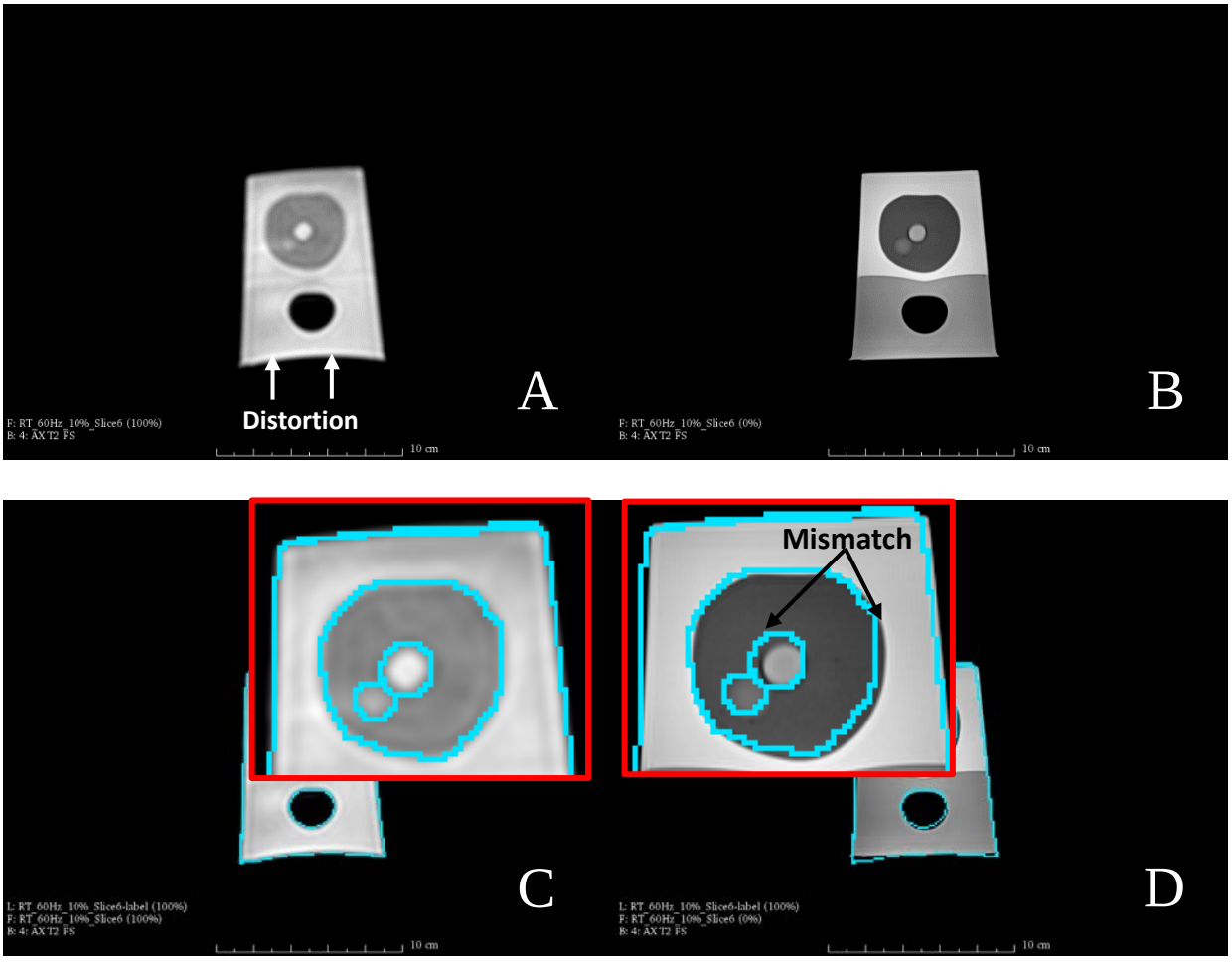

Figure 5. 5 (A) Magnitude image produced by MRE pulse sequence; **(B)** axial T2W image; **(C)** segmentations performed on the magnitude image; and **(D)** segmentations from the magnitude image overlain on the axial T2W image.

This mismatch would introduce a discrepancy into radiation therapy process, affecting the precision and safety of dose delivery, but this mismatch can be corrected through registration.

Registration is commonly used in clinical practice; it is a process that structurally matches two images from different imaging modalities, measurements, or scenes by comparing their lines, borders, features, or patterns. Registration can be accomplished by many methods; however, in this work, a linear registration strategy—i.e. affine transformation—is adopted because of its high computation efficiency and excellent practicability in clinical use. The mathematical computations in affine transformation accomplish a series of basic transforms, including translation, rotation, scaling, and shearing, directly to an image. These transforms actually map an image from one coordinate system to another. This mapping is carried out by a transform matrix that takes the original coordinates as input to obtain the transformed coordinates. For a 2D image, the transform operator is defined as a 3×3 matrix. Figure 5.6 shows four types of affine transform for a 2D image.

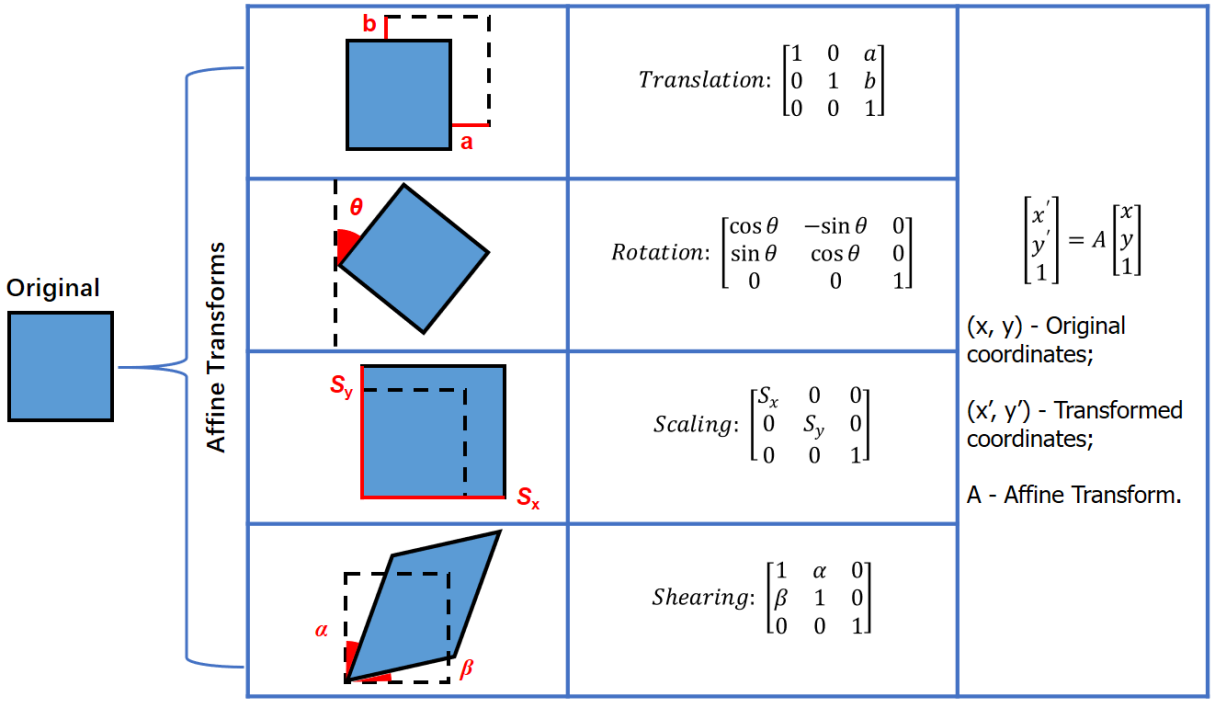

Figure 5. 6 Four types of basic affine transforms and their mathematical expressions.

The affine transform controls the registration process by setting the values of the transform matrix. Figure 5.7 shows that using 3D Slicer 4.6.2's "Transforms" module, the rotation and translation operations of the affine transform (illustrated by the green vectors in Figure 5.7) to the magnitude image can be accomplished by keeping manually calibrating the MRE magnitude image's segmentation label until it matches to the axial T2W image (the anatomical reference) where the MRE magnitude image's segmentation label well encapsulates the corresponded ROIs in the axial T2W image (see Figure 5.7). When the ROIs of the axial T2 images and the MRE magnitude image's segmentation label were matched, the associated affine transforms' matrix was finalized (and generated) within the "Transforms" module. By applying the exact affine transforms' matrix to the stiffness maps, the stiffness maps can be co-registered to the T2 images since they share the same orientation and location with the associated MRE magnitude images (see section

3.4.1), and these two co-registered image datasets can be exported as a comprehensive DICOM dataset for further clinical use.

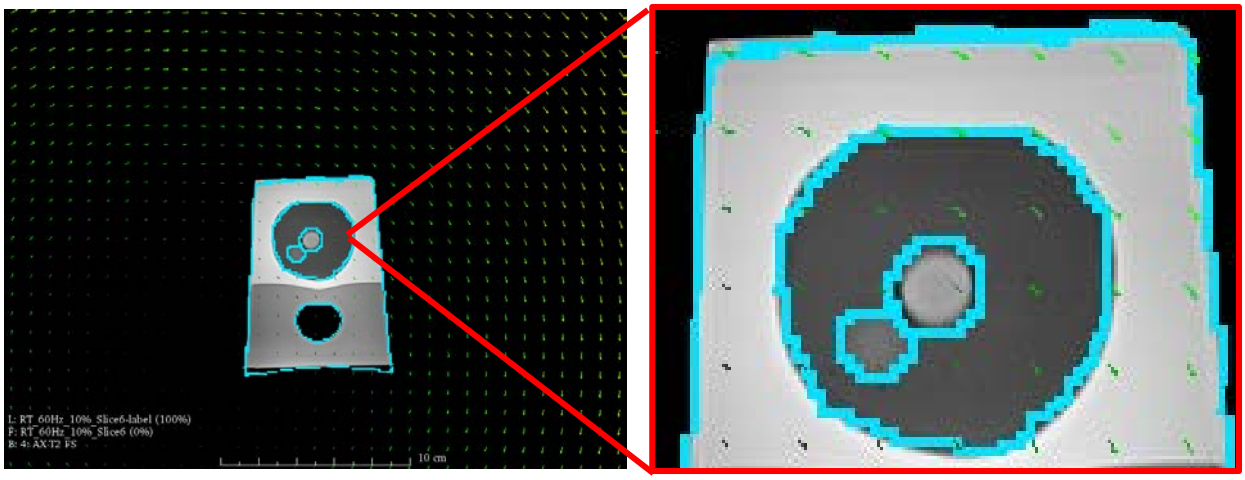

Figure 5. 7 The blue segmentation label was extracted from the MRE magnitude image of the prostate phantom and overlaid on the axial T2W image of the prostate phantom. By calibrating the blue segmentation label through affine transforms, the registration of the MRE magnitude image to the axial T2W image can be achieved. The green arrows indicate the track of translation and rotation which both are controlled by the affine transform matrixes.

5.3.1.2.3. Imaging Evaluation Method

The results of the panel tests can be evaluated qualitatively and quantitatively. The qualitative evaluation can be done by superimposing the stiffness map onto the axial T2W image to view the ROI match and other features such as boundaries or landmarks of the scanned subject in images, and by inspecting for the existence of artifacts. In the quantitative evaluation, four evaluation indices introduced in Chapter 4—Hausdorff Distance (HD), average Hausdorff Distance (aveHD), 95% Hausdorff Distance (95%HD), and Dice Similarity (DS)—were used, respectively, to evaluate the segmentations of the ROIs identified by the axial T2W image and the stiffness map. The segmentation to the stiffness map was achieved by the direct drawing tool of “Editor” within 3D Slicer (same as section 4.5.1.3). The mean HD, aveHD, 95%HD, and DS all along with standard deviations of five segmented ROIs—three lesions and the urethra respectively found on the two slices where these lesions were found—at each parameter setting were calculated through the “Segment comparison” module within 3D Slicer (same as section 4.5.1.4), and the HD (along with aveHD and 95%HD) with the minimal mean and the DS with the maximal mean, both with the least standard deviations, would jointly decide the best candidate in the quantitative evaluation. However, the best panel test result was chosen by evaluating both the qualitative (human) judgments and quantitative assessments from the comparison of the indices.

5.3.1.3. Part 2 Development of an MRE-Integrated Radiation Therapy Plan

5.3.1.3.1. Proposed MRE-Integrated Radiation Therapy Framework

A MRE-integrated comprehensive radiation therapy (RT) scan protocol is shown in Figure 5.8.

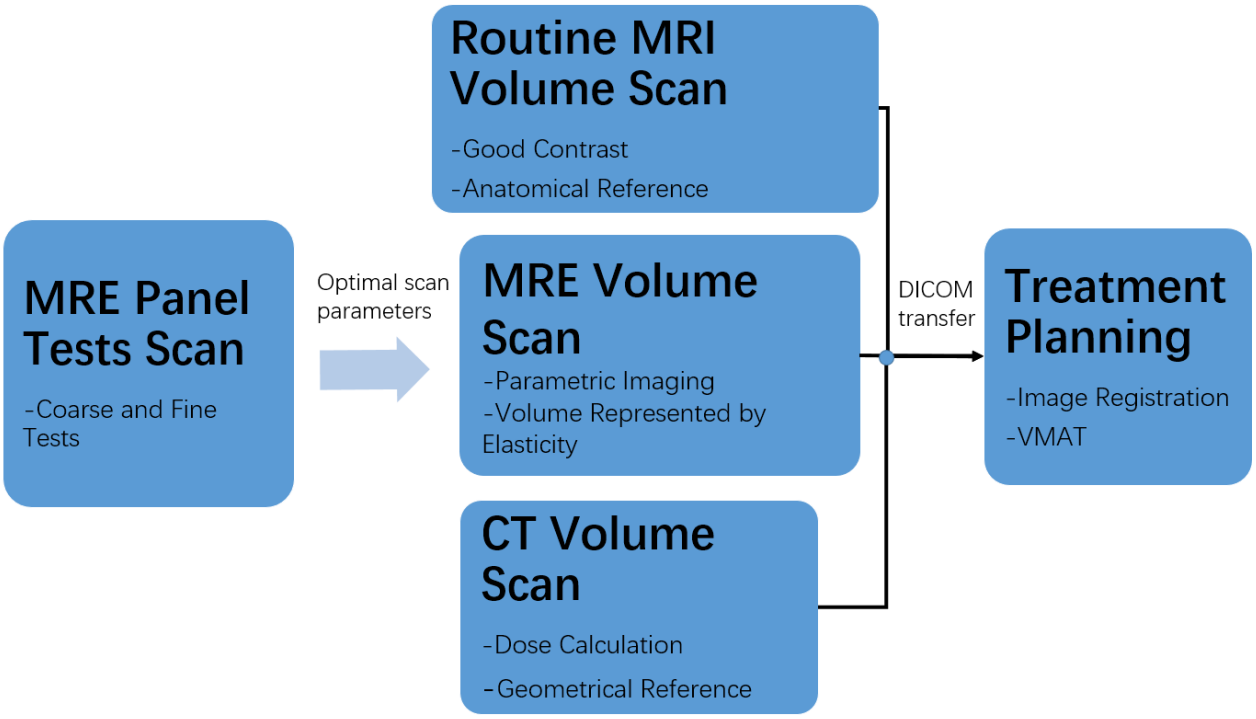

Figure 5. 8 Proposed MRE-integrated radiation therapy (RT) framework.

Firstly, in this designed RT framework, compared to CT, a routine MRI scan is able to provide a better contrast in soft tissues. A high resolution volumetric T1-weighted (T1W) or T2-weighted (T2W) image series can be used as an anatomical reference, indicating the location or the anatomical representation of tissue volumes delineated by the elastogram. In this work, multi-slice T2W images were collected from a 3T platform (section 5.3.1.1).

Secondly, the MRE panel-test scan is part of this framework because it is used to pinpoint the critical parameters (frequency and amplitude) that will be prescribed to the MRE volume scan. Given that the prostate in this case is approximately 5 cm in length, the volume is acquired in 10 slices with a slice thickness of 5 mm and without a gap, as shown in Figure 5.9. The multi-slice MRE data were collected from the 3T scanner with the aid of the Resoundant® driver system. After acquisition of the whole volume was completed, each individual slice was subjected to the inversion and post-processing procedures demonstrated in Figure 5.3 to produce a volume represented by elastic information. Although the volume acquisition process can be simply repeated from slice to slice, the subsequent inversion and post-processing can be tedious. That is, each individual plane may have to be adapted to different cutoff frequencies to filter out the compressional wave, or it might require a unique affine transform (matrix) to achieve the registration (to T2W images) due to the possible uncertain distortion or mismatch of each slice. After all the registered stiffness maps are converted to a DICOM format, they were evaluated slice

by slice as parametric images to improve the lesion detection confidence. As well, they were also aligned as a 3D volume that can be subjected to an effective radiation delivery.

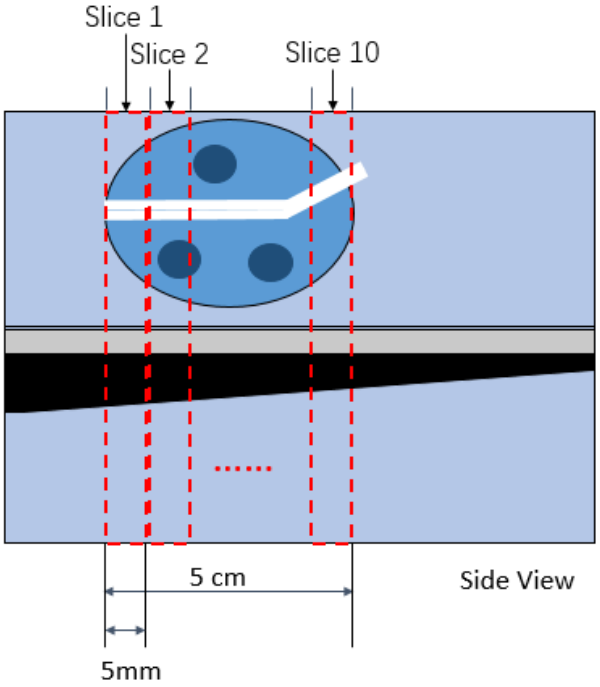

Figure 5. 9 Multi-slice MRE scan scheme for RT.

Thirdly, the CT scan provides images that can be used for the dose calculation. The dose calculation is the basis of dose control in the tumour targets and OARs in the subsequent treatment planning. Unlike the MRI scan, the CT scan is insensitive to the geometrical distortion of the image, providing a good geometrical reference for other images to register on. Therefore, other anatomical/parametric images can be fused to the spatial locations indicated by the CT images, allowing the external beam delivery to be precisely controlled. In this work, the CT images were acquired from the GE Lightspeed CT simulator (section 5.3.1.1).

Lastly, once the combined MRE/MRI scans and CT scan are sequentially obtained, the MRE/MRI images will be fused to the CT images using Eclipse treatment planning software. Then, an external beam radiation treatment will be planned utilizing volumetric modulated arc therapy (VMAT). VMAT is a sophisticated radiation delivery technique that achieves a conformal dose distribution, boosting the dose on the targets while reducing the dose on the surrounding healthy tissue or OARs as illustrated in Figure 5.10. This procedure has been shown to be an effective treatment strategy for prostate cancer with DILs defined [123]. The principle and technical realization of VMAT are beyond the scope of this thesis, but a detailed review of VMAT can be found in [118].

In this work, all the contouring of the volumes and the VMAT planning were performed within the Varian Eclipse treatment planning system. The plan was designed such that the DILs were boosted as defined by the MRE scans.

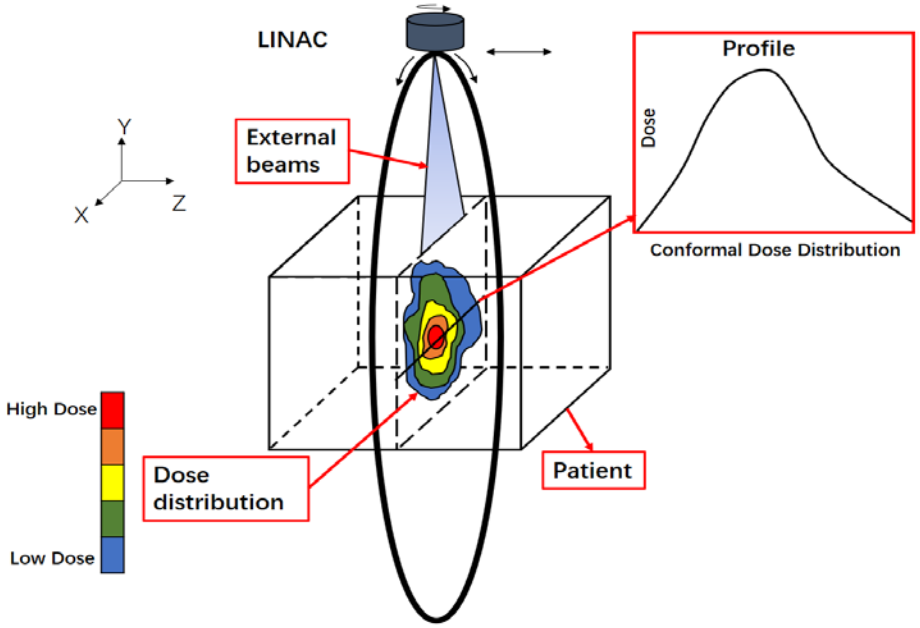

Figure 5. 10 Fundamental principles and technical realization of VMAT.

5.3.1.3.2. 3D Simulation

To achieve a more realistic simulation, several anatomical structures adjacent to the prostate—such as femur, bladder, and rectum—were simulated using CT data as shown in Figure 5.11. Such anatomical structures are categorized as OARs in the radiation therapy for prostate cancer, and each bears a different dose limit (see Appendix B). These CT-simulated anatomical structures were combined with the comprehensive data scanned on the prostate phantom to simulate a more realistic scenario for treatment of a patient with prostate cancer. This process can further validate the potential feasibility and safety of the proposed MRE-integrated RT procedure.

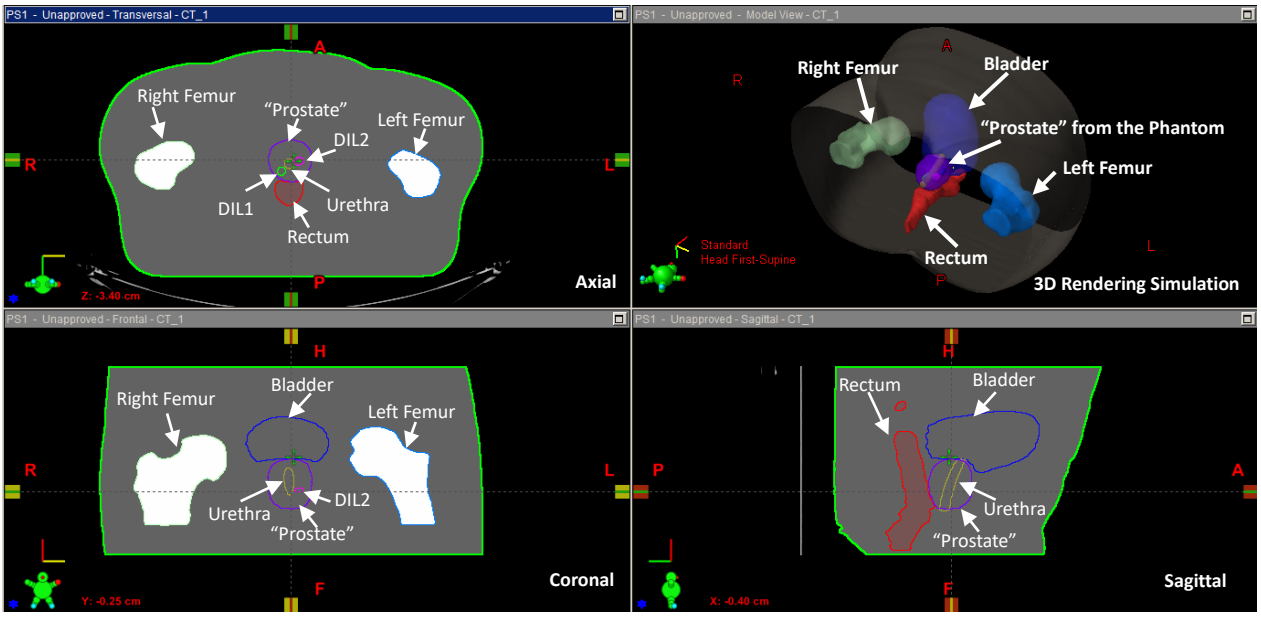

Figure 5. 11 Combined data integrated with the introduction of femurs, rectum, and bladder to provide a more realistic simulation.

5.3.1.3.3. Prostate's and DILs' Delineation

Due to the potential movements of the prostate along with the DILs during the treatment process, during the treatment planning process, additional margins are added to the periphery of the prostate volume to account for patient motion. In addition, the DILs might independently experience the potential movements as well, likewise additional margins we added to the periphery of the DIL volumes to assure the DILs to effectively receive the radiation boost. These margins help define a planning target volume (PTV) which tolerates the uncertainties in patient setup [130]. The volume encapsulating the whole prostate with the margins is defined as PTVp in this study; while the volume encapsulating all the DILs with the margins is defined as PTVd in this study; and in this case, PTVp overlaps and includes PTVd. According to the Saskatchewan Cancer Agency's (SCA) guideline of VMAT treatment planning for prostate (see Appendix B), with the aid of the treatment planning system (TPS), the prescription dose was 78 Gy[9] in 39 fractions to PTVp. Bauman et al., in their 2013 review paper, proposed a dose escalation strategy which boosted the DILs up to 94.5 Gy [131]. In this work, the PTVd was escalated to a maximum boost dose of 84 Gy. The implemented planning procedure in this study is presented in Table 5.1. The novelty of this study is using the MRE-defined DILs to create a more precisely targeted PTV that receives the boosted dose.

[9]"The SI derived unit used to measure the energy absorbed by a substanceper unit weight of the substance when expo sed to radiation. One gray isequal to one joule per kilogram, or 100 rads. The gray is named after British physicist Louis Harold Gray (1905-1965)"—gray. Dictionary.com. *The American Heritage® Science Dictionary*. Houghton Mifflin Company. http://www.dictionary.com/browse/gray (accessed: March 14, 2017).

Table 5. 1 Implemented VMAT planning procedure for prostate

Step	Action	Operations
1	Add margins to the prostate defining a planning target volume—PTVp	• Add 5 mm to an inferior direction; • Add 7 mm to superior, anterior, posterior, left, and right directions.
2	Add margins to the DILs identified by MRE defining another planning target volume—PTVd	• Add 3 mm to all the directions including inferior, superior, anterior, posterior, left, and right directions [131].
3	Perform the treatment planning	• Place external beams (three); • A prescribed dose of 78 Gy to PTVp; • A prescribed dose of 84 Gy to PTVd for boosting; • Treatment parameter optimization.
4	Plan normalization	• 100% to target mean.

5.3.1.3.4. Evaluation Method of Radiation Therapy Plan

In this work, a dose-volume histogram (DVH) was reported for examining if the doses of all the target and OAR volumes were well within the normal tissue tolerance guidelines (see Appendix B, Table B.2). To evaluate the effectiveness of the planning, the conformity index was calculated for the prostate and DILs, respectively [132]–[134]. The conformity index is used to evaluate the dose conformity of the VMAT in daily practice. The Conformity Index (CI) proposed by the Radiation Therapy Oncology Group (RTOG) in 1993 is defined as

$$\mathrm{CI} = \frac{\mathrm{V_{RI}}}{\mathrm{TV}}, \tag{5.1}$$

where $\mathrm{V_{RI}}$ represents the volume of the reference dose and TV denotes the target volume. If the conformity index equals to 1, it suggests that the treatment plan achieve an ideal conformation; if the conformity index is greater than 1, it suggests that the irradiated volume is greater than the target volume and includes healthy tissues; and if the conformity index is less than 1, the target volume is only partially irradiated [132]. However, the conformity index's ideal value, 1, is difficult to obtain in practice [132]. Because of this, according to the RTOG, if the CI is between 1 and 2, the treatment is considered as expected; ranges of 2–2.5 and 0.9–1 are considered as a minor violation; a CI below 0.9 or above 2.5 is considered a major violation [132]–[134].

5.3.2. Results and Discussion

5.3.2.1. Part 1 Establishment of Qualified Elastograms for Radiation Therapy

Prior to the panel tests, a multi-slices high resolution axial T2W scan was obtained to present a clear anatomical delineation of the phantom. Figure 5.12 (A) and (B) show the slices clearly displaying the ROIs of the phantom, and the panel tests were carried out on these slices. The following imaging parameters for the T2W scan were used: FOV = 300*243.75 mm^2, slice thickness = 5 mm, resolution = 512*416, voxel size = 0.59*0.59*5 mm^3, the time to echo (TE) = 101 ms, and the time to repetition (TR) = 7580 ms.

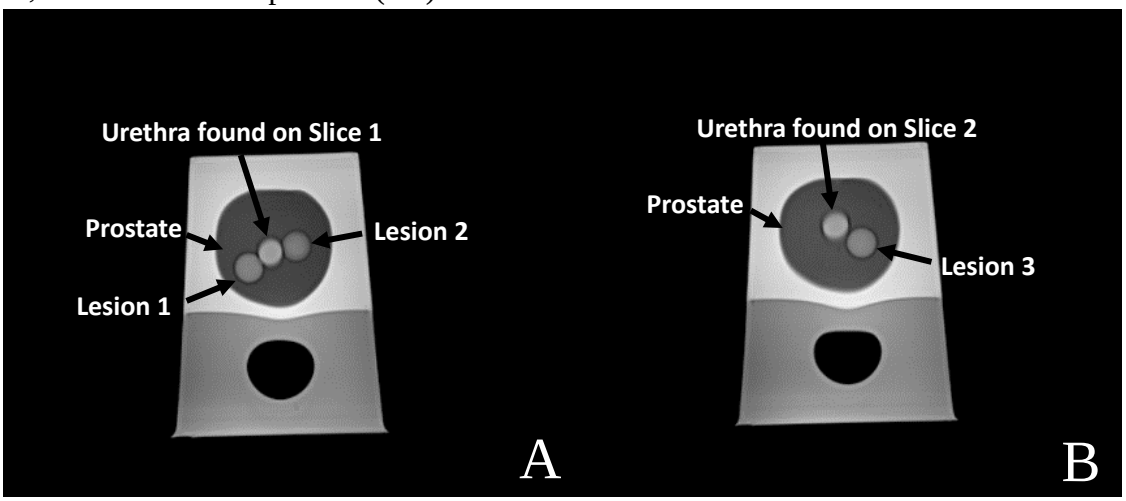

Figure 5. 12 Axial T2W images at (A) slice 1 where two lesions and a urethra were found, and at (B) slice 2 where a lesion and a urethra were found.

The panel tests for MRE were divided into two levels—coarse and fine tests. The coarse tests were set at a larger interval of frequency with all possible amplitudes to search for the optimal frequency range. The fine panel tests with a smaller interval of frequency helped to narrow down the frequency range so that reasonable ranges of amplitude and frequency can be pinpointed to obtain high quality MRE data. The data acquired from the MRE scan was subject to the pre-processing, the calculation of the stiffness map, and the post-processing steps as described above.

The results of the coarse panel tests of the two slices are shown from Figure 5.13 to Figure 5.15. Figure 5.13 (A) and (B) are stiffness maps, and Figure 5.14 (A) and (B) are stiffness maps fused with the T2W images. Under the multi-frequency and multi-amplitude tests, all the hard lesions and the urethra, both described as stiff by the manufacturer, are detected by MRE within the corresponding regions in the T2W image (Figure 5.14 (A) and (B)) even though they are presented at different qualities. The scale bar under each frequency is tuned to present the best qualitative results of the stiffness map, since a target's elasticity distribution revealed by MRE is dependent on the relative dimensions of the target versus the varied wavelength within the target according to the quality assurance measurements on the QA phantom from Chapter 4, sections 4.5.2.1. and 4.5.2.2. Figure 5.15 (A)–(D), respectively, show the mean HD, aveHD, 95%HD, and

DS (all with standard deviations) of all five ROIs that include lesions 1, 2, 3 and the urethra found on slices 1 and 2, as indicated in Figure 5.12. Given the performance of both qualitative and the quantitative evaluations, it can be speculated that the potential optimal frequency range is around 60 Hz and that the MRE has a superior image quality, including better shape and location matches to the anatomical reference, with fewer artifacts on the background, and a lower mean HD, aveHD, and 95%HD and a higher mean DS than other frequency settings (90 and 120Hz). At the same relatively higher amplitude (50%, 70%, and 90%), the quantitative evaluation at 120 Hz shows a better performance than the evaluation at 60 Hz, that is, the lesions and urethra identified at 120 Hz appear to be located more precisely than the targets at 60 Hz. However, the evident artifacts at 120 Hz severely degrade the quality of the stiffness map. Therefore, the qualitative and quantitative evaluations should be combined for considerations. Above 120 Hz the signal attenuation becomes significant, similar to the pattern observed on the QA phantom tested in Chapter 4.

The best MRE data are generated at 60 Hz with 10% amplitude. However, the results in Chapter 4 suggest that small ROIs have sensitive frequency requirements. Therefore, it is worthwhile to explore whether a smaller frequency interval around 60 Hz will yield a better MRE result. Thereby, a further detailed investigation of both frequency and amplitude should be undertaken.

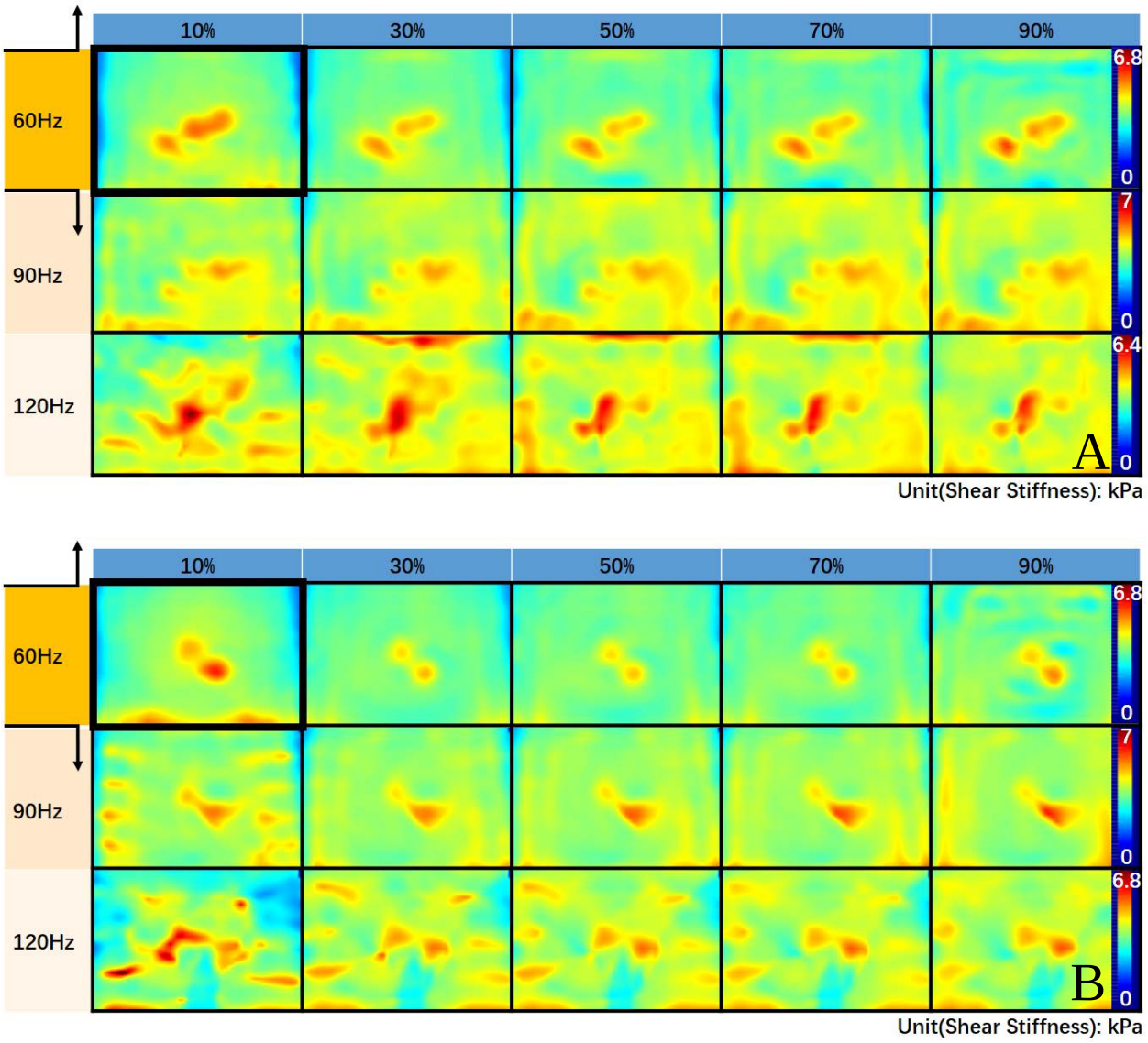

Figure 5. 13 Qualitative results and analyses of coarse panel tests. **(A)** Stiffness maps of slice 1; and **(B)** stiffness maps of slice 2. (MRE scans: FOV = 300*243.75 mm^2, slice thickness = 10 mm, resolution = 256*208, voxel size = 1.17*1.17*10 mm^3. All the results demonstrated here were windowed out for presentation)

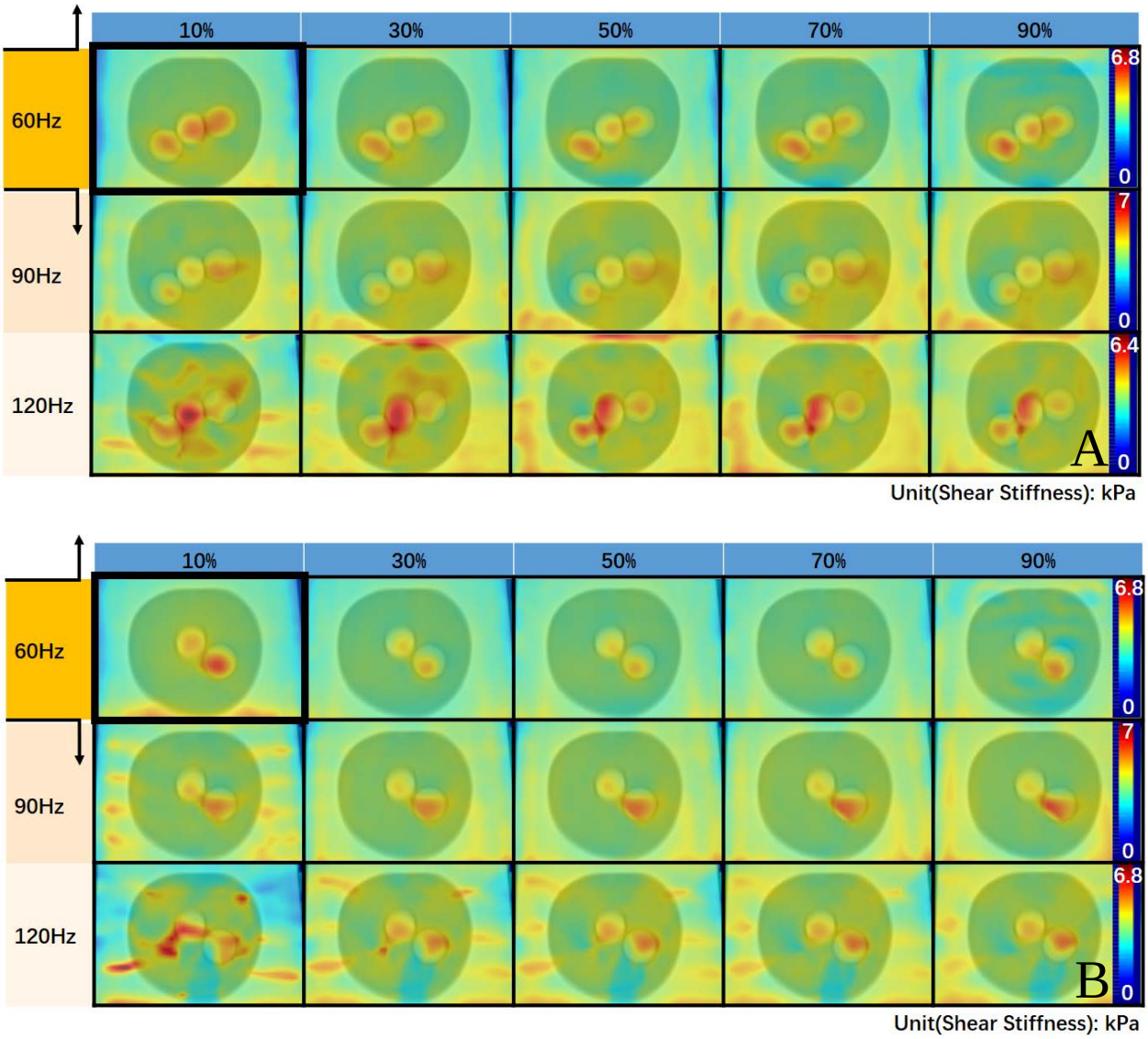

Figure 5. 14 Qualitative results and analyses of coarse panel tests. **(A)** Stiffness maps of slice 1 fused with the axial T2W anatomical reference; and **(B)** stiffness maps of slice 2 fused with the axial T2W anatomical reference.

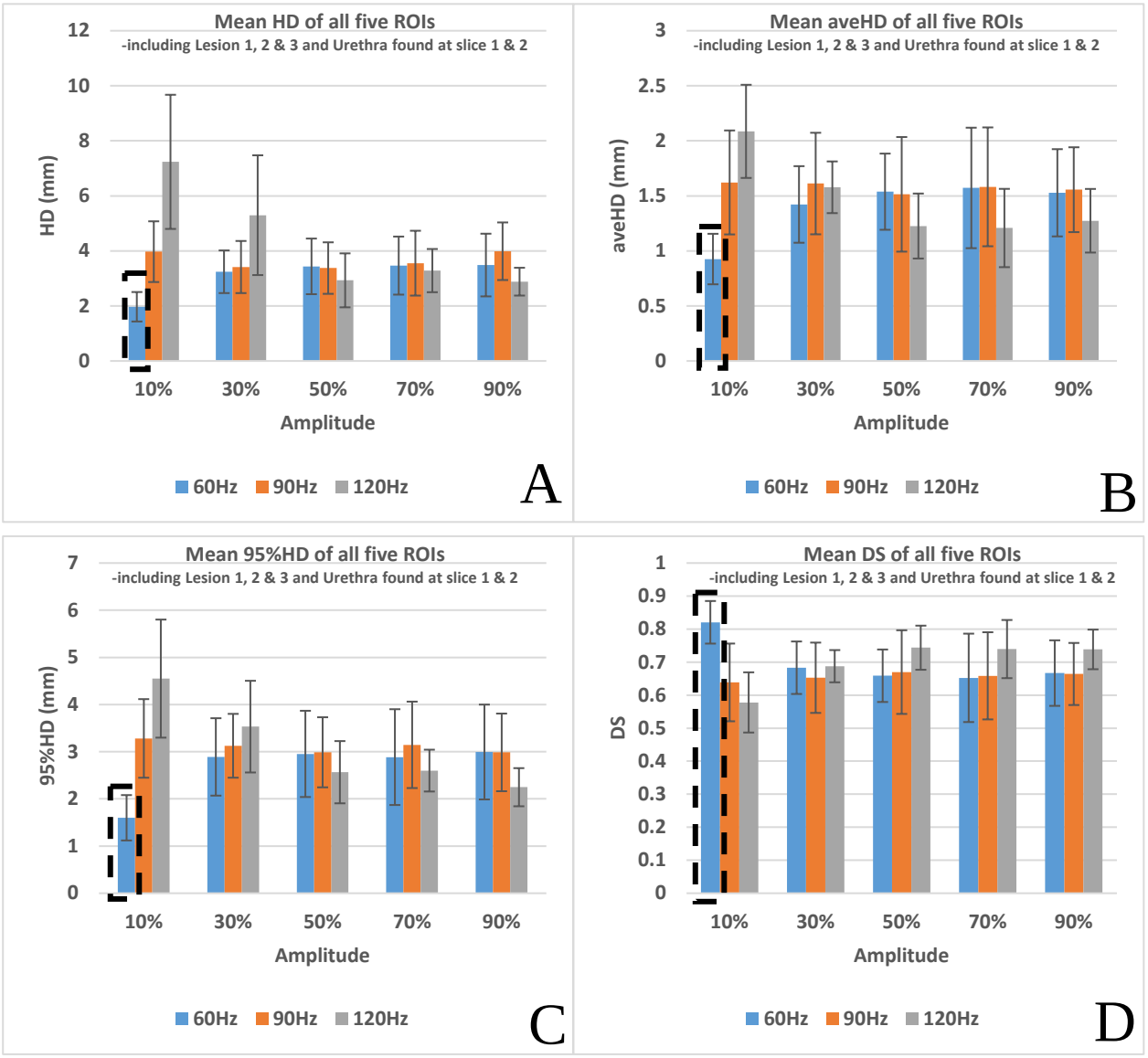

Figure 5. 15 Quantitative results and analyses of coarse panel tests. **(A)** The mean HD of all five ROIs, including lesions 1, 2, and 3, and the urethra found at slices 1 and 2; **(B)** The mean aveHD of all five ROIs, including lesions 1, 2, and 3, and the urethra found at slices 1 and 2; **(C)** The mean 95%HD of all five ROIs, including lesions 1, 2, and 3, and the urethra found at slices 1 and 2; and **(B)** the mean DS of all five ROIs, including lesions 1, 2, and 3, and the urethra found in slices 1 and 2.

To determine the best frequency/amplitude combination, fine panel tests were performed with a shorter interval (10 Hz) of the frequency as shown from Figure 5.16 to Figure 5.18. In Figure 5.16 (A) and (B), the difference in MRE scan quality is significant at smaller frequency intervals, indicating that the fine panel test is necessary. Conclusions obtained from QA measurements in Chapter 4 can be used as a guideline to determine the optimal parameters. For instance, with an increase in frequency, wave attenuation begins, leading to artifacts in the scan, and as the amplitude

is strengthened, the artifacts caused by the wrapped phases become severe. Similar conclusions can be drawn from the results of the fine panel tests shown in Figure 5.16 (A) and (B). In Chapter 4 it was shown that phase wrapping is incurred by a high amplitude in the wave signal set at the driver, ultimately leading to artifacts on the stiffness map. Previous experiments showed that attenuation of the wave signal occurs at high frequency, causing artifacts on the stiffness map as well. In summary, the essential factor producing artifacts is the signal intensity of the propagating wave (in the phantom or tissue). Nevertheless, the effects brought by amplitude and frequency can counteract each other to some degree because enhancing the amplitude improves the propagating wave intensity, while increasing the frequency brings it down. In Figure 5.16, 50 Hz/90% and 80 Hz/10% are the two extreme cases of frequency/amplitude conditions, providing the strongest and the weakest propagating wave intensities, respectively. The former is affected the most by the phase wrapping and the least by the signal attenuation, and the latter is affected the most by the signal attenuation and the least by the phase wrapping. The artifacts from the high frequency/low amplitude degrade the quality of the stiffness map more on the background, whereas the artifacts from the low frequency/high amplitude not only affect the background but also distort the ROIs.

However, by combining both the qualitative and the quantitate evaluations from Figure 5.17 (A) and (B) and Figure 5.18 (A)–(D), superior results are found in the 60–70 Hz range, under a low amplitude of 10–30%. Similar to the conclusions in Chapter 4, section 4.5.2.2, a higher frequency will enhance the quality of the MRE data because a higher frequency allows more wavelengths or a more complete wavelength to be included within a specific area, which is informative for the inversion algorithm to calculate the stiffness map, reflecting the elasticity distribution. More specifically, as shown in Figure 5.17 (A) and (B), the ROIs detected by MRE gradually show closer matches in size, shape and location to the ROIs delineated by T2 axial scans when the frequency rises from 50 Hz to 70 Hz. However, the quality of the stiffness map is reduced when the frequency is increased over a limit, because the higher the frequency, the weaker the intensity of the propagating wave, making the background noise more evident, as shown in Figure 5.16 (A) and (B). That is, as shown at 70–80 Hz from the fine panel test in Figure 5.16 (A) and (B) or at 60–120 Hz from the coarse panel test in Figure 5.13 (A) and (B) (or even in a direct comparison of 70 Hz, 80 Hz, 90 Hz, and 120 Hz in Figure 5.13 and Figure 5.16), all kinds of artifacts or mal-matches (in shape or location) start showing up when the frequency is increased.

Combined with the qualitative and the quantitative analyses, the best candidates of MRE images were obtained at the settings of 60Hz/10%, 70Hz/10%, and 70Hz/30%, as highlighted by the black bold solid blocks from Figure 5.16 to Figure 5.18. In addition, for the settings of 60Hz/10%, 70Hz/10%, and 70Hz/30%, Figure 5.18 reports a comparable match accuracy between the segmentation to the T2 images and the segmentation to the elastograms considering the diameter of the DILs and urethra are 10 mm in axial view (especially for the mean aveHD measures with standard deviation which are under 1.5 mm). Once the optimal scan settings for MRE are determined through the panel tests, these parameters can be prescribed to the multi-slice MRE scan

across the whole prostate, collected as a 3D volume represented by elasticity for the subsequent radiation therapy procedure.

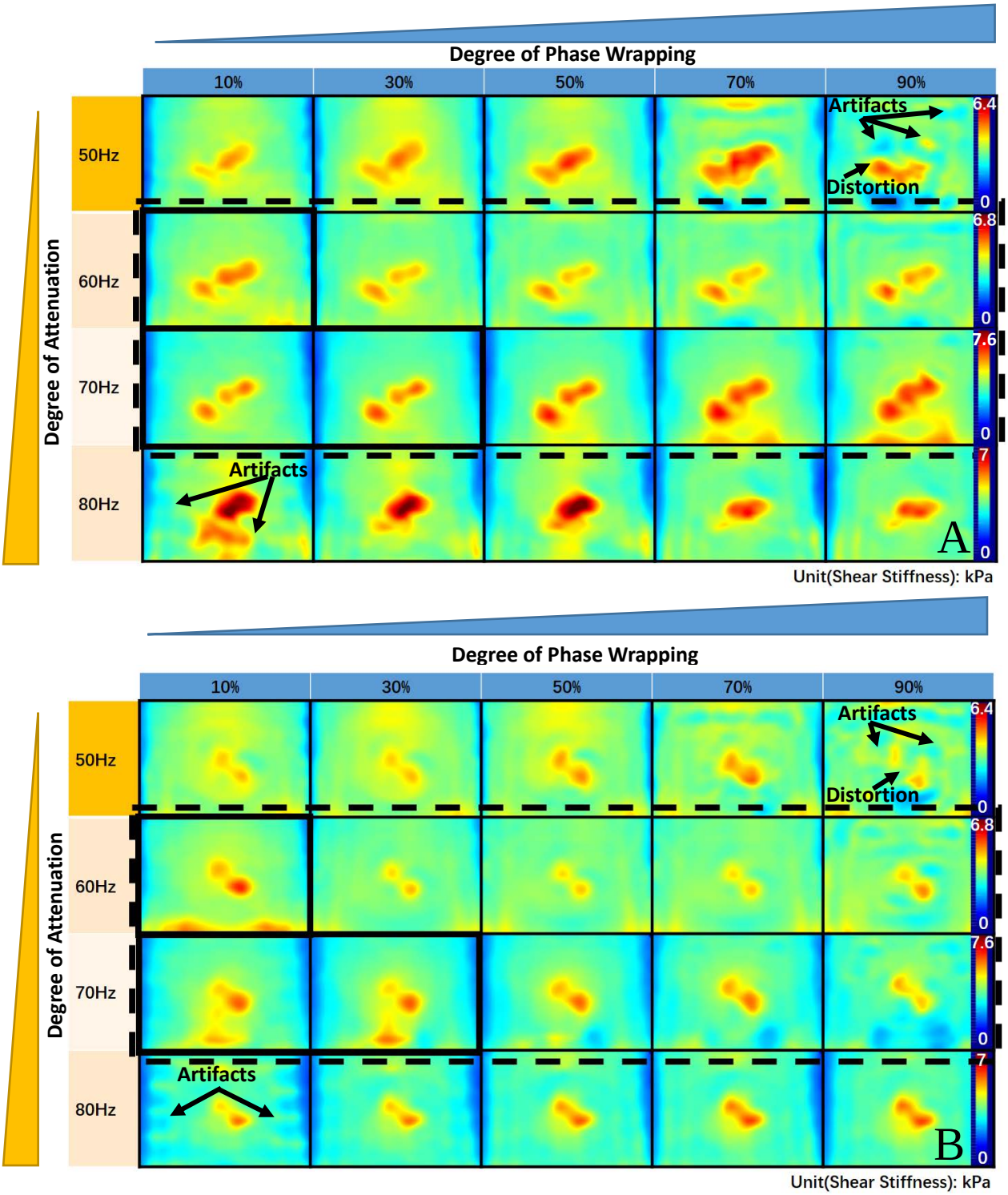

Figure 5. 16 Qualitative results and analyses of fine panel tests. **(A)** Stiffness maps of slice 1; and **(B)** stiffness maps of slice 2. (MRE scans: FOV = 300*243.75 mm^2, slice thickness =10 mm, resolution = 256*208, voxel size = 1.17*1.17*10 mm^3. All the results demonstrated here were windowed out for presentation)

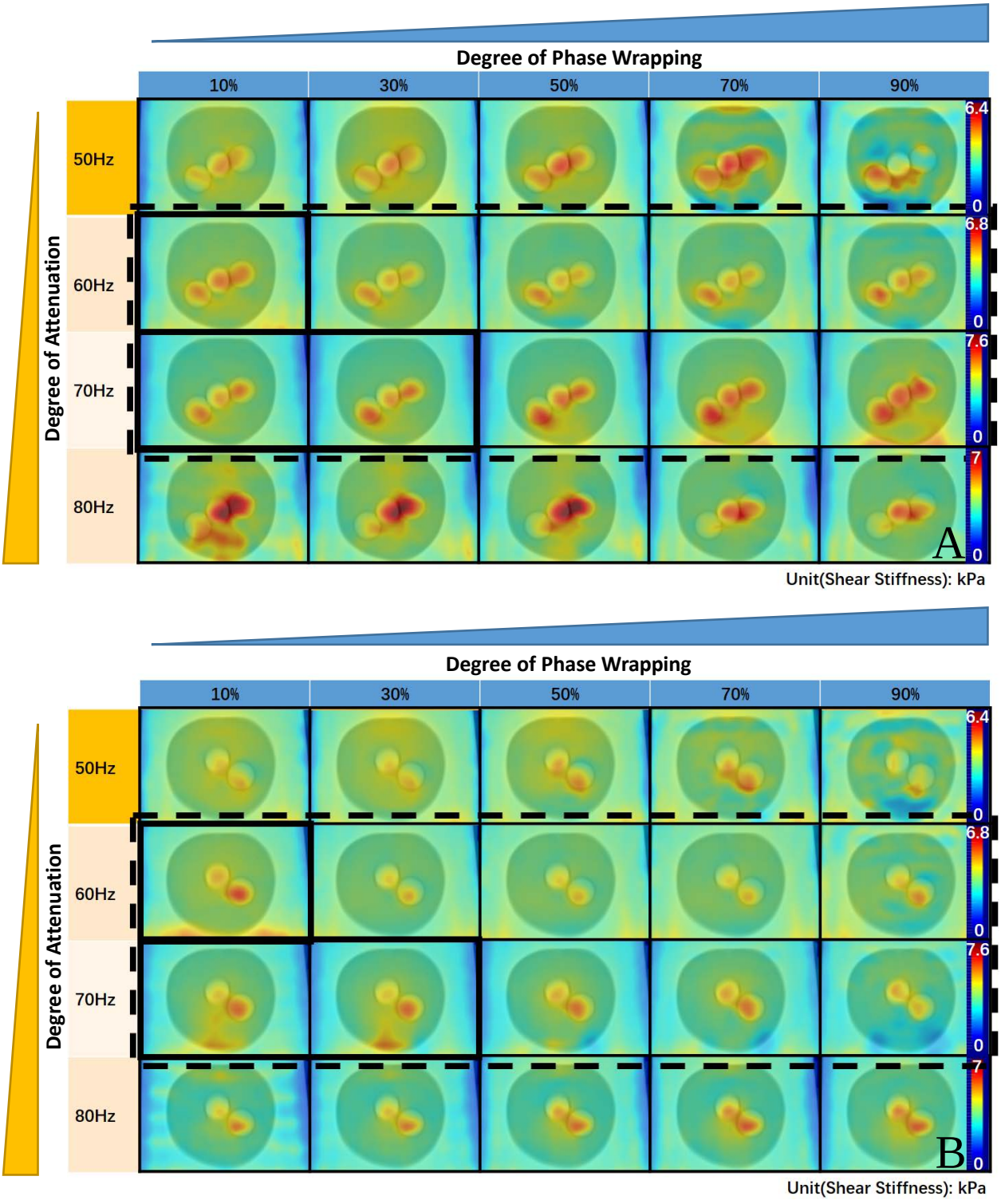

Figure 5. 17 Qualitative results and analyses of fine panel tests. **(A)** stiffness maps of slice 1 fused with the axial T2W anatomical reference; and **(B)** stiffness maps of slice 2 fused with the axial T2W anatomical reference.

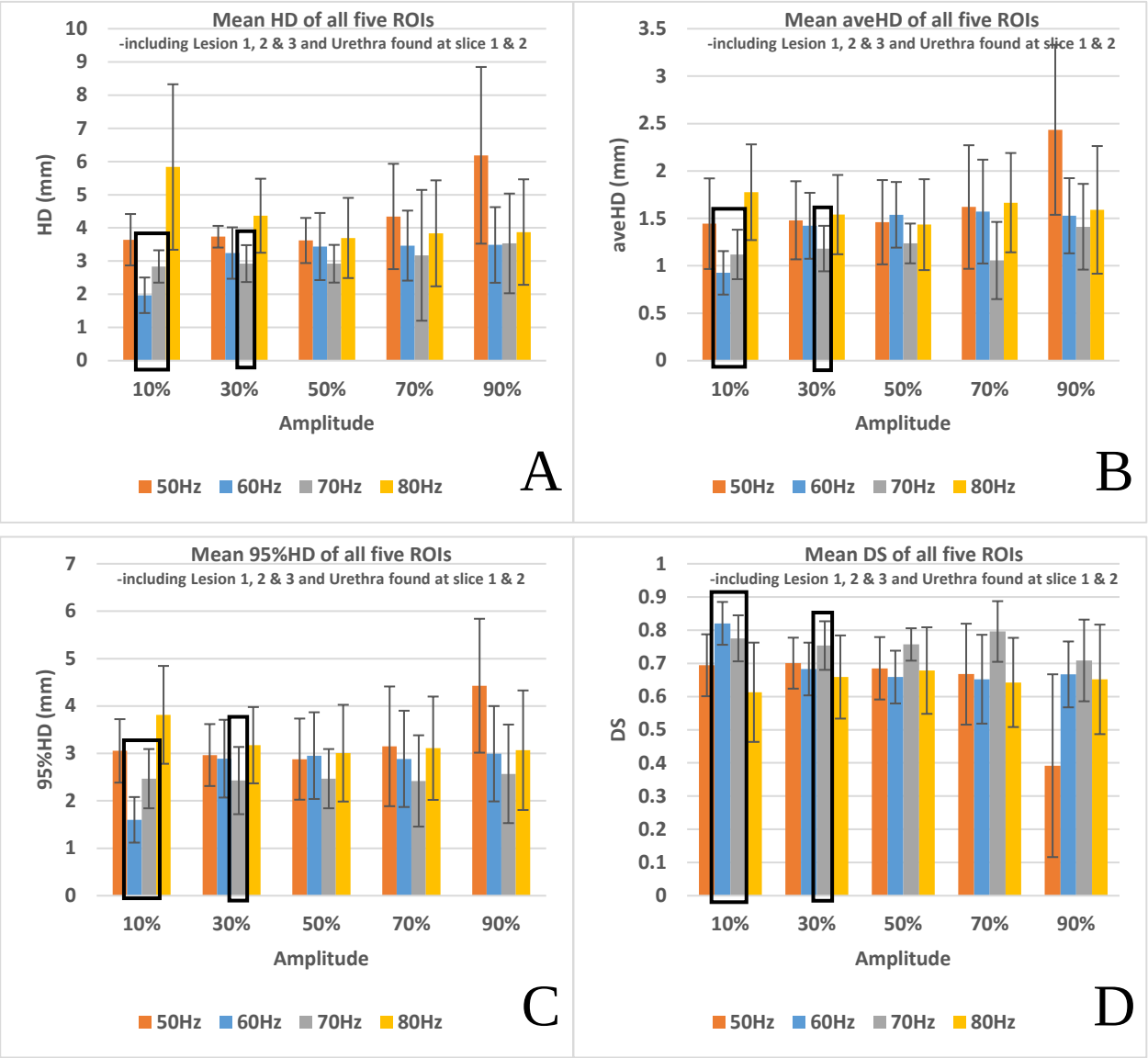

Figure 5. 18 Quantitative results and analyses of fine panel tests. **(A)** The mean HD of all five ROIs, including lesions 1, 2, and 3, and the urethra found at slices 1 and 2; **(B)** The mean aveHD of all five ROIs, including lesions 1, 2, and 3, and the urethra found at slices 1 and 2; **(C)** The mean 95%HD of all five ROIs, including lesions 1, 2, and 3, and the urethra found at slices 1 and 2; and **(D)** the mean DS of all five ROIs, including lesions 1, 2, and 3, and the urethra found in slices 1 and 2.

5.3.2.2. Part 2 Proposed MRE-Integrated Radiation Therapy Planning

Figure 5.19 shows the results of the proposed comprehensive volume scan protocols combining routine MRI, MRE, and CT. The optimal parameters pinpointed by the panel tests are propagated to the MRE volume scan. Figure 5.19 (A) shows the results of the routine MRI and CT

scans. The following imaging parameters for the routine MRI scan were used: FOV = 300*243.75 mm^2, slice thickness = 5 mm, resolution = 512*416, voxel size = 0.59*0.59*5 mm^3, TE/TR = 101/7580 ms; the following imaging parameters for the CT scan were used: slice thickness=2.5 mm, resolution = 512*512, voxel size = 0.98*0.98*2.5 mm^3; and the following imaging parameters for MRE scans were used: FOV = 300*243.75 mm^2, slice thickness = 5 mm, resolution = 256*208, voxel size = 1.17*1.17*5 mm^3.

Figure 5.19 (B), (C), and (D) show that the ROIs on each slice are successfully detected by the MRE scans using the optimal parameters. That is, all the ROIs identified by the MRE scans show relatively higher stiffness values than the prostate, which meets with the description provided by the manufacturer. After the registration operation, the three groups of data mutually demonstrate a good match in the ROIs' location, shape, and size on each slice. The integrated data include the anatomical delineation, the dose information, and the mechanical properties (the elasticity information)—fused as a comprehensive block of information—for each individual ROI spotted on each plane. Though the relationship between this comprehensive information (especially for the stiffness map) and the pathologic state of the tissue or organ need to be further studied through *in vivo* clinical investigations, these comprehensive scan protocols can provide a promising way to multiple parametric assessments in the detection and diagnosis of tumours, particularly for prostate tumours where the DILs are usually harder than the surrounding normal tissue.

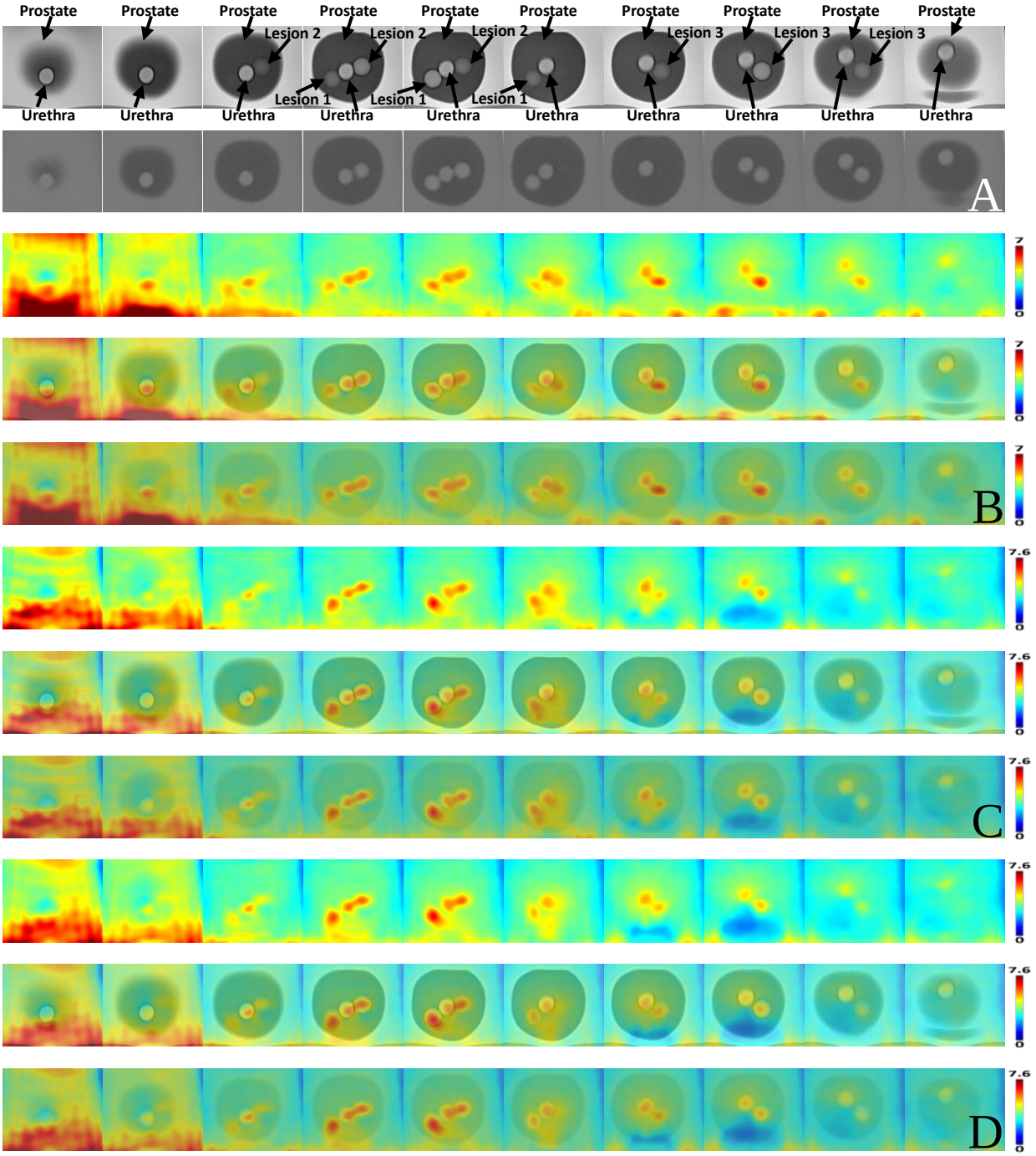

Figure 5. 19 (A) Anatomical reference – multi-slice axial T2W images and CT images across the prostate volume; **(B)** stiffness maps, fusions with the T2W images, and fusions with the CT images—60 Hz/10%; **(C)** stiffness maps, fusions with the T2W images, and fusions with the CT images—70 Hz/10%; and **(D)** stiffness maps, fusions with the T2W images, and fusions with the CT images—70 Hz/30%. All the results demonstrated here were windowed out for presentation.

A slice-by-slice inspection of all the ROIs scanned by the comprehensive scan protocols is necessary for the subsequent 3D volume alignment that will be used in planning treatment. Figure 5.20 (A) and (B) show that with the aid of the 3D Slicer, after registration, the ROIs of the aligned MRE volume from one of the candidates at 70 Hz frequency and 30% amplitude in sagittal and coronal views are clearly revealed and closely matched to both the co-registered T2W and CT volumes in the same views. Thus, MRE data can help identify DILs and contribute to the treatment planning by defining the tumours with elasticity information. The anatomical delineation, dose information, and elasticity information of the volumes-of-interest in the prostate phantom are successfully defined; they are available to be inspected in all three anatomical views and are ready to be imported to the TPS. For better visual perception, the MRE volume can be rendered into a 3D model as shown in Figure 5.20 (A) and (B).

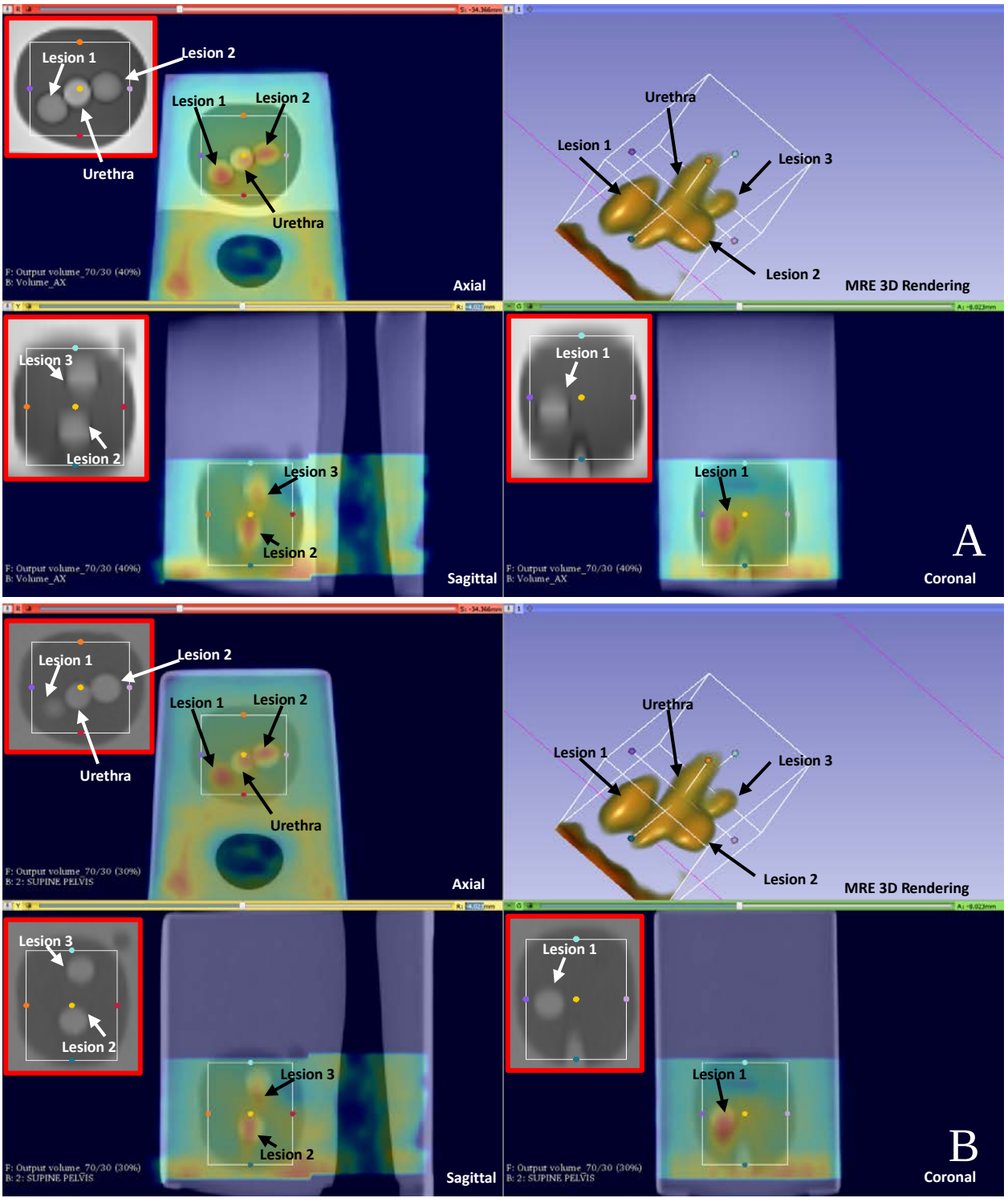

Figure 5. 20 (A) The stiffness volume fused with the T2W volume in three views, and the MRE 3D rendering; and **(B)** the stiffness volume fused with the CT volume in three views, and the MRE 3D rendering.

The data volumes were imported to the TPS for image fusion and treatment planning. After all the scanned data (MRI, MRE, and CT) were imported to the TPS, the MRI and the MRE data were registered and fused to the CT images. Figure 5.21 shows the MRE data that were imported to the TPS; after the registration, the DILs were detected and defined in the MRE data by the auto-contouring function. Under this auto-contouring function, the three DILs were segmented as shown in Figure 5.21 (A) and (B). The CT data reports that each DIL's volume is 0.94 cm^3; by contrast, the MRE data reports that DIL1's, DIL2's, and DIL3's volumes are 0.44 cm^3, 0.22 cm^3, and 0.31 cm^3 after the auto-contouring. If approximating all the DIL volumes (in the CT and the MRE data) to globes, the diameter of each DIL volume can be estimated: in the CT data, each diameter of the defined DILs is 1.21 cm; while in the MRE data, the diameters of the defined DILs are respectively 0.94 cm, 0.74 cm, and 0.83 cm. According to the manufacturer, each DIL in this phantom is approximately 1.00 cm in diameter. These results are summarized in Table 5.2 and show that the DILs' diameters reported by the CT and the MRE data are close to the manufacturer's report, even though the difference among the DILs are significant when comparing them in the volume. In summary, the MRE data slightly underestimates the DILs' volumes but does not significantly affect to use them in the treatment planning, since the added margins around the DILs can tolerate this underestimation. However, the cause of this underestimation might be due to the auto-contouring function in defining the DILs; specifically, there are no sufficient data to explicitly state that what is the most reasonable cut-off elasticity value for defining DIL in prostate cancer, currently. This suggests that in the future work, more *in vivo* experiments are needed to investigate the relation between the elasticity value and the pathology state of prostate tissue. However, the focus of this study is to investigate the potential feasibility of the dose boost in the MRE-defined DIL volumes. In addition, in this study, the anatomical delineation of ROIs with MRI data increases the credibility of the DILs' definitions, and the CT data indicates the precise treatment locations and aid the dose calculation.

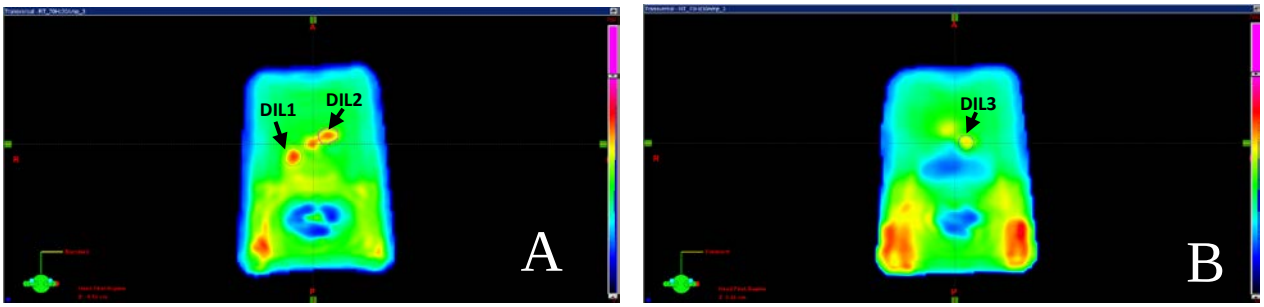

Figure 5. 21 MRE data imported to the TPS; DILs are detected and defined in the MRE data by the auto-contouring function. **(A)** the slice where the DIL1 and DIL 2 are found; **(B)** the slice where the DIL3 is found.

Table 5. 2 Comparison of the DILs' diameters and volumes among in the CT data, MRE data, and manufacturer's report

	CT data			MRE data			The manufacturer's report		
	DIL1	DIL2	DIL3	DIL1	DIL2	DIL3	DIL1	DIL2	DIL3
Diameter* (cm)	1.21	1.21	1.21	0.94	0.74	0.83	1.00	1.00	1.00
Volume* (cm^3)	0.94	0.94	0.94	0.44	0.22	0.31	0.52	0.52	0.52

*All the DILs are approximated to globes.

Figure 5.22 shows that the dose boost within the PTVd region encapsulating the DILs was successful by using the VMAT treatment planning. That is, in the axial, coronal, and sagittal views, all the PTVd regions were boosted to a relatively high dose distribution (indicated by the red color); while PTVp, which includes the whole prostate, was kept at a relatively low dose with a uniform distribution (indicated by the green color).

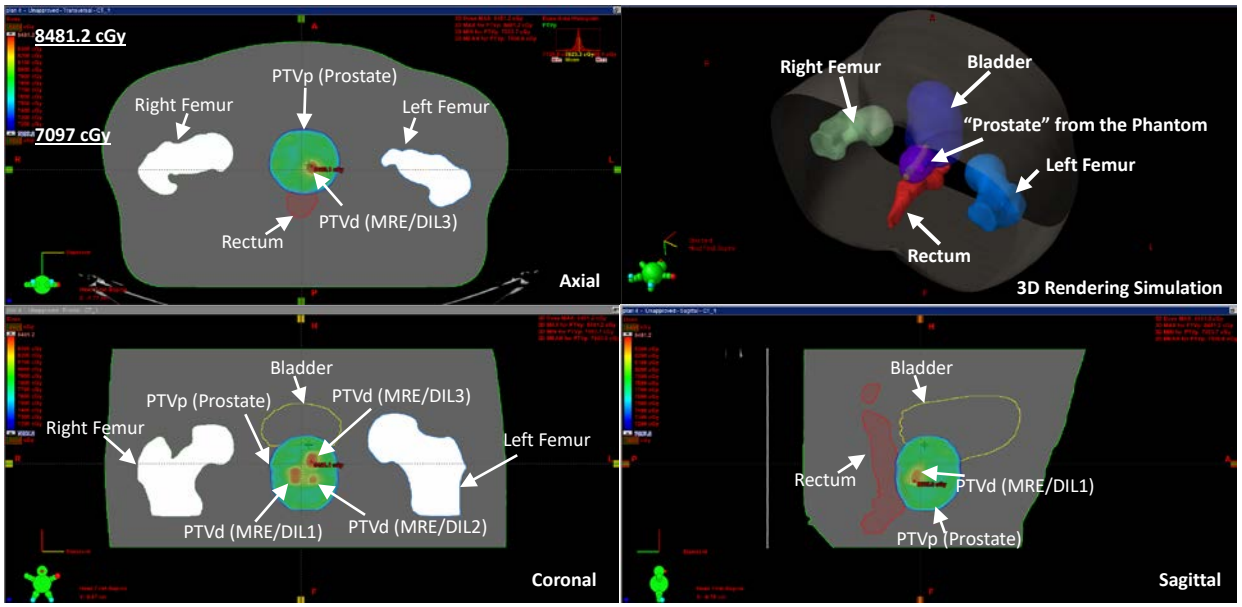

Figure 5. 22 Dose distribution of using the VMAT treatment planning for prostate. Dose range displays from 70.97 Gy (91.0% of the prescribed dose) to 84.81 Gy (108.7% of the prescribed dose).

To inspect if the implemented treatment planning complied with the safety requirements in the Saskatchewan Cancer Agency, a DVH was as reported showing in Figure 5.23. Figure 5.23 shows that each OAR including the rectum, bladder, and both femurs has a rapidly descending ratio of (its) total structure volume with the growth of dose, and in the relatively high dose range (above around 7500 cGy), they have a significantly low ratio of total structure volume. More specifically, referring to Table 5.3's standard constraints, Figure 5.23 reports that all the critical targets and OARs are under the dose limits formulated by the Saskatchewan Cancer Agency, and the exact

dose values are listed in Table 5.3's measurements. This suggests that the implemented treatment planning satisfy the safety requirements.

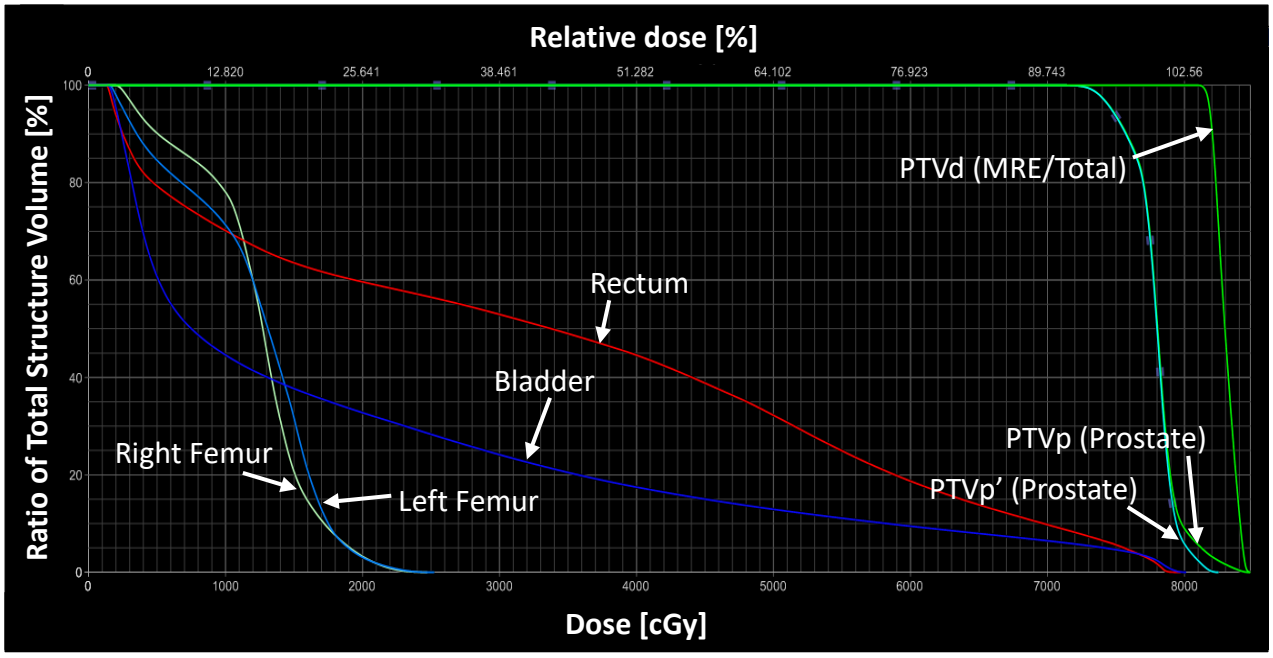

Figure 5. 23 DVH of the targets and OARs. PTVp' defines a volume that is equilvant to PTVp excluding PTVd, but in treatment planning, we usually evaluate PTVp.

Table 5. 3 Dose limits for the targets and OARs (Subjected to the protocol of VMAT treatment planning for prostate in Saskatchewan Cancer Agency, Saskatoon, SK, Canada**)**

Importance	Structure	Standard Constraints	Measurements (From the DVH)
1	PTV (for the prostate, i.e., PTVp)	D_{max} (*) ≤ 107-110%	D_{max} = 108.7%
		Mean ≥ 100%	Mean = 100%
2	Rectum	V_{75Gy} (**) ≤ 15%	V_{75Gy} = 5.6%
		V_{70Gy} ≤ 25%	V_{70Gy} = 9.7%
		V_{60Gy} ≤ 35%	V_{60Gy} = 18.7%
		V_{50Gy} ≤ 50%	V_{50Gy} = 32.2%
3	Bladder	V_{75Gy} ≤ 15%	V_{75Gy} = 4.6%
		V_{70Gy} ≤ 25%	V_{70Gy} = 6.4%
		V_{65Gy} ≤ 35%	V_{65Gy} = 7.9%
		V_{55Gy} ≤ 50%	V_{55Gy} = 11.1%
4	R Femoral Head	V_{45Gy} ≤ 10%	V_{45Gy} = 0.0%
		D_{max} ≤ 50Gy	D_{max} = 24.8Gy
	L Femoral Head	V_{45Gy} ≤ 10%	V_{45Gy} = 0.0%
		D_{max} ≤ 50Gy	D_{max} = 25.3Gy

* “D” refers to “Dose”;
** “V” refers to “Volume”.

The SCA usually requires a dose coverage from 95% to 110% of the prescribed dose into the 100% target volume for the prostate treatment planning using VMAT, so Figure 5.24 shows the dose distribution ranging from 95% to 108.7% (the maximum) of the prescribed dose (78 Gy). Observed in the axial, coronal, and sagittal views, Figure 5.24 (A)—(E) qualitatively show that the dose from 95.0% (74.10 Gy) to 108.7% (84.81 Gy) of the prescribed dose well covered PTVp. Figure 5.24 also shows the representative boost results within the DILs in different views: Figure 5.24 (A)—(C) show the boost results in the axial slices containing all the DILs; Figure 5.24 (D) shows the boost results in the coronal slice containing all the DILs; and Figure 5.24 (E) shows the boost results in the sagittal slice containing DIL1. These results show that PTVd encapsulating the DILs were boosted to around 83 Gy, while the peripheral prostate tissues were approximately kept below around 81 Gy. To further analyze the dose distribution, Table 5.4 shows the statistical data of the dose in the boosted targets, the OARs, and the body. The statistical results indicate that the targets’ dose mainly concentrates around 82.6–83.0 Gy (close to the prescribed dose, 84 Gy) based on the mean, modal, and median doses; the prostate’s dose mainly concentrates around 77.8–79.0 Gy (close to the prescribed dose, 78 Gy) according to the mean, modal, and median doses as well, and the prostate’s small standard deviation—1.78 Gy—suggests that this relatively low dose has a uniform distribution over the prostate; and other OAR’s dose are all mainly kept within a significantly low range. To summary, combing the results in Figure 5.24 and Table 5.4, the VMAT

treatment planning can successfully boost the DILs to a relatively high dose but kept the OARs at a relatively low dose.

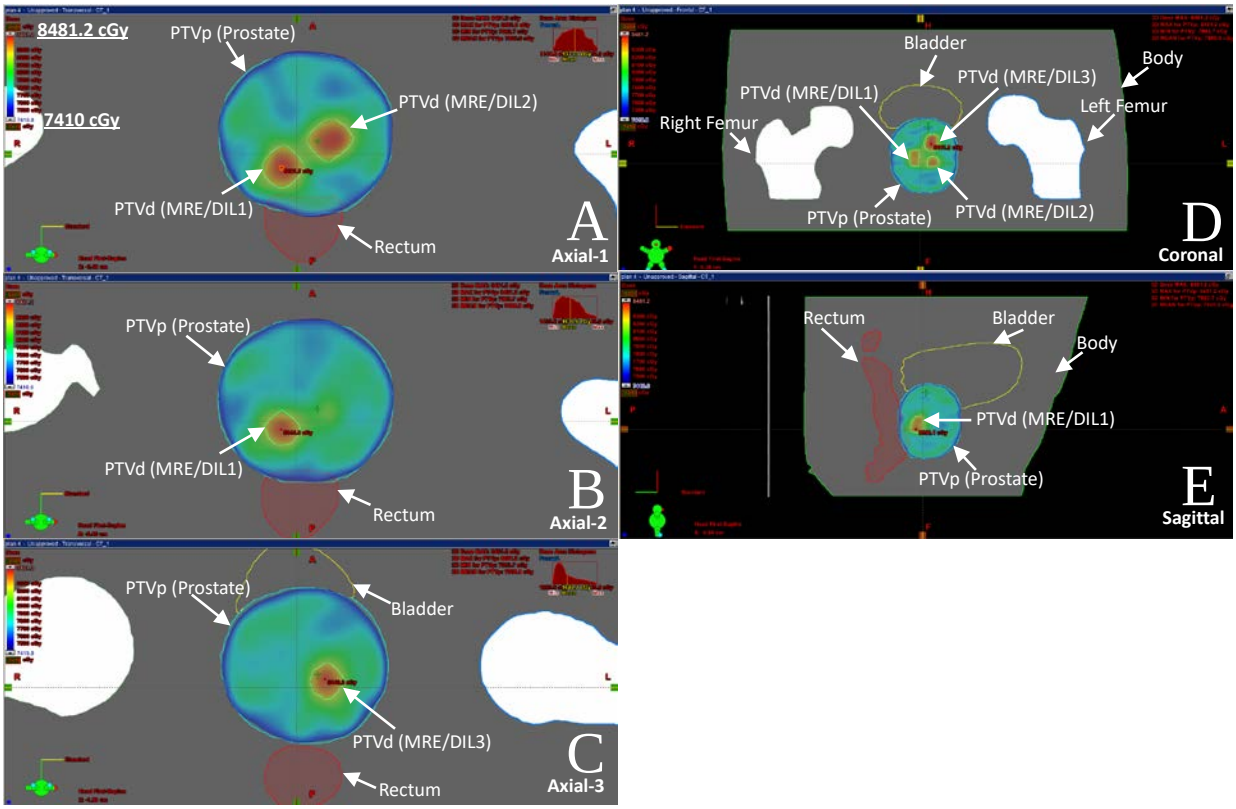

Figure 5. 24 Dose coverage and boost results in different slices and views: **(A)** dose coverage and boost results in the axial slice containing DIL1 and DIL2; **(B)** dose coverage and boost results in the axial slice containing DIL1; **(C)** dose coverage and boost results in the axial slice containing DIL3; **(D)** dose coverage and boost results in the coronal slice containing DIL1, DIL2, and DIL3; and **(E)** dose coverage and boost results in the sagittal slice containing DIL1. Dose range displays from 74.10 Gy (95.0% of the prescribed dose) to 84.81 Gy (108.7% of the prescribed dose).

Table 5. 4 Dose statistics for the targets and OARs

	Structure	Volume (cm^3)	Min Dose (Gy)	Max Dose (Gy)	Mean Dose (Gy)	Modal Dose (Gy)	Median Dose (Gy)	Standard Deviation (Gy)
Targets	PTVd (MRE/total DILs)	5.4	80.90	84.81	83.00	82.56	82.95	0.76
OARs	Prostate	56.5	76.33	84.81	79.02	77.75	78.38	1.78
	Rectum	67.6	1.31	79.75	33.48	1.63	33.78	25.38
	Right Femur	187.6	1.97	24.80	12.21	12.83	12.72	4.27
	Left Femur	194.8	1.52	25.29	12.02	15.10	13.10	5.07
	Bladder	309.1	1.36	80.20	19.35	3.22	7.51	22.33
Total	Body	14103.6	0.05	84.81	8.90	0.55	2.51	13.30

To further investigate the efficacy of the targeted radiation dose escalation, a line profile was drawn across the boosted region as shown in Figure 5.25 (A). Figure 5.25 (B) shows this profile's rapid rise and fall of the dose gradient around PTVd. In addition, Table 5.5 reports the CIs for PTVp encapsulating the prostate and PTVd encompassing the MRE-defined DILs. In Table 5.5, when setting the reference dose as 95% of the prescribed dose, the CI for PTVp is 0.98 which is nearly close to the ideal plan with a CI equal to 1. However, for the DILs, there is currently not a unified standard for selecting the reference dose; when setting the reference dose as 105% of the prescribed dose, the CI for PTVd is 0.91 which still suggests a highly conformal dose escalation.

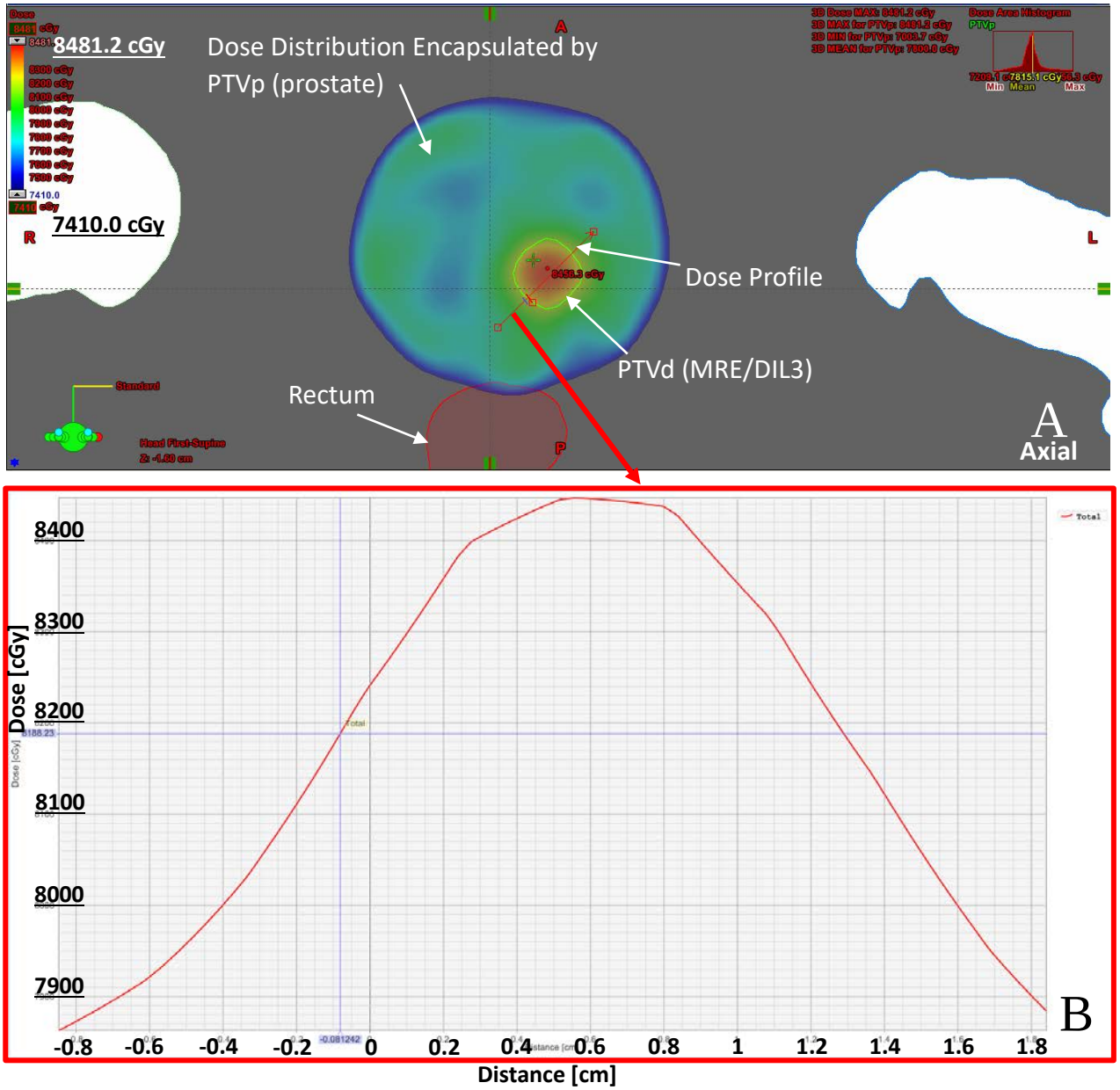

Figure 5. 25 Observation of a line dose profile through the DIL boost region: **(A)** a dose profile through the DIL boost region was drawn in the axial slice containing DIL3; **(B)** the dose profile through the DIL boost region.

Table 5. 5 CI for PTVp (prostate) and PTVd (MRE/total)

Structure	Target Volume (cm^3)	Volume of the reference dose		CI
		reference dose (%/Gy)	Volume (cm^3)	
PTVp (prostate)	160.08	95/74.10	157.02	0.98
PTVd (MRE/total)	5.36	105/82.00	4.86	0.91

5.4. Conclusion

First, it can be concluded that the optimal scan setting for MRE of the most critical parameters—frequency and amplitude—may vary when the scan scenario shifts from one case to another. Therefore, the scan schema of the two-level panel test is a systematic and rapid solution to pinpoint the best scan parameters for MRE.

Second, the proposed MRE-integrated RT framework is able to produce a comprehensive data set including the MRE, MRI, and CT data for the subsequent radiation treatment planning. The MRE data can help to define the DILs for the radiation treatment planning, and the MRI data provides a clear anatomical delineation of ROIs and increases the credibility of the DILs' definitions, and the CT data indicates the precise treatment locations and aid the dose calculation. Subsequently, with the aid of this comprehensive data, using a VMAT technique is able to achieve a highly conformal plan for the prostate phantom embedded with DILs, demonstrating the potential feasibility of using the MRE-integrated comprehensive data for the targeted radiation dose escalation in the DILs.

Chapter 6

Summary, Conclusion, Challenges, and Future Work

Chapter Synopsis

Chapter 6 summarizes the accomplished work in this thesis and the conclusion drawn from the experiment parts. This chapter also states the challenges encountered in this work and discusses the potential future applications of Magnetic Resonance Elastography (MRE) technique.

6.1. Summary of Work

In this work, a commercial Magnetic Resonance Elastography (MRE) system, including a 3T Magnetic Resonance Imaging (MRI) scanner and a Resoundant® driver system, was used to carry out all the MRE scans. Additionally, a works-in-progress (WIP) pulse sequence based on Spin Echo-Echo Planar Imaging (SP-EPI) technique helped to accomplish all the investigation on MRE since it contains a flexible parameter selection feature, such as the frequency of motion encoding gradient (MEG). Moreover, an offline inversion algorithm based on the local frequency estimation (LFE) was adopted to realize the generation of elastograms. These components constitute an available and reliable mechanism to obtain a high-quality elastogram.

The main accomplishments in this thesis are

- The development of a novel, specialized MRE Quality Assurance (QA) phantom (Chapter 4),
- The validation of elasticity imaging and optimization of imaging parameter for the MRE system with this new QA phantom (Chapter 4), and
- The proposition of an MRE-integrated radiation therapy (RT) framework carried out on a prostate phantom (Chapter 5).

6.2. Conclusion

In Chapter 4, the developed QA phantom and QC tests summarized that

- A target's elasticity can be closely reproduced by MRE when its size is relatively larger than the wavelength of the mechanical wave provided by the driver system. When the size of the target is relatively smaller than the wavelength, there will be a deviation in the elasticity value, but the target can still be qualitatively (visibly) detected;
- The applied frequency of the mechanical wave affects the imaging quality of MRE: (1) the improvement of frequency within a range can enhance the quality of an elastogram due to its relatively shorter wavelength; and (2) a high frequency will cause attenuation of the wave propagation, which potentially leads to the presence of artifacts on the elastogram;

- The amplitude of the mechanical wave controls the quality (intensity) of the wave propagation and indirectly affects the calculation of the stiffness map. A wave with a low frequency should not be partnered with a relatively higher amplitude due to the production of phase wrapping artifacts on the phase contrast images; a wave with a high frequency should not be set with a relatively lower amplitude because of the attenuation of the mechanical wave signal occurring on the phase contrast images. Either phenomenon stated above can produce artifacts in the stiffness map. Thus, the amplitude must be chosen according to the selected frequency;
- The testing programs developed for this QA phantom can provide a guideline for other MRE applications.

In Chapter 5, the proposed MRE-integrated RT framework carried out on the prostate phantom can conclude that

- The two level (the coarse and fine) is a feasible scan strategy that can quickly pinpoint the optimal MRE scan parameters to produce high-quality elastograms,
- MRE has demonstrated the potential feasibility of direct integration into a modern treatment planning system,
- Using the MRE data allows a simultaneous boost to the dominant intraprostatic lesions (DIL) to 84 Gy, while maintaining the rest of the prostate to the prescription dose of 78 Gy, and
- Using a volumetric modulate arc therapy (VMAT) technique achieves a highly conformal plan: the conformity index for the prostate and combined DILs is 0.98 and 0.91.

6.3. Challenges

The first primary challenge encountered in this work is the limited resolution of elastogram which is 256*256 in maximum. A higher resolution can provide more information in revealing small targets. In the future, the modification of the MRE pulse sequence can help resolve this challenge.

The second major challenge is the inversion algorithm that is for calculating elastogram. Though the LFE-based inversion software adopted in this thesis can produce qualified and satisfactory results, the quality of elastogram can still be improved by using more sophisticated inversion algorithms such as Direct Inversion (DI) or Finite Element Method (FEM).

The third key challenge is that the cutoff frequencies for the filtering of wave images are difficult to choose since this processing plays a significant role in the quality of the resultant elastogram. In this work, the repeated experiments and experience provide a feasible way to select the cutoff frequencies practically.

6.4. Future work

In future work, the *in vivo* experiments on MRE need to be conducted to interpret the correlation between the pathologic/healthy states and the stiffness values in specific organs. However, this correlation may vary depending on the examined organs or the types of disease or tumour, and it requires the other established methods or techniques to compare with verify. Furthermore, the physicians or oncologists have the final decision on appropriateness of use, the clinical perspective.

The results of proposed MRE-integrated RT framework in Chapter 5 demonstrate the potential feasibility of planning a VMAT treatment on the MRE-defined lesions from a prostate phantom. The next goal is to find out whether MRE can aid to detect the lesions from patients, providing an additional benefit to diagnosing tumours in combination with multi-parametric MRI and other imaging modalities or examining approaches [122], [123]. The ultimate goal is to carry out this MRE-integrated RT framework to the day-to-day clinical procedure.

As an imaging tool, there is considerable potential in implementing MRE to detect and characterize tumours at more clinical sites (such as cervix and breast) and developing the corresponding MRE-integrated RT framework that is suitable for each different type of cancer.

APPENDICES

A. Filtering of Wave Images

The filtering is the most important step during the inversion procedure, affecting the correctness of the calculation of the stiffness maps. Specifically, due to the means of excitation, the wave propagation in MRE usually mixes the shear wave and the compressional wave: these two wave components have distinct differences in velocity. The shear wave usually has a relatively low velocity (around 10 m/s) in soft tissue at a low frequency of excitation, while the compressional wave has a relatively high velocity (around 1540 m/s [88]) at the same settings. These waves, with different velocities driven by the same frequency, will present different spatial wavelengths within a certain region. Within this region, the compressional wave corresponds to the low frequency spatial component, while the shear wave corresponds to the high frequency spatial component. As the presence of compressional waves can affect the accuracy of the stiffness calculation, compressional waves must be filtered out [88]. Figure A.1 shows a wave propagation acquired from the liver of a healthy volunteer. Figure A.1 (A) shows the axial T2W image of this healthy liver. Figure A.1 (B) shows the wave images without filtering at eight different continuous moments, and it is observed that the shear wave propagating across the plane with a shorter wavelength is clouded by the compressional wave propagating along the out-of-plane direction with a longer wavelength. Figure A.1 (C) depicts the same wave images after filtering; it can be seen that the shear wave propagation is enhanced by filtering out the compressional wave component. The average stiffness value corresponding to the liver areas in the unfiltered case (Figure A.1 (B)) is (69.386 ± 51.125) kPa, while in the filtered case (Figure A.1 (C)) the average stiffness value is (2.849 ± 0.9163) kPa (reported in shear modulus). The average stiffness of a normal liver is around 1.54~2.87 kPa, according to reports in the literature, however, the stiffness of a healthy liver is an ongoing research question, and is beyond the scope of this thesis [22]. In summary, the long wavelength (low frequency) component, the compressional wave, may bias the estimated results, especially for the LFE inversion algorithm.

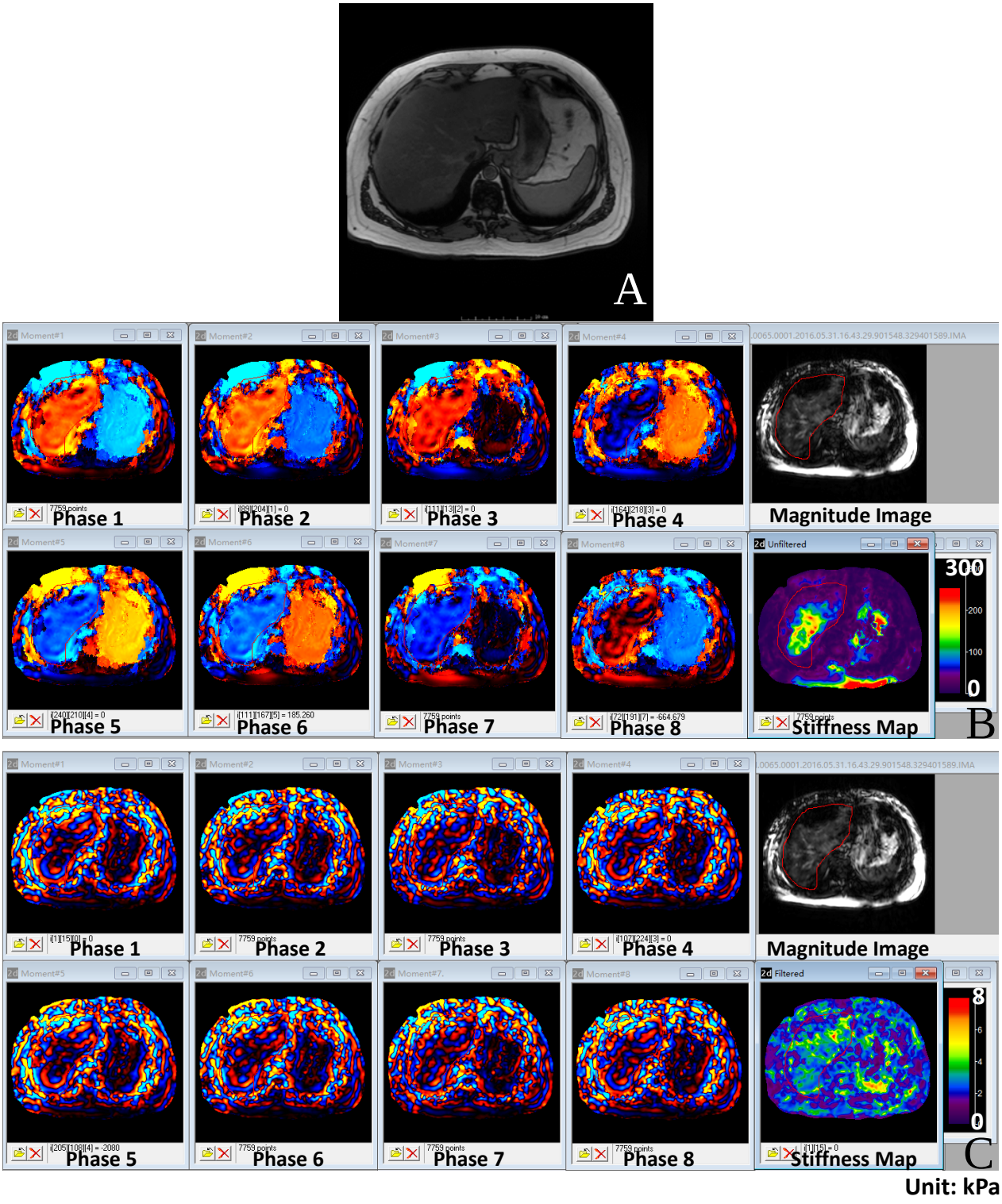

Figure A. 1 (A) Axial T2W image of a healthy volunteer's liver; **(B)** MRE images with compressional wave presence (without filtering); and **(C)** MRE images without (or with less) compressional wave presence (after filtering).

Figure A.2 shows that there is a significant improvement in the quality of the stiffness map, i.e., a clearer delineation of detailed structure in all three stiff targets, after the compressional wave is removed from the wave propagation. This result indicates that the existence of the compressional wave will degrade the quality of the stiffness map and thus affect the MRE detection ability. By setting up two cutoff frequencies, a bandpass filter is implemented which can jointly remove the low frequency compressional wave and existing high frequency background noise. However, there is a logical paradox in selecting the cutoff frequency because the "correct" wave propagation cannot be defined without knowing the exact elasticity distribution in a tissue (object), meanwhile, the exact elasticity distribution cannot be known without a "correct" wave propagation. Therefore, it is not easy to select the most appropriate cutoff frequency. Figure A.2 shows that the stiffness map from cutoff frequency#2 is superior to the stiffness map from cutoff frequency#1, even though the compressional waves in both cases are visually removed. In addition, the cutoff frequency–the number of waves per field of view (FOV)—largely relies on the driven frequency, the size of the field of view, and the dimensions of ROIs, which means the appropriate cutoff frequency will vary in different scenarios. To sum up, the selection of the cutoff frequencies must not only guarantee the removal of the compressional wave and the noise, but it must also avoid over-filtering the shear wave that must be retained to provide the elasticity information.

Figure A. 2 A comparison between the unfiltered case and the filtered cases with different cutoff frequencies.

As the wave length of the shear wave is much more sensitive to different elasticities than the wave length of the compressional wave, most MRE techniques only need to acquire the shear wave propagation. This has the disadvantage of obtaining only the shear properties of tissue rather than both shear and compressional properties of tissue [88]. Though some techniques can solve both the shear and compressional properties—the shear modulus and the first Lamé parameter—simultaneously in the presence of both shear and compressional waves, the difference between

these two types of waves can be orders of magnitude, which results in a huge difference between the shear and compressional properties as well. Therefore, it is challenging for current strategies to estimate both properties accurately at the same time, such as Finite Element Method (FEM)-based inversion algorithm [18].

Given this practical consideration, removing compressional waves and calculating the stiffness map based on the shear wave propagation is the alternative usually adopted. However, because there is a significant variation in the wavelength of the shear wave when it propagates through targets with different stiffness levels, the relatively longer wavelength extended by the stiffer target might overlap with the coexisting compressional wave in low spatial frequency spectrum, making the cutoff frequency more difficult to determine. The same situation occurs when a relatively shorter wavelength shrunk by a softer target might overlap with high frequency noise in high spatial frequency spectrum. In either case, inappropriate selection of the cutoff frequency can cause an over-filtering. Figure A.3 shows an example of over-filtering through the modified Quality Assurance (QA) phantom) including soft and the stiff targets on a moderately stiff background. The inclusions are arranged from the softest to the hardest from left to right, and the stiffness value of the background is in a medium range that allows equal amounts of shorter and longer wavelengths to be exposed on the same FOV. Figure A.3 (A) indicates a case where the stiffness map clearly delineates the inclusions and reports their corresponding elasticities. The wave propagates smoothly from moment to moment; the wavelengths within the inclusions change as they are supposed to—the harder target extends the wavelength while the softer target shrinks the wavelength; and the calculated stiffness map presents a qualitatively fine quality. In this case, the pair of cutoff frequencies (10 ~ 50 waves/FOV) chosen here is recognized as an appropriate filtering. Based on this reference, when the low limit of the cutoff frequency is set too high, the hardest inclusion with the longest wavelength is the first one to disappear from the stiffness map. Moreover, by tracking back to the wave propagation, it can be found that the wave propagations through these areas are disturbed, that is to say, they fail to follow the propagation path or/and they present some signal loss as shown in Figure A.3 (B). Such disturbed wave propagations are labeled by black circles, and are more prone to be observed from the animated wave propagation frames. This is equally true in Figure A.3 (C) where the black circles indicate that the high limit of the cutoff frequency is set too low, which causes the softest inclusion with the shortest wavelength to vanish from the stiffness map. These observations repeated in several trials help the user to decide what cutoff frequencies are appropriate, but the selection of cutoff frequencies is still a tricky and tedious process. In a nutshell, monitoring of the filtering process can assure the quality of the stiffness map, and since the FOV, the driven frequency, and the wavelength changes differ with each scan, the factors that decide the selection of cutoff frequency should be customized and guided by observing and monitoring the quality of wave propagation.

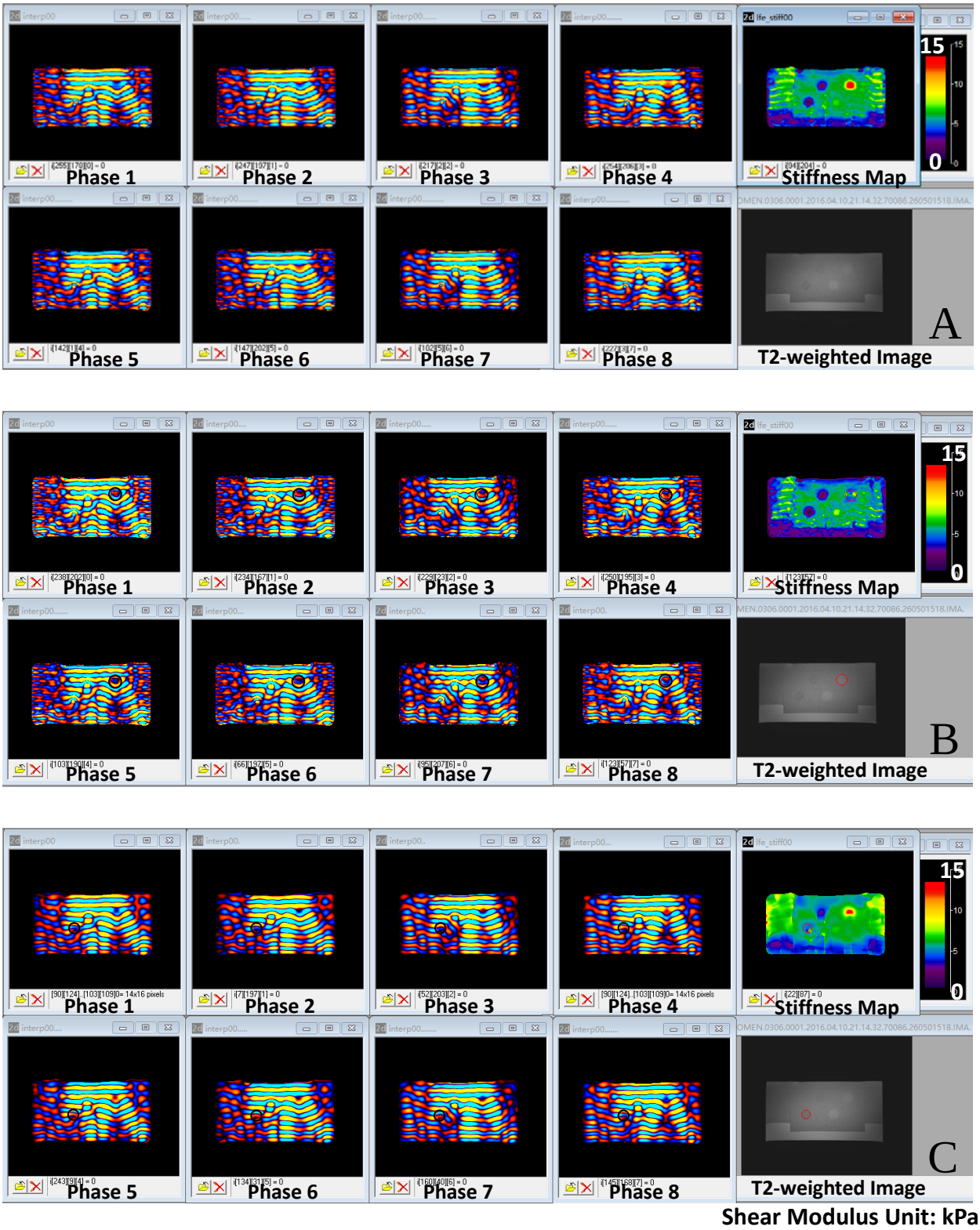

Figure A. 3 (A) Results with appropriately selected cutoff frequencies; **(B)** over-filtering of the low frequency component; and **(C)** over-filtering of the high frequency component.

B. Summary of the Saskatchewan Cancer Agency's guideline of VMAT treatment planning for prostate

Prescription Intent

- Prescibed dose up to and including 78 Gy.

- The following is a typical examples of fractionation,
    - 78 Gy in 39 fractions
    - 74 Gy in 37 fractions

- Nonstandard:
    - Approved Clinical Trials

Table B. 1 Structure Set

Structure Set	Contour Definition	Contour Colour	Structure SCA nomenclature
GTV* (optional)	Physician defined	Blue	GTV
CTV**	Physician defined	Magenta	CTVp (Prescription)
PTV	CTV + margin*	Cyan	PTVp (Prescription)
Proximal Seminal Vesicles	Proximal 1.0 cm	Burnt Orange	SeminalVesProx
Seminal Vesicles	Whole organ	Lt Orange	SemincalVesicle
Rectum	Ischial Tuber to Ant Flexure	Red	Rectum
Bladder	Whole organ	Green	Bladder
R Femoral Head	Head to greater Trochanter	LtGreen	FemurR
L Femoral Head	Head to greater Trochanter	TruBlue	FemurL

Author's note: * "GTV" represents "gross target volume";
** "CTV" represents "clinical target volume".

- Margin: A typical CTV-to-PTV expansion would be 1.0 cm (0.7 cm posterior). A smaller margin may be used in cases where gold seed fiducial markers and/or CBCT imaging are employed.

Table B. 2 Dose Limits

Importance	Structure	Standard Constraints
1	PTV	$D_{max} \leq$ 107-110%
		Mean $\geq$ 100%
2	Rectum	$V_{75Gy} \leq 15\%$
		$V_{70Gy} \leq 25\%$
		$V_{60Gy} \leq 35\%$
		$V_{50Gy} \leq 50\%$
3	Bladder	$V_{75Gy} \leq 15\%$
		$V_{70Gy} \leq 25\%$
		$V_{65Gy} \leq 35\%$
		$V_{55Gy} \leq 50\%$
4	R Femoral Head	$V_{45Gy} \leq 10\%$
		$D_{max} \leq$ 50Gy
	L Femoral Head	$V_{45Gy} \leq 10\%$
		$D_{max} \leq$ 50Gy
6	CTV	$V_{98\%} \geq 98\%$

LIST OF REFERENCES

[1] H. K. Walker, W. D. Hall, and J. W. Hurst, Eds., *Clinical Methods: The History, Physical, and Laboratory Examinations*, 3rd ed. Boston: Butterworths, 1990.

[2] F. H. Schröder *et al.*, "Evaluation of the digital rectal examination as a screening test for prostate cancer," *J. Natl. Cancer Inst.*, vol. 90, no. 23, pp. 1817–1823, 1998.

[3] J. Fenner, A. C. Stacer, F. Winterroth, T. D. Johnson, K. E. Luker, and G. D. Luker, "Macroscopic Stiffness of Breast Tumors Predicts Metastasis," *Sci. Rep.*, vol. 4, Jul. 2014.

[4] N. H. Afdhal and D. Nunes, "Evaluation of Liver Fibrosis: A Concise Review," *Am. J. Gastroenterol.*, vol. 99, no. 6, pp. 1160–1174, Jun. 2004.

[5] D. S. Cooper *et al.*, "Management guidelines for patients with thyroid nodules and differentiated thyroid cancer: The American Thyroid Association Guidelines Taskforce," *Thyroid*, vol. 16, no. 2, pp. 109–142, 2006.

[6] D. Ilic, M. M. Neuberger, M. Djulbegovic, and P. Dahm, "Screening for prostate cancer," in *Cochrane Database of Systematic Reviews*, John Wiley & Sons, Ltd, 2013.

[7] P. Charney, U. Boynton, and D. H. Barad, "The gynecologic examination," *Pract. Gynecol. Guide Prim. Care Physician Phila. Am. Coll. Physicians*, vol. 1, 2002.

[8] R. Unkels, "Gynecological History Taking and Examination."

[9] I. Leconte *et al.*, "Mammography and subsequent whole-breast sonography of nonpalpable breast cancers: the importance of radiologic breast density," *Am. J. Roentgenol.*, vol. 180, no. 6, pp. 1675–1679, 2003.

[10] E. A. Sickles, "Mammographic features of 300 consecutive nonpalpable breast cancers," *Am. J. Roentgenol.*, vol. 146, no. 4, pp. 661–663, 1986.

[11] J. I. Epstein, P. C. Walsh, M. Carmichael, and C. B. Brendler, "Pathologic and clinical findings to predict tumor extent of nonpalpable (stage t1 c) prostate cancer," *Jama*, vol. 271, no. 5, pp. 368–374, 1994.

[12] L. A. Eskew, R. L. Bare, and D. L. McCullough, "Systematic 5 Region Prostate Biopsy is Superior to Sextant Method for Diagnosing Carcinoma of the Prostate," *J. Urol.*, vol. 157, no. 1, pp. 199–203, Jan. 1997.

[13] S. Ohsumi, S. Takashima, K. Aogi, M. Ishizaki, and K. Mandai, "Breast Biopsy for Mammographically Detected Non-palpable Lesions Using a Vacuum-assisted Biopsy Device (Mammotome) and an Upright-type Stereotactic Mammography Unit," *Jpn. J. Clin. Oncol.*, vol. 31, no. 11, pp. 527–531, Nov. 2001.

[14] E. D. Pisano *et al.*, "Fine-Needle Aspiration Biopsy of Nonpalpable Breast Lesions in a Multicenter Clinical Trial: Results from the Radiologic Diagnostic Oncology Group V," *Radiology*, vol. 219, no. 3, pp. 785–792, Jun. 2001.

[15] A. Sarvazyan, T. J. Hall, M. W. Urban, M. Fatemi, S. R. Aglyamov, and B. S. Garra, "An overview of elastography–an emerging branch of medical imaging," *Curr. Med. Imaging Rev.*, vol. 7, no. 4, p. 255, 2011.

[16] K. J. Parker, M. M. Doyley, and D. J. Rubens, "Imaging the elastic properties of tissue: the

20 year perspective," *Phys. Med. Biol.*, vol. 56, no. 1, p. R1, 2011.
[17] P. N. Wells and H.-D. Liang, "Medical ultrasound: imaging of soft tissue strain and elasticity," *J. R. Soc. Interface*, vol. 8, no. 64, pp. 1521–1549, 2011.
[18]Y. K. Mariappan, K. J. Glaser, and R. L. Ehman, "Magnetic resonance elastography: a review," *Clin. Anat.*, vol. 23, no. 5, pp. 497–511, 2010.
[19] A. M. Aisen, W. Martel, E. M. Braunstein, K. I. McMillin, W. A. Phillips, and T. F. Kling, "MRI and CT evaluation of primary bone and soft-tissue tumors," *Am. J. Roentgenol.*, vol. 146, no. 4, pp. 749–756, 1986.
[20] R. Muthupillai, D. J. Lomas, P. J. Rossman, J. F. Greenleaf, A. Manduca, and R. L. Ehman, "Magnetic resonance elastography by direct visualization of propagating acoustic strain waves," *Science*, vol. 269, no. 5232, pp. 1854–1857, 1995.
[21] "Magnetic resonance elastography - Mayo Clinic." [Online]. Available: http://www.mayoclinic.org/tests-procedures/magnetic-resonance-elastography/basics/definition/prc-20013647. [Accessed: 06-Dec-2016].
[22] S. Venkatesh and R. Ehman, "Magnetic resonance elastography of abdomen," *Abdom. Imaging*, vol. 40, no. 4, pp. 745–759, 2015.
[23] L. D. Brown, L. M. Franco, N. Rafeh, and T. Hatzell, *Quality assurance of health care in developing countries*. Quality assurance project, 1992.
[24] H. L. Oestreicher, "Field and impedance of an oscillating sphere in a viscoelastic medium with an application to biophysics," *J. Acoust. Soc. Am.*, vol. 23, no. 6, pp. 707–714, 1951.
[25] H. E. von Gierke, H. L. Oestreicher, E. K. Franke, H. O. Parrack, and W. W. von Wittern, "Physics of vibrations in living tissues," *J. Appl. Physiol.*, vol. 4, no. 12, pp. 886–900, 1952.
[26] R. J. Dickinson and C. R. Hill, "Measurement of soft tissue motion using correlation between A-scans," *Ultrasound Med. Biol.*, vol. 8, no. 3, pp. 263–271, 1982.
[27] M. Tristam, D. C. Barbosa, D. O. Cosgrove, D. K. Nassiri, J. C. Bamber, and C. R. Hill, "Ultrasonic study of in vivo kinetic characteristics of human tissues," *Ultrasound Med. Biol.*, vol. 12, no. 12, pp. 927–937, Dec. 1986.
[28] M. Tristam, D. C. Barbosa, D. O. Cosgrove, J. C. Bamber, and C. R. Hill, "Application of fourier analysis to clinical study of patterns of tissue movement," *Ultrasound Med. Biol.*, vol. 14, no. 8, pp. 695–707, 1988.
[29] L. S. Wilson and D. E. Robinson, "Ultrasonic measurement of small displacements and deformations of tissue," *Ultrason. Imaging*, vol. 4, no. 1, pp. 71–82, Jan. 1982.
[30] Y. Yamakoshi, J. Sato, and T. Sato, "Ultrasonic imaging of internal vibration of soft tissue under forced vibration," *IEEE Trans. Ultrason. Ferroelectr. Freq. Control*, vol. 37, no. 2, pp. 45–53, Mar. 1990.
[31] R. M. Lerner, S. R. Huang, and K. J. Parker, "'Sonoelasticity' images derived from ultrasound signals in mechanically vibrated tissues," *Ultrasound Med. Biol.*, vol. 16, no. 3, pp. 231–239, Jan. 1990.
[32] K. J. Parker, S. R. Huang, R. A. Musulin, and R. M. Lerner, "Tissue response to mechanical vibrations for 'sonoelasticity imaging,'" *Ultrasound Med. Biol.*, vol. 16, no. 3, pp. 241–246, Jan. 1990.

[33] J. Ophir, I. Cespedes, H. Ponnekanti, Y. Yazdi, and X. Li, “Elastography: a quantitative method for imaging the elasticity of biological tissues,” *Ultrason. Imaging*, vol. 13, no. 2, pp. 111–134, 1991.

[34] L. Sandrin *et al.*, “Transient elastography: a new noninvasive method for assessment of hepatic fibrosis,” *Ultrasound Med. Biol.*, vol. 29, no. 12, pp. 1705–1713, 2003.

[35] V. de Lédinghen *et al.*, “Liver Stiffness Measurement in Children Using FibroScan: Feasibility Study and Comparison With Fibrotest, Aspartate Transaminase to Platelets Ratio Index, and Liver Biopsy:,” *J. Pediatr. Gastroenterol. Nutr.*, vol. 45, no. 4, pp. 443–450, Oct. 2007.

[36] J.-L. Gennisson, T. Deffieux, M. Fink, and M. Tanter, “Ultrasound elastography: Principles and techniques,” *Diagn. Interv. Imaging*, vol. 94, no. 5, pp. 487–495, May 2013.

[37] S. Franchi-Abella, C. Elie, and J.-M. Correas, “Ultrasound elastography: Advantages, limitations and artefacts of the different techniques from a study on a phantom,” *Diagn. Interv. Imaging*, vol. 94, no. 5, pp. 497–501, May 2013.

[38] J. A. Talwalkar, M. Yin, J. L. Fidler, S. O. Sanderson, P. S. Kamath, and R. L. Ehman, “Magnetic resonance imaging of hepatic fibrosis: emerging clinical applications,” *Hepatology*, vol. 47, no. 1, pp. 332–342, 2008.

[39] I. Sack, B. Beierbach, U. Hamhaber, D. Klatt, and J. Braun, “Non-invasive measurement of brain viscoelasticity using magnetic resonance elastography,” *NMR Biomed.*, vol. 21, no. 3, pp. 265–271, 2008.

[40] C. J. Lewa, M. Roth, L. Nicol, J.-M. Franconi, and J. D. de Certaines, “A new fast and unsynchronized method for MRI of viscoelastic properties of soft tissues,” *J. Magn. Reson. Imaging*, vol. 12, no. 5, pp. 784–789, Nov. 2000.

[41] D. B. Plewes, J. Bishop, A. Samani, and J. Sciarretta, “Visualization and quantification of breast cancer biomechanical properties with magnetic resonance elastography,” *Phys. Med. Biol.*, vol. 45, no. 6, p. 1591, 2000.

[42] J. Bishop, A. Samani, J. Sciarretta, and D. B. Plewes, “Two-dimensional MR elastography with linear inversion reconstruction: methodology and noise analysis,” *Phys. Med. Biol.*, vol. 45, no. 8, p. 2081, 2000.

[43] P. J. Rossman, R. Muthupillai, and R. L. Ehman, *Driver device for MR elastography*. Google Patents, 1999.

[44] M. M. Doyley, J. B. Weaver, E. E. Van Houten, F. E. Kennedy, and K. D. Paulsen, “Thresholds for detecting and characterizing focal lesions using steady-state MR elastography,” *Med. Phys.*, vol. 30, no. 4, pp. 495–504, 2003.

[45] K. Uffmann, C. Abicht, W. Grote, H. H. Quick, and M. E. Ladd, “Design of an MR-compatible piezoelectric actuator for MR elastography,” *Concepts Magn. Reson.*, vol. 15, no. 4, pp. 239–254, 2002.

[46] Q. C. C. Chan, G. Li, R. L. Ehman, R. C. Grimm, R. Li, and E. S. Yang, “Needle shear wave driver for magnetic resonance elastography,” *Magn. Reson. Med.*, vol. 55, no. 5, pp. 1175–1179, 2006.

[47] Y. K. Mariappan, P. J. Rossman, K. J. Glaser, A. Manduca, and R. L. Ehman, “Magnetic

resonance elastography with a phased-array acoustic driver system," *Magn. Reson. Med.*, vol. 61, no. 3, pp. 678–685, Mar. 2009.
[48] "Resoundant |," *Resoundant | Developers of MR Elastography*. [Online]. Available: http://www.resoundant.com. [Accessed: 06-Dec-2016].
[49] M. Honarvar, R. S. Sahebjavaher, S. E. Salcudean, and R. Rohling, "Sparsity regularization in dynamic elastography," *Phys. Med. Biol.*, vol. 57, no. 19, p. 5909, 2012.
[50] M. J. Siegel, A. Priatna, B. D. Bolster Jr, and J. J. Kotyk, "Pediatric MR Elastography of the Liver."
[51] J. Zhang *et al.*, "Short-Term Repeatability of Magnetic Resonance Elastography at 3.0 T: Effects of Motion-Encoding Gradient Direction, Slice Position, and Meal Ingestion," *J. Magn. Reson. Imaging*, 2015.
[52] P. R. Moran, "A flow velocity zeugmatographic interlace for NMR imaging in humans," *Magn. Reson. Imaging*, vol. 1, no. 4, pp. 197–203, 1982.
[53] V. Wedeen *et al.*, "Projective imaging of pulsatile flow with magnetic resonance," *Science*, vol. 230, no. 4728, pp. 946–948, Nov. 1985.
[54] M. J. Graves, "Magnetic resonance angiography.," *Br. J. Radiol.*, vol. 70, no. 829, pp. 6–28, 1997.
[55] R. Sinkus *et al.*, "Imaging anisotropic and viscous properties of breast tissue by magnetic resonance-elastography," *Magn. Reson. Med.*, vol. 53, no. 2, pp. 372–387, Feb. 2005.
[56] J. Rydberg, R. Grimm, S. Kruse, J. Felmlee, P. McCracken, and R. Ehman, "Fast spin-echo magnetic resonance elastography of the brain," in *Proceedings of the International Society for Magnetic Resonance in Medicine*, 2001, p. 1647.
[57] S. A. Kruse, R. C. Grimm, D. S. Lake, A. Manduca, and R. L. Ehman, "Fast EPI based 3D MR elastography of the brain," in *Proceedings of the International Society for Magnetic Resonance in Medicine*, 2006, p. 3385.
[58] D. a. Herzka, M. s. Kotys, R. Sinkus, R. i. Pettigrew, and A. m. Gharib, "Magnetic resonance elastography in the liver at 3 Tesla using a second harmonic approach," *Magn. Reson. Med.*, vol. 62, no. 2, pp. 284–291, Aug. 2009.
[59] O. Bieri, S. Maderwald, M. e. Ladd, and K. Scheffler, "Balanced alternating steady-state elastography," *Magn. Reson. Med.*, vol. 55, no. 2, pp. 233–241, Feb. 2006.
[60] S. K. Venkatesh, M. Yin, and R. L. Ehman, "Magnetic resonance elastography of liver: technique, analysis, and clinical applications," *J. Magn. Reson. Imaging*, vol. 37, no. 3, pp. 544–555, 2013.
[61] A. Manduca, R. Muthupillai, P. J. Rossman, J. F. Greenleaf, and R. L. Ehman, "Local wavelength estimation for magnetic resonance elastography," in *Image Processing, 1996. Proceedings., International Conference on*, 1996, vol. 3, pp. 527–530.
[62] A. Manduca *et al.*, "Magnetic resonance elastography: Non-invasive mapping of tissue elasticity," *Med. Image Anal.*, vol. 5, no. 4, pp. 237–254, Dec. 2001.
[63] A. Arani, D. Plewes, A. Krieger, and R. Chopra, "The feasibility of endorectal MR elastography for prostate cancer localization," *Magn. Reson. Med.*, vol. 66, no. 6, pp. 1649–1657, Dec. 2011.

[64] A. J. T. Suraj D Serai, “Pediatric Liver MR Elastography,” *Dig. Dis. Sci.*, vol. 57, no. 10, pp. 2713–9, 2012.
[65] K. Xiang, X. L. Zhu, C. X. Wang, and B. N. Li, “MREJ: MRE elasticity reconstruction on ImageJ,” *Comput. Biol. Med.*, vol. 43, no. 7, pp. 847–852, Aug. 2013.
[66] A. J. Towbin, S. D. Serai, and D. J. Podberesky, “Magnetic Resonance Imaging of the Pediatric Liver: Imaging of Steatosis, Iron Deposition, and Fibrosis,” *Magn. Reson. Imaging Clin. N. Am.*, vol. 21, no. 4, pp. 669–680, Nov. 2013.
[67] G. Thörmer *et al.*, “Novel technique for MR elastography of the prostate using a modified standard endorectal coil as actuator,” *J. Magn. Reson. Imaging*, vol. 37, no. 6, pp. 1480–1485, 2013.
[68] S. D. Serai *et al.*, “Magnetic Resonance Elastography of the Liver in Patients Status-Post Fontan Procedure: Feasibility and Preliminary Results,” *Congenit. Heart Dis.*, vol. 9, no. 1, pp. 7–14, Jan. 2014.
[69] S. A. Xanthakos *et al.*, “Use of Magnetic Resonance Elastography to Assess Hepatic Fibrosis in Children with Chronic Liver Disease,” *J. Pediatr.*, vol. 164, no. 1, pp. 186–188, Jan. 2014.
[70] G. Low *et al.*, “Reliability of magnetic resonance elastography using multislice two-dimensional spin-echo echo-planar imaging (SE-EPI) and three-dimensional inversion reconstruction for assessing renal stiffness,” *J. Magn. Reson. Imaging*, 2014.
[71] D. B. Wallihan, D. J. Podberesky, B. S. Marino, J. S. Sticka, and S. Serai, “Relationship of MR elastography determined liver stiffness with cardiac function after Fontan palliation,” *J. Magn. Reson. Imaging*, vol. 40, no. 6, pp. 1328–1335, Dec. 2014.
[72] T. E. Oliphant, A. Manduca, R. L. Ehman, and J. F. Greenleaf, “Complex-valued stiffness reconstruction for magnetic resonance elastography by algebraic inversion of the differential equation,” *Magn. Reson. Med.*, vol. 45, no. 2, pp. 299–310, 2001.
[73] E. E. W. Van Houten, K. D. Paulsen, M. I. Miga, F. E. Kennedy, J. B. Weaver, and others, “An overlapping subzone technique for MR-based elastic property reconstruction,” *Magn. Reson. Med.*, vol. 42, no. 4, pp. 779–786, 1999.
[74] E. E. Van Houten, M. I. Miga, J. B. Weaver, F. E. Kennedy, and K. D. Paulsen, “Three-dimensional subzone-based reconstruction algorithm for MR elastography,” *Magn. Reson. Med.*, vol. 45, no. 5, pp. 827–837, 2001.
[75] E. Park and A. M. Maniatty, “Shear modulus reconstruction in dynamic elastography: time harmonic case,” *Phys. Med. Biol.*, vol. 51, no. 15, p. 3697, 2006.
[76] M. D. J. McGarry *et al.*, “Multiresolution MR elastography using nonlinear inversion,” *Med. Phys.*, vol. 39, no. 10, pp. 6388–6396, 2012.
[77] M. Honarvar, “Dynamic elastography with finite element-based inversion,” 2015.
[78] Y. Zhu, T. J. Hall, and J. Jiang, “A finite-element approach for Young’s modulus reconstruction,” *IEEE Trans. Med. Imaging*, vol. 22, no. 7, pp. 890–901, Jul. 2003.
[79] A. A. Oberai, N. H. Gokhale, and G. R. Feijóo, “Solution of inverse problems in elasticity imaging using the adjoint method,” *Inverse Probl.*, vol. 19, no. 2, p. 297, 2003.
[80] H. Eskandari, S. E. Salcudean, R. Rohling, and J. Ohayon, “Viscoelastic characterization of soft tissue from dynamic finite element models,” *Phys. Med. Biol.*, vol. 53, no. 22, p. 6569,

2008.
[81] M. Yin *et al.*, “Assessment of hepatic fibrosis with magnetic resonance elastography,” *Clin. Gastroenterol. Hepatol.*, vol. 5, no. 10, pp. 1207–1213, 2007.
[82] Y. Wang *et al.*, “Assessment of chronic hepatitis and fibrosis: comparison of magnetic resonance elastography (MRE) and diffusion-weighted imaging (DWI),” *AJR Am. J. Roentgenol.*, vol. 196, no. 3, p. 553, 2011.
[83] R. Rustogi *et al.*, “Accuracy of MR elastography and anatomic MR imaging features in the diagnosis of severe hepatic fibrosis and cirrhosis,” *J. Magn. Reson. Imaging*, vol. 35, no. 6, pp. 1356–1364, 2012.
[84] S. K. Venkatesh and R. L. Ehman, “Magnetic resonance elastography of liver,” *Magn. Reson. Imaging Clin. N. Am.*, vol. 22, no. 3, pp. 433–446, 2014.
[85] J. T. Poterucha *et al.*, “Magnetic Resonance Elastography: A Novel Technique for the Detection of Hepatic Fibrosis and Hepatocellular Carcinoma After the Fontan Operation,” in *Mayo Clinic Proceedings*, 2015, vol. 90, pp. 882–894.
[86] A. Srinivasa Babu *et al.*, “Elastography in chronic liver disease: modalities, techniques, limitations, and future directions,” *RadioGraphics*, vol. 36, no. 7, pp. 1987–2006, 2016.
[87] S. K. Venkatesh and R. L. Ehman, *Magnetic Resonance Elastography*. Springer, 2014.
[88] K. J. Glaser, A. Manduca, and R. L. Ehman, “Review of MR elastography applications and recent developments,” *J. Magn. Reson. Imaging*, vol. 36, no. 4, pp. 757–774, 2012.
[89] R. S. Sahebjavaher, A. Baghani, M. Honarvar, R. Sinkus, and S. E. Salcudean, “Transperineal prostate MR elastography: initial in vivo results,” *Magn. Reson. Med.*, vol. 69, no. 2, pp. 411–420, 2013.
[90] R. S. Sahebjavaher *et al.*, “Prostate MR elastography with transperineal electromagnetic actuation and a fast fractionally encoded steady-state gradient echo sequence,” *NMR Biomed.*, vol. 27, no. 7, pp. 784–794, 2014.
[91] R. S. Sahebjavaher *et al.*, “MR elastography of prostate cancer: quantitative comparison with histopathology and repeatability of methods,” *NMR Biomed.*, vol. 28, no. 1, pp. 124–139, 2015.
[92] R. S. Sahebjavaher *et al.*, “MR elastography and diffusion-weighted imaging of ex vivo prostate cancer: quantitative comparison to histopathology,” *NMR Biomed.*, vol. 28, no. 1, pp. 89–100, 2015.
[93] P. C. Lauterbur, “Image formation by induced local interactions: examples employing nuclear magnetic resonance,” 1973.
[94] P. Suetens, *Fundamentals of Medical Imaging*. Cambridge University Press, 2009.
[95] Z.-P. Liang and P. C. Lauterbur, *Principles of magnetic resonance imaging: a signal processing perspective*. “The” Institute of Electrical and Electronics Engineers Press, 2000.
[96] R. A. de Graaf, *In Vivo NMR Spectroscopy: Principles and Techniques*. John Wiley & Sons, 2013.
[97] M. A. Bernstein, K. F. King, and X. J. Zhou, *Handbook of MRI Pulse Sequences*, 1 edition. Amsterdam ; Boston: Academic Press, 2004.
[98] B. Lautrup, *Physics of Continuous Matter, Second Edition: Exotic and Everyday Phenomena*

in the Macroscopic World, 2 edition. Boca Raton: CRC Press, 2011.

[99] "Solid Mechanics Part I." [Online]. Available: http://homepages.engineering.auckland.ac.nz/~pkel015/SolidMechanicsBooks/Part_I/index.html. [Accessed: 02-Dec-2016].

[100] "Introduction to Aerospace Structures (ASEN 3112) Course Material." [Online]. Available: http://www.colorado.edu/engineering/CAS/courses.d/Structures.d/. [Accessed: 04-May-2017].

[101] O. C. Zienkiewicz and R. L. Taylor, *Finite Element Method: Volume 1, Fifth Edition*, 5 edition. Oxford ; Boston: Butterworth-Heinemann, 2000.

[102] I. S. Sokolnikoff, R. D. Specht, and others, *Mathematical theory of elasticity*, vol. 83. McGraw-Hill New York, 1956.

[103] T. E. Oliphant, *Direct methods for dynamic elastography reconstruction: optimal inversion of the interior Helmholtz problem*. 2001.

[104] A. Bedford and D. S. Drumheller, *Elastic wave propagation*. Wiley, 1994.

[105] F. Saeed, "Magnetic resonance elastography," 2011.

[106] B. Bolster, T. Abe, and S. Kannengießer, *Spin-echo Echo Planar Imaging based Magnetic Resonance Elastography (Works in progress)*. Siemens, 2014.

[107] H. Knutsson, C.-F. Westin, and G. Granlund, "Local multiscale frequency and bandwidth estimation," in *Image Processing, 1994. Proceedings. ICIP-94., IEEE International Conference*, 1994, vol. 1, pp. 36–40.

[108] T. E. Oliphant, J. L. Mahowald, R. L. Ehman, and J. F. Greenleaf, "Complex-valued quantitative stiffness estimation using dynamic displacement measurements and local inversion of conservation of momentum," in *1999 IEEE Ultrasonics Symposium. Proceedings. International Symposium (Cat. No.99CH37027)*, 1999, vol. 2, pp. 1641–1644 vol.2.

[109] "Standard Test Methods for Rubber Properties in Compression." [Online]. Available: http://www.astm.org/cgi-bin/resolver.cgi?D575-91(2012). [Accessed: 13-Mar-2017].

[110] J. Oudry, J. Chen, K. J. Glaser, V. Miette, L. Sandrin, and R. L. Ehman, "Cross-validation of magnetic resonance elastography and ultrasound-based transient elastography: A preliminary phantom study," *J. Magn. Reson. Imaging*, vol. 30, no. 5, pp. 1145–1150, Nov. 2009.

[111]G. E. Leclerc *et al.*, "Characterization of a hyper-viscoelastic phantom mimicking biological soft tissue using an abdominal pneumatic driver with magnetic resonance elastography (MRE)," *J. Biomech.*, vol. 45, no. 6, pp. 952–957, 2012.

[112] R. Sinkus, J. Lorenzen, D. Schrader, M. Lorenzen, M. Dargatz, and D. Holz, "High-resolution tensor MR elastography for breast tumour detection," *Phys. Med. Biol.*, vol. 45, no. 6, p. 1649, 2000.

[113] E. L. Madsen *et al.*, "ANTHROPOMORPHIC BREAST PHANTOMS FOR TESTING ELASTOGRAPHY SYSTEMS," *Ultrasound Med. Biol.*, vol. 32, no. 6, pp. 857–874, Jun. 2006.

[114] "MRE/Wave - Magnetic Resonance Imaging Lab: Richard L. Ehman - Mayo Clinic Research." [Online]. Available: http://www.mayo.edu/research/labs/magnetic-resonance-

imaging/mre-wave?_ga=1.251021446.1640793623.1433887874. [Accessed: 10-Nov-2015].
[115] C. Pinter, A. Lasso, A. Wang, D. Jaffray, and G. Fichtinger, "SlicerRT: Radiation therapy research toolkit for 3D Slicer," *Med. Phys.*, vol. 39, no. 10, pp. 6332–6338, 2012.
[116] M.-P. Dubuisson and A. K. Jain, "A modified Hausdorff distance for object matching," in *Pattern Recognition, 1994. Vol. 1-Conference A: Computer Vision & Image Processing., Proceedings of the 12th IAPR International Conference on*, 1994, vol. 1, pp. 566–568.
[117] "plastimatch: Hausdorff_distance Class Reference." [Online]. Available: http://plastimatch.org/doxygen/classHausdorff__distance.html#details. [Accessed: 18-Aug-2017].
[118] M. Teoh, C. H. Clark, K. Wood, S. Whitaker, and A. Nisbet, "Volumetric modulated arc therapy: a review of current literature and clinical use in practice," *Br. J. Radiol.*, 2014.
[119] K. P. McGee *et al.*, "MRI in radiation oncology: Underserved needs," *Magn. Reson. Med.*, vol. 75, no. 1, pp. 11–14, 2016.
[120] M. Cruz *et al.*, "Characterization of low-intensity lesions in the peripheral zone of prostate on pre-biopsy endorectal coil MR imaging," *Eur. Radiol.*, vol. 12, no. 2, pp. 357–365, 2002.
[121] N. Venugopal, "Magnetic resonance spectroscopic imaging for improved treatment planning of prostate cancer," 2012.
[122] J. V. Hegde *et al.*, "Multiparametric MRI of Prostate Cancer: An Update on State-of-the-Art Techniques and Their Performance in Detecting and Localizing Prostate Cancer," *J. Magn. Reson. Imaging JMRI*, vol. 37, no. 5, pp. 1035–1054, May 2013.
[123] P. Ost *et al.*, "Volumetric arc therapy and intensity-modulated radiotherapy for primary prostate radiotherapy with simultaneous integrated boost to intraprostatic lesion with 6 and 18 MV: a planning comparison study," *Int. J. Radiat. Oncol. Biol. Phys.*, vol. 79, no. 3, pp. 920–926, 2011.
[124] K. C. Siegmann, T. Xydeas, R. Sinkus, B. Kraemer, U. Vogel, and C. D. Claussen, "Diagnostic value of MR elastography in addition to contrast-enhanced MR imaging of the breast—initial clinical results," *Eur. Radiol.*, vol. 20, no. 2, pp. 318–325, 2010.
[125] T. Xydeas, K. Siegmann, R. Sinkus, U. Krainick-Strobel, S. Miller, and C. D. Claussen, "Magnetic resonance elastography of the breast: correlation of signal intensity data with viscoelastic properties," *Invest. Radiol.*, vol. 40, no. 7, pp. 412–420, 2005.
[126] A. L. McKnight, J. L. Kugel, P. J. Rossman, A. Manduca, L. C. Hartmann, and R. L. Ehman, "MR elastography of breast cancer: preliminary results," *Am. J. Roentgenol.*, vol. 178, no. 6, pp. 1411–1417, 2002.
[127] R. Sinkus, K. Siegmann, T. Xydeas, M. Tanter, C. Claussen, and M. Fink, "MR elastography of breast lesions: Understanding the solid/liquid duality can improve the specificity of contrast-enhanced MR mammography," *Magn. Reson. Med.*, vol. 58, no. 6, pp. 1135–1144, Dec. 2007.
[128] J. Lorenzen *et al.*, "MR elastography of the breast: preliminary clinical results," in *RöFo-Fortschritte auf dem Gebiet der Röntgenstrahlen und der bildgebenden Verfahren*, 2002, vol. 174, pp. 830–834.
[129] E. N. van Lin *et al.*, "IMRT boost dose planning on dominant intraprostatic lesions: gold

marker-based three-dimensional fusion of CT with dynamic contrast-enhanced and 1 H-spectroscopic MRI," *Int. J. Radiat. Oncol. Biol. Phys.*, vol. 65, no. 1, pp. 291–303, 2006.

[130] N. G. Burnet, S. J. Thomas, K. E. Burton, and S. J. Jefferies, "Defining the tumour and target volumes for radiotherapy," *Cancer Imaging*, vol. 4, no. 2, pp. 153–161, Oct. 2004.

[131] G. Bauman, M. Haider, U. A. Van der Heide, and C. Ménard, "Boosting imaging defined dominant prostatic tumors: a systematic review," *Radiother. Oncol.*, vol. 107, no. 3, pp. 274–281, 2013.

[132] L. Feuvret, G. Noël, J.-J. Mazeron, and P. Bey, "Conformity index: a review," *Int. J. Radiat. Oncol. Biol. Phys.*, vol. 64, no. 2, pp. 333–342, 2006.

[133] S. Petkovska, C. Tolevska, S. Kraleva, and E. Petreska, "Conformity index for brain cancer patients," in *CONFERENCE ON MEDICAL PHYSICS AND BIOMEDICAL ENGINEERING*, 2010, p. 56.

[134] K. Ohtakara, S. Hayashi, and H. Hoshi, "The relation between various conformity indices and the influence of the target coverage difference in prescription isodose surface on these values in intracranial stereotactic radiosurgery," *Br. J. Radiol.*, vol. 85, no. 1014, pp. e223–e228, Jun. 2012.

RELATED WORK

1. Abstract: "**Development of a novel phantom for routine quality assurance of an MR elastography system**".
2. Abstract: "**Utilization of MR Elastography for selective boost to dominant intraprostatic lesions**".

Development of a novel phantom for routine quality assurance of an MR elastography system

Lumeng Cui[1,2], Conrad Yuen[3], Ted Lynch[4], Paul Babyn[5], Francis M. Bui[6], and Niranjan Venugopal[1,5]

[1]Department of Medical Physics, Saskatchewan Cancer Agency, Saskatoon, SK, Canada, [2]Division of Biomedical Engineering, University of Saskatchewan, Saskatoon, SK, Canada, [3]Department of Medical Physics, BC Cancer Agency, Vancouver, BC, Canada, [4]Non-ionizing Radiation, CIRS Inc., Norfolk, VA, United States, [5]Department of Medical Imaging, University of Saskatchewan, Saskatoon, SK, Canada, [6]Department of Electrical & Computer Engineering, University of Saskatchewan, Saskatoon, SK, Canada

Synopsis

Magnetic Resonance Elastography (MRE) is a new imaging technique that combines the acoustic waves and MRI to retrieve elastic properties of tissue. Because MRE is non-invasive, there is great clinical interest for its use in the detection of cancer. In this work, we focus on the design of an MRE phantom to be used in the clinical commissioning of an MRE System. With the aid of newly designed pulse sequences and inversion algorithms we have developed a quality assurance process to validate the efficacy of MRE for applications to many clinical sites (i.e. prostate, cervix, uterus).

Introduction

Magnetic Resonance Elastography (MRE) is a new imaging technique that combines the acoustic waves and Magnetic Resonance Imaging (MRI) to retrieve elastic properties of tissue[1]. Because MRE is non-invasive, there is great potential and interest for its use in the detection of cancer[1–4]. Many institutes have dedicated a number of studies determining the optimal experimental parameters and methods to perform MRE in vivo [2,5–8]. At present, the only commercial FDA approved system available for clinical use is the Resoundant System (Rochester, MN). To commission the MR Elastography system, prior to clinical implementation, a set of quality control (QC) tests are needed to verify the efficacy of the MR elastography data (i.e. reproduce predefined stiffness values from phantom data). At present, there are no commercially available phantoms that fit the dimensions of the Resoundant system. As well, limitations using scanner software do not allow for a thorough evaluation over a range of stiffness's required for quality assurance. In this work, we focus on designing a practical MRE phantom that works alongside the Resoundant MRE System. With the aid of newly designed pulse sequences and inversion algorithms we are developing a quality assurance process to validate the efficacy of MRE for applications to other clinical sites (i.e. prostate, cervix, uterus).

Methods and Materials

To verify the efficacy of the MRE technique in a clinical setting, a set of QC tests was performed with two phantoms: an elasticity phantom containing rods of varying stiffness (049A, CIRS Inc., Norfolk, VA) and a prostate phantom containing intraprostatic lesions (053L CIRS Inc., Norfolk, VA). All experiments were carried out on a 3T Skyra platform (Siemens Healthcare, Erlangen, Germany) with the Resoundant system. We employed the Siemens production pulse sequence which encodes the acoustic motion using a 2D gradient echo-based imaging technique. MRE image acquisitions were also repeated using a newly developed spin-echo planar imaging technique (Siemens WIP 923, VE11A). Elastograms were reconstructed using the Siemens scanner inversion program, and MRE/Wave inversion software[9].

Results and Discussions

The dimensions of the paddle used by the Resoundant system is 18.5 cm in diameter, however the surface dimension for 049A phantom is 17×10 cm. This mismatch in the size of paddle and the phantom causes a number of problems. Firstly, the housing of phantom is not flat with the scanning surface as shown in Figure 1 (A). The air gap between the paddle and scanning surface creates an interface between the wave source and the phantom. Additionally, the small housing causes apparent reflections of the shear waves at the sides of housing wall, and therefore generates significant interference and loss of data integrity[10] (as seen by the checkered region in Figure 2). In order to address these issues, a novel phantom was designed based on the 049A phantom, as seen in Figure 1 (D). The original 049A gel block (white area) was placed in a larger housing filled with a dispersive Zerdine gel (grey area) which minimizes wave reflections from the side walls. As well, the new housing was designed with a larger diameter to fit Resoundant paddle. In figures 3 B and C, we present reconstructed stiffness maps calculated by two different inversion algorithms, the Siemens product software, and the MRE/Wave inversion software. For Lesion #1, the mean shear stiffness was 2.59±0.70 kPa versus 11.82±1.10 kPa respectively. The urethra was 1.63±0.81 kPa versus 14.03±1.72 kPa, and for lesion #2, it was 2.20±0.83 kPa versus 11.04±1.67 kPa. The reason for this difference is because the current scanner's inversion program was designed for the Liver, and as such limits the stiffness range

to 0-8 kPa. The large discrepancies observed demonstrates the limited applications of the MRE system to other sites (i.e. cervix cancer, prostate cancer, etc.) using the system configuration as is. But using the newer Siemens WIP, Resoundant system, and MRE/Wave together expands the range of applications for which MRE can be used. Utility of the modified phantom allows us to perform QC tests to verify the reproducibility of the MRE technique for varying stiffness.

Conclusion

In this work we have identified the limited utility of current commercial phantoms available for routine QC tests using the Resoundant MRE system. In collaboration with the manufacturer, we developed a phantom for robust verification of the MRE system over a wide range of stiffness's, thus expanding the clinical utility to other clinical sites (i.e. prostate, cervix, uterus).

Acknowledgements

No acknowledgement found.

References

1. Mariappan, Y. K., Glaser, K. J. & Ehman, R. L. Magnetic resonance elastography: A review. Clin. Anat. 23, 497–511 (2010).

2. McKnight, A. L. et al. MR elastography of breast cancer: preliminary results. Am. J. Roentgenol. 178, 1411–1417 (2002).

3. Frangioni, J. V. New technologies for human cancer imaging. J. Clin. Oncol. 26, 4012–4021 (2008). 4. Venkatesh, S. K. et al. Magnetic resonance elastography of liver tumors-preliminary results. AJR Am. J. Roentgenol. 190, 1534 (2008).

5. Kruse, S. A. et al. Tissue characterization using magnetic resonance elastography: preliminary results. Phys. Med. Biol. 45, 1579 (2000).

6. Plewes, D. B., Bishop, J., Samani, A. & Sciarretta, J. Visualization and quantification of breast cancer biomechanical properties with magnetic resonance elastography. Phys. Med. Biol. 45, 1591 (2000).

7. Green, M. A., Bilston, L. E. & Sinkus, R. In vivo brain viscoelastic properties measured by magnetic resonance elastography. NMR Biomed. 21, 755–764 (2008).

8. Sahebjavaher, R. S., Baghani, A., Honarvar, M., Sinkus, R. & Salcudean, S. E. Transperineal prostate MR elastography: Initial in vivo results. Magn. Reson. Med. 69, 411–420 (2013).

9. MRE/Wave - Magnetic Resonance Imaging Lab: Richard L. Ehman - Mayo Clinic Research. at <http://www.mayo.edu/research/labs/magnetic-resonance-imaging/mre-wave?_ga=1.251021446.1640793623.1433887874>

10. Yin, M., Manduca, A. & Grimm, R. C. in Magnetic Resonance Elastography (eds. Venkatesh, S. K. & Ehman, R. L.) 19–37 (Springer New York, 2014).

Figures

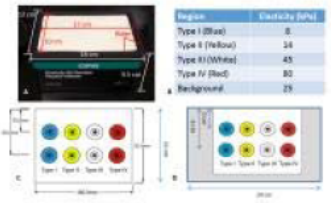

Figure 1. A: 049A phantom; B: Stiffness values reported by the manufacturer; C: Side view of the original phantom; D: Side view of the modified (original gel block is in white) phantom.

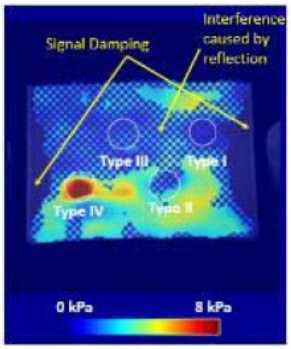

Figure 2. 95% stiffness confidence map overlaid with MRI image displaying interference and signal damping in 049A (FOV=239mm×300mm, 10mm slice thickness, 256×204 resolution, TE=23ms, TR=50ms, and time=19s. The driver amplitude was set to 15% and a frequency of 60Hz).

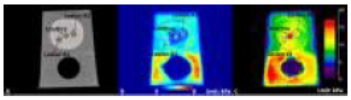

Figure 3. A: T1 weighted MRI Image; B: Stiffness map reconstructed by scanner software; C: Stiffness map reconstructed by MRE/Wave (FOV=119mm×150mm, 5mm slice thickness, 256×204 resolution, TE=23ms, TR=50ms, and time=19s. The driver amplitude was set to 25% and a frequency of 60Hz).

Proc. Intl. Soc. Mag. Reson. Med. 24 (2016)
1957

Utilization of MR Elastography for selective boost to dominant intraprostatic lesions

Lumeng Cui[1,2], Paul Babyn[3], Francis Bui[4], and Niranjan Venugopal[1]

[1]Medical Physics Department, Saskatoon Cancer Centre, Saskatchewan Cancer Agency, Saskatoon, SK, Canada, [2]Division of Biomedical Engineering, University of Saskatchewan, Saskatoon, SK, Canada, [3]Department of Medical Imaging, University of Saskatchewan and Saskatoon Health Region, Saskatoon, SK, Canada, [4]Department of Electrical & Computer Engineering, University of Saskatchewan, Saskatoon, SK, Canada

Synopsis

MRE has the ability to distinguish between elastic properties of the tissue. Furthermore, it is maturing as a technique to differentiate normal and cancerous tissue. In this work we present a strategy to establish high quality MRE data, and present a method to incorporate this information into a radiation treatment planning framework. This new information is used to evaluate the efficacy of dose escalation to dominant intraprostatic lesions using a volumetric modulated arc therapy technique.

Purpose

MRE has shown the ability of quantitatively revealing the mechanical properties of both healthy and cancerous tissue 1,2. This information could be used to segment a dominant intraprostatic lesion (DIL) and then use this information to boost the amount radiation to the DIL, in turn increasing tumour control probability. To improve workflow, an optimized scan procedure designed for radiation treatment planning was developed which includes fusing MRI, MRE and CT scans. This work focuses on investigating the feasibility of integrating the MRE into the Radiation Therapy (RT) process with the aid of a tissue-equivalent prostate phantom.

Materials and Methods

To conduct a feasibility experiment, we utilized a prostate phantom with three DILs (053L CIRS Inc., Norfolk, VA). All MRE/MRI and CT images were carried out on a 3T Skyra MRI system (Siemens Healthcare, Erlangen, Germany) and GE Lightspeed CT simulator (GE Healthcare, Chicago, USA). The MRE scans were obtained using the Resoundant Inc. (Rochester, MN) system in combination with MRE WIP SE-EPI sequence (WIP 923B, Siemens VE11A) for acquisition, and MRE/Wave software 3. To determine the optimal MRE scan parameters to identify "stiff" and "soft" structures, we performed a panel test examining critical parameters including slice thickness, driver frequency and relative signal amplitude. The phantom characteristics, and panel test schema is shown in Figure 1. Using the panel test, we determined the best MRE scan parameters based on how close the MRE defined volume matched the DILs defined on anatomical scans. Once, the combined MRE/MRI scan was obtained, we fused the MRE/MRI to the planning CT scans using Eclipse treatment planning software (Varian Medical Systems, Pal Alto, USA). An external beam radiation treatment was generated utilizing volumetric modulated arc therapy (VMAT). DILs identified on the MRE scans were boosted to 85 Gy, while keeping the dose the prostate gland to 78Gy. Dose coverage, and conformity index were calculated for the prostate and DILs.

Results and Discussions

In our previous work, we demonstrated that the Resoundant MRE system may potentially be used outside the its intended use for liver, and presented quality assurance measurements on a novel phantom design specifically designed for the system 4. The results of the coarse and fine panel tests are shown in Figure 2. The coarse panel test helped narrow the range of frequencies, and the fine panel tests demonstrate the minimum, and maximum frequencies/amplitudes that could be used to obtain good quality MRE data. Figure. 2 (b) and (c) shows, that for this phantom, good quality MRE images can be obtained over the range of 50- 70 Hz, and between 10-30% relative driver amplitude. The lesions and urethra of this phantom are clearly visible on the MRE scans. In comparison to the T2 axial image (Figure.2 (a)) the shape and size of the ROIs match closely to the volumes identified by the MRE images. The best MRE image (see Figure 3) were obtained with settings at 60Hz/10%, 70Hz/10% and 70Hz/30%. Multi-slice MRE scans across the whole prostate were obtained (see Figure. 3). The results in Figure 3 verified that all the "stiff" regions in the prostate are well detected. High quality MRE data provides a direct avenue to integrate this information into radiation treatment planning. In Figure 4, we show an axial view of the dose distribution over-layed on top of the fused MRE/MRI and CT scan of the prostate. Using the combined information were able to boost the MRE defined DILs to 85 Gy, while keeping the prostate 75 Gy. Using a VMAT technique we were able to achieve a highly conformal plan (conformity index for the prostate and combined DILs was 1.1 and 1.25, demonstrating the feasibility of using MRE data for targeted radiation dose escalation.

Conclusion

In this work we have validated a strategy for identifying optimal parameters for MRE data acquisitions. Using a prostate like phantom we showed that the reconstructed MRE images of the DILs matched closely to the anatomical MRI images. Using the optimized workflow we collected MRE/MRI data and fused them to the CT planning scan and achieved an optimized radiation treatment plan with intraprostatic boost to MRE defined regions. The culmination of this work demonstrates the feasibility of using MRE data for radiation treatment planning.

Acknowledgements

No acknowledgement found.

References

1. Mariappan, Yogesh K., Kevin J. Glaser, and Richard L. Ehman. "Magnetic Resonance Elastography: A Review." Clinical Anatomy 23, no. 5 (2010): 497–511.

2. Glaser, Kevin J., Armando Manduca, and Richard L. Ehman. "Review of MR Elastography Applications and Recent Developments." Journal of Magnetic Resonance Imaging 36, no. 4 (2012): 757–774.

3. MRE/Wave - Magnetic Resonance Imaging Lab: Richard L. Ehman - Mayo Clinic Research. at <http://www.mayo.edu/research/labs/magnetic-resonance-imaging/mre-wave?_ga=1.251021446.1640793623.1433887874>

4. Cui, Lumeng, Conrad Yuen, Ted Lynch, Paul Babyn, Francis Bui, and Niranjan Venugopal. "Development of a Novel Phantom for Routine Quality Assurance of an MR Elastography System." Proceedings of the 16th Annual Meeting ISMRM, 2016.

Figures

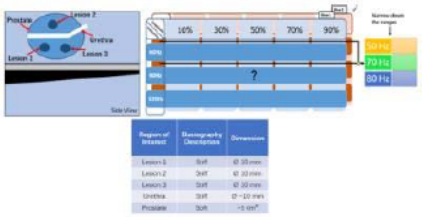

Figure 1: In (a) we present a diagram of the phantom with 3 DILs (i.e. lesions) of increased stiffness compared to the whole prostate. In (b) we present our panel schema to optimize the scan parameters.

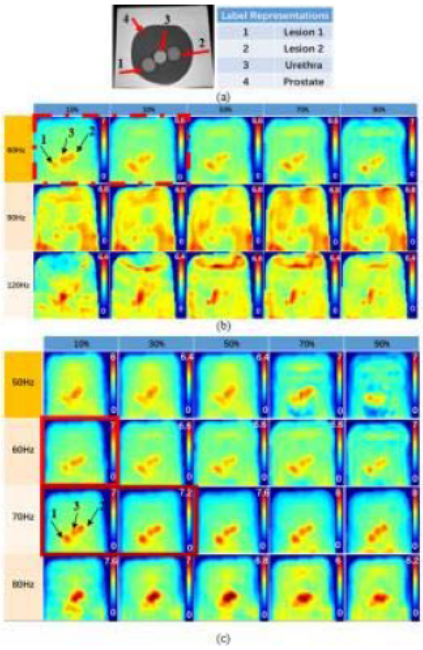

Figure 2: (a) T2 AX Scans (TE/TR 101/7580 ms, FOV 243.75*300 mm2, Resolution 416*512 and Slice Thickness 5 mm); (b) Stiffness maps from the coarse panel tests (FOV 243.75*300 mm2, Resolution 208*256 and Slice Thickness 10 mm); and (b) Stiffness maps from the fine panel tests (FOV 243.75*300 mm2, Resolution 208*256 and Slice Thickness 10 mm). The quantity and unit in stiffness map is recorded as Shear Stiffness and kPa.

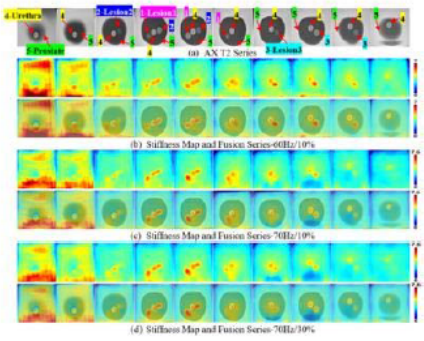

Figure 3: (a) T2 AX series (TE/TR 101/7580 ms, FOV 243.75*300 mm2, Resolution 416*512 and Slice Thickness 5 mm); (b) Stiffness map and fusion series-60Hz/10% (TE/TR 47/1500 ms, FOV 243.75*300 mm2, Resolution 208*256 and Slice Thickness 5 mm); and (c) Stiffness map and fusion series-70Hz/10% (TE/TR 43/1000 ms, FOV 243.75*300 mm2, Resolution 208*256 and Slice Thickness 5 mm); and (d) Stiffness map and fusion series-70Hz/30% (TE/TR 43/1000 ms, FOV 243.75*300 mm2, Resolution 208*256 and Slice Thickness 5 mm);The stiffness map is recorded by Shear Stiffness with unit kPa.

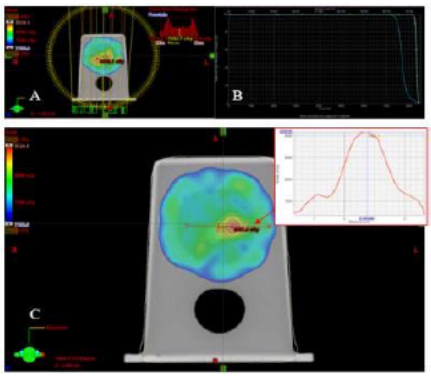

Figure 4: (a) we present an external beam radiation treatment plan using a single arc VMAT technique delivering 78 Gy to the whole prostate, and 85 Gy to the DILs. The conformity index of the 95% of the prescription dose to the prostate volume is 1.1, the conformity index of 95% of the boost dose to the DIL is 1.25. (b) we present the dose volume histogram of the prostate volume and DILs. (c), we observe a line dose profile through the DIL boost region, showing the rapid rise and fall of the dose gradient around the MRE identified region.

Proc. Intl. Soc. Mag. Reson. Med. 25 (2017)
1373